Patient-specific CFD workflows for haemodynamics assessment of Aortic Dissection interventions informed by multimodal clinical data

Louis Girardin

A dissertation submitted for the degree of

Doctor of Philosophy

Department of Mechanical Engineering

Faculty of Engineering Sciences
University College London
18 April 2025

Declaration of Authorship

I, Louis Girardin, confirm that the work presented in this thesis, titled Patient-specific CFD workflows for haemodynamics assessment of Aortic Dissection interventions informed by multi-modal clinical data, is my own. Where information has been derived from other sources, I confirm that this has been indicated in the thesis.

To my beloved Ginette, André and Jean.

Abstract

Type-B Aortic Dissection (TBAD) is a severe cardiovascular disease caused by a tear in the descending aorta, creating an intimal flap (IF) that separates the aortic wall into two lumina. This condition leads to complications such as aortic growth, increased pressure, and partial thrombosis, posing significant risks to patient health. While surgical intervention is often necessary to prevent adverse outcomes, the impact of such procedures and their long-term effects remain poorly understood, highlighting the need for improved tools to guide treatment and follow-up. The coupling of compliant CFD simulations with clinical data, such as MRI images, helps mitigating the limitations of each method. Such pipeline can be used to assess aortic haemodynamics and compliance behaviour, particularly post-surgery when mismatches occur between the native vessel and the implanted device. However, numerous assumptions regarding material properties and the multi-compliance of the reconstructed TBAD, fail to capture physiological dynamics and limit the clinical relevance of the simulation results. The present thesis presents computational pipelines, bypassing the aforementioned limitations, in which compliant CFD simulations enhance routine patient-specific in vivo data, enabling the exploration of virtual surgeries and their effects on TBAD haemodynamics and compliance. Different grafting strategies with varying graft lengths and compliance were first evaluated in a chronic dissection case to assess the impact of compliance mismatch on heart and left ventricular load. Next, a multi-compliant modelling framework was used to evaluate the impact of IF compliance on haemodynamics and disease progression risks. Finally, a method using the pulse wave velocity, a routinely used clinical marker, was used in a patient-specific CFD workflow and facilitated the agreements against in vivo data. This thesis complements efforts in addressing critical modelling assumptions and introducing advanced computational pipelines, this thesis contributes to enhancing the accuracy and clinical applicability of CFD simulations in the assessment and treatment of TBAD, ultimately improving patient-specific outcomes and guiding surgical decision-making.

Impact Statement

Aortic dissection (AD) is a complex cardiovascular condition that poses a significant health risk and burden on healthcare systems worldwide. In the UK and Ireland alone, over 2,000 people lose their lives annually due to AD, surpassing the number of deaths from road traffic accidents. Type B aortic dissection (TBAD), which affects the descending aorta, requires careful management and monitoring to prevent long-term complications. Up to 30% of TBAD patients may develop aneurysmal dilatation of the false lumen within four years, a complication that often necessitates surgical intervention to prevent further risks. Following surgery, reconstructed aortas typically experience compliance loss and mismatch due to the implanted device, negatively affecting cardiovascular function. This can lead to increased strain on the left ventricle and local stress which may further disrupt the aortic wall.

Coupling CFD with *in vivo* data can improve disease progression predictions, personalise treatments, and refine risk assessments. CFD simulations can also identify high-risk patients and optimise treatment, potentially reducing invasive procedures and improving outcomes. To achieve reliable results, CFD simulations need to be compliant and use patient-specific boundary conditions. However, computational models either lack patient-specific *in vivo* data, and use rigid wall and simplified material property assumptions. As a result, such models fail to account for the patient-specific multi-compliance of reconstructed TBAD and introduce inaccuracies.

This thesis focuses on using routinely available clinical *in vivo* data to develop and advance the state of the art of compliant modelling to understand better TBAD post-surgery. First, a novel CFD framework was developed to evaluate the impact of aortic grafts post open surgery in TBAD, using only clinically available data. The results provide critical insights into the role of graft length and material in influencing haemodynamics outcomes, potentially guiding personalised surgical planning. Second, a fully MRI-based patient-specific framework was introduced to simulate the motion of the aortic wall and intimal flap (IF) in TBAD. This work highlighted the crucial role of IF displacement in influencing TBAD haemodynamics, revealing significant impacts on haemodynamics markers influencing aortic disruption risks.

Finally, a new CFD framework incorporating regional pulse wave velocity was proposed, providing an accurate alternative to cross-sectional area variation-based models when compared to *in vivo* haemodynamics. This modelling approach could offer valuable insights into aortae experiencing, natural or surgery-induced, compliance mismatch.

The findings have been disseminated through journal publications and conference presentations, making valuable contributions to the literature. The advancements outlined in this work not only influence best practices in vascular modelling but also support the development of tailored management strategies for TBAD. Ultimately, these contributions may extend beyond aortic disease, thereby enhancing the translation of simulation techniques into clinical practice.

Research Paper Declaration Form A

- 1. For a research manuscript that has already been published
 - a) What is the title of the manuscript?
 Patient-Specific Haemodynamics Analysis of Virtual Grafting Strategies in
 Type-B Aortic Dissection: Impact of Compliance Mismatch
 - b) Please include a link to or doi for the work 10.1007/s13239-024-00713-6
 - c) Where was the work published?Journal of Cardiovascular Engineering and Techonology
 - d) Who published the work? (e.g. OUP)
 Springer
 - e) When was the work published?
 March 2024
 - f) List the manuscript's authors in the order they appear on the publication
 Louis Girardin, Catriona Stokes, Myat Soe Thet, Aung Ye Oo, Stavroula
 Balabani, Vanessa Díaz-Zuccarini
 - g) Was the work peer reviewed?
 - h) Have you retained the copyright?
 - Yes

 i) Was an earlier form of the manuscript uploaded to a preprint server? (e.g.

Yes, medRxiv: https://doi.org/10.1101/2023.06.20.23288122

medRxiv). If 'Yes', please give a link or doi)

2. For multi-authored work, please give a statement of contribution covering all authors (if single-author, please skip to section 4)

Louis Girardin: Investigation, Conceptualisation, Methodology, Writing – original draft, Visualisation. Catriona Stokes: Conceptualisation, Writing -review. Myat Soe Thet: Resources, Clinical insight. Aung Ye Oo: Resources, Clinical insight.

Yes

Stavroula Balabani: Supervision, Conceptualisation, Writing – review editing. Vanessa Díaz-Zuccarini: Supervision, Conceptualisation, Writing – review editing.

3. In which chapter(s) of your thesis can this material be found?

Chapter 2

4. e-Signatures confirming that the information above is accurate (this form should be co-signed by the supervisor/ senior author unless this is not appropriate, e.g. if the paper was a single-author work)

Candidate

Louis Girardin

Date:

15/07/2024

Supervisor/ Senior Author (where appropriate)

Vanessa Díaz-Zuccarini

Date

01/04/2025

Research Paper Declaration Form B

- 1. For a research manuscript prepared for publication but that has not yet been published (if already published, please skip to section 3)
 - a) What is the current title of the manuscript?
 Impact on TBAD haemodynamics of residual intimal flap displacement post TEVAR in compliant patient-specific CFD simulations informed by MRI
 - b) Has the manuscript been uploaded to a preprint server? (e.g. medRxiv; if 'Yes', please give a link or doi)

Yes, https://doi.org/10.1101/2024.09.25.24313546,

- c) Where is the work intended to be published? (e.g. journal names)
 Annals of Biomedical Engineering
- d) List the manuscript's authors in the intended authorship order
 Louis Girardin, Niklas Lind, Hendrik Von Tengg-Kobligk, Stavroula Balabani,
 Vanessa Díaz-Zuccarini
 - e) Stage of publication (e.g. in submission)Submitted in Review
- 2. For multi-authored work, please give a statement of contribution covering all authors (if single-author, please skip to section 4)

Louis Girardin: Investigation, Conceptualisation, Methodology, Writing – original draft, Visualisation. Niklas Lind Stokes: Resources. Hendrik Von Tengg-Kobligk: Resources, Clinical insight. Stavroula Balabani: Supervision, Conceptualisation, Writing – review editing. Vanessa Díaz-Zuccarini: Supervision, Conceptualisation, Writing – review editing.

3. In which chapter(s) of your thesis can this material be found?

Chapter 4

4. e-Signatures confirming that the information above is accurate (this form should be co-signed by the supervisor/ senior author unless this is not appropriate, e.g. if the paper was a single-author work)

Candidate

Louis Girardin

Date:

20/08/2024

Supervisor/ Senior Author (where appropriate)

Vanessa Díaz-Zuccarini

Date

01/04/2025

Research Paper Declaration Form C

- 1. For a research manuscript prepared for publication but that has not yet been published (if already published, please skip to section 3)
 - a) What is the title of the manuscript?

Patient-Specific Compliant Simulation Framework Informed by 4DMRI-Exctracted Pulse Wave Velocity: Application Post-TEVAR

- b) Please include a link to or doi for the work
- 10.1016/j.jbiomech.2024.112266
- c) Where was the work published?

Journal of Biomechanics

d) Who published the work? (e.g. OUP)

Elsevier

e) When was the work published?

September 2024

- f) List the manuscript's authors in the intended authorship order Louis Girardin, Niklas Lind, Hendrik Von Tengg-Kobligk, Stavroula Balabani, Vanessa Díaz-Zuccarini
- 2. For multi-authored work, please give a statement of contribution covering all authors (if single-author, please skip to section 4)

Louis Girardin: Investigation, Conceptualisation, Methodology, Writing – original draft, Visualisation. Niklas Lind Stokes: Resources. Hendrik Von Tengg-Kobligk: Resources, Clinical insight. Stavroula Balabani: Supervision, Conceptualisation, Writing – review editing. Vanessa Díaz-Zuccarini: Supervision, Conceptualisation, Writing – review editing.

3. In which chapter(s) of your thesis can this material be found?

Chapter 3

4. e-Signatures confirming that the information above is accurate (this form should be co-signed by the supervisor/ senior author unless this is not appropriate, e.g. if the paper was a single-author work)

Candidate

Louis Girardin

Date:

15/07/2024

Supervisor/ Senior Author (where appropriate)

Vanessa Díaz-Zuccarini

Date

01/04/2025

Acknowledgements

The completion of my doctoral studies marks the end of an incredible journey, one that would not have been possible without the support, guidance, and encouragement of so many people.

First and foremost, I would like to express my deepest gratitude to my supervisors, Professor Vanessa Díaz-Zuccarini and Professor Stavroula Balabani. Their unwavering support allowed me to pursue my research with curiosity and ambition, fostering an environment where I could explore new ideas while embracing collaboration. Their trust in my work and encouragement to push boundaries made this experience intellectually rewarding and deeply fulfilling.

This work would not have been possible without the support of the Department of Mechanical Engineering at University College London and the British Heart Foundation through the VIRTUOSO project (A Virtual Platform for Precision Vascular Surgery). I am deeply grateful to everyone whose efforts contributed to securing the funding for my research.

I am also sincerely thankful to Prof. Aung and Myat Soe Thet for their invaluable clinical insights throughout our collaboration with St Bartholomew's Hospital. Their expertise provided a strong clinical foundation for my research, ensuring its relevance and impact.

My appreciation extends to Prof. Hendrick von Tengg-Kobligk and Niklas Lind from Bern Inselspital. Working with them was not only a pleasure but also an inspiration, their enthusiasm and joy in their work reinforced the importance of collaboration and the ultimate goal of research: improving patient outcomes.

To my colleagues, I am grateful for the friendships and guidance that enriched my journey. Special thanks to Catriona and Mirko, whose teaching and mentorship helped shape my academic growth. Federica, Qianhui, Manuel, Bab, Theofilos, and Anestis—thank you for your camaraderie and support. A special mention goes to my dear friend Aloma, with whom I shared countless lunches, conversations, and moments of encouragement, as well as a shared passion for sport.

I could fill pages thanking my friends and family, without whom I would not have made it through these four years. I am deeply grateful to have been surrounded by an abundance of dear friends and family members who not only cared about me and my well-being but also debated whether it truly rained more in London than in Burgundy. Among them, I would like to thank Gregoire, Edouard, Matthieu, Pierre, Maxime, Valentin, Thibaut, Lucas, and Mael, whose friendship has been a source of strength.

To my grandparents, and to those we have lost, who taught me that perseverance, resilience, and love can move mountains—your lessons remain with me. To Annie, who can understand when I dream about aortic pressure and whose love and support never failed to cheer me up.

And finally, to my mom, my dad, and my sister—without your daily presence, unwavering encouragement, and unconditional support, I would not have been able to see this thesis through to the end. This achievement is as much yours as it is mine.

Scientific Dissemination

Journal Publications

- Louis Girardin, Catriona Stokes, Myat Soe Thet, Aung Ye Oo, Stavroula Balabani, Vanessa Díaz-Zuccarini, Patient-Specific Haemodynamics Analysis of Virtual Grafting Strategies in Type-B Aortic Dissection: Impact of Compliance Mismatch, Journal of Cardiovascular Engineering and Technology, 2024. DOI:10.1007/s13239-024-00713-6.
- Louis Girardin, Niklas Lind, Hendrik Von Tengg-Kobligk, Stavroula Balabani, Vanessa Díaz-Zuccarini, Patient-Specific Compliant Simulation Framework Informed by 4DMRI-Extracted Pulse Wave Velocity: Application Post-TEVAR, Journal of Biomechanics, 2024. DOI: 10.1016/j.jbiomech.2024.112266.
- Louis Girardin, Niklas Lind, Hendrik Von Tengg-Kobligk, Stavroula Balabani, Vanessa Díaz-Zuccarini, A novel formulation of the moving boundary method for compliant patient-specific simulations of TBAD: impact of thick intimal flap movement, Annals of Biomedical Engineering, in review (2024)

Oral Presentations

- Louis Girardin, Catriona Stokes, Myat Soe Thet, Aung Ye Oo, Stavroula Balabani, Vanessa Díaz-Zuccarini, Compliant Pre/Post-Op Patient-Specific CFD Simulations of Type-B Aortic Dissections Informed by Routine Clinical Datasets, UCL Mechanical Engineering Summer Session 2022, 06/2022 University College London, London, UK.
- Louis Girardin, Catriona Stokes, Myat Soe Thet, Aung Ye Oo, Stavroula Balabani, Vanessa Díaz-Zuccarini, Compliant Pre/Post-Op Patient-Specific CFD Simulations of Type-B Aortic Dissections Informed by Routine Clinical

Datasets, BioMedEng Conference 2022, 8-9/09/2022, University College London, London, UK.

- Louis Girardin, Catriona Stokes, Myat Soe Thet, Aung Ye Oo, Stavroula Balabani, Vanessa Díaz-Zuccarini, Compliant Pre/Post-Op Patient-Specific CFD Simulations of Type-B Aortic Dissections Informed by Routine Clinical Datasets, Aorta: Structure to Rupture 2022, 31/03/2022, Liverpool (presented remotly), UK.
- Louis Girardin, Catriona Stokes, Myat Soe Thet, Aung Ye Oo, Stavroula Balabani, Vanessa Díaz-Zuccarini, Patient-Specific Haemodynamics Analysis of Virtual Grafting Strategies in Type-B Aortic Dissection: Impact of Compliance Mismatch, UCL Mechanical Engineering Summer Session 2023, 06/2023, University College London, London.
- Louis Girardin, Catriona Stokes, Myat Soe Thet, Aung Ye Oo, Stavroula Balabani, Vanessa Díaz-Zuccarini, Patient-Specific Haemodynamics Analysis of Virtual Grafting Strategies in Type-B Aortic Dissection: Impact of Compliance Mismatch, European Society of Biomechanics 2023, 9-12/07/2023 Maastricht, Netherlands.
- Louis Girardin, Niklas Lind, Hendrik Von Tengg-Kobligk, Stavroula Balabani, Vanessa Díaz-Zuccarini, Patient-Specific Compliant Simulation Framework Informed by 4DMRI-Exctracted Pulse Wave Velocity: Application Post-TEVAR, European Society of Biomechanics 2024, 30/06-03/07/2024, Edinburgh, UK.

Poster Presentations

 Louis Girardin, Catriona Stokes, Myat Soe Thet, Aung Ye Oo, Stavroula Balabani, Vanessa Díaz-Zuccarini, Compliant Pre/Post-Op Patient-Specific CFD Simulations of Type-B Aortic Dissections Informed by Routine Clinical Datasets, UCL Mechanical Engineering Summer Session 2021, 06/2021 University College London, London.

- Louis Girardin, Catriona Stokes, Myat Soe Thet, Aung Ye Oo, Stavroula Balabani, Vanessa Díaz-Zuccarini, Compliant Pre/Post-Op Patient-Specific CFD Simulations of Type-B Aortic Dissections Informed by Routine Clinical Datasets, UCL Mechanical Engineering Summer Session 2022, 06/2022 University College London, London.
- Louis Girardin, Catriona Stokes, Myat Soe Thet, Aung Ye Oo, Stavroula Balabani, Vanessa Díaz-Zuccarini, Compliant Pre/Post-Op Patient-Specific CFD Simulations of Type-B Aortic Dissections Informed by Routine Clinical Datasets, BioMedEng Conference 2022, 8-9/09/2022 University College London, London, UK.
- Louis Girardin, Catriona Stokes, Myat Soe Thet, Aung Ye Oo, Stavroula Balabani, Vanessa Díaz-Zuccarini, Patient-Specific Haemodynamics Analysis of Virtual Grafting Strategies in Type-B Aortic Dissection: Impact of Compliance Mismatch, Aortic Awareness Day 2022, 31/10/2022, London, UK.
- Louis Girardin, Catriona Stokes, Myat Soe Thet, Aung Ye Oo, Stavroula Balabani, Vanessa Díaz-Zuccarini, Patient-Specific Haemodynamics Analysis of Virtual Grafting Strategies in Type-B Aortic Dissection: Impact of Compliance Mismatch, UCL Mechanical Engineering Summer Session 2023, 06/2023 University College London, London, UK.

Contents

DECLARATION OF AUTHORSHIP	4
ABSTRACT	8
IMPACT STATEMENT	10
RESEARCH PAPER DECLARATION FORM A	13
RESEARCH PAPER DECLARATION FORM B	15
RESEARCH PAPER DECLARATION FORM C	17
ACKNOWLEDGEMENTS	20
SCIENTIFIC DISSEMINATION	23
CONTENTS	27
LIST OF FIGURES	32
LIST OF TABLES	38
LIST OF ABBREVIATIONS	41
LIST OF SYMBOLS	44
INTRODUCTION	47
1.1. Background	47
1.2. ANATOMY OF THE AORTA	50
1.3. AORTIC DISSECTION: CLINICAL OVERVIEW	53
1.3.1. Classification	53
1.3.2. Aetiology and Risk Factors	54
1.3.3. Clinical Diagnosis	55
1.4. CLINICAL MANAGEMENT OF AORTIC DISSECTION	58
1.4.1. Outcomes and Management	58
1.4.2. Repairs and Interventions	60
1.5. TBAD FLOW DYNAMICS: A DETAILED ANALYSIS	63
1.5.1. Haemodynamics Descriptors	63
1.5.2. TBAD Haemodynamics	65
1.5.3. Clinical Techniques	67
1.5.3.1. 2D Flow MRI	67
1 5 3 2 4D Flow MRI	67

1.:	5.3.3.	Doppler Ultrasound		70
1.:	5.3.4.	Blood Pressure Measurements	S	70
1.5.4	. Caro	liovascular Flow Modelling		71
1.:	5.4.1.	Lumped Parameter Models		72
1.:	5.4.2.	Three-Dimensional Models		74
1.6.	COMPU	TATIONAL MODELLING OF TBA	AD	75
1.6.1	. Nun	nerical Methods		75
1.6.2	. Ima	ge Segmentation		76
1.6.3	. Inle	t Boundary Conditions		78
1.6.4	. Out	et Boundary Conditions		79
1.6.5	. Aor	tic Compliance Modelling		80
1.6.6	. Bloo	od Rheology		83
1.6.7	. Turl	oulent Flow Modelling		84
1.7.	APPLIC	ATIONS OF TBAD MODELLING	i	87
1.7.1	. TBA	AD Morphology: Impact on Ha	aemodynamics	87
1.7.2	. Virt	ual Interventions and Digital T	wins	90
1.7.3	. Mod	lel Validation		93
1.8.	CFD F	OR TBAD: CHALLENGES AND I	NSIGHTS	94
1.9.	OBJECT	TIVES AND OUTLINE OF THE TH	FSIS	96
			ESIS	, ,
VIRTUAL	GRA	AFTING STRATEGIES:		HAEMODYNAMICS
·		AFTING STRATEGIES: ICAL OPTIMISATION FOI	EVALUATING	
OUTCOMES AND	SURG	ICAL OPTIMISATION FO	EVALUATING	HAEMODYNAMICS 98
OUTCOMES AND 2.1.	SURG Introi	ICAL OPTIMISATION FOR	EVALUATING	HAEMODYNAMICS 98 98
2.1. 2.2.	SURG Introi Metho	ICAL OPTIMISATION FOR DUCTION DODS	EVALUATING	HAEMODYNAMICS 98 98 100
2.1. 2.2. 2.2.1	SURG INTROI METHO . Clin	ICAL OPTIMISATION FOR DUCTION DDS ical data	EVALUATING	### HAEMODYNAMICS 98 100 100
2.1. 2.2. 2.2.1 2.2.2	SURG INTROI METHO Clin Geo	ICAL OPTIMISATION FOR DUCTION DDS ical data metry	EVALUATING	HAEMODYNAMICS 98 100 100 102
2.1. 2.2. 2.2.1 2.2.2 2.2.3	SURG INTROI METHO Clin Geo Mes	ICAL OPTIMISATION FOR DUCTION DDS ical data metry h	EVALUATING	98 98 100 100 102 102
2.1. 2.2. 2.2.1 2.2.2 2.2.3 2.2.4	INTROI METHO Clin Geo Mes	ICAL OPTIMISATION FOR DUCTION DDS ical data metry h w boundary conditions	EVALUATING	98 98 100 100 102 102 103
2.1. 2.2. 2.2.1 2.2.2 2.2.3 2.2.4 2.2.5	INTROI METHO Clin Geo Mes Flow	ICAL OPTIMISATION FOR DUCTION DDS ical data metry h w boundary conditions I compliance	EVALUATING	98 98 100 100 102 102 103 110
2.1. 2.2. 2.2.1 2.2.2 2.2.3 2.2.4 2.2.5 2.2.6	INTROI METHO Clin Geo Hes Flov Wal	ICAL OPTIMISATION FOR DUCTION DDS ical data metry h w boundary conditions I compliance O Simulation	EVALUATING	98 98 100 100 102 102 103 110 111
2.1. 2.2. 2.2.1 2.2.2 2.2.3 2.2.4 2.2.5	INTROI METHO Clim Geo Hes Flow Under CFI Hae	DUCTION DUCTION DDS ical data metry th v boundary conditions l compliance D Simulation modynamics Analysis	EVALUATING	HAEMODYNAMICS 98 100 100 102 102 103 110 111 112
2.1. 2.2. 2.2.1 2.2.2 2.2.3 2.2.4 2.2.5 2.2.6 2.2.7	INTROI METHO Clim Geo Mes Flov Wal CFI Hae	DUCTION DUCTION DDS ical data metry th v boundary conditions l compliance D Simulation modynamics Analysis	EVALUATING	98 98 100 100 102 102 103 110 111
2.1. 2.2. 2.2.1 2.2.2 2.2.3 2.2.4 2.2.5 2.2.6 2.2.7 2.3.	INTROI METHO Clin Geo Mes Flov Wal CFI Hae RESULT	DUCTION DOS ical data metry h v boundary conditions I compliance O Simulation modynamics Analysis	EVALUATING	HAEMODYNAMICS 98 100 100 102 102 103 110 111 112 113
2.1. 2.2. 2.2.1 2.2.2 2.2.3 2.2.4 2.2.5 2.2.6 2.2.7 2.3. 2.3. 2.3.1	INTROI METHO Clim Geo Hes Flow Vali RESULT Flow	DUCTION DUCTION DDS ical data metry th v boundary conditions I compliance D Simulation modynamics Analysis TS dation of the Baseline Case v and Pressure Distributions	EVALUATING R TBAD	HAEMODYNAMICS 98 100 100 102 102 103 110 111 112 113 114
2.1. 2.2. 2.2.1 2.2.2 2.2.3 2.2.4 2.2.5 2.2.6 2.2.7 2.3. 2.3.1 2.3.2	INTROI METHO Clim Geo Mes Flov Wal CFI Hae RESULT Flov Wal	ICAL OPTIMISATION FOR DUCTION DDS ical data metry h w boundary conditions I compliance D Simulation modynamics Analysis TS dation of the Baseline Case	EVALUATING R TBAD	HAEMODYNAMICS 98 100 100 102 102 103 110 111 112 113 114 115
2.1. 2.2. 2.2.1 2.2.2 2.2.3 2.2.4 2.2.5 2.2.6 2.2.7 2.3. 2.3.1 2.3.2 2.3.3	INTROI METHO Clim Geo Mes Flov Wal CFI Hae RESULT Flov Wal	ICAL OPTIMISATION FOR DUCTION DDS ical data metry h w boundary conditions I compliance D Simulation modynamics Analysis TS dation of the Baseline Case w and Pressure Distributions I Displacement and Energy Lo S-Based Indices	EVALUATING R TBAD	HAEMODYNAMICS 98 100 100 102 102 103 110 111 112 113 114 115 124

	2.6.	Conclusions	133
A	NOVEL	COMPUTATIONAL FRAMEWORK INTEGRATING INTIMAL	FLAP
COMPLIA	ANCE: II	MPACT ON AORTIC HAEMODYNAMICS	136
	3.1.	Introduction	136
	3.2.	METHODS	138
	3.2.1.	Data Acquisition	138
	3.2.2.	Geometry & Mesh	140
	3.2.3.	Wall Compliance	141
	3.2.4.	Flow Boundary Conditions	142
	3.2.5.	CFD Simulation	143
	3.2.6.	Haemodynamic Analysis	143
	3.3.	RESULTS	144
	3.3.1	. Pressures and Flows	144
	3.3.2	. Patient-Specific Displacement	147
	3.3.3	. IF Displacement, TMP and Pressure Contour	147
	3.3.4	. Rotational Flow Features	150
	3.3.5	. Wall Shear Stress Indices	153
	3.4.	DISCUSSION	156
	3.5.	LIMITATIONS	161
	3.6.	Conclusions	161
PA	ATIENT-	SPECIFIC COMPLIANT SIMULATION FRAMEWORK INFORM	ED BY
4DMRI-E	XTRACT	TED PULSE WAVE VELOCITY: APPLICATION POST-TEVAR	165
	4.1.	Introduction	165
	4.2.	METHODS	167
	4.2.1.	Data Acquisition	167
	4.2.2.	Geometry & Mesh	168
	4.2.3.	Wall Compliance	169
	4.2.4.	Boundary Conditions	172
	4.2.5.	CFD Simulation	173
	4.2.6.	Haemodynamics Analysis	173
	4.3.	RESULTS	174
	4.3.1.	Validation	174
	4.3.2.	Flow Characteristics	175
	4.3.3.	Wall Shear Stress Indices	180
	4.4.	DISCUSSION	185
	4.5.	LIMITATIONS	187
	4.6.	Conclusions	188

CONCLU	SIONS AND FUTURE WORK	190
5.1.	Contributions	190
5.2.	Main Findings	191
5.3.	LIMITATIONS	193
5.4.	FUTURE WORK	195
APPENI	DIX A	199
A.1.	MESH SENSITIVITY ANALYSIS	199
A.2.	COMPARISON BETWEEN LAMINAR AND TURBULENT FLOW SIMULATIONS	201
APPENI	DIX B	205
B.1.	MESH SENSITIVITY ANALYSIS	205
B.2.	THREE ELEMENT WINDKESSEL PARAMETERS	207
B.3.	AREA CHANGES OVER THE CARDIAC CYCLE	207
APPENI	DIX C	209
C.1.	MESH SENSITIVITY ANALYSIS	209
C.2. THREE ELEMENT WINDKESSEL PARAMETERS AND OUTLET BOUNDARY CONDITIONS		OITIONS
		210
REFERI	ENCES	213

List of Figures

Figure 1. 2 Schematic of the aortic wall structure. Source: Blausen.com staff
(2014). "Medical gallery of Blausen Medical 2014". WikiJournal of
Medicine 1. DOI:10.15347/wjm/2014.010. ISSN 2002-4436
Figure 1. 3 Schematic of the DeBakey and Standford AD classifications 50
Figure 1. 4. (A) CTA scan of a dissected aorta including a sagittal view, a zoom
on the arch using a coronal view, and an axial view of calcification at the DA. (B)
4DMRI of the dissected aorta shows the high velocity in the AA and the lumen
perfusion
Figure 1.5 Left is an open surgery (OS) showing the graft replacing a dissected
portion of a TBAD. Right is a thoracic endovascular aortic repair (TEVAR) where the
endograft has been placed in the TL of a TBAD
Figure 1. 6 Electric components and their hydraulic analogy69
Figure 1. 7: Schematic of the two-element (WK2) and three-element (WK3)
Windkessel models
Figure 2. 1. (A) Automatic 3D rendering of the CTA angiography, showing, in
red, the aortic vessel and, in green, the graft; the segmented post-operative DA
resulting from the CTA angiography is shown next to it-namely the baseline case. (B)
The three virtual surgical scenarios created from the baseline case by varying the
length of graft. The red centreline from which the grafts have been swept is shown on
the post-operative geometry. Red and green dashed lines indicate the extent of the
$32 \mathrm{mm}$ and $28 \mathrm{mm}$ diameter thoracoabdominal graft of ETR, respectively. The length
of each graft is indicated in blue. (C) aortic segments defined along the centreline
using anatomical landmarks to account for proximal variations of stiffness. The
numbers indicate: 1 ascending aorta, 2 arch, 3 brachiocephalic trunk, 4 left common
carotid, 5 left subclavian, 6 isthmus, 7 graft, 8 descending aorta, 9 coeliac trunk, 10
superior mesenteric artery, 11 left renal, 12 right renal, 13 abdominal aorta, 14 left
iliac, 15 right iliac95

Figure 1. 1 Schematic of the aorta with major branches and sections........47

Figure 2. 2. (A) 2DMRI plane showing in blue and green the false and true
lumen respectively; below are the extracted raw and rescaled by 30% flow rates. (B)
An asterisk indicates the WK3 boundary condition used at the outlets. Flow split are
shown at the outlets: 30% of the flow leaves through the supra-aortic branches, and
40% of the remaining DA flow leaves through the abdominal arteries following the
TL and FL shown in (C). (C) The remaining abdominal false and true lumen flows are
split as 70/30% between the exterior and interior iliac arteries; the right exterior (REI)
and interior (RII) iliac arteries are shown as an example. (D) Sample cine-MRI planes
used to measure the stiffness of the aorta. The aortic arch of BC1 is zoomed in to show
the distribution of local stiffness values K obtained for the case of a compliant graft.
98
Figure 2. 3 Velocity magnitude distributions at peak systole shown for every
case using streamlines
Figure 2. 4 Velocity magnitude distributions at end of diastole shown for every
case using streamlines
Figure 2. 5 Pressure contours at peak systole for every cases
Figure 2. 6 Pressure contours at end of diastole for every cases
Figure 2. 7 Y-axis represents systolic and diastolic pressures (Psys, Pdia), EL,
PWV, and maximum diameter variation at the ascending aorta (D_AA), left common
carotid (D_LCC), and graft (D_Graft) for the baseline case. The X-axis shows values
of the metrics of interest for five additional cases, each labelled with their respective
errors. Bold lines denote the metric values for the baseline case and those
corresponding to 0% of relative change
Figure 2. 8 Front view of the TAWSS. On the left, values over 5 Pa are found
at the PET, the abdominal arteries, and the left iliac of the baseline case. The black
arrow indicates the maximum TAWSS at the PET. On the right, the TAWSS differences
between the baseline and the five cases are shown. A zoom is made on the AA and
aortic arch as regions of interest where the TAWSS is high
Figure 2. 9 Back view of the TAWSS. On the left, values over 5 Pa are found
at the PET and sutures with the graft of the baseline case. The black arrow indicates
the maximum TAWSS at the sutures with the graft. On the right, the TAWSS

differences between the baseline and the five other cases are shown. A zoom is made
on the AA and aortic arch as regions of interest where the TAWSS is high 118
Figure 2. 10 ECAP distributions, front view. On the left, ECAP absolute values
for baseline case; values over $1.4\ Pa-1$ are noted in the aneurysm. The black arrow
indicates the maximum ECAP value in the aneurysm. On the right, ECAP differences
between the baseline and the five virtual cases
Figure 3. 1. (A) Patient-specific model of the domain showing the boundary
conditions used and the aortic wall stiffness. T0 is mid-acceleration, T1 is peak systole,
T2 is mid-deceleration, and T3 is end of diastole. (B) Planes in red are used to extract
variables in the post-processing at the ascending aorta (AA), PET, descending aorta
(DA), VAO and abdominal aorta (ABAO). (C) The MBM is applied both at the
exterior aortic wall and the IF. The rightmost part of the figure illustrates the patching
technique used for the IF, showing how TL/FL pairs of patches, coloured in black and
green respectively, share the same surface normal
Figure 3. 2. Velocity magnitude comparisons between patient-specific
simulations (D1), 4DMRI and rigid wall simulations (D0) at mid-acceleration (T0),
peak systole (T1), mid-deceleration (T2), and end of diastole (T3) in selected locations
(AA, PET, DA, VAO and ABAO)136
Figure 3. 3. Validation of the aortic wall and IF displacement in the patient-
specific case D1 against cine-MRI measurements. The left panel in each subset shows
the cine MRI and the right one shows the simulated cross-sections, with the boundary
colour indicating
Figure 3. 4. IF displacement at the PET, DA and VAO over the cardiac cycle
and TMP starting from the PET at T0, T1, T2 and T3 for all cases
Figure 3. 5. Pressure contours for D1 and point-wise difference against
additional cases at T1 and T2
Figure 3. 6. Vorticity contours and overlapping streamlines for every case at
the PET, DA and VAO at T0, T1, T2 and T3
Figure 3. 7. Contours of TAWSS for the patient-specific simulation (D1) and
point-wise differences against additional cases
Figure 3. 8. Contours of OSI for D1 and point-wise differences against
additional cases

Figure 3. 9. Contours of RRT for D1 and point-wise differences against
additional cases
Figure 4. 1. Patient-specific compliant simulation model showing the boundary
conditions used at the inlet and outlets
Figure 4. 2. (A) Red lines depict the 4DMRI planes on which the flow rates
were measured. (B) schematic of the cross-correlation method used to calculate the
PWV between planes A and B (Markl et al., 2010, Fielden et al., 2008)163
Figure 4. 3. Stiffness maps derived from area- and RPWV-based distensibility
to compare S1 and S2, using a logarithmic scale in both the colour bar and the contours
to highlight differences in stiffness across regions introduced by the RPWV-based
stiffness tuning
Figure 4. 4. Comparison of predicted RPWVs, S1 (orange) and S2 (green),
against 4DMRI extracted (blue)
Figure 4. 5. Contours of velocity magnitude at different flow phases for the
4DMRI, the area- (S1) and RPWVs-based (S2) simulations at the AA (i), endograft
(ii) and VAO (iii) at T0 (mid-acceleration), T1 (peak systole), T2 (mid-deceleration),
and T3 (end diastole). The value on top of each contour is the maximum velocity
magnitude
Figure 4. 6. Comparison between 4DMRI (blue) measured and predicted, area-
(S1, orange) and RPWVs-based (S2, green) simulations SFRR values along the aortic
domain
Figure 4. 7. IRF for the area- (S1, blue) and RPWVs-based (S2, orange)
simulations with the difference between the two cases reported next to the bar, such
as $\Delta\% = IRFS2 - IRFS1IRFS2 + IRFS12 * 100$
Figure 4. 8. Contours of TAWSS, OSI, RRT and ECAP for S1 (left) and S2
(centre) and point-wise differences such as S1-S2 (right). Values on regions discussed
in the core text are reported with dotted circles and lines
Figure I. Left is the geometry on which regions, numbered from 1 to 7, and
planes of interest, highlighted by a black line, are depicted. Tables gather mean
TAWSS, mean and max velocity relative error and GCI comparisons

Figure II. TAWSS, OSI and ECAP contour map of the laminar simulation	and
point-wise differences between the laminar and turbulent simulations. The table sho	ows
the mean and max point differences for TAWSS, OSI and ECAP	190
Figure III. Mean TAWSS, mean and max velocity relative error and C	ЗСI
comparisons. Below the tables is the geometry on which regions and planes of inter-	est,
denoted by capital letters and numbers, respectively, are depicted	193
Figure IV. Cross-sectional area variation over the cardiac cycle in selection	eted
locations for all simulated cases	195
Figure V. On the left side are planes and regions of interest, denoted	by
numbers and capital letters. On the right side, tables display the relative error and G	ЗСI
comparison for M1, M2, and M3 regarding the mean TAWSS and mean and maxim	ıum
velocity	197

List of Tables

Table 2. 1 Mean flow rates at the outlets for each case. Flow splits are very
close between the post-operative, MDA and CDA cases due to close morphological
similarities. Differences are found in the abdominal and iliac arteries of the ETR case
due to idealised abdominal branches of the graft
Table 2. 2 WK3 parameters for the Baseline, MDA, CDA and ETR cases, Rp
and Rd are in (mmHg*s/mL), CWK3 is in (mL/mmHg)102
Table 2. 3 Systolic Psa and diastolic Pda pressures, mean flow rate Qi at the
registered plane location, and maximum diameter variation at regions of interest are
reported for the baseline simulation and clinical measurements. $\Delta\%$ represents the
relative change between the baseline simulation and clinical data107
Table 3. 1. Targeted values of inlet pressures and outlet mean flow rates against
simulation results. 132
Table 3. 2. IRF measured at the AA and ABAO, and in both lumina at the PET,
DA, and VAO for every case at T0, T1, T2 and T3.
Table 4. 1. Target mean flow rates at outflow boundaries and inlet systolic and
diastolic pressures against CFD values
Table 4. 2. Minimum, maximum and mean values per region for S2. Also
shown are percentage differences ($\Delta\%$) values such as
$\Delta\% = metricS2 - metricS1 metricS2 + metricS12*100. \\ 172$
Table I. Mean flow rates at the outlets, inlet systolic and diastolic pressures,
energy loss and pulse wave velocity for the laminar and turbulent simulation; the last
column is the difference between the laminar and turbulent simulations191
Table II. Element count of M1, M2 and M3 and percentage change between
M1/M2 and M2/M3
Table III. Three-element Windkessel parameters used for all simulations in the
paper
Table IV. Element count of M1, M2 and M3 and % change between
coarse/medium and medium/fine

Table V	. Three-eleme	ent Windkessel	parameters	for S1 a	and S2. l	R1 and I	R2 are
in [mmHg.mL.s	s] and C is in	[mL/mmHg]					198

List of Abbreviations

2DMRI Two-Dimensional Magnetic Resonance Imaging

3D Three-Dimensional

4DMRI Four-Dimensional Magnetic Resonance Imaging

AA Ascending Aorta

AAS Acute Aortic Syndromes

AD Aortic Dissection

BC Boundary Condition

BMT Best Medical Treatment

BT Brachiocephalic Trunk

CFD Computational Fluid Dynamics

CTA Computed Tomography

CTA Celiac Trunk Artery

DA Descending Aorta

DNS Direct Numerical Simulation

ECAP Endothelial Cell Activation Potential

ECG Electrocardiogram

EVAR Endovascular Aortic Repair

FEM Finite Element Method

FL False Lumen

FSI Fluid-Structure Interaction

FVM Finite Volume Method

IB Immersed Boundary

IF Intimal Flap

IMA Inferior Mesenteric Artery

IRF In-Plane Rotational Flow

IVP Inlet Velocity Profile

LES Large Eddy Simulation

LCC Left Common Carotid

LRA Left Renal Artery

LSA Left Subclavian Artery

MBM Moving Boundary Method

ML Machine Learning

MRI Magnetic Resonance Imaging

MPS Malperfusion Syndromes

OSI Oscillatory Shear Index

OS Open Surgery

PDEs Partial Differential Equations

PET Primary Entry Tear

PIV Particle Image Velocimetry

PWV Pulse Wave Velocity

RANS Reynolds Averaged Navier Stokes

RBFs Radial Basis Functions

RCC Right Common Carotid

RETs Re-Entry Tears

RRA Right Renal Artery

RSA Right Subclavian Artery

RRT Relative Residence Time

SMA Superior Mesenteric Artery

SNR Signal-to-Noise Ratio

SST Shear Stress Transport

TAAD Type-A Aortic Dissection

TAWSS Time-Averaged Wall Shear Stress

TBAD Type-B Aortic Dissection

TL True Lumen

VENC Velocity Encoding

WK2 Two-Element Windkessel

WK3 Three-Element Windkessel

WSS Wall Shear Stress

E Young's Modulus

List of Symbols

```
A Cross-sectional area (m^2)
C Compliance (mL/mmHg)
D Diameter (m)
D_k Distensibility (1/mmHg)
ECAP Endothelial cell activation potential (1/Pa)
EL Energy Loss (W)
F Force (N)
FF Form factor
IRF In-plane rotational flow (1/s)
K Stiffness coefficient (N/m<sup>3</sup>)
L Inductance (mmHg·s^2/mL)
l Length (m)
OSI Oscillatory shear index
p Pressure (mmHg)
P_d Diastolic pressure (mmHg)
P<sub>p</sub> Pulse pressure (mmHg)
P_s Systolic pressure (mmHg)
\Delta p Pressure drop (mmHg)
PWV Pulse wave velocity (m/s)
Q Flow rate (mL/s)
r Radial position (m)
R Radius (m)
R Resistance (mmHg·s/mL)
Re Reynolds number
R_d Total resistance (mmHg·s/mL)
R_p Proximal resistance (mmHg·s/mL)
Re<sub>c</sub> Critical Reynolds number
```

Re_p Peak Reynolds number

RRT Relative resident time (1/Pa)

SFFR Systolic flow reversal ratio

T Cardiac cycle period (s)

TAWSS Time average wall shear stress (Pa)

TD Time delay (s)

TMP Transmural pressure (mmHg)

TP Total pressure (mmHg)

u=u(x,y,z,t) Velocity (m/s)

 $V Volume (m^3)$

 V_p Peak velocity (m/s)

- w vorticity (1/s)
- α Womersley number
- δ Displacement (m)
- μ Fluid dynamic viscosity (kg/m.s)
- ρ Fluid density (kg/m³)
- **τ** WSS vector.
- ω Angular frequency (1/s)

Chapter 1

Introduction

This chapter presents the motivation and background behind the work conducted in this thesis. An introduction to the physiology and pathology of aortic dissection (AD) follows. A review of aortic blood flow and current cardiovascular modelling approaches and findings is presented, focusing on Type-B aortic dissection (TBAD). Finally, the thesis outline and objectives are presented in the last section.

1.1. Background

AD is a severe and rare cardiovascular disease with high mortality rates; worldwide, the disease has an incidence of about 4.4/100000 people every year (DeMartino et al., 2018). In AD, blood flows inside the aortic wall due to an intramural tear (Kaufman, 2004). Consequently, wall separation occurs, forming a false lumen beside the original true lumen (FL, TL). The development of the condition varies depending on the patient's anatomy and physiology. The dissection may extend along the whole aorta, including the main aortic branches and key feeding arteries, such as the supra-aortic branches or the visceral and iliac arteries. This may lead to organ and limb malperfusion and can be lethal (Gargiulo et al., 2014).

AD symptoms are shared with many other cardiovascular diseases, making diagnosis challenging. Patients often describe a sharp pain in the back at the site of the aortic rupture, though symptoms can present in any region or organ, further complicating diagnosis. Additionally, increasing awareness of acute AD among both the general population and clinical staff is crucial for ensuring quicker and more accurate diagnosis. Aortic Awareness UK, a charity dedicated to improving understanding and outcomes for aortic diseases, recently published the first-ever national guidance on acute AD. The guidance aims at "helping regional aortic centres

to improve their service but also to raise awareness on AD to lower the regional variation in care and outcomes" (aorticdissectionawareness.org).

The Stanford classification of AD is based on the primary entry tear (PET) location at the rupture. AD is classified as Type-A aortic dissection (TAAD) when the PET is located in the ascending aorta (AA) and TBAD when the PET is in the descending aorta (DA). TAAD is a medical emergency requiring surgery as soon as possible to reduce the risk of death of the patient (Nienaber and Clough, 2015). TBAD can be medically treated, but in the case of complications such as organ malperfusion, ongoing aortic growth and large aneurysms, and symptomatic patients who do not respond to medical therapy, a surgical procedure will be considered.

Two primary surgery types, endovascular aortic repair (EVAR) and open surgery (OS), are commonly employed, with EVAR showing better early outcomes and being less invasive than OS (Coselli et al., 2016, Li et al., 2018). However, OS remains the preferred option when the dissection is complex, unsuitable for endovascular treatment, or when tissue disorders affect the regions targeted for EVAR, compromising the endovascular landing zones (Boufi et al., 2019, Tian et al., 2014).

The management of AD relies primarily on a combination of clinical examination and advanced imaging techniques, with Computed Tomography (CTA) playing a pivotal role (Evangelista et al., 2023). These methods are essential for localisation, classification, and obtaining precise anatomical measurements, which are crucial for planning appropriate treatment strategies. Clinical management of AD requires a comprehensive approach, considering multiple factors. Clinicians closely monitor key indicators such as aortic diameter, pressures within the aorta, and haemodynamics including blood flow patterns, recirculation, and vortex formation (Sultan et al., 2023).

There is a growing interest in predicting the outcomes of AD and surgical interventions, as well as understanding their progression over time. This includes evaluating the impact of different medical device types and sizes used in AD surgical treatment (Trahanas et al., 2022). However, testing various devices during surgery is not feasible due to the high-risk nature of the procedure, the expense of the devices, and the additional costs associated with extended operating times and clinical resources.

To address these challenges and enhance patient care, clinicians are increasingly turning to advanced imaging techniques. Magnetic resonance imaging (MRI), including two-dimensional MRI (2DMRI) and four-dimensional flow MRI (4DMRI) methods, are valuable in visualising and quantifying blood flow in AD patients (Ramaekers et al., 2023, van Hout et al., 2020). However, these techniques have several limitations, including long acquisition times, high costs, limited availability, and susceptibility to noise. The noise can be attributed to the small structures in aortic dissection, rapid flow in narrowed regions, and interference from implanted devices.

For these reasons, the diagnostic and therapeutic challenges have increasingly driven medical research toward advanced computational methods. Computational Fluid Dynamics (CFD) simulations, coupled with routine *in vivo* imaging, offer the potential to quantify aortic haemodynamics. Haemodynamics markers linked to disease progression can be calculated from these simulations and, in the future, could potentially be integrated into clinical settings to support surgical decision-making. Additionally, CFD simulations can be used to virtually test different surgical scenarios, device configurations, and treatment strategies without the risks, ethical concerns, and substantial costs associated (Song et al., 2023, Zhu et al., 2023).

However, several limitations impact the accuracy of current simulation approaches, one example being the treatment of the aortic wall. Many simulations use rigid wall assumptions due to the complexity of modelling and limited patient-specific data on wall displacement. This simplification, while computationally efficient, introduces inaccuracies as it fails to account for the natural compliance of the aorta and dynamic response to blood flow (Boccadifuoco et al., 2018). For simulations that account for wall compliance, additional limitations arise: some models use non-patient-specific compliance values or assume a uniform compliance field throughout the aorta. This approach overlooks regional variations in aortic stiffness, which can significantly impact haemodynamics, especially with aging or in the presence of implanted devices.

This thesis aims to enhance the accuracy and reliability of CFD simulations in TBAD by addressing common modelling assumptions, with the ultimate goal of making these simulations robust enough for clinical use. A key effort in this work is

the integration of routinely acquired *in vivo* clinical data into novel patient-specific modelling frameworks. By improving the representation of aortic compliance, these advancements aim to produce robust simulations capable of supporting surgical decision-making, optimising surgical planning, and improving the monitoring of TBAD progression.

1.2. Anatomy of the Aorta

The aorta is the largest artery in the body and originates directly from the heart. It is the primary conduit for oxygenated blood throughout the systemic circulation. Structurally, it can be divided into several distinct segments. The initial portion, the AA, spans approximately 50-70 mm and emerges from the left ventricle (LV) immediately following the aortic valve (Figure 1. 1). At its root, the AA features three small pockets known as the sinuses of Valsalva, housing the origins of the left and right coronary arteries, crucial for myocardial oxygenation (Erbel and Eggebrecht, 2006).

Continuing from the AA, the vessel forms a loop over the left pulmonary artery and the bifurcation of the pulmonary trunk, creating the aortic arch, which ultimately curves to the left of the trachea. Typically, three primary branches stem from the aortic arch: the brachiocephalic trunk (BT), the left common carotid artery (LCC), and the left subclavian artery (LSA). The BT promptly divides into the right common carotid artery (RCC) and the right subclavian artery (RSA). The descent of the aorta commences at the intervertebral disc level between the fourth and fifth thoracic vertebrae, where the DA initiates (Popieluszko et al., 2018).

Subsequently, the DA is anatomically separated by the diaphragm into two segments: the thoracic and abdominal aorta (di Gioia et al., 2023). From the thoracic aorta, branches such as the intercostal, subcostal, and left bronchial arteries arise. In contrast, the abdominal aorta gives rise to significant arterial branches before bifurcating into the left and right common iliac arteries. Notable branches from the abdominal aorta include the celiac trunk (CTA), the superior mesenteric artery (SMA), the inferior mesenteric artery (IMA), and the left and right renal arteries (LRA, RRA) (Komutrattananont et al., 2019). This intricate vascular network underscores the

crucial role of the aorta in systemic circulation, delivering vital oxygen and nutrients to various organs and tissues throughout the body.

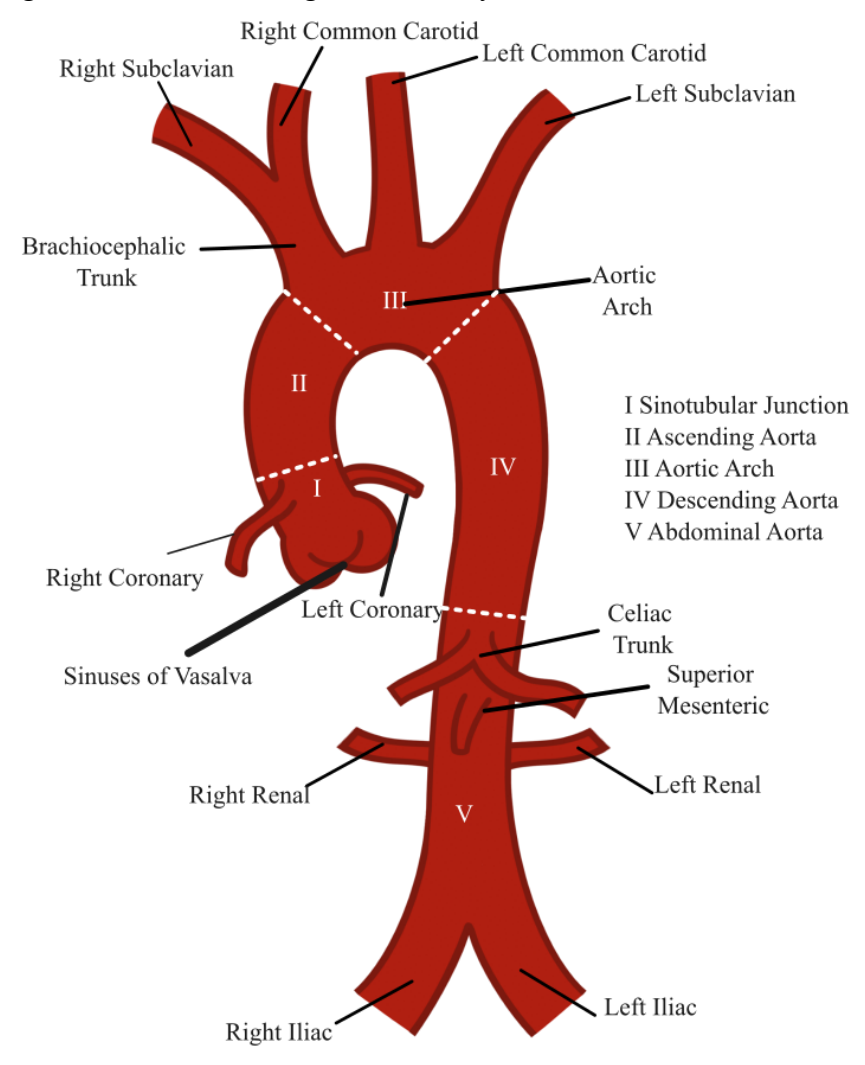


Figure 1. 1 Schematic of the aorta with major branches and sections, such as: I:Sinotubular Junction, II:Ascending Aorta, III:Aortic Arch, IV:Descending Aorta and V:Abdominal Aorta. Source: Louis Girardin.

Blood vessels, vital conduits for systemic circulation, comprise a diverse network of arteries, arterioles, capillaries, venules, and veins, each characterised by a distinct structure and function. These vessels share a typical three-layered architecture: the tunica intima, tunica media, and tunica adventitia. The tunica intima, the innermost layer, consists of three sub-layers, with the endothelium forming its innermost component (Camasão and Mantovani, 2021) (Figure 1. 2). This endothelial lining

plays a pivotal role in regulating thrombosis and platelet adherence while also contributing to the modulation of blood flow and pressure through the production of vasodilator and vasoconstrictor molecules. Furthermore, it plays a crucial role in various physiological functions, including angiogenesis and tissue repair, and its dysregulation is implicated in numerous pathological conditions such as atherosclerosis and hypertension. Adjacent to the tunica intima lies the tunica media, comprising smooth muscle cells and elastic tissue, which confer remarkable distensibility and elasticity to compliant arteries like the aorta. Finally, the outermost layer, the tunica adventitia, reinforced by the external elastic lamina, provides structural integrity and houses the vasa vasorum, which supports the arterial wall cells (Buetow and Laflamme, 2017). Additionally, beyond its conduit function, the aorta intricately regulates systemic vascular resistance and heart rate, underscoring its pivotal role in systemic haemodynamics and cardiovascular equilibrium (Humphrey et al., 2015, Michel et al., 2018).

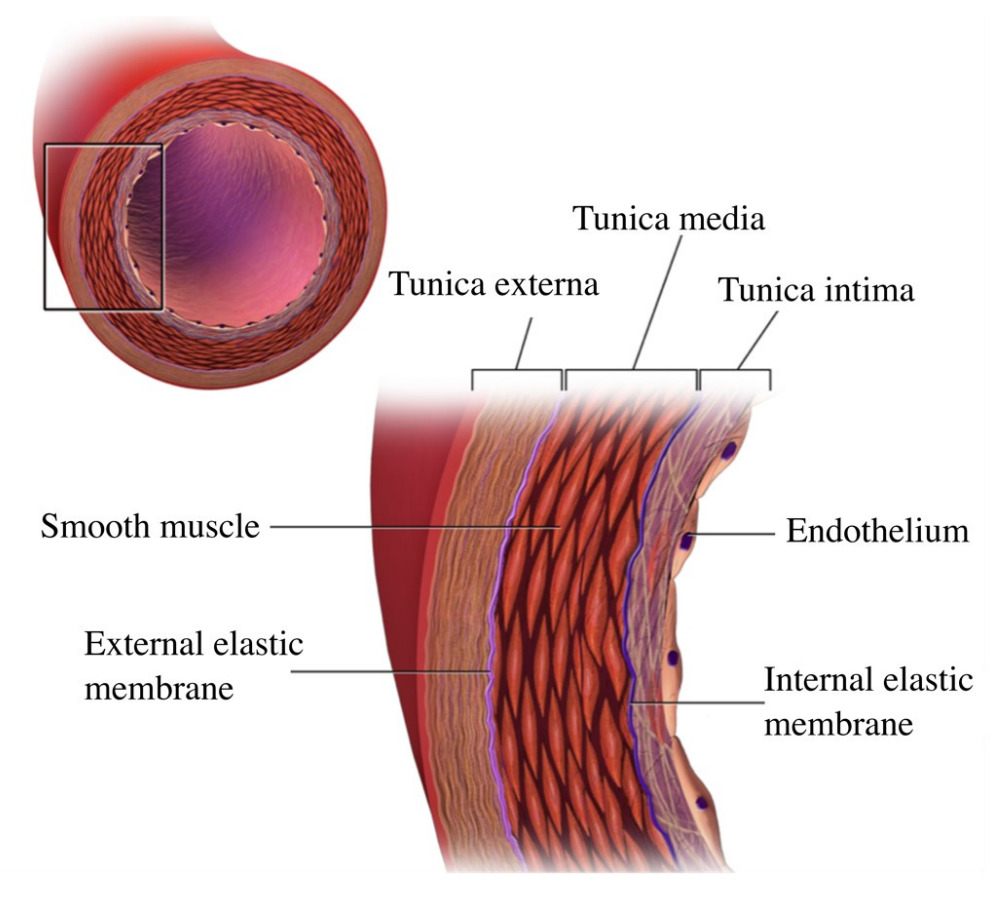


Figure 1. 2 Schematic of the aortic wall structure. Source: Blausen.com staff (2014). "Medical gallery of Blausen Medical 2014". WikiJournal of Medicine 1. DOI:10.15347/wjm/2014.010. ISSN 2002-4436.

1.3. Aortic Dissection: Clinical Overview

AD is classified as one of the Acute Aortic Syndromes (AAS) and represents the most common and clinically significant type within this category (Nienaber and Clough, 2015). AAS encompasses a group of severe vascular disorders with significant morbidity and mortality rates (Vilacosta et al., 2021). AAS share common pathophysiological mechanisms, clinical features, and diagnostic and therapeutic approaches, with intramural haematoma and penetrating atherosclerotic aortic ulcer representing the other clinical entities within this classification. AD is characterised by a tear in the aortic wall, which develops in the tunica intima, allowing pressurised blood to flow between the intima and the tunica media, thereby separating them by the

intimal flap (IF). This condition typically presents acutely, although degenerative changes in the tunica media often precede the dissection event by many years (Murillo et al., 2021). Intramural haematoma, another form of AAS, involves the leakage of blood through the endothelium into the aortic wall without an accompanying tear and is considered an early stage of AD.

1.3.1.Classification

AD can be categorised based on their location and extent, mainly via the Stanford or DeBakey systems (Figure 1. 3). DeBakey categorises AD based on the location of the entry tear and the extension of the dissection. Type I involves the AA, aortic arch, and DA; Type II involves only the AA, while Type III has entry tears in the DA, propagating distally in the thoracic or abdominal aorta. The Stanford classification categorises aortic dissection into two main groups: Type A and Type B. Type A dissection affects the AA and can propagate to the aortic arch and DA (i.e., DeBakey Types I and II), with the tear able to originate anywhere along this path. In contrast, Type B dissection involves the DA without affecting the ascending portion. Additionally, modifications to the Stanford classification introduce Type-C dissections, encompassing aortic arch involvement with or without descending extension and non-A non-B dissections (Christodoulou et al., 2023). Retrograde TAAD (RTAAD) occurs when the dissection initiates in the arch or DA but extends into the AA. It has been reported that Type-C AD represents 11% of AD diagnoses and is associated with increased risk and intervention rates compared to other types (Qanadli et al., 2020).

Based on the time elapsed since the onset of the dissection, an AD is classified into four phases: hyperacute (within the first 24 hours of the onset of the dissection); acute (from 24 hours to 7 days); sub-acute (8 days to 30 days) followed by the chronic phase (after 30 days) (Booher et al., 2013).

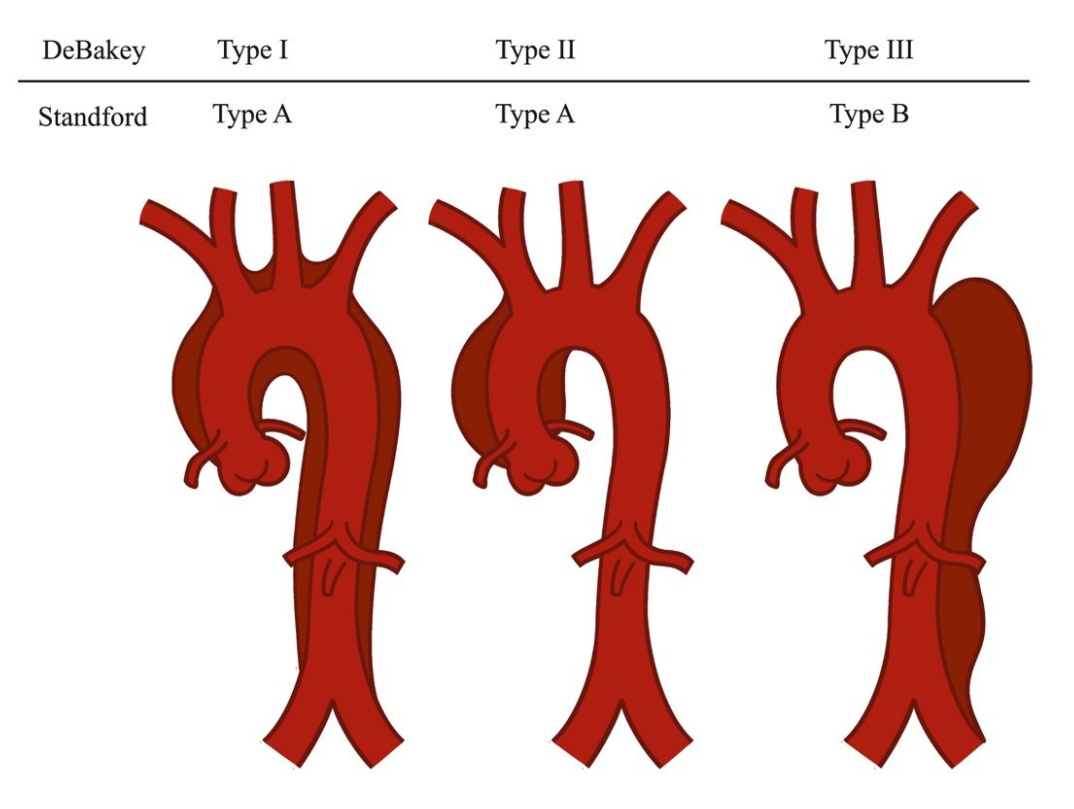


Figure 1. 3 Schematic of the DeBakey and Standford AD classifications. Source: Louis Girardin.

1.3.2. Aetiology and Risk Factors

AD impacts approximately 4.4 in 100,000 individuals worldwide (DeMartino et al., 2018), with Type A dissection TAAD accounting for 67% of cases and TBAD for 33% (Lombardi et al., 2020). Chronic cases, with an expected incidence of 42 per 100,000, often demonstrate a seven-year survival duration (Fleischmann et al., 2022). AD predominantly affects males (9.1 vs 5.4 per 100000), with an average age of 60 compared to an average age of 67 years old for women (Bossone et al., 2022). Notably, AD in younger patients often correlates with a family history of vascular disorders or connective tissue conditions such as Marfan syndrome and Ehlers-Danlos syndrome (Cury et al., 2013).

The initiation of dissections can result from rapid body deceleration, emotional stress, or intense physical exertion, leading to elevated heart rate and blood pressure (Carrel et al., 2023, Zhou et al., 2022). Factors such as motor vehicle accidents, recreational drug use and smoking, and specific medical procedures can also trigger

dissection events. Uncontrolled hypertension is the primary risk factor for AD, prevalent in over 53% of cases, followed by atherosclerosis (Nienaber and Yuan, 2022).

Anatomical features like thoracic aortic diameter may not be the best risk predictor for AD. While larger aortic diameters have been associated with increased cardiovascular risk, the relationship is not straightforward or consistent across all studies (Rueda-Ochoa et al., 2022, Tadic et al., 2022). The predictive value of aortic diameter is based on a limited number of studies with varying methodologies, imaging techniques, and definitions of aortic phenotypes. Furthermore, a single measurement of aortic diameter may not reliably indicate vascular damage or accurately predict future events, especially when not related to body size. The complex interplay of genetic factors, haemodynamics, and underlying tissue abnormalities in the development of AD cannot be fully captured by anatomical measurements alone. Additionally, the rate of aortic growth and other dynamic factors may be more indicative of dissection risk than static measurements (Kauhanen et al., 2022, Olson et al., 2021, Erbel and Eggebrecht, 2006).

1.3.3. Clinical Diagnosis

Prompt and accurate diagnosis of AD is crucial due to its life-threatening nature, with mortality rates increasing rapidly within the first 48 hours if untreated. However, diagnosing AD is very challenging as symptoms can vary widely and affect almost all body parts and organs, often resembling other severe conditions, which result in 1/3 of cases being misdiagnosed (Lovatt et al., 2022, Zhan et al., 2012). Common symptoms include severe chest or back pain described as a tearing sensation, reported in 67% and 25 % of AD patients, and non specific symptoms like limb ischemia, especially in patients with TBAD. This complexity leads to misdiagnosis in about one-third of cases, highlighting the need for correct and quick diagnosis to avoid giving treatments that could make the condition worse. Hence, the patient-specificity of AD makes it necessary to rely on advanced imaging techniques for accurate identification and treatment.

CTA is an important part of diagnosing AD, serving as the primary diagnostic modality in most (75%) cases and used to visualise the intricate morphology of the aorta with high resolution (Litmanovich et al., 2009). By employing multiple X-ray images and the administration of a contrast agent, CTA generates detailed threedimensional reconstructions of the aorta, allowing clinicians to identify the TL and FL, as well as the IF (Meng et al., 2019, Murillo et al., 2021). Unlike conventional Xray imaging, CTA comprehensively visualises the entire aorta in a single scan, facilitating prompt and accurate diagnosis of acute aortic pathologies (Figure 1. 4). The synchronisation of image acquisition with the cardiac cycle through electrocardiogram (ECG) gating ensures optimal image quality, minimising artefacts that could obscure crucial details, such as tears in the aortic wall. While contrastenhanced CTA remains the standard approach for AD diagnosis, its utility may be limited in individuals with contraindications to contrast agents, such as those with allergies or chronic kidney disease (Musajee et al., 2023, Rawson and Pelletier, 2013). Nevertheless, recent advancements in machine learning techniques have enabled the detection of AD using non-contrast CTA scans in conjunction with other imaging modalities, representing a promising alternative (Dong et al., 2024, Ma et al., 2023). MRI plays a crucial role in diagnosing and evaluating AD, offering several advantages over other imaging modalities. MRI demonstrates high sensitivity and specificity, with accuracy for detecting thoracic AD. This non-invasive technique provides detailed information about the aorta's structure and function without exposing patients to ionising radiation or iodinated contrast material. MRI excels in visualising soft tissues, making it particularly effective for assessing the aortic wall, TL, FL, PET, and IF. MRI techniques offer unique insights into aortic pathology, enhancing the diagnostic and prognostic capabilities in cases of AD (Sherrah et al., 2015). Phase-contrast imaging allows for the quantification of potentially prognostic haemodynamics parameters, including complex flow patterns and pulse wave velocity (PWV). This is complemented by 2DMRI and 4DMRI, which enable visualisation and measurement of time-resolved, two- and three-dimensional blood flow dynamics, offering valuable insights into flow patterns, velocity, and areas of turbulence or recirculation (Figure 1. 4) (Catapano et al., 2020, Takahashi et al., 2022). However, MRI scans typically require longer acquisition times and may be less suitable than CTA for emergency

scenarios or post-operative imaging due to artefacts from metallic implants. Additionally, MRI scanners are not available in all aortic centres, and their use is costly (Sherrah et al., 2015, van Hout et al., 2020).

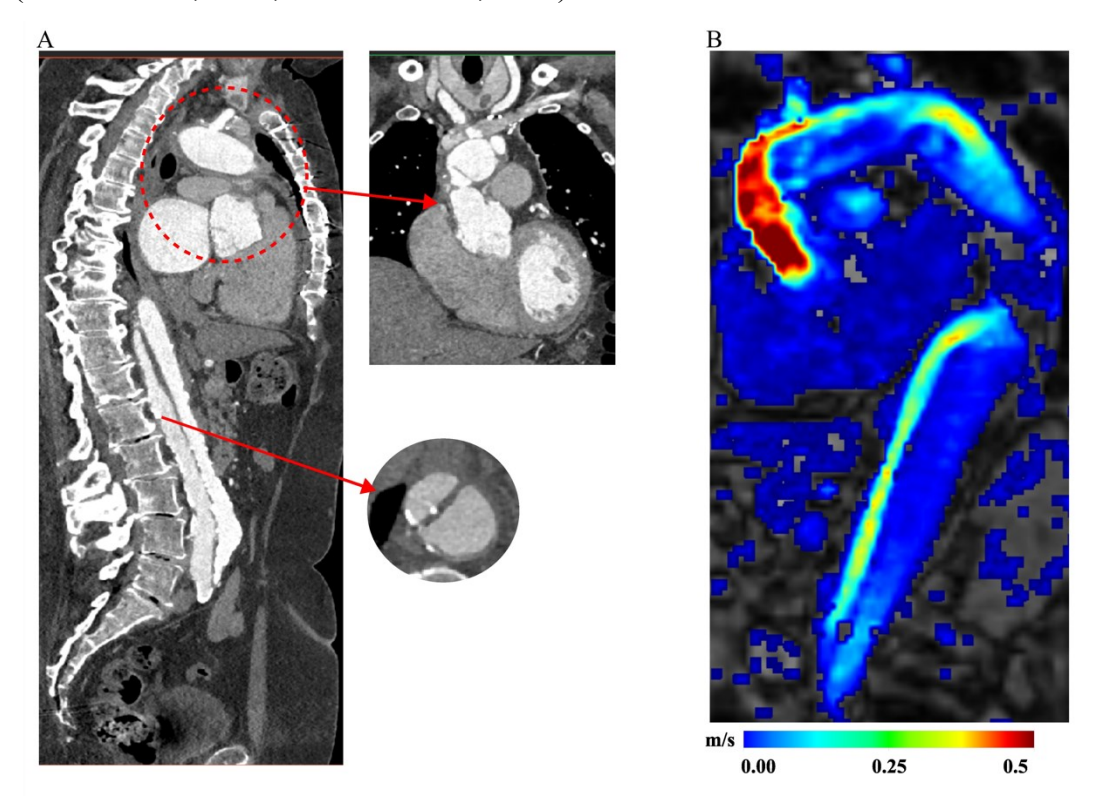


Figure 1. 4. (A) CTA scan of a dissected aorta including a sagittal view, a zoom on the arch using a coronal view, and an axial view of calcification at the DA. (B) 4DMRI of the dissected aorta shows the high velocity in the AA and the lumen perfusion. Source: Louis Girardin.

1.4. Clinical Management of Aortic Dissection

This section elaborates on the different scenarios after the development of an AD, including the complications of the disease, the medical and surgical treatments, and the markers used for prognostic evaluation.

1.4.1.Outcomes and Management

The outcomes and complications of AD management vary depending on interventions and patient-specific factors. Initial measures focus on controlling

systolic blood pressure between 100-120 mmHg, heart rate (60-80 bpm), and pain to prevent disease progression (Flower et al., 2023).

For TAAD, immediate surgery is often necessary due to life-threatening complications with mortality increasing by 1-2% every hour without intervention (Mylonas et al., 2023, Lu et al., 2020). Surgical intervention seeks at resecting the PET, restoring normal blood flow, preventing aortic rupture and addressing aortic valve involvement to prevent life-threatening complications with post-operative survival rates of 51-82% at five years (Nappi et al., 2023, Santini et al., 2006).

In contrast, acute TBAD is generally less severe, with lower in-hospital mortality rates ranging from 0 to 4 % in uncomplicated cases (Fleischmann et al., 2022, Yuan et al., 2023). However, in complex TBAD cases, in-hospital mortality can increase significantly, reaching up to 8-20% (Carrel et al., 2023, Gouveia e Melo et al., 2022, Hysa et al., 2021). Predictors of death in complicated cases include hypotension, shock, and branch vessel involvement (Suzuki et al., 2003, Tolenaar et al., 2014).

TBAD complications include malperfusion syndromes (MPS), persistent pain, uncontrolled hypertension, and aortic rupture—the most lethal outcome (Tadros et al., 2019). MPS occur when aortic branch vessels become occluded due to hematoma, thrombosis, or displacement of the IF, resulting in dynamic or static obstruction (Lopes et al., 2023; Mohajeri et al., 2023). Symptoms may involve limbs, organs, or the brain, and can lead to severe consequences such as acute renal failure or paraplegia. Among these, ischaemic complications represent some of the most critical and life-threatening outcomes of AD, particularly when they affect visceral or spinal circulation. These complications arise from impaired perfusion to vital organs and limbs due to IFinduced obstruction or dissection extension into branch vessels. Visceral, renal, spinal, or limb ischaemia can result in devastating outcomes, including mesenteric infarction, acute kidney injury, and irreversible neurological damage. The incidence of malperfusion syndromes has been reported in up to 30% of TBAD cases and is a major predictor of in-hospital mortality and poor long-term prognosis (Hiratzka et al., 2010; Yang et al., 2018). Prompt recognition and targeted intervention—through endovascular fenestration, stenting, or surgical revascularisation—are therefore essential to improving outcomes. While initial aortic remodelling occurs rapidly, it slows over time due to fibrosis of the aortic media and IF stiffening (Azoulay et al., 2024; Wada et al., 2022). However, chronic TBAD remains a concern, as dissected aortae continue to grow faster than non-dissected ones, particularly due to progressive false lumen (FL) expansion. Patients may experience recurrent MPS, new dissection tears, or aneurysmal degeneration (Sueyoshi et al., 2004; Trahanas et al., 2022). Moreover, FL thrombosis influences disease progression—while total thrombosis is considered protective, the implications of partial thrombosis remain debated (Ruiz-Muñoz et al., 2024; Trimarchi et al., 2013).

TBAD may be managed conservatively with medication with the aim of slowing down the heart rate, decreasing blood pressure and LV ejection force, reducing stress on the weakened aortic wall and limiting the propagation or rupture of the dissection (Wee et al., 2019). This is typically achieved through medications such as opioids, analgesia, and beta- or calcium-channel blockers. In contrast, despite the effectiveness of the best medical treatment (BMT), in uncomplicated cases, long-term outcomes remain suboptimal, with aneurysmal growth of the FL considered inevitable, which may necessitate intervention (Blount and Hagspiel, 2009, Kamman et al., 2017a). While the one-year mortality rate for TBAD is around 15%, up to 50% of patients may experience late adverse events, and intervention-free survival rates range between 40-50% at five years (Akin and Nienaber, 2020, Fleischmann et al., 2022). Moreover, ten-year total survival rates are likely well below 50% (Hysa et al., 2021, Luebke and Brunkwall, 2014).

The choice between medical and invasive management remains contentious, with varying outcomes in terms of survival rates and aortic remodelling (Hsieh et al., 2019). More extensive trials are needed to determine the most effective approach for managing stable TBAD and improving patient outcomes.

However, if the risk of rupture is deemed unacceptably high, surgical, endovascular, or hybrid treatments are typically indicated, with imaging playing a vital role in assessing eligibility and planning the treatment approach (MacGillivray et al., 2022, Schepens, 2018).

1.4.2.Repairs and Interventions

Prior to the advent of endovascular therapies, OS using synthetic grafts was the mainstay treatment for patients with complications. Surgical repairs were indicated for large aneurysms, rapid aortic growth, persistent back pain, and chronic malperfusion (Tian et al., 2014, Uchida and Sadahiro, 2018). In cases where endovascular treatments are not feasible, such as in the case of a dissection extending to the abdominal aorta with a structurally inadequate stent landing zone, OS remains the frontline treatment. OS for AD involves making a large incision in the chest to access the aorta directly. The procedure typically requires stopping the heart and using a heart-lung bypass machine to maintain circulation. The surgeon removes the dissected portion of the aorta and replaces it with a synthetic graft, which is sewn into place to reinforce the vessel wall and restore normal blood flow (Figure 1.5). The goal is to prevent further tearing, reduce the risk of rupture, and ensure adequate blood supply to the organs. This approach provides a durable repair for complex or extensive dissections (Figure 1. 5). OS carries a high risk, with 30-day in-hospital mortality of 16-19% for TAAD and 12-14% for TBAD, and 2-3-year mortality of 21-30% and 10-19% for the respective conditions (Benedetto et al., 2022, Pape et al., 2015, Sadi et al., 2012). Such mortality rates can be attributed to complications such as bleeding, stroke, acute kidney injury, respiratory failure, sepsis and malperfusion syndrome (Hou et al., 2023, Lee et al., 2020). Concerns about fairly rigid grafts include the loss of vessel compliance, which can lead to adverse outcomes such as LV hypertrophy, stroke, and increased pressure (Spadaccio et al., 2016).

EVAR is a minimally invasive procedure for treating aortic aneurysms, in contrast, thoracic aortic aneurysms and TBAD are typically treated using TEVAR (Atkins et al., 2023, Howard et al., 2021). The procedure involves inserting a stent-graft, a metal mesh tube covered with fabric, into the weakened area of the aorta. This stent-graft provides a new path for blood flow, diverting pressure away from the damaged section of the aorta. The EVAR procedure is typically performed under general anaesthesia and takes about 90 minutes to complete. A small incision is made in the groin area, and a catheter is threaded through a blood vessel to the aorta. The surgeon then uses imaging techniques such as X-rays to guide the stent-graft into place. Once positioned correctly, the stent-graft is expanded, and the catheter is removed.

TEVAR involves the deployment of a stent-graft to the DA via the iliac artery to cover and seal the PET while providing structural support (Figure 1. 5) (Isselbacher et al., 2022, MacGillivray et al., 2022). Multiple studies showed that TEVAR has lower early mortality rates than BMT and OS, about 7-9 % versus 11-15% (Harky et al., 2019, Liu et al., 2020). However, long-term mortality rates have been higher or smaller in different studies (Chou et al., 2015, Jubouri et al., 2022, Takazawa et al., 2024). Such study variations are linked to patient group sizes and the era during which the procedures were performed (reflecting advancements in technology and techniques). TEVAR leads to a higher rate of reinterventions compared to OS, about 15-17% against 5-6% (Ahmed et al., 2024, Cheng et al., 2023, Takazawa et al., 2024). Such reinterventions involve additional imaging and follow-ups for the patient, contributing to a reported poorer long-term quality of life (Orelaru et al., 2023).

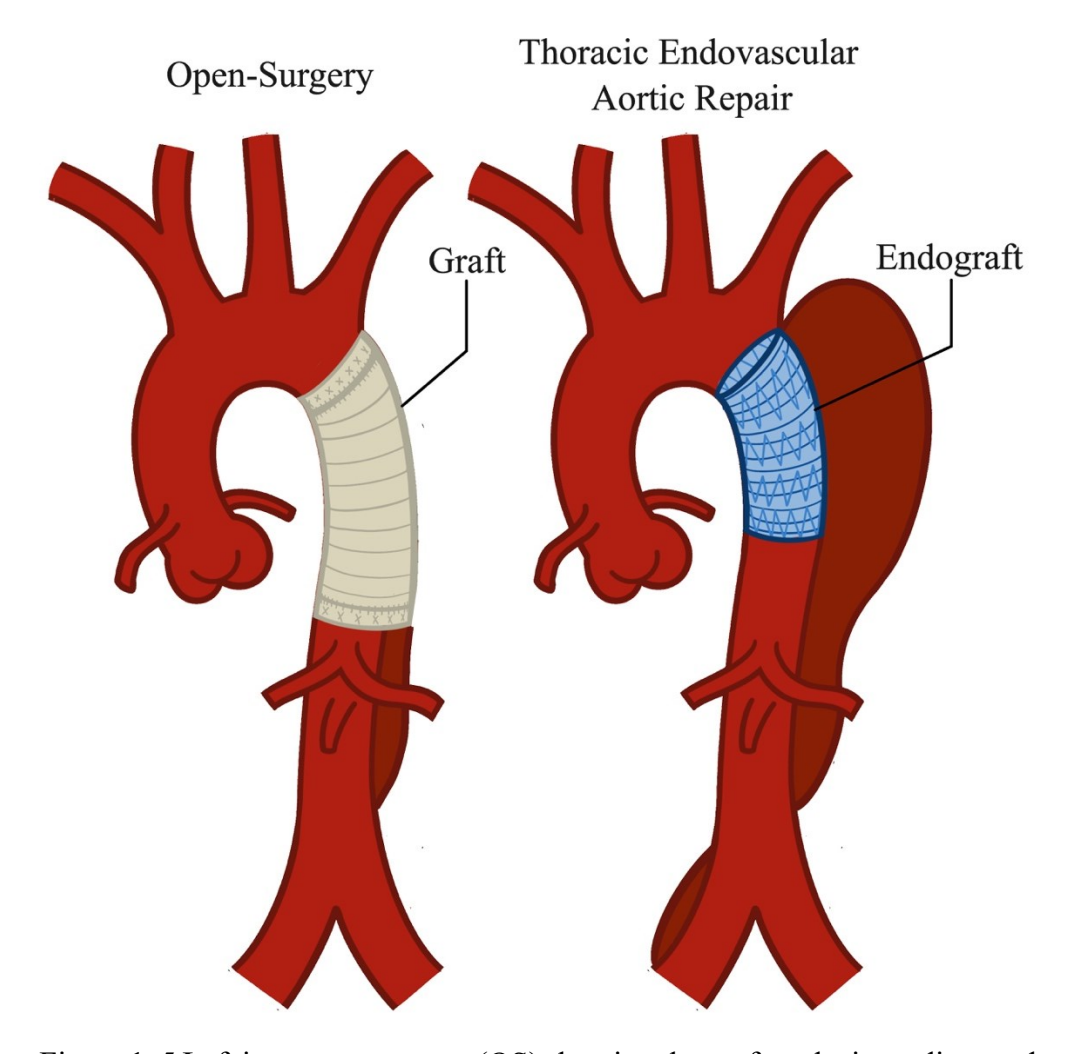


Figure 1. 5 Left is an open surgery (OS) showing the graft replacing a dissected portion of a TBAD. Right is a thoracic endovascular aortic repair (TEVAR) where the endograft has been placed in the TL of a TBAD.

Complications leading to these reinterventions and death are mainly due to endoleaks. An endoleak occurs when blood continues to flow into the aneurysm sac or FL after TEVAR, accounting for 26-33% of cases (Cheng et al., 2023, Zhang et al., 2016). Aneurysmal dilation occurs when the FL remains perfused, accounting for 20-22% of reinterventions. Additional reinterventions may be due to the development of a new dissection, a distal stent-graft-induced new entry tear (dSINE), a distal aneurysmal degeneration or a retrograde TAAD (Lopez-Marco et al., 2022). RTAAD is a serious and potentially fatal complication involving the dissection of the aorta extending backwards into the AA.

1.5. TBAD Flow Dynamics: A Detailed Analysis

As discussed in previous sections, TBAD management encompasses various outcomes and surgical interventions. The complexity of AD, influenced by patient-specific factors and the nature of the dissection, highlights the importance of understanding disease progression and planning optimal treatment strategies. As medical and surgical treatments evolve and complications potentially arise, forecasting outcomes becomes essential for improving survival rates and ensuring effective aortic remodelling. To this end, analysis and predictions can be made using *in vivo*, *in vitro*, or *in silico* studies coupled with medical imaging techniques. Comprehensive prognostic evaluations enable clinicians and engineers to tailor interventions more precisely, enhancing patient care and long-term prognosis. The following sections focus on TBAD which is the type of AD this thesis is concerned with.

1.5.1. Haemodynamics Descriptors

Understanding aortic flow dynamics involves examining blood flow and the forces driving circulation, which are key to analysing blood pressure regulation within the aorta. This regulation is influenced by cardiac output, vascular resistance, and blood volume. Systolic pressure (P_s) , the peak force exerted during heart contraction, and diastolic pressure (P_d) , the lowest force during relaxation, collectively determine the arterial pressure waveform (Levick, 2018). The difference between these, known as pulse pressure $(P_p = P_s - P_d)$, reflects the dynamic interaction between the heart and the vascular system. Pressure gradients, shaped by these parameters, move blood from higher to lower pressure areas, ensuring proper circulation.

The wall shear stress (WSS) plays a crucial role in regulating endothelial function within the aorta. It is the frictional force exerted by blood flow on the inner surface of blood vessels, particularly affecting the endothelial cells lining the vessel

walls (Davies, 2009, Zhou et al., 2023). High WSS generally promotes adaptive dilation and structural remodelling of the artery wall through endothelium-dependent mechanisms, which are considered protective against atherosclerosis. In CFD, WSS is used to derive additional hemodynamic metrics that provide deeper insights into the mechanobiological stimuli experienced by endothelial cells. The most common metrics are the time-averaged wall shear stress (TAWSS), oscillatory shear index (OSI), relative residence time (RRT), and endothelial cell activation potential (ECAP), and are defined as follows (Di Achille et al., 2014, Himburg et al., 2004, Ku et al., 1985, Malek et al., 1999):

$$TAWSS = \frac{1}{T} \int_0^T |\boldsymbol{\tau}| dt$$
 1. 1

$$OSI = 0.5 \left[1 - \left(\frac{\left| \int_0^T \tau dt \right|}{\int_0^T |\tau| dt} \right) \right]$$
 1. 2

$$RRT = \frac{1}{(1 - 2.0SI).TAWSS}$$
 1. 3

$$ECAP = \frac{OSI}{TAWSS}$$
 1.4

where T is the cardiac cycle period (s), and τ the instantaneous WSS vector.

TAWSS is a metric used to quantify the average WSS experienced by the endothelium over a cardiac cycle. It provides insight into the overall haemodynamics environment and is often used to identify regions prone to atherosclerosis development when low (<0.4 Pa) (Malek et al., 1999). Additionally, a TAWSS >5 Pa is generally considered high in the aorta. Some studies even classify TAWSS >3 Pa as elevated for example, in ascending aortic aneurysm patients, regions with TAWSS exceeding 3 Pa were found on the aneurysm's outer curvature and linked with wall degradation risk (Salmasi et al., 2021).

OSI quantifies the cyclic departure of the WSS vector from its predominant axial alignment. It varies between 0 and 0.5. High OSI values indicate areas where the flow direction changes frequently during the cardiac cycle. These regions of oscillatory flow are often correlated with endothelial dysfunction and increasedsusceptibility to atherosclerosis (Di Achille et al., 2014).

RRT is another important parameter in assessing the local haemodynamics environment. It represents the relative time blood particles spend near the vessel wall. Areas with high RRT are associated with increased particle-wall interactions, potentially leading to a greater accumulation of atherogenic particles and an increased risk of plaque formation. Research suggests that values around 20-30 Pa⁻¹ represent a threshold above which there is a higher likelihood of promoting cell deposition (Stokes et al., 2023a, Xu et al., 2017, Xu and Avila, 2018).

ECAP combines various haemodynamics parameters to predict areas where the endothelium is likely to become dysfunctional or "activated." It typically incorporates low TAWSS and high OSI. Regions with high ECAP (>1.4 Pa⁻¹) are more susceptible to endothelial activation, leading to increased inflammation and atherosclerosis (Deyranlou et al., 2021, Di Achille et al., 2014).

1.5.2.TBAD Haemodynamics

TBAD is characterised by unique haemodynamics features that significantly impact patient outcomes and treatment strategies. The AA often exhibits dilation, leading to a reduction in velocity and mean WSS in this region, consequently diminishing the typical helicity development found in healthy aorta (Callaghan et al., 2019, Frydrychowicz et al., 2012). This dilation increases WSS immediately distal to the LSA, where the PET is typically found, proximal to the LSA and allows blood to enter the FL (Liu et al., 2022, Weiss et al., 2012). This creates a jet-like flow that can impinge on the opposite FL wall, potentially leading to further expansion or complications (Li et al., 2021, Saitta et al., 2021).

The flow in the aorta is typically laminar. However, in TBAD, blood flow is disrupted, exhibiting turbulence and recirculation patterns that can develop in both TL and FL. The high flow velocity found in the vicinity of entry tears can lead to high Reynolds numbers (Re), causing turbulence (Takahashi et al., 2021). This turbulence increases energy dissipation, leading to higher pressure losses and risks of blood damage, such as hemolysis and platelet activation, which can contribute to thrombosis and local dilatation (Andersson and Karlsson, 2021, Kaji, 2018, Spanos et al., 2019).

Thrombosis in AD is closely linked to luminal pressure differences, particularly in TBAD. Studies have shown that proximal FL thrombosis is associated with lower FL pressure, which can lead to fewer complications (Parker et al., 2022). This relationship between thrombosis and pressure differences has important implications for patient outcomes and treatment strategies.

The pressure difference between the TL and FL is a critical haemodynamic factor in TBAD, and associated links to thrombosis have been widely studied (Lawrence and Gooch, 2009, Marlevi et al., 2021, Zilber et al., 2021, Parker et al., 2022).

The size and location of entry and re-entry tears influence the luminal pressure gradient in TBAD. A larger entry tear typically results in higher FL pressurisation, while a smaller entry tear can increase the pressure difference between the TL and FL (Zimmermann et al., 2023, Chen et al., 2022a). The size of the exit tear also plays a crucial role; a smaller one can led to negative pressure differences between the TL and FL, potentially causing FL expansion (Cuellar-Calabria et al., 2021). Additionally, the number, size, and location of tears significantly influence TBAD haemodynamics. Multiple re-entry tears can help decompress the FL, potentially stabilising the dissection, while fewer are associated with progressive aortic dilatation (Jafarinia et al., 2023, Kotelis et al., 2016).

The pulsatile nature of blood flow adds another layer of complexity to TBAD haemodynamics (Birjiniuk et al., 2017). The wall elasticity differences between the TL and FL result in varying rates of flow and pressure wave propagation within each lumen, depending on the number and shape of luminal communications (Brandon et al., 2024, Veger et al., 2021). During systole, the pressure and flow in the FL increase, potentially causing expansion of the FL (Bellala et al., 2024), and displacement of the IF (Karmonik et al., 2012c, Rudenick et al., 2013). These differences can cause desynchronised TL and FL pressure gradients, which drive the motion of the IF and could potentially lead to malperfusion (Mega et al., 2006, Sakata et al., 2015).

Over time, FL dilatation leads to modified lumen perfusion, reduced flow velocities near the FL wall, and significant decreases in WSS and total pressure (Higashigaito et al., 2021, Kotelis et al., 2016, Ruiz-Muñoz et al., 2022). This

dilatation might serve as a compensatory mechanism to minimise stresses on the vessel wall tissue (Chen et al., 2013a; Ruiz-Muñoz et al., 2024).

Assessing TBAD haemodynamics can be done clinically using medical imaging; the following section reviews the most common techniques employed.

1.5.3. Clinical Techniques

1.5.3.1. 2D Flow MRI

Through-plane phase-contrast MRI, also known as 2DMRI, is a valuable non-invasive imaging technique for assessing haemodynamics in patients with TBAD. This method measures blood flow velocity within the aorta, capturing flow data in a single plane perpendicular to the specified direction (Dillon-Murphy et al., 2016). It provides critical insights into blood flow dynamics, essential for understanding the progression and management of TBAD.

However, the application of 2D-Flow MRI in assessing aortic flow presents several challenges. Aortic blood flow rarely adheres to a single, straightforward trajectory, with secondary flow structures such as helical and retrograde flows inherent in healthy and pathological aortae, making it challenging to capture the full extent of flow dynamics (Garcia et al., 2019). Aligning the imaging plane perfectly perpendicular to the flow can be difficult, as the primary flow direction is not known in advance, potentially leading to inaccurate or misleading data. Furthermore, 2D-Flow MRI captures only a single component of the velocity vector.

While 2DMRI offers valuable insights, it is often complemented by 4DMRI, which provides a more comprehensive assessment of blood flow throughout the entire aorta.

1.5.3.2. 4D Flow MRI

4DMRI is an advanced imaging technique that has revolutionised the visualisation and quantification of complex flow patterns within the cardiovascular

system, particularly in TBAD. This technique allows for the measurement of three-component, three-dimensional velocity fields throughout a volumetric region, providing a comprehensive view of blood flow dynamics in the TL and FL of the dissected aorta (Clough et al., 2012, Takahashi et al., 2022). Unlike traditional 2D imaging techniques, 4DMRI captures flow data over the cardiac cycle, providing a dynamic view of blood flow changes during systole and diastole. This temporal information is crucial for understanding the pulsatile nature of flow in TBAD. The technique covers the entire aorta, allowing for a holistic assessment of flow patterns from the aortic root to the abdominal aorta, which is particularly valuable in TBAD, where the dissection can extend over a large portion of the aorta (Catapano et al., 2020, Lescan, 2022).

The detailed haemodynamics data provided by 4DMRI aids in the risk stratification of TBAD patients and can guide treatment decisions. Those with more complex flow patterns or higher FL flow parameters may be at greater risk of adverse outcomes, potentially requiring more aggressive management or earlier intervention. The technique allows the assessment of thrombosis within the FL, which is crucial for predicting outcomes (Stankovic et al., 2013, Zhuang et al., 2021).

Recent developments in 4DMRI have focused on reducing acquisition times through compressed sensing acceleration techniques (Kilinc et al., 2023, Pathrose et al., 2021). These advancements allow for significantly faster scan times without compromising the quality of haemodynamics measurements, which is particularly beneficial for TBAD patients who may have difficulty with prolonged scanning.

One of the key advantages of 4DMRI is the ability to extract velocity vectors from any plane, enabling the computation of related indices from the data (Callaghan and Grieve, 2018, Kolipaka et al., 2017, Veger et al., 2021). This helps to detect complex flow patterns and velocity distributions *in vivo*, even in cases where vessel structures or the size of dissection tears are not well-defined (Allen et al., 2023, Liu et al., 2023). Additionally, 4DMR has been used with numerical methods to extract intravascular pressure fields, showing promise in supporting the diagnosis and prognosis of TBAD and the timing of interventions (Bock et al., 2011, Meier et al., 2010).

However, several challenges remain for widespread clinical implementation. Long acquisition times have historically limited use, though recent advances have reduced scan times to a few minutes (Callaghan et al., 2016, Markl et al., 2012). The large data volumes necessitate the spatial and temporal resolution to be compromised, with 1–5 mm and 35–50 ms typically used for a ortic imaging (Cherry et al., 2022). This limited spatial resolution contributes to partial volume effects and underprediction of velocities, which are especially problematic near the vessel wall and in smaller arteries. In these regions, the velocity gradients are steep, and the inability to accurately capture flow near the wall leads to errors in the estimation of critical hemodynamic parameters, such as WSS (Berhane et al., 2020, Juffermans et al., 2021, Marin-Castrillon et al., 2023, Zimmermann et al., 2018). Additionally, nearwall resolution issues can exacerbate inaccuracies in vessel wall segmentation, particularly when the boundary between blood and vessel wall is blurred due to voxel averaging or in small vessels where the wall-to-lumen ratio is higher (Levilly et al., 2020, Markl et al., 2011a, Soudah et al., 2017). Deep learning techniques can be used to improve the segmentation of the aorta significantly and enhance the quality of 4DMI images (Fujiwara et al., 2022, Sundström and Laudato, 2023). Automating the segmentation process can minimise the variability and potential errors associated with manual segmentation, leading to more consistent and reliable results that are particularly important for accurate WSS calculation.

The limitations of cycle-averaging in capturing the dynamic nature of blood flow are significant, as it fails to account for the pulsatile variations that occur with each heartbeat. Moreover, the influence of respiratory and proximal cardiovascular motion can introduce additional inaccuracies in flow measurements. A critical challenge in flow imaging is the need to predetermine a velocity encoding (VENC) value, which represents the anticipated maximum velocity and varies among patients (van Ooij, 2024). Selecting an excessively high VENC can compromise the signal-to-noise ratio (SNR) in areas of slow flow. At the same time, an overly low VENC may lead to inaccuracies in regions of rapid flow and potentially cause aliasing artefacts. This issue is particularly pronounced in TBAD, where extreme velocity variations are commonly observed throughout the affected area (Kroeger et al., 2021). Although multi-VENC techniques have been developed to address this problem and are

recommended for use in TBAD cases, their adoption in clinical practice remains limited (Moersdorf et al., 2019, Sherrah et al., 2017).

While 4DMRI shows great promise for assessing haemodynamics in TBAD, ongoing efforts have focused on validating its measurements, assessing limitations and standardising protocols across centres to enable widespread clinical adoption and multi-centre studies (Wang et al., 2022, Mongeon et al., 2016). Integrating 4DMRI data with CFD models can enhance the images, provide more accurate insights into TBAD haemodynamics and potentially improve predictive capabilities for disease progression and treatment outcomes (Armour et al., 2020a, Armour et al., 2022, Armour et al., 2020b, Stokes et al., 2023b).

1.5.3.3. Doppler Ultrasound

Doppler ultrasound is an effective diagnostic tool for detecting and managing thoracic aortic dissection (TBAD), particularly in emergency settings. Its ability to provide real-time haemodynamic information makes it valuable for rapid decision-making, including the detection of dissection flaps, blood flow abnormalities, and complications such as false lumen thrombosis (Brubakk, 1982). The technique is non-invasive, widely accessible, and critically, non-ionising, making it a safer option for repeated assessments and follow-up, especially in vulnerable or haemodynamically unstable patients. Doppler ultrasound also facilitates ongoing monitoring of cardiac function, offering estimates of stroke volume and cardiac output, which contribute to a broader understanding of cardiovascular health.

However, there are limitations to using Doppler ultrasound in this context. Doppler may only provide comprehensive information about the extent of the dissection or the involvement of branch vessels. The resolution of ultrasound images can be limited compared to other imaging modalities, such as CTA or MRI, which offer more detailed anatomical visualisation (Nauta et al., 2016, Donati et al., 2015). Similar to 2DMRI, Doppler ultrasound can be prone to measurement inaccuracies stemming from the selection of the imaging plane. This technique also yields inaccurate results in areas characterised by intricate flow patterns. Additionally, the

accuracy of Doppler ultrasound can be operator-dependent, requiring significant expertise to interpret the findings correctly.

1.5.3.4. Blood Pressure Measurements

While 4DMRI imaging provides detailed insights into blood flow patterns and velocities, it does not directly measure blood pressure, which is essential for assessing the severity and progression of TBAD. Integrating blood pressure measurements with flow imaging modalities offers a comprehensive understanding of haemodynamics in TBAD patients (Zhou et al., 2017). Regular blood pressure measurements guide antihypertensive therapy, which is a crucial aspect of medical management in TBAD.

Invasive arterial pressure monitoring, involving the cannulation of a peripheral artery, remains the gold standard for obtaining accurate, localised pressure measurements in segments affected by dissection (Hernandez et al., 2022, Ruszala et al., 2014). This technique provides real-time data on arterial waveform morphology and quantitative pressure values, which is particularly valuable in critically ill patients or those undergoing surgical interventions. However, in TBAD, where the integrity of the aortic wall is compromised, invasive monitoring is cautiously used due to the risk of further damage to fragile vessel walls (Nguyen and Bora, 2023).

Non-invasive methods, such as brachial sphygmomanometry, are commonly employed to measure systemic blood pressure (Chung et al., 2013, Meidert and Saugel, 2017). While these measurements reflect systemic pressure at the brachial artery, they do not provide information about pressures within specific segments of the aorta affected by dissection (Chung et al., 2013, Sultan et al., 2023). Moreover, they do not capture the waveform morphology of aortic pressure, which is crucial for diagnosing and managing TBAD effectively. The ankle-brachial index can help detect malperfusion syndromes associated with TBAD, but it has limitations in accurately determining pressures within the dissected aorta (Sultan et al., 2023, Memiç Sancar et al., 2022).

1.5.4. Cardiovascular Flow Modelling

CFD plays a crucial role in understanding and simulating the complex haemodynamics of the cardiovascular system. In engineering terms, the cardiovascular system is analogous to a network of pipes through which blood flows, subject to varying geometries and boundary conditions (BCs). The study of blood flow dynamics is governed by fundamental principles of fluid mechanics, primarily the conservation laws of mass and momentum.

Blood flow is described by nonlinear partial differential equations (PDEs), namely the continuity and the Navier-Stokes equations. Two well-known analytical solutions that provide foundational understanding are the Poiseuille Flow and Womersley Flow (Loudon and Tordesillas, 1998, Sutera and Skalak, 1993, Womersley, 1955). Poiseuille Flow describes the steady-state laminar flow in a straight, rigid pipe with a constant circular cross-section driven by a constant pressure gradient. The velocity profile for Poiseuille Flow is parabolic, given by:

$$u(r) = \frac{\Delta p}{4\mu L} (R_a^2 - r^2)$$
 1.5

where Δp is the pressure drop (Pa), L is the pipe length (m), R_a is radius (m), and r is radial position (m). On the other hand, Womersley Flow describes the pulsatile, laminar flow in a straight, rigid pipe with a constant circular cross-section driven by a periodic pressure gradient. It accounts for the oscillatory nature of blood flow due to the heartbeat. The Womersley number characterises the relative importance of pulsatile inertial forces to viscous forces, such as:

$$\alpha = R_a \sqrt{\frac{\omega \rho}{\mu}}$$
 1. 6

Where ω is the angular frequency (1/s) of pulsation. The velocity profile for Womersley Flow is more complex and involves Bessel functions to account for the oscillatory nature of the flow.

However, the complexity of real-world cardiovascular flows necessitates using numerical methods to approximate solutions. For TBAD applications, both zero-dimensional (0D) and three-dimensional (3D) models play a crucial role. Zero- (0D)

provide efficient simulations of wave propagation and global haemodynamics, while 3D models offer detailed local flow analysis.

1.5.4.1. Lumped Parameter Models

The 0D lumped parameter model is a simplified, yet effective, approach to simulate cardiovascular system haemodynamics, including the aorta. This modelling technique treats the vascular system as interconnected compartments characterised by lumped parameters: resistance (R), compliance (C), and inertance (L). These parameters represent hydraulic analogies to electrical components in a circuit, where pressure (P) and flow rate (Q) are functions of time (t) rather than spatial coordinates. R is analogous to friction losses in the vascular system, C represents the elasticity and deformability of vessel walls, and L is analogous to the inertial effects of blood flow (Figure 1. 6) (Schönfeld, 1954). The table below summarises the hydraulic-electric analogy of the RLC components, their equation and electrical schematic.

Electric	Hydraulic	Component	Equation
Resistance	Friction losses	Q P R	$\Delta P = RQ$
Capacitance	Compliance	$P\left(\begin{array}{c} \downarrow Q \\ \overline{\downarrow} \end{array}\right) C$	$Q = \frac{CdP}{dt}$
Inductance	Inertance	$Q \xrightarrow{P}$	$\Delta P = \frac{LdQ}{dt}$

Figure 1. 6 Electric components and their hydraulic analogy.

Lumped-parameter models can represent the vasculature using either single or multiple blocks. A single block describes an entire vascular compartment or the vasculature using R, L and C (Loudon and Tordesillas, 1998, Sutera and Skalak, 1993). The Windkessel model is a fundamental concept in cardiovascular modelling,

representing the arterial system as a lumped parameter model in a single block. The two-element Windkessel (WK2) model, first proposed by Stephen Hales in 1733 and mathematically formulated by Otto Frank in 1899, consists of a capacitor (*C*) and a resistor (*R*) in parallel. The capacitor represents the elastic properties of large arteries, while the resistor models the resistance of small peripheral vessels (Westerhof et al., 2009, Zhou et al., 2019). Despite its simplicity, the WK2 model provides a basic representation of arterial behaviour, particularly useful for estimating total arterial compliance when the peripheral resistance and the aortic pressure waveform are known. However, it has limitations in capturing high-frequency components associated with pressure reflections in the arterial network.

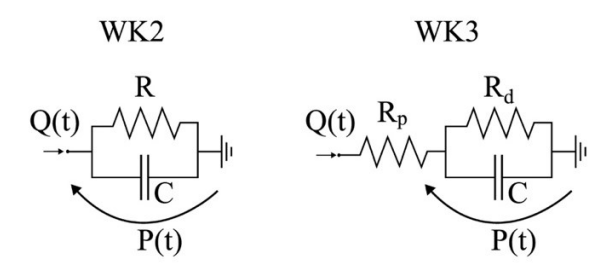


Figure 1. 7: Schematic of the two-element (WK2) and three-element (WK3) Windkessel models.

To address these limitations, a three-element Windkessel (WK3) model is commonly employed, which includes a proximal impedance element (R_p) in parallel with the distal resistance (R_d) which is in series with the original compliance (C) (Westerhof et al., 1969, Westerhof et al., 2009). This additional resistance represents the ratio of oscillatory pressure to oscillatory flow rate in the absence of reflective waves. In the WK3 model, the total resistance $(R_T = R_p + R_d)$ equals the systemic vascular resistance of the WK2 model, while C continues to represent arterial elasticity. The introduction of R_d significantly improves the model's high-frequency performance.

In more complex scenarios, the vascular system is modelled as a network of these 0D building blocks, each representing a vessel segment with its own R, C, and L parameters. This approach allows for a more detailed representation of pressure and flow dynamics throughout the cardiovascular system, accounting for interactions between different vascular segments (Shi et al., 2011, Zhou et al., 2019).

1.5.4.2. Three-Dimensional Models

Three-dimensional (3D) CFD models are essential tools for studying TBAD. These models are based on the fundamental governing equations of fluid dynamics, the continuity and Navier-Stokes equations. For an incompressible, isotropic, and Newtonian fluid, the continuity equation expresses mass conservation, stating that the divergence of the velocity field must be zero, such as:

$$\frac{\partial \rho}{\partial t} + \nabla \cdot (\rho \mathbf{u}) = 0 \tag{1.7}$$

Where ρ is the fluid density (kg/m³) and $\mathbf{u} = \mathbf{u}(x,y,z,t)$ is the three-dimensional velocity vector. The Navier-Stokes equations represent the conservation of momentum, accounting for forces such as pressure gradients, viscous forces, and fluid-wall interactions, such as:

$$\rho\left(\frac{\partial \boldsymbol{u}}{\partial t} + \boldsymbol{u}.\boldsymbol{\nabla}\boldsymbol{u}\right) = -\boldsymbol{\nabla}p + \mu\boldsymbol{\nabla}^2\boldsymbol{u} + f$$
 1.8

Where p is the pressure (Pa), μ the dynamic viscosity (N. $\frac{s}{m^2}$) and f represents body forces ($\frac{N}{m^3}$).

To solve these equations computationally, the process begins with mesh generation, where the geometry of the aorta is discretised into a finite number of small elements. The partial derivatives in the continuity and Navier-Stokes equations are then approximated using finite difference, finite volume, or finite element methods. These approximations transform the PDEs into a system of algebraic equations that can be solved numerically. The choice of discretisation scheme significantly affects the accuracy and stability of the numerical solution, with higher-order schemes often employed to improve precision.

To capture the transient nature of blood flow within the aorta, the temporal derivative in the Navier-Stokes equations must be discretised using appropriate time-stepping methods. This involves approximating the unsteady term $\frac{\partial u}{\partial t}$ over discrete time intervals, Δt , transforming the problem into a sequence of time-dependent algebraic equations (Ferziger et al., 2020, Versteeg et al., 2007). Common time integration schemes include explicit methods, which calculate the solution at the next

time step directly but require small time steps for stability, and implicit methods, which allow larger time steps by solving coupled equations at each step but at a higher computational cost. Semi-implicit schemes, such as the Crank-Nicolson method, offer a balance between stability and accuracy. Additionally, the nonlinear convective term \boldsymbol{u} . $\nabla \boldsymbol{u}$ is often linearised or treated with specialised discretisation schemes to prevent numerical instabilities and ensure accurate representation of complex flow patterns. The selection of the time step size is crucial; it must be small enough to resolve important transient phenomena and maintain numerical stability, but large enough to allow efficient computation. Adaptive time stepping techniques are sometimes employed to optimise this balance dynamically throughout the simulation. Overall, careful temporal discretisation and time-stepping strategy are essential to achieve stable and accurate unsteady CFD simulations of blood flow in thoracic aortic dissections.

1.6. Computational Modelling of TBAD

1.6.1. Numerical Methods

Numerical methods are essential for solving the complex Navier-Stokes and continuity equations in most practical applications, as these partial differential equations typically lack unique analytical solutions. The Finite Volume Method (FVM) is the most widely adopted approach, which discretises the flow domain into small control volumes (McDavid, 2001). The governing equations are integrated within each volume, and flow variables are assumed constant therein. This method effectively transforms the differential equations into a set of algebraic equations that can be solved numerically. FVM has gained popularity due to its robustness and ability to handle complex geometries, making it the foundation of many commercial and open-source CFD software packages.

While FVM dominates fluid simulations, the Finite Element Method (FEM) is sometimes employed in aortic simulations for fluid-structure interaction (FSI) modelling (Hirschhorn et al., 2020). FEM excels at modelling solid mechanics and

can be coupled with FVM to simulate scenarios where fluid flow influences structural deformation and vice versa. This coupling enables more comprehensive simulations of phenomena like blood flow in flexible vessels, albeit at a significantly higher computational cost.

To address the computational demands of full 3D simulations, Reduced Order Modelling and Machine Learning (ML) techniques have attracted considerable attention in recent years (Hahn et al., 2021, Pegolotti et al., 2024, Tahir et al., 2023). These approaches aim to capture the essential physics of complex flows while reducing computational complexity. One such method is Proper Orthogonal Decomposition, which decomposes velocity data into a set of orthonormal modes and their temporal dynamics (Chatpattanasiri et al., 2023, Han et al., 2020). This technique has been applied to enhance the resolution of medical imaging data and analyse flow features in cardiovascular systems.

Another promising development is using Physics Informed Neural Networks (Du et al., 2023, Zhang et al., 2023). These ML models incorporate the Navier-Stokes equations directly into their loss functions, allowing them to reconstruct detailed flow fields from limited data more efficiently than traditional numerical solvers.

1.6.2.Image Segmentation

Segmentation of TBAD from medical imaging data, mainly CTA scans and MRI sequences, is a critical step in generating image-based, patient-specific CFD models. This process involves delineating the aortic wall's boundaries and identifying and characterising the TL, FL, IF, and any tears present (Pepe et al., 2020).

Although highly accurate, manual segmentation is challenging and time-consuming, especially in complex cases. It relies heavily on the expertise of operators (Preim and Botha, 2014), and this dependence can introduce inconsistencies in the geometrical representation of the aorta, potentially influencing subsequent CFD results, particularly in estimated haemodynamics parameters such as WSS, as discussed in section 1.5.2.

The complex geometry of TBAD presents a significant challenge for segmentation (Nienaber et al., 2009, Pepe et al., 2023). The aorta morphology in

TBAD patients can vary widely, affecting the shape, size, and tortuosity of both lumina. Despite the high resolution of CTA imaging, tears can be subtle and challenging to differentiate from other structures within the aorta, which can be crucial for accurately simulating flow dynamics in TBAD.

In MRI, anatomical sequences like TrueFISP delineate the aortic lumen and IF, providing better soft tissue contrast than CTA (Babin et al., 2014, Wörz et al., 2014). Flow-based segmentation using 4DMRI data can refine the segmentation, particularly in distinguishing the TL from the FL based on flow patterns. However, 4DMRI data often suffers from lower SNR than CTA, especially in slow or complex flow regions, such as in the FL as the flow can be stagnant in some cases. This low SNR can make accurate segmentation challenging, particularly for automated algorithms (Juffermans et al., 2021, Marin-Castrillon et al., 2023, Ramaekers et al., 2023).

Given these challenges, there is a growing interest in automated and semi-automated segmentation techniques. Semi-automated methods often employ region-growing algorithms, where a seed point is placed in the TL or FL, and the algorithm expands to fill the lumen based on intensity thresholds (Ashok and Gupta, 2021, Jin et al., 2021, Krissian et al., 2014, Sieren et al., 2021). Additionally, hybrid approaches, including AI/ML algorithms for initial segmentation, are increasingly being adopted, followed by human review and refinement (Dey et al., 2019, Lim et al., 2020, Szabo et al., 2022). Convolutional neural networks have shown promise in automating the segmentation of aortic structures from CTA (Cao et al., 2019, Chen et al., 2022b, Gu and Cai, 2021). These methods learn from annotated datasets to accurately delineate the aortic wall, lumens, and tears. They aim to improve segmentation accuracy, reduce operator dependence, and streamline the process for large-scale simulation studies of TBAD.

Rigid and elastic registration techniques allow to reconcile differences in patient positioning during different scans and to help compare CFD simulations based on a different dataset, for example, pre- and post-surgery (Bian et al., 2022, Biesdorf et al., 2012, Schenkenfelder et al., 2021). Rigid registration aligns images by applying translation and rotation without accounting for deformations, making it suitable for bony structures or minimally distorted anatomy. In contrast, elastic registration allows for local deformations, enabling the alignment of soft tissue structures that may shift

or deform between scans. For example, CTA-based segmentation can be elastically registered to other imaging modalities, such as 4DMRI, to incorporate additional geometric details and refine the accuracy of the model.

1.6.3.Inlet Boundary Conditions

The concept of inlet boundary conditions (BCs) in TBAD simulations involves specifying the velocity profile of blood as it enters the aorta from the heart. The inlet plane in aortic simulations usually lies near the aortic root. Patient-specific inlet velocity profiles (IVP) can be extracted from imaging modalities such as 2DMRI and 4DMRI, which provide two- and three-directional IVPs, respectively (Saitta et al., 2023, Yokosawa et al., 2005). These waveforms capture the pulsatile nature of blood flow, offering a realistic representation of haemodynamics throughout the cardiac cycle. Preserving this variability is essential for accurately reflecting patient-specific haemodynamics.

Idealised flow profiles, such as Poiseuille or uniform flow, are often employed when detailed patient-specific inlet data is unavailable. These profiles typically consist of normalised physiological flow waveforms or flat velocity distributions with assumed stroke volumes and heart rates. However, their application may not accurately capture the intricate TBAD flow dynamics present *in vivo* (Alimohammadi et al., 2014, Chen et al., 2013, Dillon-Murphy et al., 2016, Tse et al., 2011).

The choice of IVP can significantly affect the predicted haemodynamics in TBAD simulations. Studies have shown that different IVPs can lead to variations in flow patterns, WSS, and other haemodynamics parameters, particularly in the AA and aortic arch (Armour et al., 2020a, Morbiducci et al., 2013, Stokes et al., 2023a). In TBAD cases, where the PET is often located just distal to the left subclavian artery, the influence of the IVP can be substantial (Pirola et al., 2017, Stokes et al., 2023b, Youssefi et al., 2018). It was also proposed that the helicity and counter-rotation vortices in the AA could not be represented with non-patient specific or flat profiles in TBAD (Bozzi et al., 2017, Youssefi et al., 2018). Similar conclusions were obtained in studies involving valve abnormalities or prostheses (Bruening et al., 2018, Jayendiran et al., 2020, Pirola et al., 2018). However, this influence diminishes as the

flow progresses downstream, with the effects on the DA being limited or minimal compared to the upstream regions (Mariotti et al., 2023, Tajeddini et al., 2023).

1.6.4. Outlet Boundary Conditions

Zero-pressure, flow split, and dynamic (lumped parameter models) BCs are the three most common types of outlet BCs used in CFD simulations for TBAD. Accurate outlet BCs are critical for achieving realistic haemodynamics predictions. Zero-pressure outlet BCs have been commonly used in the past at the supra-aortic and abdominal outlets .(Chi et al., 2022, Osswald et al., 2017). However, this method has been shown to inadequately replicate physiological flow and pressure conditions compared to more advanced techniques (Morbiducci et al., 2010, Pirola et al., 2017). It is well understood that the flow distribution among vascular branches is highly dependent on the downstream vasculature. Implementing a zero-pressure boundary condition at the outlets causes the flow split to be determined solely by the impedance of the 3D domain (Vignon-Clementel et al., 2006). However, this approach can result in unrealistic flow distributions and pressure gradients, as it neglects the influence of downstream vascular resistance and compliance. Furthermore, it is crucial to calculate realistic pressures for deformable models, especially at the aortic wall as the fluid force drives the vessel's deformation. Some studies use time-dependent pressure waves from previous research (Tse et al., 2011). However, it is important to note that pressures in TBAD can differ significantly from those in healthy individuals.

Murray's Law, which states that flow in a vessel is proportional to its diameter cubed, has been employed more recently to determine the proportion of flow exiting each outlet in the absence of patient-specific data (Brüning et al., 2018; McElroy and Keshmiri, 2018). However, this law relies on several assumptions that may not be applicable to flow in large arteries, and its accuracy is even more questionable for smaller vessels. Small vessels are generally defined as those with diameters less than approximately 300–500 μm, such as coronary arteries, where the effects of blood's non-Newtonian behaviour, vessel tortuosity, and local geometric variations become increasingly significant (Padro et al., 2020, Sherman, 1981). In addition to small vessels, low shear rate conditions are also observed in aneurysms and false lumens,

regions characterised by disturbed or stagnant flow. At low shear rates, blood exhibits non-Newtonian properties such as increased viscosity due to erythrocyte aggregation, which can significantly alter local haemodynamics and wall shear stress distributions (Cho et al., 1991). Ignoring these effects when defining flow splits at outlets can lead to unrealistic flow separations and reattachments, substantially impacting the accuracy of WSS predictions (Boccadifuoco et al., 2018; Gallo et al., 2012).

Dynamic BCs, such as lumped parameter models, have emerged as the preferred choice for TBAD simulations. Among these, the WK3 model, described in Section 1.5.4.1, is widely regarded as the optimal approach for coupling with 3D simulations to create multi-scale models of the vascular system (Vignon-Clementel et al., 2010). This method addresses the limitations of traditional boundary conditions by prescribing a pressure-flow relationship at the outlet, which accounts for the impedance of the downstream vasculature that is not included in the 3D domain. WK3 models are particularly effective in capturing the dynamics of distal vessel compliance, making them an ideal compromise for simulating peripheral vasculature (Westerhof et al., 2018).

Windkessel model parameters can be tuned using patient-specific data when available to optimize simulation accuracy. This process typically involves extracting flow rates from 2DMRI and 4DMRI data, measuring or estimating pressure values at key locations, and adjusting the model parameters to match the observed data (Armour et al., 2022; Boccadifuoco et al., 2018; Bonfanti et al., 2019, 2020; Pirola et al., 2019). Recent advancements in computational methods have significantly improved the calibration process of WK3 parameters (Black et al., 2023; Li et al., 2023; Romarowski et al., 2018). Whether utilizing Bayesian approaches or least-square methods, the calibration aims to adjust the parameters more rapidly to enable faster and more accurate deployment of patient-specific CFD simulations.

1.6.5. Aortic Compliance Modelling

Modelling aortic wall compliance is crucial for accurately simulating haemodynamics in TBAD, where the behaviour of the aortic wall, the IF and its interaction with blood flow significantly influence disease progression and treatment

outcomes. The ability of the aortic wall to expand and store blood during systole and contract and eject during diastole plays a vital role in maintaining proper blood flow and pressure throughout the cardiovascular system. This results in lower peak flow rates and often negative flow rates during systole and diastole, respectively. Additionally, the compliance reduces the peak pressure and the PWV (Schiffrin, 2004). PWV is a measure of how quickly pressure waves travel through the arteries, with higher PWV typically indicating stiffer, less compliant arteries.

In TBAD, the vessel's cross-sectional area can dynamically expand by up to 10% during the cardiac cycle (Zhu et al., 2022a). Additionally, the mobility of the IF varies from acute to chronic cases, with acute cases often exhibiting significant flap movement, reported up to 8-10 mm, and chronic cases showing reduced mobility, between 0-2mm (Ganten et al., 2009, Lortz et al., 2019, Yang et al., 2014). After surgical interventions such as a stent or graft placement, the compliance of the aortic wall can be significantly altered. These devices are typically made from materials much stiffer than the natural aortic wall, leading to a compliance mismatch that can affect haemodynamics within the aorta (Rovas et al., 2023, Sultan et al., 2022). This mismatch may result in altered WSS, higher pressures and PWV, potentially contributing to increased heart load, endothelial damage, atherosclerosis, endoleak, device migration or dislocation (Mohan et al., 2001, Morris et al., 2016, Weston et al., 1996).

Consequently, the points discussed in the previous paragraphs highlight the importance of accurately modelling aortic compliance in both pre- and post-operative conditions to understand its effects on haemodynamics. Compliance alters the distribution of WSS along the vessel wall, typically showing lower peak WSS due to increased luminal areas during systole (Emendi et al., 2021, Looyenga and Gent, 2018). However, modelling compliance in CFD is complex due to the often limited availability of *in vivo* aortic wall material properties, leading many studies to rely on a rigid-wall assumption that cannot fully capture patient-specific haemodynamics of TBAD (Wang et al., 2023a).

To accurately model these complex fluid wall interactions, FSI, previously mentioned in section 1.5.4.1, is commonly method. FSI modelling involves the coupling of CFD and FEM, enabling the simulation of both fluid (blood) and solid

(aortic wall) interactions to capture the compliant behaviour of the aorta (Wang et al., 2023a). CFD, governed by the Navier-Stokes equations, simulates the fluid dynamics, while FEM models the mechanical response of the aortic wall, typically represented as a hyperelastic material to account for its compliant nature (Hirschhorn et al., 2020). FEM captures the deformation of the aortic wall under varying pressure conditions, including systole and diastole. The FSI coupling integrates these two models by allowing data to transfer between the fluid and solid domains at each time step. CFD provides the pressure and velocity fields, which act as forces on the aortic wall, and FEM uses these forces to compute the resulting deformation. The deformed geometry of the aortic wall from FEM is then fed back into the CFD model to update the flow field, enabling a dynamic and accurate simulation of the FSIs.

When modelling the mechanical behaviour of the aortic wall and intimal flap (IF) in fluid-structure interaction (FSI) simulations, the vessel material is often assumed to behave as a linear elastic solid, characterised primarily by its Young's modulus (E). This linear elastic assumption simplifies the complex, inherently nonlinear and anisotropic properties of arterial tissue, enabling more tractable computational analysis. However, it does not fully capture the hyperelastic and viscoelastic behaviour exhibited by the aortic wall under physiological loading conditions (Holzapfel et al., 2000; Humphrey, 2002). Consequently, this simplification introduces inaccuracies in stress-strain predictions, which may impact the fidelity of simulated haemodynamics and wall deformation. Moreover, the E values employed in literature vary widely—from approximately 0.4 MPa up to 7 MPa for the aortic wall and from 1 MPa to 6 MPa for the intimal flap (Alimohammadi et al., 2015; Bäumler et al., 2020; Chen et al., 2016; Chong et al., 2020; Zhu et al., 2022b; Zimmermann et al., 2021)—reflecting both variability in tissue properties and the lack of patientspecific data. These challenges are compounded by the limited availability of in vivo measurements to characterise the true hyperelastic material behaviour of the dissected aortic tissue (Deplano and Guivier-Curien, 2024). Thus, while FSI provides valuable insights into TBAD haemodynamics and mechanics, the assumption of linear elasticity and variability in E values remain significant limitations affecting simulation accuracy.

To bypass the aforementioned limitations of FSI, alternative methods have been developed that can achieve physiologically realistic simulations without the computational cost of fully coupled FSI and material properties assumptions. One such method is using Radial Basis Functions (RBFs), which are mathematical functions that depend on the distance from a central point, allowing for smooth interpolation between known data points. RBFs have been used for AD simulations to morph and deform the computational mesh of the aorta based on dynamic CTA data, to account, for example, for longitudinal and radial aortic displacements and aortic root motion (Calò et al., 2023, Capellini et al., 2021, Capellini et al., 2018). The advantage of using RBFs in this context is their ability to handle complex geometries and large deformations while maintaining mesh integrity.

Additionally, the immersed boundary (IB) FEM has emerged as a powerful tool for simulating blood flow in complex geometries such as the aorta (Bourantas et al., 2021, Fumagalli and Vergara, 2024, Zorrilla et al., 2020). The IB FEM reduces computational costs as it does not require remeshing at every time step like FSI, which is particularly beneficial for aortic simulations involving large deformations.

Another method is the Moving Boundary Method (MBM) developed by Bonfanti et al., (2017), which describes the wall motion by relating the displacement of mesh nodes to pressure on the luminal surface. The MBM was validated against both *in vitro* and *in vivo* data, showing the successful ability to capture flow and pressure waves in a TBAD (Bonfanti et al., 2020). It has also been validated against FSI and was found to agree to within 1.8% and 1.3% in predicting flow and pressure waveforms, respectively, using an average relative difference calculation (Bonfanti et al., 2018); similar WSS-indices contours were also calculated. The MBM was also applied in the work of Stokes et al., (2021) in which they used cine-MRI and 4DMRI to inform the simulation framework. They showed closely matched luminal area expansion against the cine-MRI, and pressure and mean flow rate were simulated within 3% of error against the *in vivo* target.

However, the MBM has several limitations in its current implementation. While it provides accurate predictions of flow and pressure dynamics in compliant vessels, it does not account for longitudinal displacements and relies on a linear elastic relationship between displacement and force, which oversimplifies the material

behaviour of the aorta. Additionally, the temporal resolution of 4DMRI and cine-MRI images of TBAD is often insufficient to capture transient changes in the radial and non-elastic behaviour of the aorta, preventing the implementation of the method with a nonlinear and anisotropic tissue response.

1.6.6.Blood Rheology

Blood is a complex fluid composed of 45% red blood cells suspended in plasma, which makes up about 55% of its volume (Alexy et al., 2022). While plasma is considered as a Newtonian fluid, where shear stress and shear rate are linearly related with viscosity, μ , as the constant of proportionality, blood exhibits more intricate rheological properties (Meiselman and Baskurt, 2003), due to its particulate nature. These include yield stress, viscoelasticity, shear-thinning, and thixotropy. At shear rates exceeding approximately 100 s^{-1} , blood tends to behave more like a Newtonian fluid. This characteristic has led many researchers to adopt a simplified approach in CFD simulations of aortic flow, assuming a constant viscosity of about $4 \times 10^{-3} \text{ Pa·s}$ (Skiadopoulos et al., 2017). This simplification is often applied in models of AD as well, given the typically high shear rates in large arteries (Pirola et al., 2017, Polanczyk et al., 2018, Salmasi et al., 2021).

However, recent studies have highlighted the importance of considering non-Newtonian effects in certain regions of the dissected aorta, particularly in areas with low shear rates, such as the closed-end sections of the FL (Jafarinia et al., 2020, Qiao et al., 2019b). The most commonly used non-Newtonian viscosity model is the Carreau-Yasuda, for which empirical parameters are obtainer using measurements of blood (Beris et al., 2021)

1.6.7. Turbulent Flow Modelling

The modelling of blood flow in AD involves critical considerations regarding laminar and turbulent flow. While blood flow in the aorta is traditionally regarded as laminar, specific aortic conditions, such as an AD or coarctations, can lead to the formation of high-velocity regions and turbulence, particularly in the vicinity of the

PET (Helps and McDonald, 1954, Liepsch and Wallis, 1986). The onset of turbulence in steady fluid flows has been extensively studied, with the Re playing a critical role in characterising this transition.

For AD modelling, the choice of assumption is often justified using empirical correlations to determine critical and peak $Re(Re_c \text{ and } Re_p)$ following some empirical correlations (Peacock et al., 1998). In this approach, the onset of turbulence occurs when Re_p exceeds the Re_c , as follows:

$$Re_p = \frac{DV_p\rho}{\mu}$$
 1.9

$$Re_c = 169St^{0.83}\alpha^{-0.27}$$
 1. 10

with D (m) being the inlet diameter, V_p (m/s) the peak velocity, ρ ($\frac{\text{kg}}{\text{m}^3}$) the blood density, μ ($\frac{\text{kg}}{\text{ms}}$) the blood dynamic viscosity, St the Strouhal number. However, such correlations were established on an ideal straight tube, and thus the complex, patient-specific AD geometry and haemodynamics have necessitated the use of turbulence models in many studies.

Direct numerical simulation (DNS) is a powerful computational approach for turbulent modelling which provides highly accurate results by resolving all scales of motion in the flow, from the largest eddies down to the smallest dissipative scales. However, the application of DNS to AD presents significant challenges due to the complexity of the problem. The computational cost of DNS for AD is prohibitively high, making it impractical for routine clinical use or large-scale studies. DNS has been employed in limited TBAD and aortic pathologies studies (Corso et al., 2021, Xu et al., 2018). Continuous improvement of computational resources offers a promising perspective for DNS simulation as it has also been used in intracranial aneurysms studies (Eken and Sahin, 2017, Li et al., 2019, Yadollahi-Farsani et al., 2019).

Large Eddy Simulation (LES) is used in CFD simulations of turbulent flows by directly resolving larger eddies while employing models for smaller-scale turbulence. Lantz et al., (2012) have demonstrated the capability of LES to capture intricate flow patterns in a subject-specific human aorta model. Xu et al., (2020) compared LES with laminar flow modelling in aortas with dilation, concluding that LES more accurately represents the complex flow structures and turbulence

characteristics in such pathological conditions. Similarly, Manchester et al., (2021) evaluated LES alongside other computational methodologies for predicting WSS and turbulence parameters in patient-specific aortas, finding LES to be superior in accurately capturing flow features and delivering reliable estimates of turbulence intensity and WSS. However, LES is computationally expensive in the initialisation phase of the simulation, needing about 30-50 cardiac cycles to ensure the periodicity of the results (Andersson and Karlsson, 2021, Manchester et al., 2021).

Reynold Averaged Navier Stokes (RANS) is an averaging process resulting in additional terms, such as the turbulent kinetic energy and dissipation rate, that represent the effects of turbulence. These terms are not resolved directly but are modelled, making RANS computationally less demanding than DNS and LES. However, RANS models are inherently limited by their underlying assumptions and simplifications. They often rely on isotropic turbulence models, which inadequately represent the anisotropic nature of turbulence, especially in complex geometries and pulsatile flows, such as those found in blood flow modelling. These assumptions can fail to fully capture small-scale turbulence dynamics and intricate flow characteristics (Lopes et al., 2024, MdMolla and Paul, 2017, Schwarze and Obermeier, 2006). Despite this limitation, the lower computational cost of RANS makes it widely used.

The k-ω Shear Stress Transport (SST) is a widely used formulation of RANS as it is effective for simulating complex flows like those in AD (Menter, 1994). This model blends two turbulence models: the k-ω model, which is well-suited for nearwall turbulence modelling due to its ability to accurately resolve boundary layers, making it suitable for low-Reynolds-number flows but within turbulent regime, and the k-ε model, which performs better in the free stream by effectively handling turbulent kinetic energy dissipation. By switching between these models depending on the flow region, the k-ω SST model is particularly effective at capturing flow separation and adverse pressure gradients. Chen et al., (2013) compared a fine 28 million elements mesh in a laminar simulation with k-ω SST simulation using a 2 million elements mesh. Findings suggest that while the flow in the TL remained largely laminar, regions of turbulence were observed in the FL, especially near the PET. The study reported higher turbulence kinetic energy values in FL compared to the TL. Tomasi et al., (2023) used the RANS k-ω SST model for its computational

cost tradeoff compared to LES and DNS techniques in their coupled 0D-3D CFD model with reduced-order modelling for TBAD.

The SST-Tran model, an extension of the k-ω SST model, incorporates additional equations to account for laminar-to-turbulent transition (Cheng et al., 2014, Cheng et al., 2015). The model used in published studies is relevant for AD because it accurately represents the complex flow dynamics and transitions between laminar and turbulent states, which are critical due to the altered geometry and high Re. Additional formulations, such as the Launder and Sharma k-ε model, have been used in AD simulations (Moretti et al., 2023).

The choice of flow modelling approach can significantly impact the predicted haemodynamics, affecting the understanding of disease progression and wall remodelling risks in AD. The lack of consensus on the most appropriate turbulence modelling approach underscores the need for further research to establish more reliable and clinically relevant computational methods for AD simulations.

1.7. Applications of TBAD Modelling

Simulating the haemodynamics of TBAD involves a multidimensional exploration aimed at understanding complex interactions between blood flow dynamics and aortic wall behaviour. The primary goal of these computational models is to enhance our understanding of disease progression, predict adverse events, and ultimately improve patient outcomes. Key objectives include matching aortic flow characteristics with the behaviour of the dissected aortic wall, studying thrombosis and fluid dynamics within the FL, and providing comprehensive insights into the disease (Ong et al., 2020). Additionally, computational models evaluate different treatment strategies, aiding personalised treatment planning and predicting distal aortic remodelling after interventions.

The following sections review the state-of-the-art in TBAD haemodynamics and disease progression modelling, emphasising *in silico* approaches. Virtual interventions and the validation of *in silico* work against *in vitro* and *in vivo* data are also covered.

1.7.1. TBAD Morphology: Impact on

Haemodynamics

In TBAD patients, blood flow in the FL is typically characterised by slow, recirculating patterns, while the TL exhibits faster flow. This difference arises primarily due to the compression of the TL, which shifts most of the flow into the FL. As a result, the FL, despite its relatively larger volume, has slower velocities, whereas the TL experiences higher velocities (Armour et al., 2022, Jafarinia et al., 2023). Similar findings in terms of high FL flow rate and TAWSS were described by Fatma et al., (2022) when comparing favourable and unfavourable (FL being thrombosed) follow-ups of two cases. Such findings are supported by an FSI study, which shows that the movement of the IF can significantly compress the distal TL, with compression of up to 21.4% reported (Chong et al., 2020). Feiger et al., (2021) correlated the FL/TL volume flow split with aneurysmal degeneration in a parametric study. They observed that medically managed patients had a flow split averaging about 55% vs 80% for the aneurysmal degeneration group. Shang et al., (2015) reached similar conclusions in a study evaluating 14 patients. FSI simulations also demonstrated that even small pressure differences between the FL and TL are sufficient to displace the IF and induce dynamic obstruction in acute TBAD (Kim et al., 2023). This finding is particularly relevant for understanding the mechanisms behind sudden clinical deterioration in AD patients.

The interplay between TL and FL pressure and flow variations naturally amplifies these differences, contributing significantly to the development of the disease. CFD models have shown that the FL often experiences higher pressures than the TL, especially during systole (Armour et al., 2022). Moreover, the mechanical load applied to the FL, especially high pressures, have been shown to restrict positive remodelling and lead to expansion (Xu et al., 2017). This FL/TL pressure gradient also called the transmural pressure (TMP), can contribute to the expansion of the FL over time and increase the risk of rupture (Aghilinejad et al., 2022). However, the TMP varies through the cardiac cycle and depends on the patient-specific geometry of the

aorta. For example, Cheng et al., (2015) reported a case in which the TMP was mostly positive during the cardiac cycle. Xu et al., (2021b) proposed that when TMP balance occurs distally (i.e., TMP=0 mmHg), it leads to better longitudinal aortic remodelling. A balanced pressure between the TL and FL promotes even force distribution along the aortic wall, reducing localised stress and preventing adverse remodelling, particularly in the FL. This equilibrium, often achieved through drug treatment or ET, stabilises the aorta and minimises the risk of aneurysm progression or further dissection (Fatma et al., 2022).

Flow and pressure patterns are significantly influenced by the location and size of the PET. High-velocity jet-like flow entering the FL, observed in numerous CFD studies, creates areas of elevated TAWSS, which can contribute to further tear expansion or weakening of the surrounding aortic wall (Armour et al., 2022, Bonfanti et al., 2020). The size of the PET also plays a crucial role: larger PETs are associated with patent FLs, whereas smaller PETs are linked to complete thrombosis due to reduced circulation in the FL (Jafarinia et al., 2023). The flow conditions near the PET are particularly important for thrombus formation, as flap-induced high shear stress and shear rates have been shown to transport activated platelets and trigger the coagulation cascade (Bäumler et al., 2020, Fatma et al., 2022). Aneurysmal growth in the FL has also been linked to the amount of flow passing through the PET. Shang et al., (2015), demonstrated in a large cohort study that their aneurysmal degeneration group had an average PET flow of 78%. Similarly, FL growth rates of 3-7 mm per year have been reported in CFD follow-up studies of TBAD and reconstructed TAAD, particularly when the fenestration is proximal to the LSA (Stokes et al., 2023b, Zhu et al., 2021). Near-zero helicity and vortical structures proximal to the PET have also been associated with the most pronounced aortic growth (Fatma et al., 2022, Zhu et al., 2023). Furthermore, studies have shown that low TAWSS, high OSI, and elevated ECAP are closely associated with aneurysmal growth in this region (Stokes et al., 2023b, Fatma et al., 2022). FSI simulations further reveal that wall compliance and IF motion can exacerbate these dynamics, accelerating thrombus formation and influencing long-term aortic remodelling (Bäumler et al., 2020, Fatma et al., 2022).

Similar to PETs, re-entry tears (RETs) exhibit high-velocity blood jets that can lead to elevated local shear stress, contributing to further tearing or FL enlargement

(Deplano and Guivier-Curien, 2024). A jet impingement proximal to the left renal artery has been shown to generate high TAWSS and velocities (Pirola et al., 2019). Larger RETs promote increased retrograde flow and reduce FL pressure, whereas smaller RETs increase resistance, elevating FL pressure and retrograde velocities (Zadrazil et al., 2020). The highest WSS values are found at the edges of RETs, and larger RET sizes tend to amplify WSS more. RET diameter strongly correlates with TMP; larger RETs equalise pressures, while smaller RETs contribute to higher TMP differences (Keramati et al., 2020). Multiple RETs can stabilise the dissection by redistributing flow between the TL and FL, hence reducing retrograde flow in the FL, redistributing pressure, and lowering FL growth rates (Wan Ab Naim et al., 2014, Armour et al., 2020b). The proximity of RETs further influences flow dynamics: closely spaced RETs increase FL TAWSS and prevent thrombosis, whereas wider spacing reduces TAWSS, promoting thrombosis (Karmonik et al., 2012a, Karmonik et al., 2012c, Tsai et al., 2008, Armour et al., 2020b).

TBAD thrombosis has been extensively modelled using advanced computational techniques, focusing on parameters such as shear rates, fluid residence time, and platelet distributions derived from convection-diffusion-reaction transport equations (Chong et al., 2022, Menichini et al., 2016, Menichini and Xu, 2016, Menichini et al., 2018). These models incorporate platelet activation and aggregation, crucial steps in thrombus formation, through iterative approaches that simulate thrombus growth over time. Haemodynamics parameters and the likelihood of thrombosis are recalculated with each iteration as the flow domain adapts to the predicted thrombus formation, enabling personalised predictions of thrombus growth patterns, which can be validated against follow-up CTA scans (Menichini et al., 2018)

Recent advancements in computational techniques have allowed for the integration of fluid dynamics with chemical reactions involved in the coagulation cascade for in abdominal aortic aneurysm simulation (Biasetti et al., 2012, Rausch and Humphrey, 2017, Wilson et al., 2013, Wang et al., 2023b, Wang et al., 2021). The key distinction of these newer models is their incorporation of biochemical processes alongside fluid dynamics, providing a more comprehensive simulation of thrombus development. The models aim to capture the complex process of thrombus formation and growth within the aortic aneurysm. This involves platelet activation, fibrin

formation, and the interaction between the blood flow and the evolving thrombus. While such cascade models have primarily been demonstrated in the context of abdominal aortic aneurysm, they offer a promising framework that could be adapted and applied to the study of thrombus formation in TBAD.

1.7.2. Virtual Interventions and Digital Twins

CFD simulations have become a valuable tool for predicting outcomes postsurgery and evaluating potential treatment options. For instance, virtual stenting
studies by Alimohammadi et al., (2014), showed that a double-stent procedure in the
DA effectively reduces flow resistance, pulse pressure, and WSS, creating a healthier
environment for endothelial cells. Auricchio et al. (2014) conducted a patient-specific
computational study comparing the haemodynamics of a post-operative TEVAR case
with a virtual scenario in which the distal stenosis was artificially corrected. Their
simulations demonstrated that alleviating the distal stenosis led to significant reduction
in local peak velocities and pressures, and a more physiological wall shear stress
distribution throughout the thoracic aorta. These findings suggest that correcting postTEVAR geometric abnormalities—such as distal narrowing—can substantially
enhance local hemodynamics and potentially reduce long-term complications related
to flow disturbances.

These virtual experiments are not limited to standard procedures but also explore innovative techniques. Qiao et al., (2020a) and Qiao et al., (2019a), by simulating a double in situ fenestration of the LSA and the LCC, demonstrated that avoiding LSA coverage during TEVAR improved blood supply to aortic branches, enhanced TL expansion, and maintained stable pressure distribution.

Another promising aspect of virtual surgical planning is its ability to support the design of patient-specific stent-grafts. Tailored devices conform better to local anatomy, reducing stress concentrations and improving outcomes. It was demonstrated how medium-length endograft struck a balance between FL flow reversal and LV workload, minimising risks of malperfusion (Aghilinejad et al., 2022). Similarly, Bologna et al., (2023), showed that custom stent-grafts reduced Von Mises stress by

23% and improved flow patterns near aneurysms, offering a safer, more physiologically accurate solution.

When combined with compliant simulation, virtual surgery simulations offer deeper insights into post-surgical outcomes as they account for the interaction between the device and the dynamic behaviour of the aortic wall. This allows for the virtual testing of various surgical scenarios, such as different endograft lengths or device positioning strategies, to identify the optimal approach before surgery (Lee et al., 2023, Qiao et al., 2015). Qiao et al., (2020b), showed that an endograft optimised for individual anatomies (length and centreline angles) preserved flow and pressure distributions but flagged areas of high thrombosis risk, prompting the need for further refinements. Additionally, the impact of vascular interventions on cardiac function and structure provides valuable information on how procedures like TEVAR affect the heart. A study revealed a significant increase in LV stroke work and mass index following TEVAR, with both showing positive correlations with elevated mean blood pressure post-surgery (Van Bakel et al., 2019).

TEVAR modelling can also be done using only FEM simulation. The latest reviews highlighted the growing interest in evaluating the outcome of TEVAR using FEM simulation, allowing for detailed modelling of stent-graft and aortic wall interactions from a mechanical perspective (Derycke et al., 2023, Mandigers et al., 2023). Most studies model the thoracic stent-graft as two separate components, graft and nitinol, for more accurate representation. Various parameters are often evaluated, including Von Mises stresses, stent-graft apposition, and drag forces. Such predictive work prevents the kinking of the distal thoracic stent-graft, a deformation caused by excessive curvature or improper placement, and helps in selecting the most suitable stent-graft length for optimal TL expansion (Kan et al., 2024, Mandigers et al., 2023).

These virtual environments and interventions fall within the scope of Digital Twin simulations. A Digital Twin refers to a virtual representation of a physical object, system, or process that mirrors its real-world counterpart through data integration and computational modelling. In its most advanced form, a Digital Twin dynamically evolves over time by incorporating time-series or real-time data, allowing for continuous updates that reflect physiological changes and treatment effects. Specifically, a Digital Twin of the aorta is a patient-specific model that replicates

vascular structure, function, and biomechanics to simulate blood flow, predict disease progression, and support clinical decision-making (Sel et al., 2024). Although the simulations discussed here are not continuously updated with live patient data, they reflect the foundational concept of Digital Twins as a convergence of high-fidelity modelling and patient-specific clinical information.

Efforts such as the EU-funded MEDITATE project exemplify this paradigm by combining real-time haemodynamic modelling, high-resolution imaging, big data analytics, and 3D printing to replicate and investigate pathological aortic conditions (DOI: 10.3030/859836). By supporting 14 PhD researchers, the project aims to enhance individualised risk prediction, optimise surgical planning, and refine endovascular intervention strategies.

Another example is TAVR-AID, developed at Queen Mary University of London and Barts Health NHS Trust. This Digital Twin platform integrates imaging data, CFD simulations, and AI-based outcome prediction to assist in transcatheter aortic valve replacement. While it may not yet function as a real-time feedback system, it leverages pre-operative data to inform valve sizing, placement, and positioning helping clinicians reduce complications such as stroke or paravalvular leaks and improving long-term valve durability.

As Digital Twin technology evolves, it holds great promise for transforming cardiovascular care through personalised diagnostics, virtual clinical trials, and improved long-term health management.

1.7.3. Model Validation

Validating CFD simulations is a complex yet essential step to ensure their accuracy and reliability in predicting patient-specific outcomes. This process typically involves comparing CFD results with *in vivo* measurements, such as blood flow and aortic wall displacement measurements obtained from MRI data and pressure measurements from catheter or brachial measurements (Armour et al., 2022, Ong et al., 2020). However, obtaining such *in vivo* data poses significant challenges, not only in terms of accuracy but also in availability. As a result, CFD simulations often lack

precise validation against real-world data, limiting their reliability, as previously mentioned.

An alternative validation method involves in vitro modelling with 3D phantoms, which offers several advantages in CFD validation (Franzetti et al., 2019, Yazdi et al., 2018). These phantoms allow researchers to replicate complex aortic geometries under controlled conditions, enabling repeated experiments without the risks and ethical concerns associated with patient studies. Additionally, 3D phantoms are cost-effective compared to clinical trials and provide the flexibility to test various configurations, BCs, and stent designs through trial-and-error approaches. Despite their usefulness, constructing 3D phantoms presents significant challenges. Replicating the complex and patient-specific geometry is time-intensive and technically demanding, requiring precise fabrication techniques and experience to ensure anatomical accuracy and appropriate material properties (Franzetti et al., 2022). Additionally, developing compliant phantoms that mimic the elasticity of the aorta is particularly difficult due to limitations in transparent materials suitable for flow visualisation techniques like Particle Image Velocimetry (PIV) (Franzetti et al., 2022). As a result, most phantoms are rigid and idealised rather than anatomically accurate, which simplifies the fabrication process but reduces the physiological relevance of the validation (Schoenborn et al., 2022, Yazdi et al., 2018).

PIV is a non-intrusive optical technique that measures fluid instantaneous velocity fields (Abdulwahab et al., 2020). PIV works by illuminating tracer particles in the flow with a laser sheet, capturing their positions at two closely spaced time intervals, and then analysing the particle displacements to calculate velocity vectors across the entire field of view. Zadrazil et al., (2020) combined CFD and PIV on an idealised TBAD geometry to study the impact of tears. A patient-specific TBAD case was investigated using a combined *in silico* and *in vitro* approach involving CFD simulations and PIV experiments (Bonfanti et al., 2020). In both models, boundary conditions were tuned using *in vivo* measurements, ensuring realistic physiological input. The comparison between CFD and PIV revealed excellent agreement in key flow features, such as velocity fields, jet formation across the primary entry tear, flow separation patterns, and the development of vortical structures in both the true and

false lumens. Quantitatively, the velocity profiles matched closely in multiple cross-sectional planes, with minimal discrepancies in flow magnitude and direction.

As an alternative to the rigid phantom assumption, Zimmermann et al., (2021), produced an MRI-compatible compliant phantom which enabled them to validate their FSI results. The study showed overall agreement of the simulated and 4DMRI-captured TL and FL complex flow. Similarly, Comunale et al., (2021) proposed an in vitro *in silico* framework in which the design of their compliant aortic phantom was validated with FSI to ensure the right compliance of the material. Conversely, Bertoglio et al., (2014), validated the material of the phantom using *in vivo* data, then replicated and applied the material properties in an FSI simulation. In their study, they successfully demonstrated that incorporating realistic aortic wall properties improved the accuracy of FSI simulations in capturing the dynamic behavior of the aorta under physiological conditions.

1.8. CFD for TBAD: Challenges and Insights

The state-of-the-art presented in this chapter highlights the significant potential of CFD simulations in advancing the clinical understanding of the pathogenesis and progression of TBAD. Key findings include the identification of associations between adverse outcomes in TBAD and specific hemodynamic factors, such as high FL flow rate and large TMP. Furthermore, CFD simulations have revealed that the combination of high TAWSS and low OSI indices, resulting in high ECAP, correlate with rapid aortic growth rates, while regions of stagnant flow, which promote thrombus formation, are linked to high RRT (Kamada et al., 2022, Song et al., 2023).

However, accurate CFD simulations are highly dependent on the defined use of patient-specific BCs and data sets. Inlet and outlet BCs, particularly those derived from 2D or 4DMRI, are critical for reliable flow predictions, especially when using IVP and WK3 outlet BCs. Equally important is the use of compliant models, as the significant displacement of the aortic wall and IF in TBAD, due to high pressures and disturbed flow, must be captured. Among these, FSI simulations are the most commonly used; however, they are often constrained by simplified assumptions regarding material properties and the extensive computational resources required. To

address these limitations, an alternative moving boundary method has been developed (Bonfanti et al., 2017).

Despite these advances, applying CFD analysis to clinical practice for TBAD presents several challenges. Notably, inconsistent associations between flow parameters, pressure, WSS indices, and disease progression have been reported across studies. These inconsistencies often stem from differences in modelling assumptions, simulation inputs, modelling choices, and simplifications, as well as the availability of accurate *in vivo* input and validation data. From this thesis review, the following key points emerged as essential requirements to bridge the gaps identified in the literature.

First, patient-specific inlet and outlet BCs, particularly those derived from 2D or 4DMRI, are fundamental for accurate flow predictions, especially when using IVP and WK3 outlet BCs. Equally important is the use of compliant models, given the significant displacement of the aortic wall and intimal flap that occurs in TBAD due to high pressures and disturbed flow. While FSI models are often employed to capture these interactions, there are still limitations around wall properties and computational time. In response to these challenges, an alternative moving boundary method has been developed (Bonfanti et al., 2017; Capellini et al., 2021)

1.9. Objectives and Outline of the Thesis

The overarching aim of this thesis is to improve the accuracy and clinical relevance of haemodynamics modelling in TBAD by addressing key limitations in current computational approaches, as identified through a comprehensive literature review. This is achieved by developing novel, patient-specific modelling frameworks that account for graft properties, intimal flap movement, and realistic compliance using clinically accessible data.

The research focused on three main objectives:

- •The first objective was to *study the impact of graft length and compliance on TBAD*. As described in 1.5.4.4, the compliance mismatch is important in the disease progression after an OS. Additionally, available clinical data are often limited as acquiring a detailed 4DMRI data set or invasive pressure, described in 1.5.2, is not part of routine clinical practise. The first aim was, therefore, to develop a virtual surgery framework in which different graft lengths and compliances would be tested using compliant simulations. The second aim was to use a common and limited data set comprising CTA scans and a few planes of 2DMRI and cine-MRI. The third aim was to apply the MBM in a multi-compliant patient-specific case to study the graft length and compliance impact. The impacts of the grafts were evaluated on clinically used and relevant markers such as pressures, energy loss and PWV.
- The second objective was to develop a computational pipeline to analyse patient-specific haemodynamics and IF movement in TBAD. Also described in 1.5.4.4, the IF displacement impacts the TBAD haemodynamics. Such impact on haemodynamics can be observed with 4DMRI and anatomically with TRUFI MRI. Additionally, the MBM was previously applied to simulate a TBAD assuming a zero-thickness flap, which was a limitation. To this end, the first aim was to reformulate the MBM to simulate a patient-specific TBAD post-TEVAR with a more realistic finite thickness flap. The second objective was to use only MRI sequences to build and validate the entire framework. Then, the patient-specific simulation was compared against a rigid IF case and two additional cases showcasing more compliant IF to evaluate the impact on haemodynamics and WSS indices.
- The third objective was to develop a new methodology which incorporated a routine clinical measurement, the PWV, to assess reconstructed TBAD haemodynamics. The spatiotemporal resolution of

4DMRI can hinder wall displacement measurement in a large field of view when capturing the entire thoracic aorta. Hence, the area-based distensibility can be wrongly measured in distal regions. The first aim was, therefore, to use the RPWV-based distensibility to inform the MBM. The second aim was to validate the simulation results against the *in vivo* 4DMRI. Then, the simulation was compared against an area-based distensibility one to investigate the difference in disease prediction progression between both methods.

Chapters 2, 3, and 4 present the work performed to complete the objectives stated above. In each chapter, the medical data, methodology, and results are described, followed by a discussion of key findings and the limitations Finally, Chapter 5 concludes this thesis and summarise the main contributions and future work.

Chapter 2

Virtual Grafting Strategies: Evaluating Haemodynamics Outcomes and Surgical Optimisation for TBAD

2.1. Introduction

Computational Fluid Dynamics (CFD) and medical imaging play crucial roles in enhancing surgical decision-making and understanding the progression of Type-B aortic dissection (TBAD), particularly in the context of thoracic endovascular repair (TEVAR) and open-surgery (OS).

Medical imaging techniques, such as flow magnetic resonance imaging (MRI) and cine-MRI, are invaluable for assessing aortic blood velocity and wall displacement (Wang et al., 2022). These imaging methods can quantify the success of blood flow reinstatement and the impact of device placement on aortic wall behaviour post-surgery. Despite their potential, MRI is not routinely used in the clinic and is prone to spatiotemporal limitations and measurement artefacts due to the implanted devices (Krupa and Bekiesińska-Figatowska, 2015). These limitations affect the accuracy of assessing metrics like wall shear stress (WSS), which is crucial for understanding vessel wall structure and aortic degeneration (Lamata et al., 2014).

Predicting aortic surgical outcomes using CFD is a complex task due to the patient-specific nature of TBAD and the inherent variability in aortic wall properties. This variability includes differences in dissection morphology, the extent of the affected aorta, the number and location of fenestrations, and the mechanical properties of the aortic wall, all of which influence haemodynamics responses and surgical

outcomes. CFD allows for virtual testing of TBAD surgical procedures, which is impractical during surgery (Auricchio et al., 2014). As a result, many CFD studies investigate device sizing and positioning and their relationship to aortic haemodynamics changes.

However, most such studies use a rigid wall assumption, neglecting wall compliance and the compliance mismatch between the native tissue and device (Sengupta et al., 2022, Xiong et al., 2020, Ong et al., 2019). Such assumptions fail to capture the effects of septal motion and wall deformation on aortic haemodynamics. They can lead to inaccuracies in the prediction of important metrics such as WSS as demonstrated by Alimohammadi et al., (2015). Additionally, as discussed in Section 1.7.2, compliance mismatch has been linked to increased LV load and hypertrophy, a factor that rigid models fail to account for.

As mentioned in Chapter 1, compliant simulations for aortic dissection are commonly performed using fluid-structure interaction (FSI) methods. FSI models can guide treatment planning, such as selecting optimal stent-graft designs (Jayendiran et al., 2018, Qiao et al., 2021). However, they are computationally demanding and are limited by the patient-specific material properties of the aortic wall (Karlsson et al., 2023), which impacts their deployment in clinical settings (Mourato et al., 2022, Sturla et al., 2013, Vignali et al., 2021).

To circumvent these challenges, alternative methods have been developed as described in Section 1.6.5. One such method is the Moving Boundary Method (MBM), developed by Bonfanti et al., (2018) to bypass the wall material assumptions of FSI while being drastically faster in computational time. The method has been applied in TBAD and healthy aorta cases (Bonfanti et al., 2017, Stokes et al., 2021). One key advantage of the MBM is its ability to be applied with multi-compliant fields, such as the aorta post-surgery, where regions of different stiffness coexist (i.e. the implanted stiff device and the native vessel).

This chapter presents a computational framework and virtual surgical platform to evaluate grafting strategies in TBAD¹, focusing on the haemodynamics impact of aortic grafts after OS. Using a patient-specific model and leveraging the MBM, the chapter assesses the impact of graft length and compliance on key biomechanical parameters. CFD simulations, informed by routine medical imaging (CTA angiography, Cine-MRI, and 2D MRI), explore five grafting scenarios. By analysing uvelocity and pressure distributions, pulse wave velocity (PWV), energy loss (EL), and WSS—derived indices, this study provides insights into graft selection and its influence on left ventricular (LV) load and aortic haemodynamics, emphasising the need for patient-specific surgical planning.

2.2. Methods

2.2.1. Clinical Data

A patient with a complicated chronic TBAD was presented at St Bartholomew's Hospital, London, UK. The patient underwent OS, where a dissected portion of the thoracic aorta was replaced with a graft (Gealweave, Terumo Aortic, Vascutek LTD, UK), leaving two downstream lumina separated by the intimal flap. The graft was 130 mm long with a 32 mm diameter (Figure 2. 1A). Their aorta was imaged before and after OS. Following an ethically approved protocol (St Bartholomew's Hospital BioResource ethical application number 97), Cine-MRI and 2DMRI were acquired pre-operatively using a Siemens MAGNETOM Aera 1.5T (Siemens Healthcare GmbH, Erlangen, Germany) with a spatial resolution of 1.7 mm*1.7 mm and temporal of 49 ms. 2DMRI was acquired in one plane 50 mm distal to the primary entry tear (PET), located 36 mm distal to the aortic arch. CTA angiography images were also acquired as part of the routine post-operative clinical

¹ This work has been published in the Journal of Cardiovascular Engineering and Technology in 2024 (Girardin et al., 2024a) Please refer to Research Declaration Form A for details.

examination (Figure 2. 1A) using a Siemens SOMATOM Definition Edge with a resolution of 0.73 mm*0.73 mm*0.75 mm. Brachial pressures were acquired post-operatively. It should be noted that the patient was on medication with beta-blockers to reduce arterial pressure.

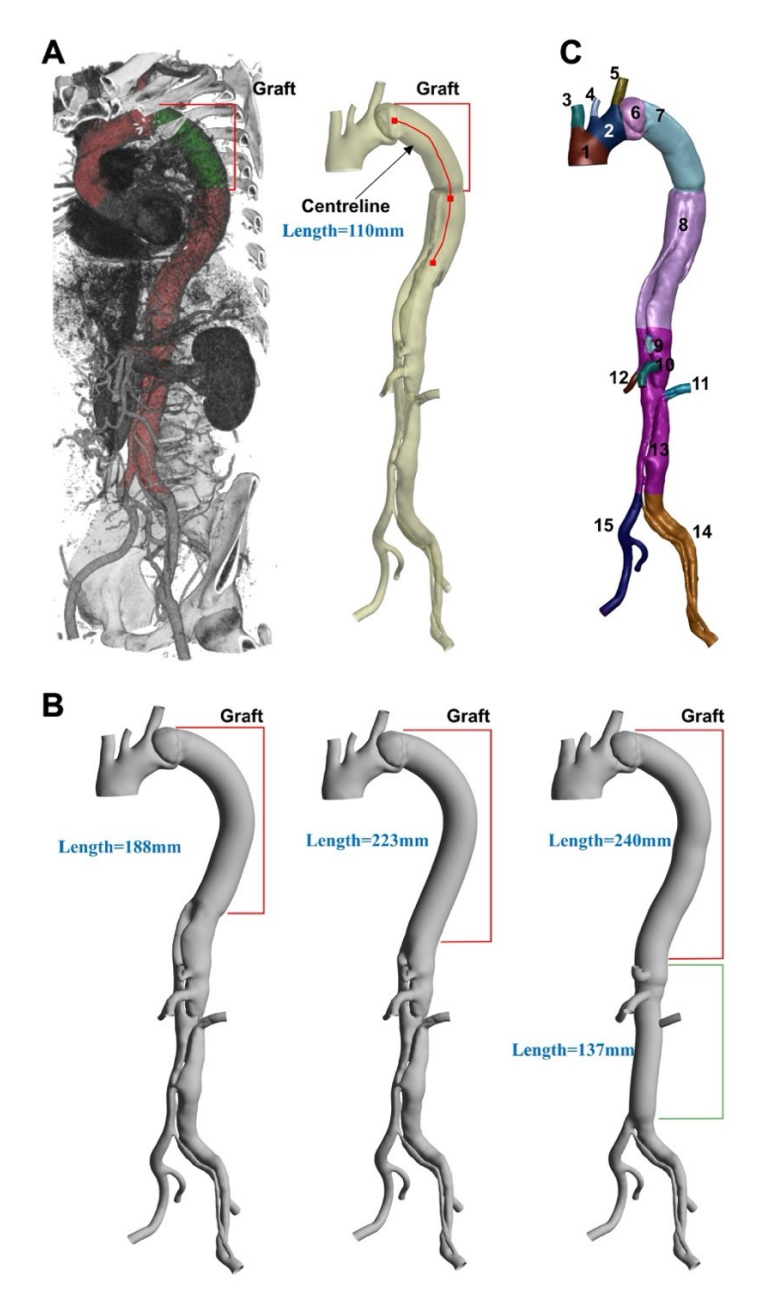


Figure 2. 1. (A) Automatic 3D rendering of the CTA angiogram showing, in red, the aortic vessel and, in green, the graft; the segmented post-operative DA resulting from the CTA angiogram is shown next to it, namely the baseline case. (B)

The three virtual surgical scenarios were created from the baseline case by varying the length of the graft. The red centreline from which the grafts have been swept is shown on the post-operative geometry. Red and green dashed lines indicate the extent of the 32mm and 28mm diameter thoracoabdominal graft of ETR, respectively. The length of each graft is indicated in blue. (C) aortic segments defined along the centreline using anatomical landmarks to account for proximal variations of stiffness. The numbers indicate: 1 ascending aorta, 2 arch, 3 brachiocephalic trunk, 4 left common carotid, 5 left subclavian, 6 isthmus, 7 graft, 8 descending aorta, 9 coeliac trunk, 10 superior mesenteric artery, 11 left renal, 12 right renal, 13 abdominal aorta, 14 left iliac, 15 right iliac.

2.2.2.Geometry

The CTA angiography data (Figure 2. 1A) were segmented using automatic thresholding and manual correction of the mask implemented in ScanIP (Synopsis Simpleware, USA). The clinical team verified the segmented geometry, confirming the location of the tears. The resulting mask was then smoothed using Meshmixer (Autodesk, USA). The inlet and all outlets were trimmed so that their cross-sectional areas were perpendicular to the flow direction using Fluent Mesh (Ansys Fluent, USA) (Figure 2. 1B). The final processed geometry obtained at this stage was denoted as the 'baseline' case (Figure 2. 1A). Three virtual grafting scenarios were subsequently created in consultation with the clinical team by extending the graft using ScanIP and Meshmixer. Two lengths corresponding to the descending half and total length of the aorta were considered, denoted as mid-descending (MDA) and complete descending (CDA) aorta, respectively. The third grafting scenario involved an entire replacement of the thoracoabdominal aorta (ETR) to the iliac bifurcation. Two additional cases with compliant grafts were simulated, termed baseline compliant 1 (BC1), and baseline compliant 2 (BC2+), described in more detail in later sections.

2.2.3.Mesh

Tetrahedral computational meshes were created for each domain using Fluent Mesh 19.0 (Ansys Inc., USA). Ten prism layers with a first layer corresponding to a y+ of 1 were used to ensure appropriate boundary layer modelling for each mesh. A

mesh independence study was conducted using the baseline case; coarse, medium, and fine meshes were generated by approximately doubling and dividing the maximum and minimum element sizes. The Grid Convergence Index was used to assess the quality of the mesh used in the baseline case (Craven et al., 2009). The index did not exceed 4.5% on every mesh for all metrics, consistent with past research. More details are available in Appendix A.1. Using the medium mesh resolution determined from the mesh independence study, the baseline, MDA, CDA, and ETR cases contained 1.35, 1.2, 1.1, and 0.9 million elements, respectively. The maximum and minimum cell sizes were identical across all cases (4 mm and 0.35 mm).

2.2.4. Flow Boundary Conditions

The inlet flow rate was extracted from the pre-operative 2DMRI data near the aortic arch using GTFlow (GyroTools LLC., Switzerland) (Figure 2. 2A). The flow rate curve was spline-interpolated in MATLAB (MathWorks Inc., USA) to match the CFD timestep of 1 ms and applied as a uniform inlet velocity profile (Figure 2. 2A).

Three-element Windkessel (WK3) outlet pressure boundary conditions were applied to mimic the effects of the peripheral vascular system (Figure 2. 2) (Westerhof et al., 2009). Target mean flow rates at each outlet, necessary for the calibration of the WK3 parameters (Bonfanti et al., 2017, Stokes et al., 2021), were split as follows: 30% of the flow was assigned to the supra-aortic branches, and the mean flow rates for each branch were calculated by dividing the total supra-aortic branches flow by their respective cross-sectional area ratio, such that:

$$\bar{Q}_{SAB,i} = 0.3\bar{Q}_{inlet} \frac{A_{SAB,i}}{A_{tot,SAB}}$$
 2. 1

where \bar{Q}_{inlet} (mL/s) is the mean flow rate at the inlet over a cardiac cycle, $A_{SAB,i}$ (m²) is the cross-sectional area of the supra-aortic branches outlet, and $A_{tot,SAB}$ (m²) the sum of the supra-aortic branches cross-sectional area. The distribution of blood flow in the abdominal region varies among patients and can be affected by the precise nature of the dissection. A study found that the blood flow leaving the abdominal branches ranged from 25% to 75% in a group of 10 patients (Amanuma et

al., 1992). After consultation with the medical team, the mean flow leaving the abdominal arteries was set as 40% of the residual flow in the descending aorta after OS. The abdominal branches are perfused by both lumens, as shown in Figure 2. 2B-C. Hence, the mean flow rates to the abdominal branches were estimated in a similar manner as equation 2.1, such that:

$$\bar{Q}_{Abdo,i} = 0.4\bar{Q}_{DA} \frac{A_{Abdo,i}}{A_{tot,Abdo}}$$
 2. 2

where \bar{Q}_{DA} and \bar{Q}_{Abdo} (mL/s) are the descending aorta and abdominal branches mean flow rates over a cardiac cycle, $A_{Abdo,i}$ (m²) is the cross-sectional area of the abdominal branches outlet, and $A_{tot,Abdo}$ (m²) the sum of the abdominal branches cross-sectional area. The remaining mean flow was split using a 70/30% balance between the external and internal iliac arteries as shown in Figure 2. 2B (Bonfanti et al., 2019). The same flow split methodology was applied to the four geometries and is summarised in Table 2. 1.

The WK3 model calibration also necessitated determining the target values of aortic systolic and diastolic pressures (P_{sa} , P_{da}) (mmHg). Diastolic pressure remains relatively constant throughout the arterial tree, so P_{da} was set equal to the diastolic brachial pressure (P_{db}). The systolic aortic pressure (P_{sa}) was derived from the systolic brachial pressure (P_{sb}) using the empirical relationship $P_{sa} \approx 0.83 P_{sb} + 0.15 P_{db}$ (Westerhof et al., 2018).

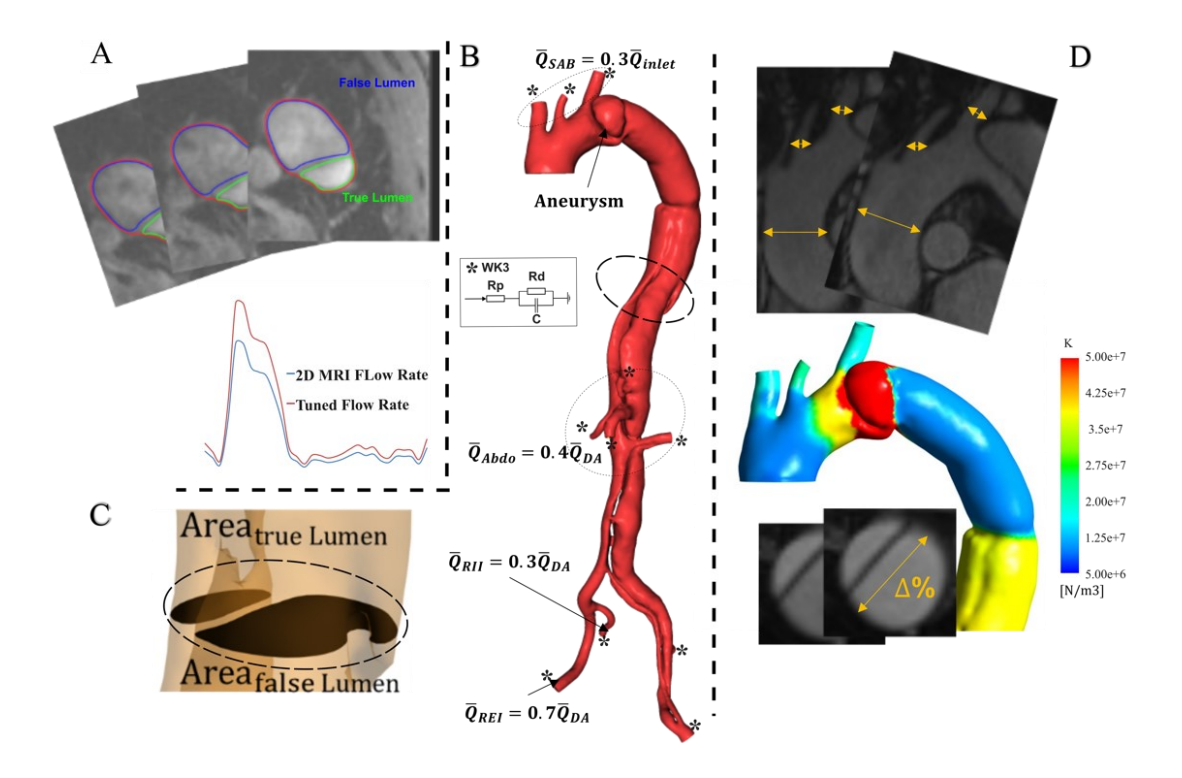


Figure 2. 2. (A) 2DMRI plane showing in blue and green the false and true lumen respectively; below are the extracted raw and rescaled by 30% flow rates. (B) An asterisk indicates the WK3 boundary condition used at the outlets. Flow splits are shown at the outlets: 30% of the flow leaves through the supra-aortic branches, and 40% of the remaining DA flow leaves through the abdominal arteries following the TL and FL shown in (C). (C) The remaining abdominal false and true lumen flows are split as 70/30% between the exterior and interior iliac arteries; the right exterior (REI) and interior (RII) iliac arteries are shown as an example. (D) Sample cine-MRI planes used to measure the stiffness of the aorta. The aortic arch of BC1 is zoomed in to show the distribution of local stiffness values K obtained for the case of a compliant graft.

Table 2. 1 Mean flow rates at the outlets for each case. Flow splits are very close between the post-operative, medium (MDA) and complete descending aorta (CDA) cases due to close morphological similarities. Differences are found in the abdominal and iliac arteries of the ETR case due to idealised abdominal branches of the graft. Arterial outlet abbreviations are as follows: brachiocephalic trunk (BT), left common carotid (LCC), left subclavian artery (LSA), coeliac trunk (CT), superior mesenteric artery (SMA), left renal artery (LR), right renal artery (RR), left internal and external iliac arteries (LII, LEI), and right internal and external iliac arteries (RII, REI).

Qmean ImL/sl	Baseline	MDA	CDA	ETR
BT	18.5	18.5	18.5	18.5
LCC	5.1	5.1	5.1	5.1
LSA	12.1	12.1	12.1	12.1
CT	15.0	15.0	14.9	10.2
SMA	28.4	28.5	27.2	10.2
LR	12.2	12.2	11.6	6.52
RR	6.7	6.6	7.9	6.52
LEI	2.9	2.9	3.4	24.2
Lll	2.5	2.5	2.8	11.7
REI	10.2	10.2	10.1	9.78
Rll	5.7	5.7	5.7	4.52

Following previous works, the calibration of the boundary conditions was performed using an analogue 0D model to obtain the WK3 parameters (Bonfanti et al., 2019, Stokes et al., 2021). The inlet flow rate, Q_{IN} , was applied at the inlet. Aortic segments k (Figure 2. 1C), were represented with RLC blocks which simulate blood pressure loss (R_k) (mmHg*s/mL), inertance (L_k) (mmHg*mL/s²) and aortic volume compliance ($C_{V,k}$) (mL/mmHg). Each resistance is calculated as the pressure drop over the mean flow on every aortic segment:

$$R_k = \frac{\Delta P_k}{\overline{Q_k}}$$
 2. 3

The pressure drop across each segment ΔP_k (mmHg) were computed using a steady-state CFD simulation with a mean pressure \bar{P}_{IN} (mmHg) condition at the inlet calculated as follows:

$$\bar{P}_{IN} = FF(P_{sa} - P_{da}) + P_{da}$$
 2.4

FF is a form factor calculated as (Chemla et al., 2002):

$$FF = \frac{P_{mean} - P_{da}}{P_{Sa} - P_{da}}$$
 2. 5

with P_{mean} (mmHg) defined as:

$$P_{mean} = P_{da} + \frac{1}{3}(P_{sa} - P_{da})$$
 2. 6

Inertances L_k were calculated for large arteries using the following expression:

$$L_k = \frac{4}{3} \frac{\rho l_k}{A_k}$$
 2.7

With A_k (m²) and l_k (m) the cross-sectional area and the length of a segment k, ρ is the fluid density (kg/m³). Volume compliances, $C_{V,k}$ (mL/mmHg), are derived from the area-based distensibility measured on the cine-MRI, and then calculated as follows:

$$C_{Vk} = V_{0k} D_{kah}$$
 2.8

Where $V_{0,k}$ (m³) is the diastolic volume of an aortic segment and the distensibility (1/mmHg) is defined as:

$$D_{k,ab} = \frac{\frac{A_{k,max} - A_{k,min}}{A_{k,min}}}{P_{sa} - P_{da}}$$
 2. 9

With $A_{k,max}$ and $A_{k,min}$ (m²) the maximum and minimum cross-sectional area of a segment k. WK3 hydro-electrical analogues consisting of a proximal resistance (R_p^i) (mmHg*s/mL), a distal resistance (R_d^i) (mmHg*s/mL) and a compliance (C_{wk3}^i)

mL/mmHg were used at each outlet i. The compliance of each WK3 outlet, $C_{WK3,i}$ was calculated as follows:

$$C_{WK3,i} = \frac{\overline{Q_i}}{\overline{Q_{inlet}}} \left(C_{tot} - \sum C_{V,k} \right)$$
 2. 10

Where one WK3 model was used to obtain the total aortic compliance C_{tot} (mL/mmHg) as described by Les et al., (2010). The total outlet resistance $R_{tot,i} = R_p^i + R_d^i$ (mmHg*s/mL) was calculated using the ratio of the predicted outlet pressure from the steady-state CFD simulation to \bar{Q}_i such as:

$$R_{tot,i} = \frac{\bar{P}_t}{\bar{O}_i}$$
 2. 11

 R_p^i and R_d^i were calculated such as for the renal arteries and 5.6% for the rest of the outlets (Les et al., 2010). The system of ordinary differential equations using 20-sim (Controllab Products, Netherlands) was solved by backward differentiation (Curtiss and Hirschfelder, 1952).

The WK3 parameters obtained after calibration for the post-operative, MDA, CDA and ETR cases are presented in Table 2. 2. The BC1 and BC2+ cases are not included in the table for clarity since the resistances are the same as those of the baseline case where the same flow split is applied to the same geometry.

Table 2. 2 WK3 parameters for the Baseline, MDA, CDA and ETR cases, R_p and R_d are in (mmHg*s/mL), C_{WK3} is in (mL/mmHg).

Baseline				MDA		
	Rp	Rd	Cwk3	Rp	Rd	Cwk3
BT	0.24	4.00	0.32	0.24	4.00	0.31
LCC	0.85	14.38	0.09	0.85	14.38	0.09
LSA	0.36	6.10	0.21	0.36	6.10	0.21
CT	0.74	12.51	0.10	0.74	12.48	0.10
SMA	0.42	7.10	0.18	0.42	7.09	0.17
LR	1.41	3.62	0.26	1.39	3.56	0.25
RR	8.45	21.74	0.04	8.54	21.95	0.04
LEI	0.15	2.48	0.50	0.15	2.48	0.48
LII	0.35	5.89	0.21	0.35	5.88	0.21
REI	0.64	10.75	0.12	0.66	11.05	0.11
RII	1.49	25.05	0.05	1.51	25.53	0.05
	FDA	-	<u>.</u>	ETR	-	
	Rp	Rd	Cwk3	Rp	Rd	Cwk3
BT	0.24	4.00	0.30	0.24	4.00	0.28
LCC	0.85	14.38	0.08	0.85	14.38	0.08
LSA	0.36	6.10	0.20	0.36	6.10	0.19
CT	0.74	12.54	0.09	0.42	7.08	0.16
SMA	0.42	7.13	0.17	0.42	7.08	0.16
LR	1.40	0.26	0.25	3.28	8.44	0.10
RR	7.95	20.44	0.04	3.28	8.44	0.10
LEI	0.15	2.61	0.45	0.17	2.94	0.37
LII	0.37	6.18	0.19	0.37	6.19	0.18
REI	0.54	9.06	0.13	0.44	7.36	0.15
RII	1.25	21.11	0.06	0.94	15.85	0.07

2.2.5. Wall Compliance

The MBM developed by Bonfanti et al., (2018) was applied to simulate aortic wall displacement. The wall displacement follows the surface node normal and is proportional to the difference between local and external pressures; the constant of proportionality is the stiffness coefficient, K_n . The local displacement of each mesh node is thus calculated as follows:

$$\delta_n = \frac{p_n - p_{ext}}{K_n} \boldsymbol{n}_i$$
 2. 12

where the local pressure is p_n (Pa), p_{ext} (Pa) is the external pressure (equal to P_{da}). The stiffness coefficient K_n (N/m³) is equal to:

$$K_n = \frac{2}{D_k} \sqrt{\frac{\pi}{A_k^0}}$$
 2. 13

where A_k^0 (m²) is the local diastolic cross-sectional area where a node n is located. Regions were defined along the centreline using anatomical landmarks to account for proximal variations of aortic stiffness (Figure 2. 1C). When axial Cine-MRI images were unavailable, for example at the aortic arch, sagittal images were used to measure wall displacement. The assumption of a circular cross-section in the aorta and supra-aortic branches was employed so that diameters could be used in lieu of the cross-sectional area to calculate distensibility. The distensibility of each region was used to calculate the stiffness coefficient K_n, which was then mapped onto its respective region of the geometry using an in-house MATLAB code. As observed in Figure 2. 2D and following the work of Stokes et al., (2021) three smoothing iterations were performed to prevent discontinuities between regions of varying stiffness. The number of iterations was chosen as the minimum required to ensure a smooth transition, preventing mesh folding at high displacements, which could otherwise lead to solver instability and crashes. Following reported graft stiffness measurements, the graft was considered to be 20-200 times stiffer than the native aorta ($K=1.0x*N/m^3$) in the baseline case, MDA, CDA and ETR cases (Ferrari et al., 2019, Tremblay et al., 2009). Two additional cases were simulated in which the graft was considered

compliant. In the first, BC1, the graft properties were assumed identical to the baseline geometry, i.e. the graft stiffness was taken equal to the measured aortic stiffness at the native ascending aorta ($K_{BC1}=7.5*10^6$ N/m³) (Fig 2 D). In the second case, BC2+, a graft stiffness half that of BC1 ($K_{BC2+}=3.75*10^6$ N/m³) was assumed with the aim of simulating a graft which was more compliant than any region of the aorta.

2.2.6.CFD Simulation

The three-dimensional, transient Navier-Stokes equations were solved using the finite-volume solver ANSYS CFX 19.0. Blood was modelled as an incompressible non-Newtonian fluid with a density of 1056 kg/m3 and a rheology described by the Carreau-Yasuda viscosity model and empirical constants from Tomaiuolo et al., (2014). The Reynolds number descriptions for pulsatile blood flow in cardiovascular systems outlined in Peacock et al., (1998), were used to calculate the peak Re_p and the critical Re_c, for transition to turbulence. An effective shear rate based on Cagney and Balabani, (2019), was used for the viscosity estimation in the Re formula and the maximum velocity obtained from the 2DMRI plane was scaled up by 30% to account for the supra-aortic branches flow loss; Re_p and Re_c were found equal to 2257, and 3890 respectively. Under these conditions, a laminar flow assumption was used. As most aortic flows are likely to exhibit some degree of transitional flow, simulations assuming laminar flow were compared against Reynolds-Averaged Navier Stokes turbulent flow simulations using the k- ω SST model. For brevity, the findings are described in Appendix A.2. The observed differences between laminar and turbulent flow simulations did not affect the conclusions of the study. As a result, the results reported herein are based on laminar flow simulations.

The solver employs the finite volume method, which is based on the integral form of the Navier-Stokes and continuity equations. An implicit, second-order time integration scheme with a time step of 1 ms was used to solve these equations. During the final cycle, all equations within each timestep achieved an absolute root-mean-square (RMS) residual value of 10⁻⁵, ensuring solution convergence. After seven cycles, the compliant simulations reached periodic conditions, i.e., less than 1%

variation in systolic and diastolic pressures between cycles. Simulations were performed using parallel computation on the high-performance computing cluster of the UCL Computer Science Department, with a computational time of approximately 23 hours per cardiac cycle.

2.2.7. Haemodynamics Analysis

In this work, energy loss (EL) and WSS-driven indices were calculated. EL is calculated from the difference in the sum of static and dynamic pressures between the inlet and outlets during a cardiac cycle and is defined as follows (Qiao et al., 2022):

$$EL = TP_{in}Q_{in} - \sum TP_{out}Q_{out}$$
 2. 14

where $TP_i = P_i + 0.5\rho |\mathbf{u}_i|^2$, ρ is the blood density (kg/m³), Q_i the volume flow rate (m³/s), P_i the pressure (Pa), and $|\mathbf{u}_i|$ the velocity magnitude (m/s) at each outlet i. EL often increases in the case of AD due to increased blood pressure (Chung et al., 2014). The heart must work harder to compensate for the increased pressure, EL, and reduced blood flow, potentially leading to heart failure (Babu et al., 2015).

WSS is defined as the tangential force per unit area exerted by blood flow on the arterial wall and is closely related to the shear rate at the vessel surface. WSS has been linked to the development of aortic disease (Sun and Chaichana, 2016). Three WSS-related indices were used in this study, the time averaged wall shear stress (*TAWSS*), oscillatory shear index (*OSI*), and endothelial cell activation potential (*ECAP*) as described in Section 1.5.1.

The *TAWSS* and *ECAP* differences between the baseline and the five cases examined in this study were computed to better elucidate the impact of the various grafting choices on the haemodynamics of the reconstructed vessel. The latter are normalised by the baseline average values as follows:

$$TAWSS_{diff} = \frac{(TAWSS_{baseline}^{i} - TAWSS_{case}^{i})}{\overline{TAWSS}_{baseline}}$$
 2. 15

$$ECAP_{diff} = \frac{(ECAP_{baseline}^{i} - ECAP_{case}^{i})}{ECAP_{baseline}}$$
 2. 16

2.3. Results

2.3.1. Validation of the Baseline Case

Validation and verification are performed via qualitative and quantitative comparisons between the CFD simulations of the baseline case and the target values from clinical data. Relevant metrics of interest are compared between the baseline and additional cases using the relative change. The relative change is defined as the difference between the metric of the baseline case and that of the compared case, divided by the metric of the compared case (Table 2. 3). The predicted P_{sa} and P_{da} vary within 1% of the measured brachial pressure cuff values. The simulated aortic wall displacements were validated against cine-MRI measurements, with the maximum observable diameter variation occurring during peak systole. Measurements at the ascending aorta and supra-aortic branches, where the largest displacement occurs, show differences under 2% (Figure 2. 2D). The 2DMRI plane coordinates were registered onto the CFD domain for comparison, yielding a 1.6% difference in mean flow rates (Table 2. 3). With simulation differences remaining below 3.2%, the model was considered suitable for additional intervention cases.

Table 2. 3 Inlet systolic P_{sa} and diastolic P_{da} pressures, mean flow rate \bar{Q}_i at the registered plane location, and maximum diameter variation at regions of interest are reported for the baseline simulation and clinical measurements. $\Delta\%$ represents the relative change between the baseline simulation and clinical data.

		Measured	Baseline	$\Delta\%$
ure Hg)	Sys	96.5	97.5	-1.0%
Pressure (mmHg)	Dia	68	68.4	-0.6%
Mean Flow Rate (mL/s)	Inlet	83.5	84.9	-1.6%
Diameter variation (mm)	$\mathbf{A}\mathbf{A}$	1.3	1.26	3.2%
	BT	0.7	0.69	1.4%
	LCC	0.5	0.49	2.0%
	LSA	0.5	0.49	2.0%

2.3.2. Flow and Pressure Distributions

Streamlines of blood flow through the aorta, coloured by velocity magnitude (m/s), are shown at peak systole and diastole in Figure 2. 3 and Figure 2. 4, respectively. In the baseline case (top-left), high velocities are observed at the PET and in narrowed regions such as the LR and left iliac arteries (Figure 2.3). A high-velocity blood flow jet passes through the PET, impacts the adjacent graft, and circulates downstream. As the flow moves toward the lower aorta, the velocity gradually decreases. Streamlines generally follow a smooth path along the aortic curvature; however, circulation zones are present in the aneurysm region and near the bottom part of the graft sutures. At diastole, the baseline case exhibits a similar blood flow distribution but with lower velocities compared to peak systole (Figure 2. 4). As at peak systole, higher velocities are observed at the PET, within the blood flow jet, and in the LR and left renal arteries.

Streamlines are also shown for the five additional virtual surgery cases at both time points (Figure 2. 3 and Figure 2. 4). Flow structures are generally similar when the graft is either longer along the DA or more compliant (MDA, CDA, BC1, and BC2+), with high velocities occurring in the same regions as in the baseline case. However, in the case of a complete thoracic graft replacement (ETR), the flow is more organised, and velocities are lower in the downstream aorta. This improvement is due to the stented geometry of the graft, which closely resembles a healthy aorta. Treating the narrowed lumina and abdominal branches helps restore a normal blood flow.

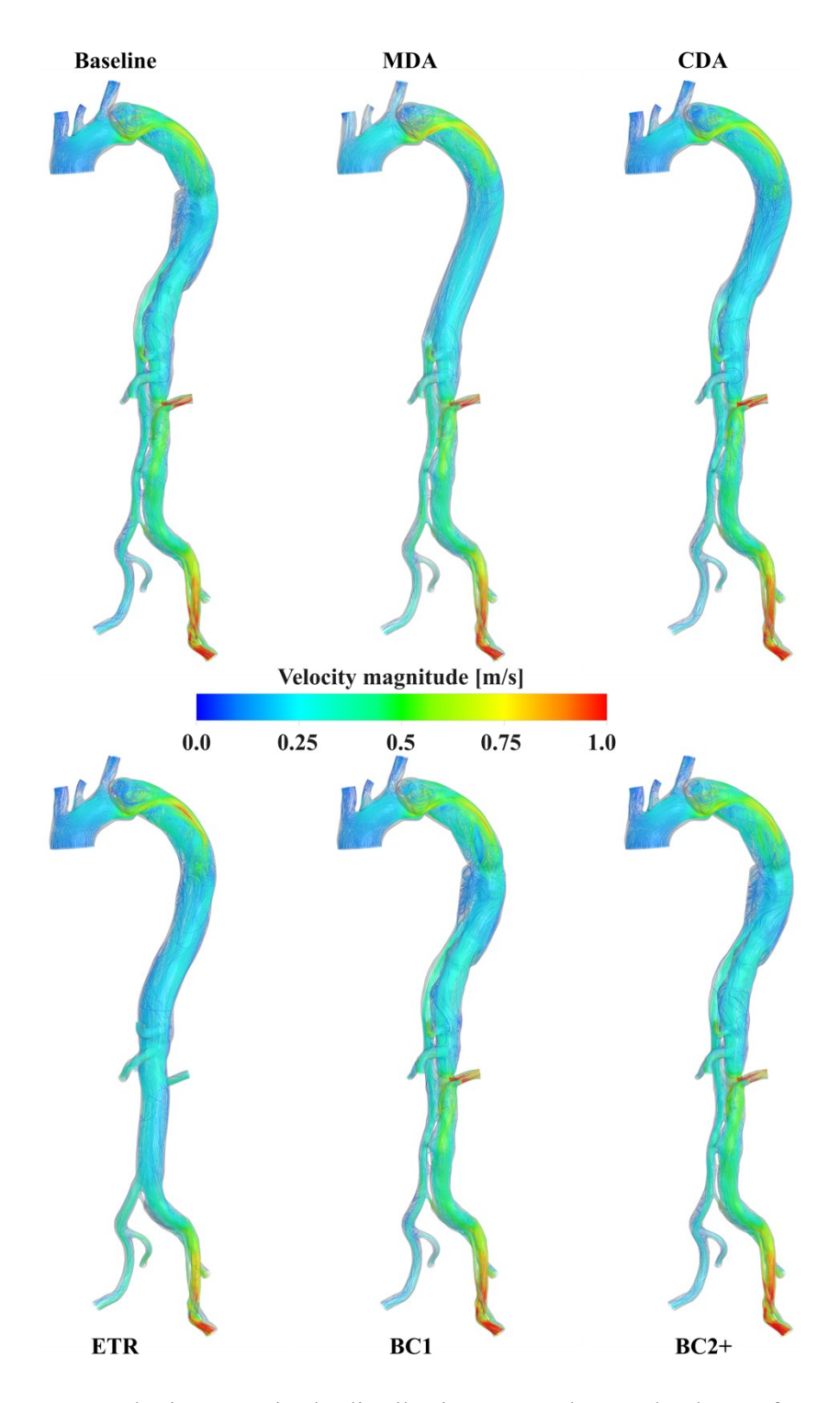


Figure 2. 3 Velocity magnitude distributions at peak systole shown for every case using streamlines.

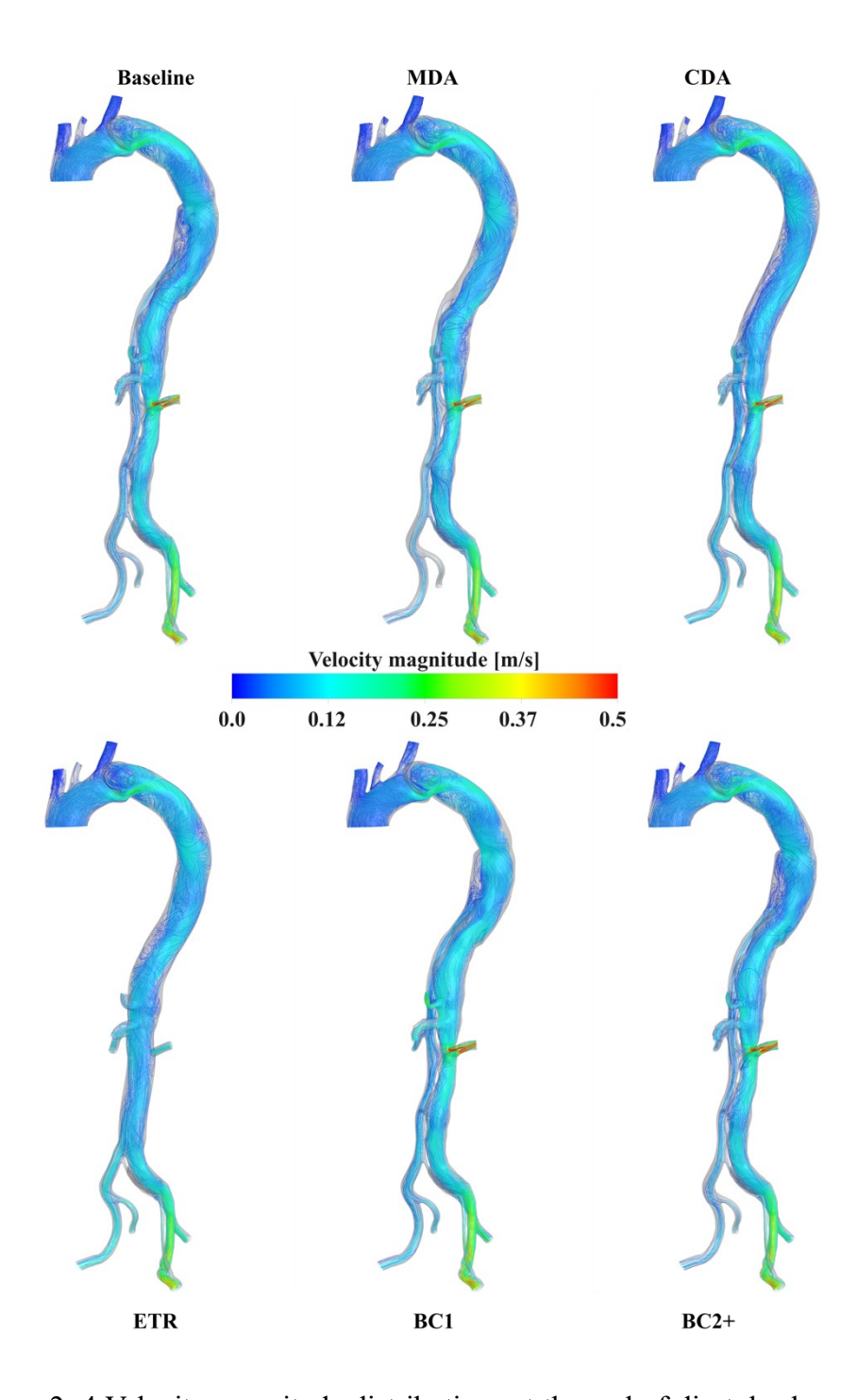


Figure 2. 4 Velocity magnitude distributions at the end of diastole shown for every case using streamlines.

Pressure contours are shown in Figure 2. 5 and Figure 2. 6, at peak systole and the end of diastole, respectively. In the baseline case, at peak systole, high pressure is observed in the ascending aorta, which gradually decreases downstream, with lower pressures found in the abdominal and iliac branches (Figure 2. 5). A high-pressure

region is collocated with the high-velocity jet impacting on the graft. At diastole, the pressure distribution is reversed, with lower pressures overall. The highest pressures are found in the downstream part of the aorta, contrasting with the peak systole distribution (Figure 2. 6).

Pressure contours for the five additional virtual surgery cases are shown in Figure 2. 5 and Figure 2. 6. Overall, similar pressure patterns and distributions are observed across all cases at peak systole (Figure 2. 5). However, pressure increases with a longer graft (MDA, CDA), with the highest increase occurring in the case of an entire thoracic graft replacement (ETR) and when the graft is more compliant than the proximal native aorta (BC2+). Additionally, in the ETR and BC2+ cases, higher pressures are observed in the downstream abdominal aorta and the right iliac arteries, compared to the baseline case. At diastole, a similar trend is observed, where pressures remain elevated in the same surgical cases (MDA, CDA, ETR, BC2+) relative to the baseline case (Figure 2. 6).

In contrast, when the graft compliance matches that of the native proximal aorta (BC1), pressures remain unchanged at peak systole compared to the baseline case (Figure 2. 5). However, at diastole, pressures in the downstream abdominal aorta are lower than in the baseline case (Figure 2. 6).

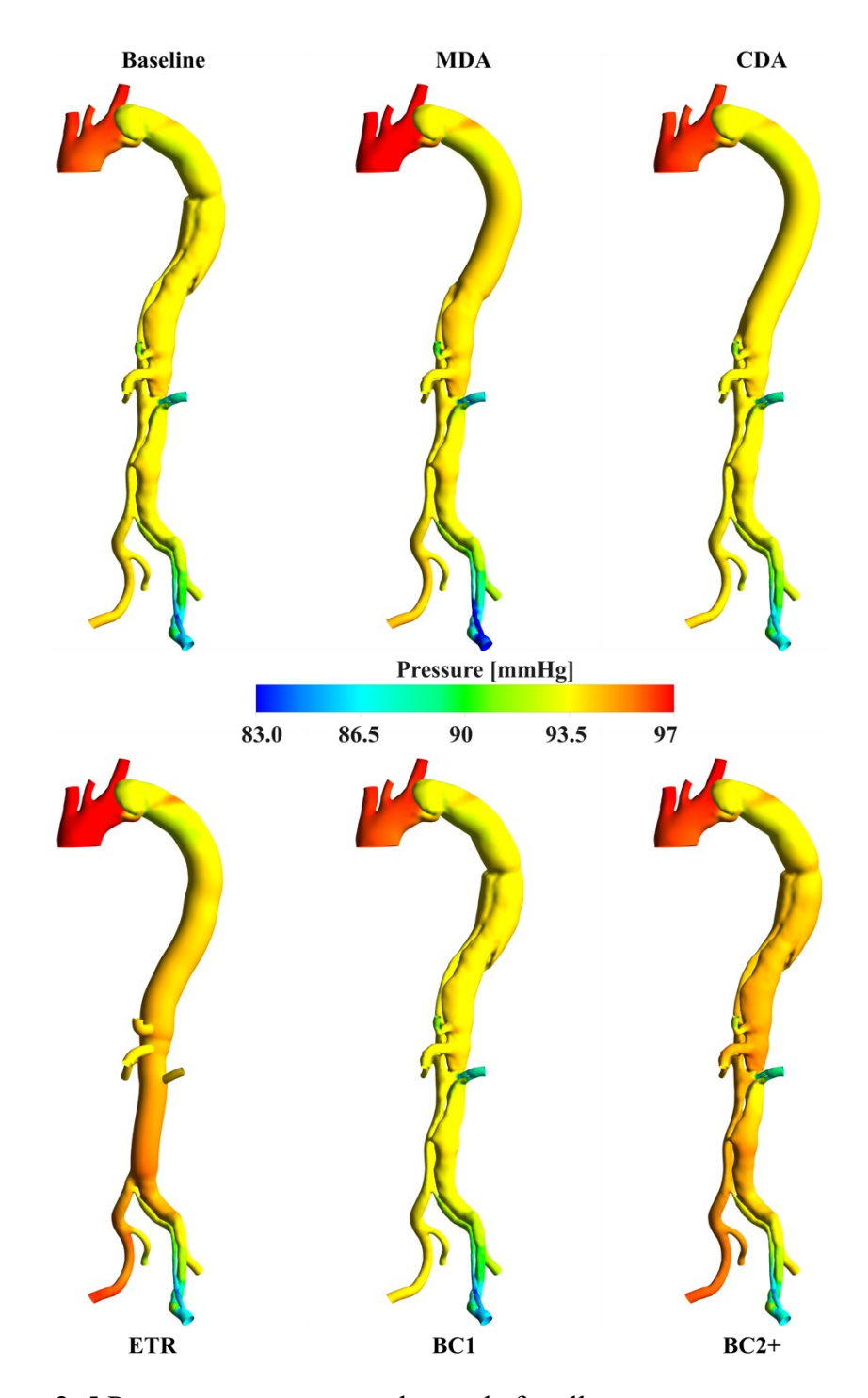


Figure 2. 5 Pressure contours at peak systole for all cases.

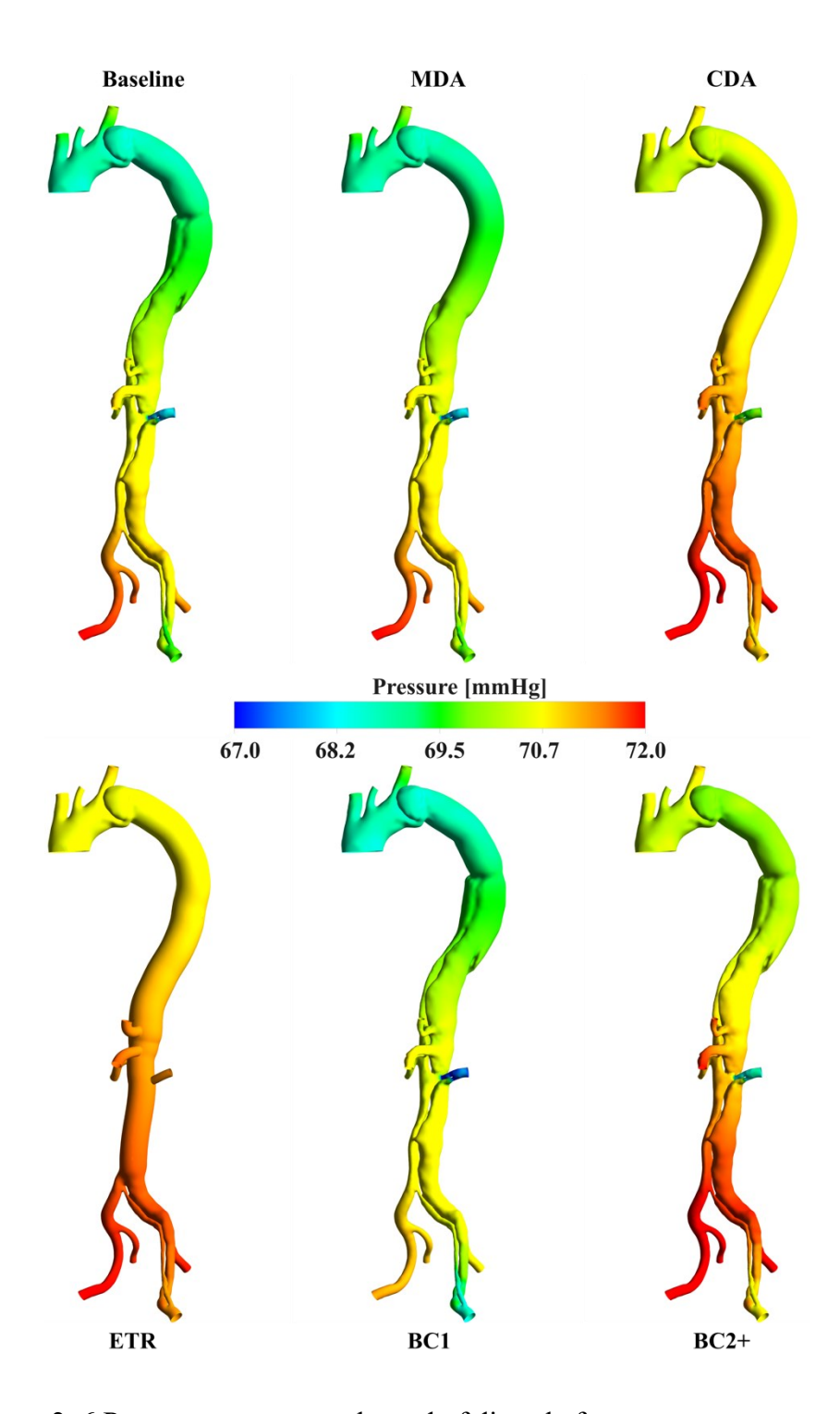


Figure 2. 6 Pressure contours at the end of diastole for every case.

The LV pressure has been reported to vary linearly with ascending aortic pressure; if the ascending aorta pressure increases, so does the LV pressure. To show the impact of the graft length and compliance on inlet pressures, P_{sa} and P_{da} were

reported at the inlet of the baseline case along with differences with the additional cases (Figure 2. 7). Inlet pressures increased with longer grafts. In the case of a complete thoracic aortic replacement, P_{sa} and P_{da} increase by 4.1% and 5.5%, respectively (ETR). Additionally, in the case of a graft mimicking the proximal vessel compliance (BC1), P_{sa} decreases and P_{da} increases, leading to a reduction in pulse pressure. Conversely, a graft with compliance exceeding that of the native proximal vessel (BC2+) increase pulse pressure.

The pulse wave velocity (PWV) is measured between the inlet plane and the plane separating segments 8 and 13 (Figure 2. 1C). The PWV is calculated as the pulse wave travel time along the aortic centreline separating those two planes (Figure 2. 7). The PWV increase by up to 15.4% in the cases where the graft was more rigid and decrease up to 7.4% in the case with the most compliant graft (BC2+).

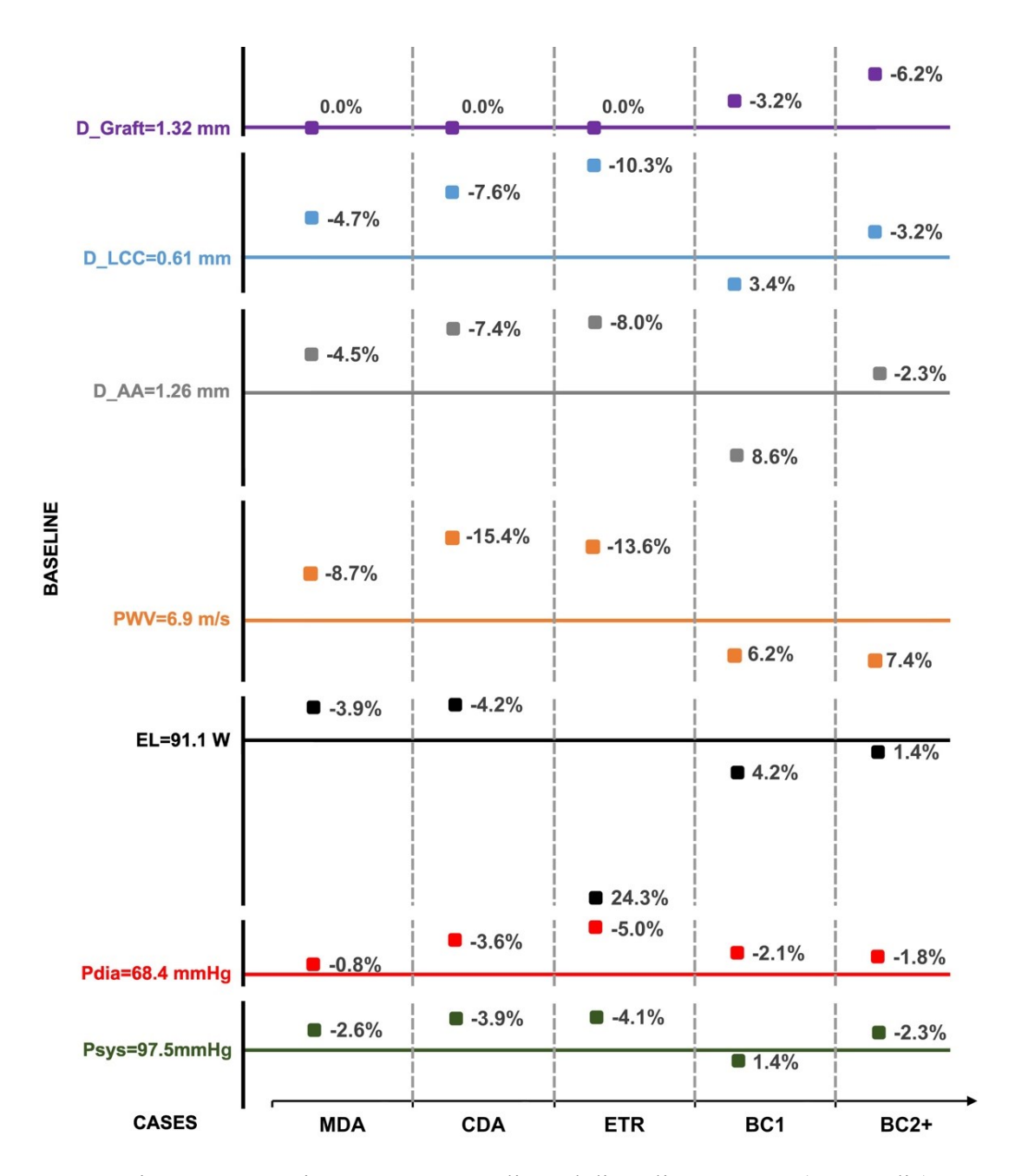


Figure 2. 7 Y-axis represents systolic and diastolic pressures (Psys, Pdia), EL, PWV, and maximum diameter variation at the ascending aorta (D_AA), left common carotid (D_LCC), and graft (D_Graft) for the baseline case. The X-axis shows values of the metrics of interest for five additional cases, each labelled with their respective errors. Bold lines denote the metric values for the baseline case and those corresponding to 0% of relative change.

2.3.3.Wall Displacement and Energy Loss(EL)

The maximum diameter variation of the ascending aorta, left common carotid, and graft is compared between the baseline and five additional virtual intervention cases. For clarity, only the left common carotid is shown in Figure 2. 7, as the displacement trends for the other supra-aortic branches are similar. In the case of a long and rigid graft, the maximum diameter variation differs by up to 10% (ETR). This pattern follows the previously described pressure increase, driven by intrinsic compliance modelling (MBM), where displacement is linked to the difference between local and external pressure. Consequently, maximum diameter variations are lower than in the baseline case when the graft matched the proximal native aorta's compliance (BC1) and higher when the graft exceeded it (BC2+).

EL increase the most, by up to 4.2% (MDA, CDA), when the virtual replacements extend to the DA. Conversely, it decreases by 4% when the graft matches the proximal native aorta's compliance (BC1). However, with the entire thoracic aorta replacement (ETR), where the graft geometry replicates a healthy aorta, EL drops significantly by 24%, highlighting the reduction in EL associated with the altered morphology and condition of TBAD in the baseline case.

2.3.4. WSS-Based Indices

Contours of TAWSS and ECAP, capped between the critical ranges (0-5 Pa) and (0-1.4 Pa⁻¹), respectively, are plotted in Figure 2. 8, Figure 2. 9 and Figure 2. 10. The left side shows the baseline case, while the right side presents contours depicting the differences between the baseline and the five additional cases. The most pronounced differences appear in key clinical regions, particularly around the aortic arch, including the PET, aneurysm, and graft sutures. To better visualise these variations, zoomed-in contours of these regions are provided. These contours are

color-coded based on the differences between the baseline and the five cases, as calculated using equations 2. 15 and 2. 16.

In the baseline case, TAWSS is globally low (Figure 2. 8 and Figure 2. 9). High TAWSS is observed in the vicinity of PET (9.73 Pa), graft sutures, and abdominal and iliac arteries due to high velocities in these narrowed locations (as observable on Figure 2. 3 and Figure 2. 4). High ECAP values (>1.4Pa⁻¹) are found at the graft sutures, around to multiple re-entry tears proximal to the abdominal branches and the narrowing of the lumina, and at the aneurysm with a maximum reported value of 4.49 Pa⁻¹ (black arrow in Figure 2. 10)

The similarity in TAWSS and ECAP distributions across all cases can be attributed to the application of identical inlet and outlet boundary conditions to geometries that share similar overall morphologies, apart from the graft length. TAWSS differences are mainly observed at the PET and graft sutures, where TAWSS is elevated. As shown in Figure 2. 8 and Figure 2. 9 (black arrow), the most significant differences are found in the case of a complete DA graft replacement (-1.37% and 1.87%, respectively). ECAP differences are most pronounced at the aneurysm, where blood velocity is low and flow stagnation occurs, such as depicted in Figure 2. 3 and Figure 2. 4. The maximum differences, observed in the complete DA replacement (CDA) case, were -16% and 20%.

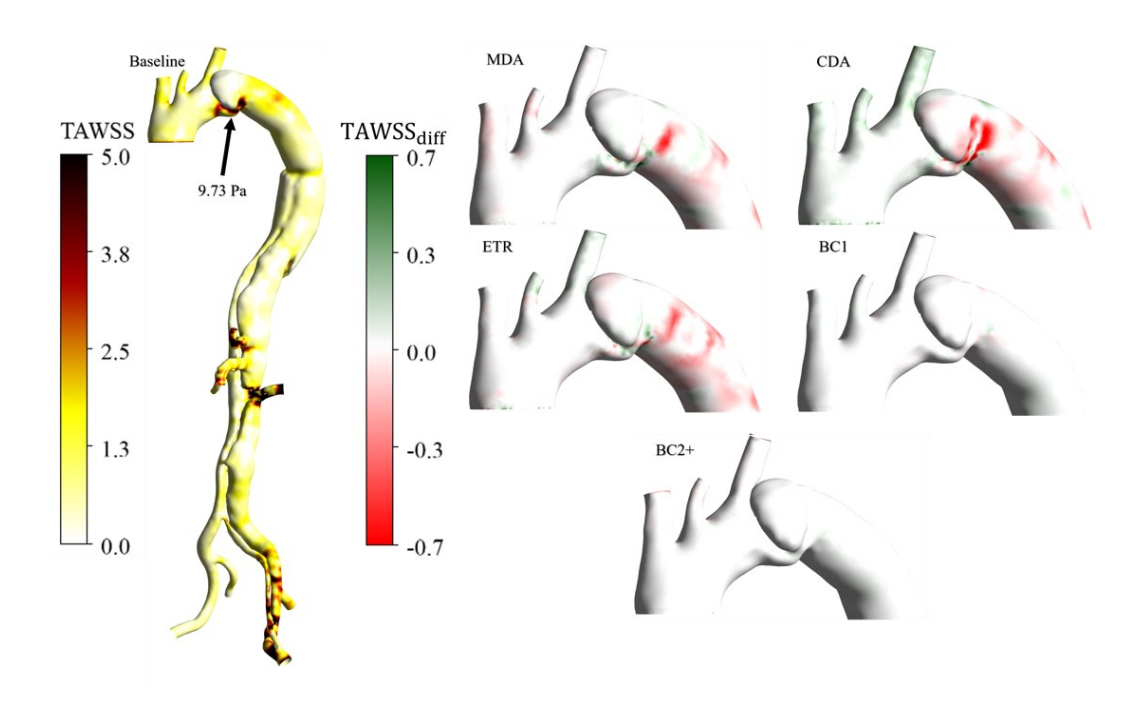


Figure 2. 8 Front view of the TAWSS. On the left, values over 5 Pa are found at the PET, the abdominal arteries, and the left iliac of the baseline case. The black arrow indicates the maximum TAWSS at the PET. On the right, the TAWSS differences between the baseline and the five cases are shown. A zoom is made on the AA and aortic arch as regions of interest where the TAWSS is high.

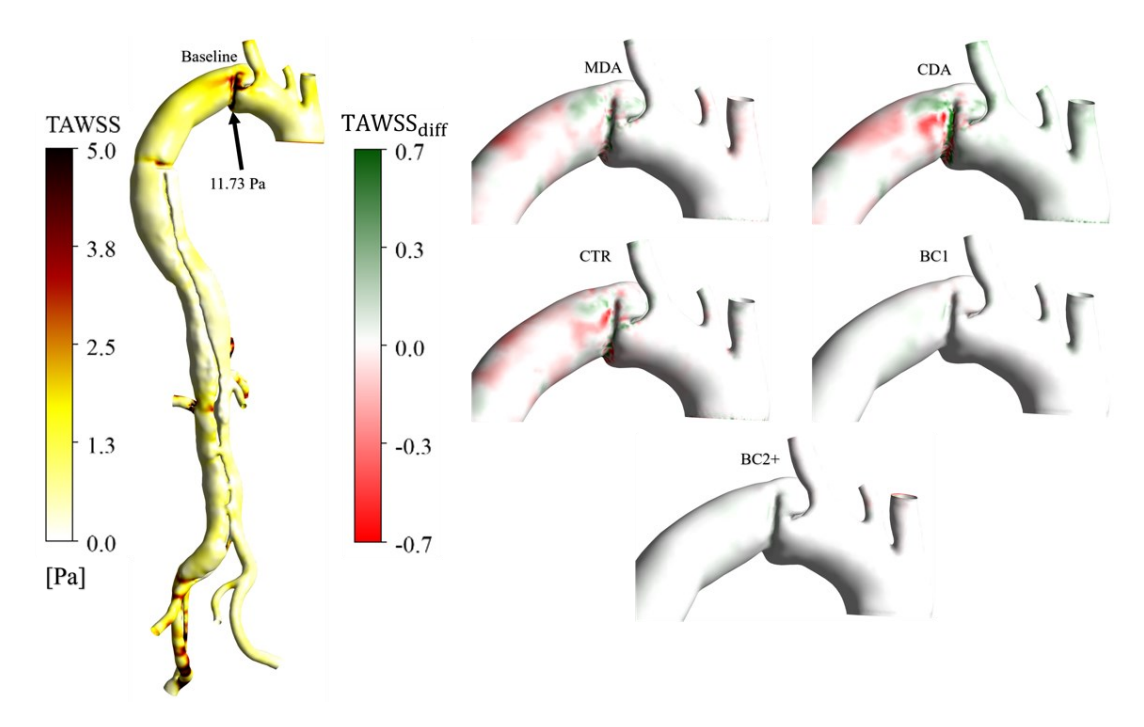


Figure 2. 9 Back view of the TAWSS. On the left, values over 5 Pa are found at the PET and sutures with the graft of the baseline case. The black arrow indicates the maximum TAWSS at the sutures with the graft. On the right, the TAWSS

differences between the baseline and the five other cases are shown. A zoom is made on the AA and aortic arch as regions of interest where the TAWSS is high.

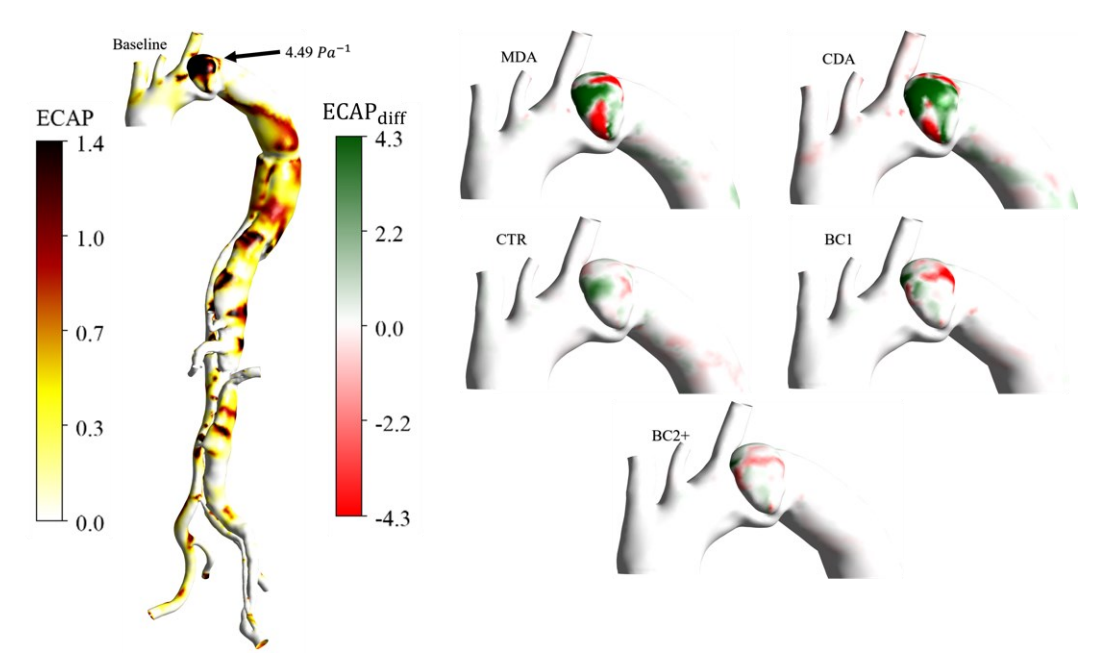


Figure 2. 10 ECAP distributions, front view. On the left, ECAP absolute values for baseline case; values over 1.4 Pa⁻¹ are noted in the aneurysm. The black arrow indicates the maximum ECAP value in the aneurysm. On the right, ECAP differences between the baseline and the five virtual cases.

2.4. Discussion

Aortic stiffening and pressure increase (Ikeno et al., 2022), as well as increased PWV (O'Rourke et al., 1968), have been shown to result in LV hypertrophy. Similarly, it has been reported that the interaction between the implanted graft and wall movement may be responsible for increased EL (Qiao et al., 2021). In an FSI study comparing a pre-and post-TEVAR case of TBAD, (Van Bakel et al., 2019) demonstrated an increase in LV stroke work after the intervention. They concluded that the increased aortic impedance and decreased aortic compliance between the endovascular stent and the aorta led to an increased LV afterload and suggested using compliant devices. Additionally, (Rong et al., 2019), and (Nauta et al., 2017) found increasing diameters in supra-aortic branches and DA after ascending and thoracic repairs due to the rigid grafts employed. They noted increased pulse pressure and

deformation of the AA and aortic arch, increasing the risk of dissection propagation or aneurysmal degeneration.

Similarly, in this study, results suggest that longer DA grafts impact cardiovascular health, including their impact on the LV load. Pressures increased up to 4% at the inlet (Figure 2. 7). The pressure values in the distributions displayed in Figure 2. 5 and Figure 2. 6 were also higher than in the baseline case. As a result, aortic wall displacements were also higher and can be attributed to the pressure-displacement relation in the MBM. Additionally, the impedance mismatch with a longer graft contributed to PWV increase, with an increase of up to 15% (CDA). The EL were also higher, with an increase of 4% in the case of a complete DA replacement.

In the entire thoracic aorta replacement (ETR) case, despite having the longest graft, the lowest aortic compliance, and the highest pressure and aortic displacement increase, the results did not show the expected rise in PWV and EL. The stented geometry of the graft, which includes four ideal abdominal branches with circular outlets, closely resembles a healthy aorta, helping to restore normal blood flow, as shown in Figure 2. 3 and Figure 2. 4. This likely reduces the reflection of pressure waves. Additionally, the stented geometry and improved flow conditions help preserve total pressure along the aorta, ultimately contributing to lower EL, as described by equation 2. 14.

If no other factors are considered, the ETR case would offer a favourable surgical option. That being said, complete replacement of the aorta has been associated with serious negative consequences, such as spinal cord injury resulting in paraplegia, as most segmental arteries are no longer attached to the aorta (Petroff et al., 2019). Additionally, in the case of a more extensive dissection, kidneys must cope with an abnormal level of perfusion. Therefore, recovering a physiologically typical flow split after surgery may lead to the deterioration of renal function (Urbanek et al., 2020).

Moreover, the simulations of the compliant graft cases were more complex to analyse, and direct conclusions were challenging to reach. In the case of a graft matching the compliance of the native proximal vessel (BC1), all metrics showed improvement compared to the baseline case (Figure 2. 5, Figure 2. 6 and Figure 2. 7). This can be attributed to the increased aortic compliance, providing an additional buffering effect that reduces pressures and wall displacement as the graft extends. This

could suggest that a patient-specific compliance-matching graft might mitigate the risk of LV hypertrophy (Takeda et al., 2014). However, such a conclusion was not readily attainable in the case of a graft exceeding the compliance of the native proximal vessel (BC2+). With the graft being twice as compliant as the native proximal vessel, a compliance mismatch was also introduced. Pulse pressure increased by 3.6% compared to the baseline case. Despite the compliant graft expanding by 6% in diameter, this buffering effect did not lead to a reduction in the diameters of the upstream inlet and supra-aortic branches compared to the baseline case (Figure 2. 7). Conversely, the PWV was reduced the most out of all cases by 7%.

These results reflect the different grafting strategies. Theoretically, greater compliance leads to a lower PWV due to the damping effect of the graft. However, the results indicate that a highly compliant graft can create a compliance mismatch with the native proximal aorta. This mismatch may be detrimental, as it can increase aortic impedance, elevate pulse pressure, and induce excessive pressure reflections. Therefore, matching the compliance of the proximal vessel appears to be the most sensible approach to ensure smoother pressure wave propagation and reduce cardiac workload.

High TAWSS has been linked with aortic wall degeneration, such as aneurysmal growth and aortic dissection propagation and is commonly found in narrowed regions such as the PET and re-entry tears due to higher velocity gradients in these regions (Munshi et al., 2020, Salmasi et al., 2021). High ECAP may indicate regions with an elevated risk of atherosclerotic plaque formation and calcification, a known risk factor for aortic rupture commonly found in TBAD (Golledge, 2003).

In this study, high TAWSS was also collocated in high-velocity regions, such as at the PET, proximal to entry and re-entry tears, and the graft sutures. These TAWSS results inform on potential risks of aortic degeneration at those locations, such as graft rupture at the sutures. Additionally, the highest ECAP values region was observed at the aneurysm, where low blood velocity magnitudes and circulating flow were observed (Figure 2. 3 and Figure 2. 4). This might indicate a high risk of aneurysmal growth.

In the five additional surgery cases, the main differences against the baseline case were collocated with the locations of high TAWSS and ECAP (Figure 2. 8, Figure

2. 9 and Figure 2. 10. Differences were the highest in the case of a complete DA replacement (CDA), especially at the PET and graft sutures. Such results could indicate a higher risk of tear expansion or local rupture with this grafting strategy. Similarly, the highest ECAP differences against the baseline case were found at the aneurysm in the CDA case. With maximum differences of -16% and 20%, respectively, suggesting that graft length may influence aneurysmal growth remodelling risks.

Results from this study suggest that compliant grafts may benefit TBAD patients after OS by reducing EL, thereby lowering the risk of LV hypertrophy and heart failure. While rigid grafts remain the standard, recent advancements in 3D bioprinting technology have shown promising progress. In recent years, tissue analogues for aortic valves and blood vessels have been successfully developed (Khanna et al., 2022). However, biomimetic technologies for compliant tissues have primarily been applied to smaller vessels (Moreno et al., 2011). Replicating the mechanical properties of the aorta remains a complex and costly challenge, with limited reports of success (Chlupác et al., 2009). By integrating *in silico* virtual grafting with *in vivo* imaging data, 3D bioprinting technology may pave the way for further research and encourage graft and stent manufacturers to explore this approach.

2.5. Limitations

In this study, the impact of graft length and compliance in a patient-specific case of chronic TBAD post-surgery was simulated using routinely acquired clinical data including limited pre-operative 2DMRI and Cine-MRI data. Using pre-operative data may introduce inaccuracies in post-intervention virtual scenarios due to changes in inlet flow rate and aortic wall compliance after the intervention. However, previous research by Pirola et al., (2018), demonstrated the feasibility of using preoperative data to tune postoperative boundary conditions using post-intervention invasive aortic pressure measurements acquired during a follow-up. They showed overall acceptable agreement with their simulated post-intervention pressure.

In this study, the aortic wall and intimal flap downstream of the graft were assumed to be stiff due to the lack of *in vivo* data. This limited the ability to fully capture the potential impact of aortic displacements downstream of the graft.

However, in a chronic dissection, especially after an OS, the dissected aorta rigidifies with age and displacements are negligible (Bissacco et al., 2022)

This study was limited by the availability of post-surgical *in vivo* clinical data. Incorporating 4D-Flow MRI and Cine-MRI datasets can improve the understanding of clinical cases, and thus the accuracy of the simulations, by refining the study's goals and providing more in-depth measurements and driven analysis. These datasets can enable a more comprehensive validation and alternative methods such as the use of PWV to inform the compliant model further as will be demonstrated in Chapter 4.

The MBM only considers radial displacements, and it was assumed that neglecting the longitudinal displacement does not affect the simulation of a stiff graft and the conclusions of the study. Previous studies have shown that Dacron graft stretching occurs mostly in the axial direction, with a ratio of about 50 between axial and radial stretching (Bustos et al., 2016, Ferrari et al., 2019, Tremblay et al., 2009). Axial stretching is approximately 20-30 times lower than the healthy ascending aorta while the radial one is 40 times. The volume compliance of the graft primarily thus stems from its axial stretching; however, it was reported that the longitudinal stretching of the thoracic aorta does not exceed 1% during the cardiac cycle (Morrison et al., 2009). Once the graft is sutured at the DA, its axial stretching is minimal due to its stiffness.

The nonlinear and anisotropic response of the aortic tissue is complex. Without access to specific tissue *in vivo* patient data, the model in this study assumes a linear relationship between pressure difference and stiffness *K* (equation 2.12 and 2.13). This approach, adopted in previous studies, has been extensively validated and keeps the workflow patient-specific as it uses in-vivo wall displacement data (Bonfanti et al., 2018, Stokes et al., 2021). Additionally, Rissland et al., (2009), and Mesri et al., (2017) suggest that while this model assumes a linear response, it can still provide valuable comparative conclusions. A higher peak WSS is anticipated in a nonlinear response, while the distribution of regions with low and high WSS would remain consistent, which would not change the comparisons and conclusions made between the baseline and five virtual surgical cases.

2.6. Conclusions

This chapter presented the simulation of a patient-specific post-operative case of TBAD and explored the impact of different surgical strategies via virtual grafting. Five virtual intervention scenarios were explored; these included three virtual surgeries using varying graft sizes (stiff grafts) and two cases with compliant grafts. The influence of various potential surgical strategies for TBAD was evaluated using velocity and pressure distributions, aortic displacements, PWV, EL, TAWSS and ECAP, considering the effects of graft length and compliance. Results illustrated that an optimal graft selection cannot be determined without considering the morphology and condition of the aorta of each patient; any results should be used as a guideline and carefully considered against clinical evidence and expertise.

As mentioned, in this chapter, the patient selected for the study underwent OS, with the surgical approach involving replacing a portion of the dissection at the DA, while leaving the downstream lumina separated by an intimal flap. Due to the lack of *in vivo* data, the intimal flap was considered rigid in this study. However, in some cases, the flap may be mobile, which may significantly impact aortic haemodynamics. Understanding these effects is crucial. To address this, the next chapter (Chapter 3) introduces a novel formulation of the MBM, applying it to a TBAD case post-TEVAR with a remaining intimal flap. Results from the patient-specific CFD simulation are compared against a rigid flap simulation and additional cases with varying levels of intimal flap compliance.

Chapter 3

A Novel Computational Framework Integrating Intimal Flap Compliance: Impact on Aortic Haemodynamics

3.1. Introduction

Surgical interventions for type-B aortic dissection (TBAD) can result in a residual intimal flap (IF) when the implanted device does not fully cover the entire dissected segment of the aorta (Trahanas et al., 2022). The persistence of a non-resected intimal tear and a patent false lumen (FL) have been identified as risk factors for delayed aneurysmal expansion, reoperation, and worse long-term survival in TBAD (Trimarchi et al., 2013, Tsai et al., 2007, Yaşar et al., 2023).

The interplay between FL and true lumen (TL) blood volume changes, driven by cyclic expansion and contraction, generates dynamic pressure differences between the lumina. This luminal pressure difference, also known as transmural pressure (TMP), contributes to the mobility of the compliant IF, which can alter haemodynamics post-surgery (Lortz et al., 2019). IF movement has been associated with the persistence of a patent FL and has been reported to affect positive aortic remodelling (MacGillivray et al., 2022). Consequently, a mobile IF can contribute to luminal growth and disrupt normal haemodynamics (Cheng et al., 2015, Xu et al., 2021a). In particular, when the IF remains mobile in the visceral aorta (VAO) region, it can lead to organ malperfusion, posing significant clinical risks (Mega et al., 2006, Kamman et al., 2017b, Kim et al., 2023).

While imaging techniques like CTA or MRI scans offer insights into the TBAD anatomy (Litmanovich et al., 2009, Sherrah et al., 2015), their limitations in spatiotemporal resolution prevent accurate measurement of IF movement (Lamata et al., 2014, Ramaekers et al., 2023). Computational fluid dynamics (CFD) simulations can complement these imaging modalities, providing a deeper understanding of the impact of IF movement on aortic haemodynamics (Wee et al., 2018).

Compliant models are essential for investigating the influence of the IF movement in TBAD, with fluid-structure interaction (FSI) being commonly employed. As discussed in Section 1.7.1, FSI facilitates the study of the effects of IF movement on aortic remodelling, FL expansion, and aneurysm progression, providing valuable data to predict disease outcomes. However, FSI-based studies are limited by the lack of *in vivo* data to describe patient-specific material properties and differences between the aortic wall and the IF (Kim et al., 2023, Qiao et al., 2015). The moving boundary method (MBM) demonstrated in the previous chapter can circumvent this challenge, allowing patient-specific simulations of the compliant behaviour of the aortic wall and IF.

In previous work by Bonfanti et al., (2018), the IF was modelled as a zero-thickness membrane, accounting only for relatively small displacements. This approach imposes limitations in capturing the cross-sectional area variations that might be encountered in TBAD. To address this, this chapter ²introduces a novel approach to modelling a thick, mobile IF, incorporating an improved MBM applied to a TBAD case post-TEVAR. The computational framework leverages 4D Flow MRI (4DMRI) and cine-MRI to inform the CFD simulation with blood flow and aortic displacement measurements, and the aortic geometry is segmented from TRUFI MRI.

The displacement of both the exterior aortic wall and the IF is simulated, treating the flap as a thick, mobile structure. This is achieved by longitudinally splitting the IF into two surfaces corresponding to the TL and FL, which are then divided into paired patches for effective modelling. Each patch pair maintains aligned

² This work is under review in the Journal Annal of Biomedical Engineering in 2025. Please refer to Research Declaration Form B for details.

surface normals, ensuring smooth displacement during simulations. The displacement is calculated using a force-based equation that incorporates local stiffness coefficients, iteratively tuned to match patient-specific displacements observed in cine-MRI.

CFD simulations are first validated against in vivo data and further compared with additional simulations. These include a rigid IF simulation and two cases where the IF has lower stiffness, leading to higher displacements. Haemodynamics markers such as pressure, velocity magnitude, aortic wall and IF displacement, TMP, and WSS-driven indices are analysed and compared across simulations.

3.2. Methods

3.2.1.Data Acquisition

A patient with chronic TBAD previously treated with TEVAR underwent follow-up imaging at Inselspital Bern, following an ethically approved protocol (Local Institutional Review Board ID 2019-00556), including patient consent. Brachial pressures were measured before the imaging procedures. MRI sequences were performed on a MAGNETOM Sola fit scanner (Siemens Healthineers). The imaging protocol included acquiring 4DMRI, two planes of cine-MRI, and T2/T1 weighted TRUFI MRI sequences, with respective pixel sizes of 2.5*2.5*2.5 mm³ 1.88*1.88 mm² and 1*1*1 mm³, to visualise the patient's thoracic aorta. Cine-MRI planes were acquired at the ascending aorta (AA) and visceral aorta (VAO) locations (shown in Figure 3. 1B). 4DMRI and cine-MRI had a temporal resolution of 37 ms. This dissection case was selected as it represents a unique scenario where TEVAR treatment left a residual mobile IF due to partial dissection coverage.

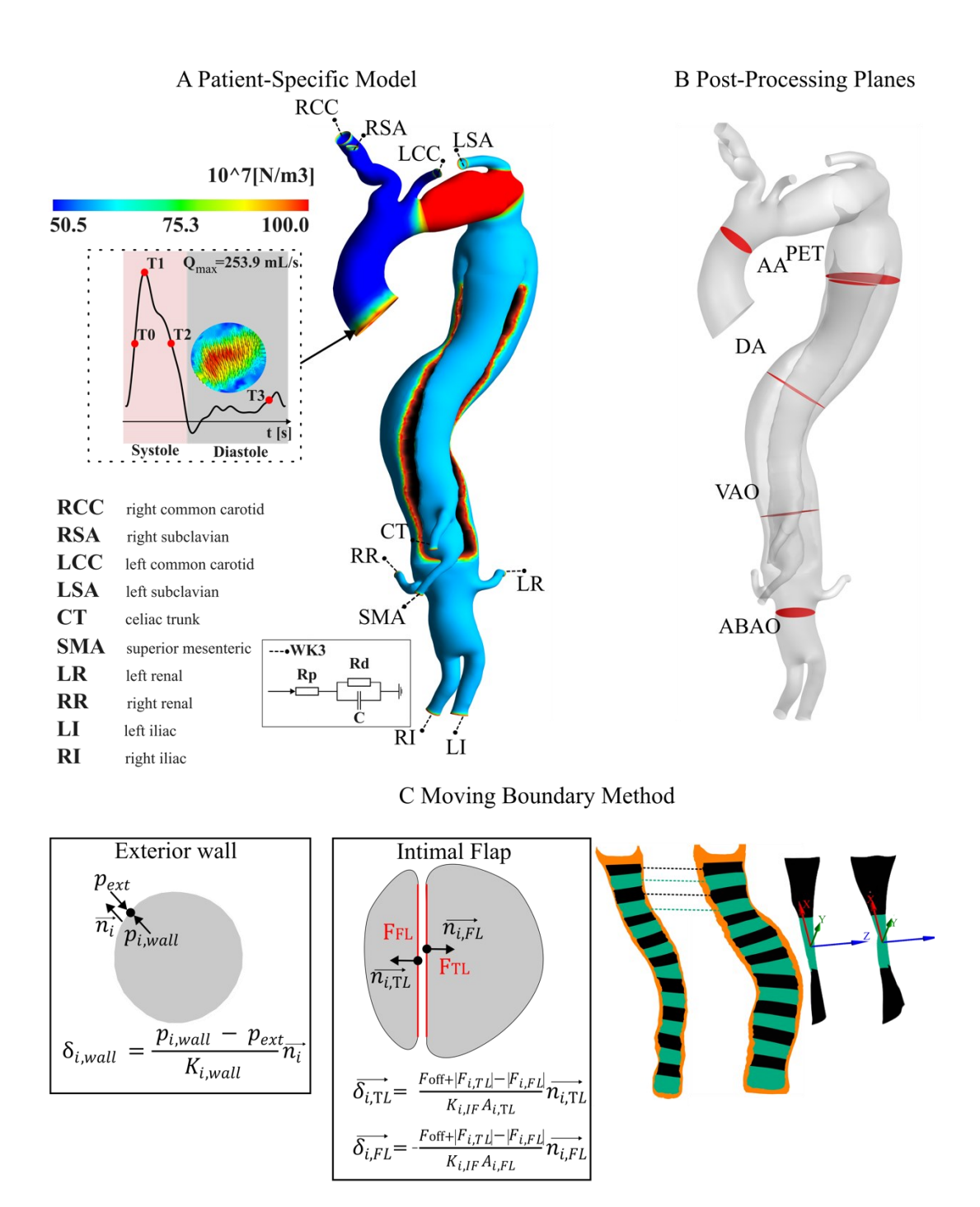


Figure 3. 1. (A) Patient-specific model of the domain showing the boundary conditions used and the aortic wall stiffness. T0 is mid-acceleration, T1 is peak systole, T2 is mid-deceleration, and T3 is end of diastole. (B) Planes in red are used to extract variables in the post-processing at the ascending aorta (AA), PET, descending aorta (DA), VAO and abdominal aorta (ABAO). (C) The MBM is applied both at the exterior aortic wall and the IF. The rightmost part of the figure illustrates the pairing technique used for the IF, showing how TL/FL pairs of patches, coloured in black and green respectively, share the same surface normal.

3.2.2.Geometry and Mesh

The aortic geometry was obtained from the T2/T1 TRUFI utilising similar semi-automatic segmentation and smoothing techniques as those in Chapter 2, implemented in ScanIP (Synopsis Simpleware, USA). The IF was split longitudinally, following its curvature, forming two separate surfaces (Figure 3.1C), with one surface belonging to the TL and the other to the FL. Each IF surface was then divided into 10 mm segments. This division resulted in pairs of segments facing each other, alternatively shown in black and green in Figure 3. 1C. This ensures that the dot product of the surface normal of corresponding nodes within each pair is one or close to one [0.97-1]. This allows smooth nodal displacement within each patch pair, facilitating the application of the moving boundary method (Figure 3. 1C). The meshing process described in Chapter 2 was followed to create a mesh with tetrahedral elements. To accurately capture the turbulent boundary layer, ten prism layers were employed, with the initial layer thickness calibrated to achieve a y+ value of approximately 1. A medium-resolution mesh, with cell sizes ranging from 2 mm to 0.5 mm, resulted in 1.9 million elements and was evaluated in a mesh independence study alongside a coarse (0.9M elements) and fine (4.2M elements) mesh. Details of the mesh sensitivity analysis used to determine the final mesh configuration are provided in B.1, along with details on sizing parameters for the coarse and fine meshes.

The planes shown in (Figure 3. 1B). were selected to observe specific localised flow characteristics and wall displacements. For instance, the DA plane was positioned equidistantly along the vessel centerline between the PET and the VAO, ensuring it is perpendicular to the vessel and sufficiently distanced from the stent to minimise noise in proximal 4DMRI measurements. The AA and VAO planes were positioned so that they matched the cine-MRI planes.

3.2.3. Wall Compliance

The MBM previously described in Chapter 2 (see section 2.2.5) was further developed so that it could be applied to simulate the displacement of the entire aorta, i.e., both the exterior wall and the thick IF.

The motion of the exterior wall of the aorta is modelled as in Chapter 2. The local exterior wall displacement δ_n (m) is estimated using equation 2. 12. The stiffness, K_n , was derived from the area-based distensibility, which was measured from the 4DMRI images (Figure 3. 1A). Limitations in aortic wall displacement measurements due to the spatial resolution of the 4DMRI are discussed in Section 3.5.

As described in section 3.2.2, the TL and FL sections of the IF were discretised in patches along the centreline (Figure 3. 1B). Each patch in the TL section was paired with the nearest patch in the FL section on the opposite side of the IF. This pairing ensured that the displacement of facing IF patches was synchronised, thereby preserving the thickness of the IF.

The displacement of a pair of patches i, is proportional to the normal force gradient of the patches and inversely proportional to a local stiffness coefficient $K_{i,IF}$ (N/m³) along the surface normal, such as:

$$\overrightarrow{\delta_{\iota,FL}} = \frac{F_{off+}|F_{\iota,TL}| - |F_{\iota,FL}|}{K_{\iota,IF}A_{\iota,FL}} \overrightarrow{n_{\iota,FL}}$$
 3. 1

$$\overrightarrow{\delta_{\iota,TL}} = -\frac{F_{off+}|F_{\iota,TL}| - |F_{\iota,FL}|}{K_{\iota,IF}A_{\iota,TL}} \overrightarrow{n_{\iota,TL}}$$
 3.2

where TL and FL denote true and false lumen, respectively, $\delta_{i,TL}$ and $\delta_{i,FL}$ (m) are their displacements, $F_{i,TL}$ and $F_{i,FL}$ (N) the average forces, $A_{i,TL}$ and $A_{i,FL}$ (m²) the surface areas, $\overrightarrow{n_{i,TL}}$ and $\overrightarrow{n_{i,FL}}$ the surface normal of each respective i patch, i.e TL/FL pair. F_{off} (N) is the pre-stress force measured on the rigid IF simulation used to start the displacement from zero and to avoid a displacement 'jump' at the first simulation time step. $K_{i,IF}$ was iteratively tuned to match the patient-specific displacement measured on the cine-MRI.

Four IF stiffness values were then considered: a rigid one (named D0), the patient-specific stiffness (D1) derived from clinical images, and two additional cases where the stiffness was two times smaller (D2) and three times smaller (D3) than in the patient-specific case. A smoothing algorithm was used between regions of different stiffness to avoid abrupt displacement transitions as shown in the previous chapter and in previous work of the group where the MBM was used (Stokes et al., 2021).

3.2.4.Flow Boundary Conditions

4DMRI was used to extract the three-dimensional inlet velocity profile (3DIVP) (Figure 3. 1A) and outlet mean flow rates using GTFlow (GyroTools LLC, Switzerland) (Table 3. 1), as described in Stokes et al., (2023a), MATLAB (MathWorks Inc., USA) was used to spline-interpolate the inlet flow rate to apply a 1 ms time-step for the CFD simulations.

Table 3. 1. Targeted values of inlet pressures and outlet mean flow rates against simulation results.

		Target	D0	D 1	D2	D3
ıre [g)	Diagtala	04.00	02.0/1.20/	02 0/1 50/	00.5/1.70/	02.1/2.20/
nss Hu	Diastole	84.00	82.9/1.3%	82.8/1.5%	82.5/1.7%	82.1/2.3%
Pressure (mmHg)	Systole	113.86	113/0.7%	114/-0.1%	114.9/-0.9%	115.6/-1.5%
	RCC	10.02	10/-0.2%	10/0.1%	10/0.0%	10/-0.2%
	RSA	6.82	6.8/-0.3%	6.8/-0.7%	6.9/-3.7%	7.1/-1.5%
	LCC	6.55	6.5/-0.3%	6.6/0.1%	6.5/0.4%	6.5/0.1%
M	LSA	10.42	10.4/1.1%	10.3/0.6%	10.4/0.3%	10.4/0.7%
Mean Flow Rate (mL/s)	CT	3.51	3.5/2.3%	3.4/-1.4%	3.6/0.6%	3.5/1.5%
	SMA	5.72	5.7/-2.1%	5.8/-1.7%	5.8/-2.1%	5.8/-4.5%
Σ	LR	6.83	6.8/-0.4%	6.9/0.6%	6.8/3.3%	6.6/3.3%
	RR	8.35	8.4/2.8%	8.1/1.2%	8.3/2.7%	8.1/2.1%
	LI	6.28	6.3/-5.2%	6.6/-1.2%	6.4/-4.8%	6.6/-4.6%
	RI	5.57	5.6/2.0%	5.5/0.9%	5.5/2.5%	5.4/2.5%

A zero-dimensional lumped parameter model of the aorta was tuned in 20-sim (Controllab Products, Netherlands), targeting the *in vivo* inlet pressures and outlet

mean flow rates (Table 3. 1). Three-element Windkessel (WK3) pressure conditions were used at the domain outlets, following the same process presented in Chapter 2 and in published works (Figure 3. 1A) (Westerhof et al., 2009). WK3 parameters are provided in Appendix B.2.

3.2.5.CFD Simulation

The simulation settings used in this chapter were identical to those in Chapter 2. As the peak and critical Reynolds numbers were 8262 and 7407, respectively, the k-ω shear stress transport model was employed to capture turbulence effects accurately (see Section 1.6.7 for details on turbulence model). A low turbulence intensity of 1% was introduced to account for the laminar-turbulent transition (Kousera et al., 2013).

3.2.6. Haemodynamics Analysis

To assess the impact of IF displacement on the TL and FL haemodynamics, the transmural pressure TMP, vorticity, in-plane rotational flow (IRF) and WSS-driven metrics were estimated and compared for all the cases simulated.

TMP (mmHg) is the pressure difference between TL and FL:

$$TMP = P_{i,TL} - P_{i,FL}$$
 3. 3

TMP values were extracted along the IF centerline, every 20 mm from the PET for four points in the cardiac cycle: mid-acceleration (T0), peak systole (T1), mid-deceleration (T2), and end of diastole (T3).

Vorticity (1/s) was used to visualise the rotational characteristics of the blood flow. The component orthogonal to the cross-sectional planes of the aortic geometry (Figure 3. 1B) was calculated as follows:

$$\omega_z = \frac{\partial v}{\partial x} - \frac{\partial u}{\partial y} \tag{3.4}$$

This vorticity was then integrated to produce the in-plane rotational flow (IRF) (m²/s) metric, which quantifies the strength of vorticity and has been correlated to the expansion of the FL (Rodríguez-Palomares et al., 2018):

$$IRF = \iint_{T_i} \boldsymbol{\omega} dS$$
 3. 5

In TBAD with residual and mobile IF, IRF measurements can provide insight into the altered haemodynamics environment and highlight potential areas contributing to the growth of the FL. The in-plane rotational flow was calculated at four points in the cardiac cycle similar to TMP, namely T0, T1, T2 and T3 at the following locations: AA, PET, DA, VAO and ABAO (see Figure 3. 1B).

Additionally, the following WSS-derived indices, previously defined in 1.5.1, were calculated: the time average wall shear stress (TAWSS), the oscillatory shear index (OSI) and the relative residence time (RRT) (see equations 1. 1, 1. 2 and 1. 3).

3.3. Results

3.3.1.Pressure and Flows

Table 3. 1 shows the target values of inlet pressures and outlet means flow rates against values of the four simulations. In the patient-specific case, where the IF stiffness is derived from displacements measured on the 4DMRI (D1, Table 3. 1) target mean flow rates and pressures are simulated with maximum differences of 1.7% and 1.5%, respectively. Aortic pressures are closely matched in all other simulations. However, in cases where the flap is more mobile (D2 and D3), mean flow rates are simulated with differences up to 4.5% at the visceral branch outlets.

In Figure 3. 2, 4DMRI planes are colored with velocity magnitudes values at mid-acceleration (T0), peak systole (T1), mid-deceleration (T2), and end of diastole (T3) in selected locations (AA, PET, DA, VAO and ABAO). Additionally, similar

planes are shown for the patient-specific case (D1) and rigid IF case (D0) for comparison.

There is a good qualitative agreement in velocity magnitude distribution and values between the patient-specific case (D1) and the 4DMRI measurements (Figure 3. 2). Particularly, the velocity magnitude distributions are well-matched at T0, T1, and T2, especially at the AA, PET, DA, and VAO where the patient-specific IF displacement impacts the flow (D1). Specifically, the three-dimensional input applied at the inlet leads to a good comparison with the 4DMRI at the AA. At the PET and DA, the patient-specific simulation (D1) aligns well with the 4DMRI at T1 and T2, especially in the TL region. At the end of diastole (T3), the comparison becomes less evident due to the overall reduction in blood velocity at this phase of the cardiac cycle. Low blood velocity leads to a weaker flow signal, which, combined with the inherent limitations of 4DMRI, results in a low signal-to-noise ratio.

In contrast, in the case of a rigid IF (D0), lower and inaccurate velocities are predicted at T1, which shows poor agreement in terms of velocity distribution with 4DMRI measurements at T2. Additionally, at the VAO, the rigid IF simulation (D0) shows excessively high FL velocity at T0 and fails to capture the velocity distribution in the TL at T1, with velocity magnitudes also significantly underpredicted.

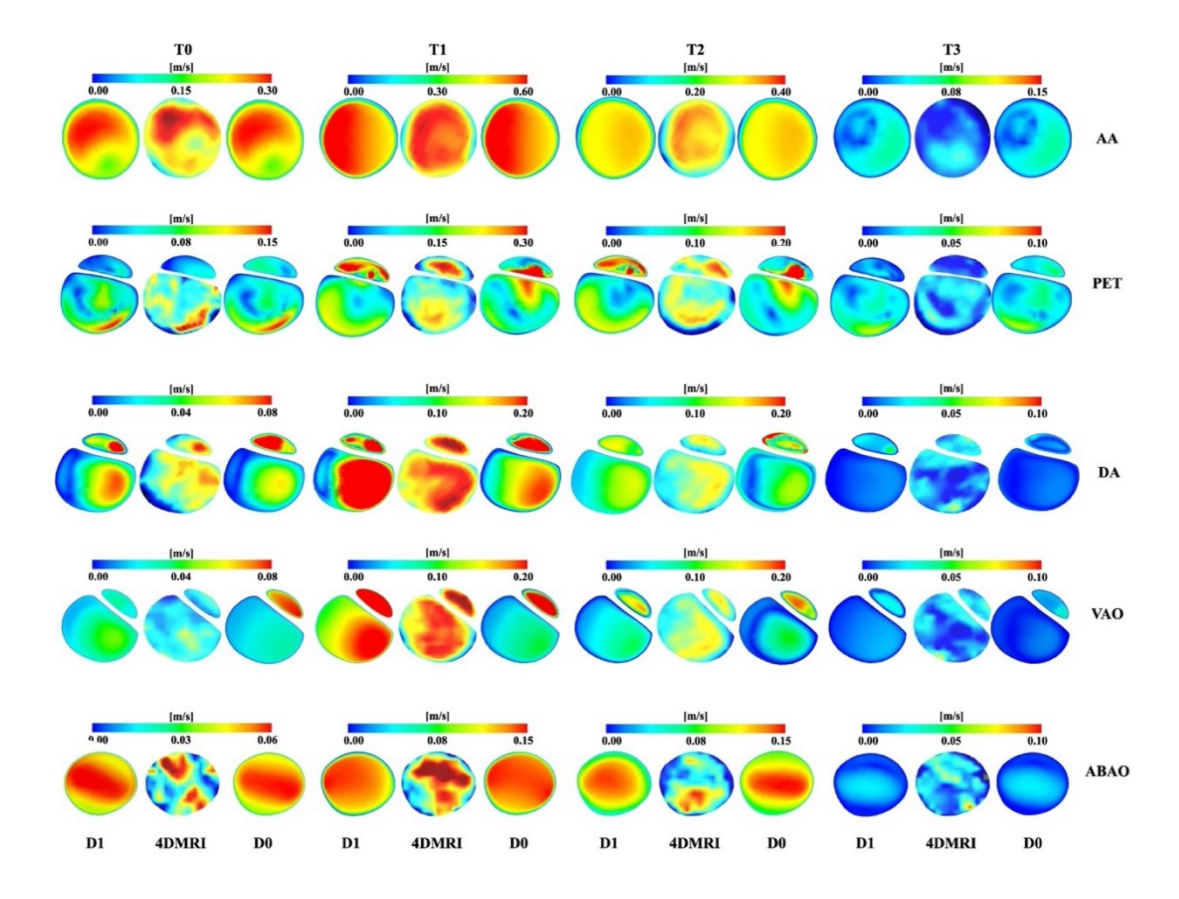


Figure 3. 2. Velocity magnitude comparisons between patient-specific simulations (D1), 4DMRI and rigid wall simulations (D0) at mid-acceleration (T0), peak systole (T1), mid-deceleration (T2), and end of diastole (T3) in selected locations (AA, PET, DA, VAO and ABAO).

3.3.2.Patient-Specific Displacement

Cine-MRI is used to verify the model by comparing the predicted displacements of the patient-specific case (D1) at the AA and VAO (Figure 3. 3). The resolution of the cine-MRI does not allow for the measurement of transient displacements of the aortic wall and IF; only the peak deformations at systole (T1) and diastole (T3) are measured and compared. The patient-specific simulations (D1) capture both the magnitude and pattern of the wall displacement between T1 and T3, with TL being compressed and FL expanding at T1.

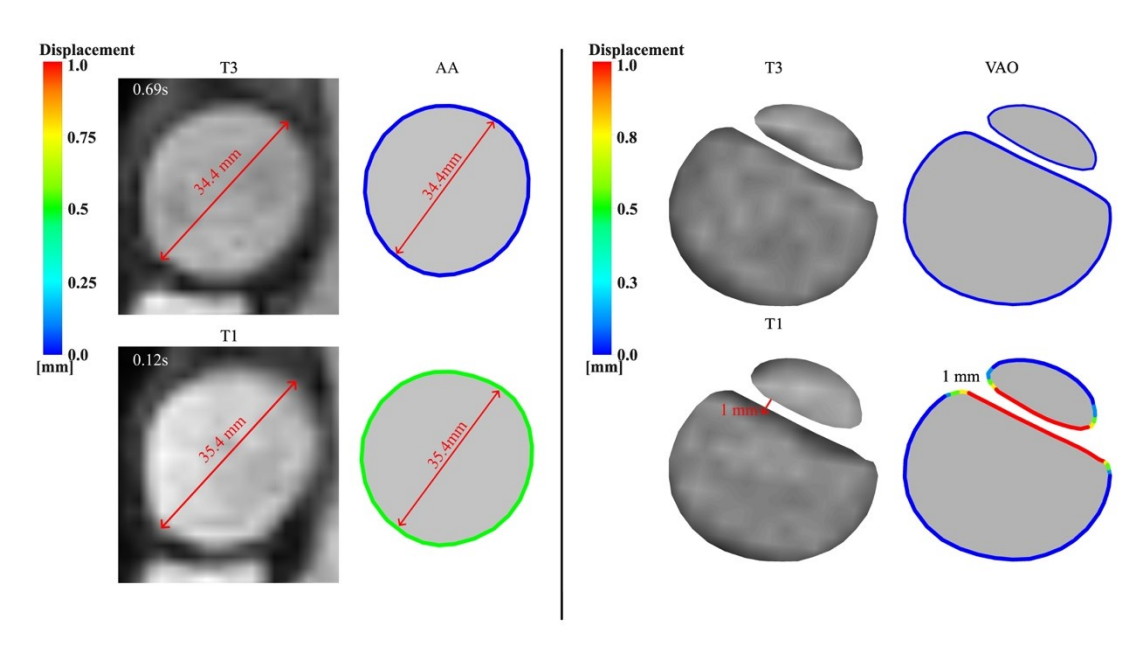


Figure 3. 3. Validation of the aortic wall and IF displacement in the patient-specific case D1 against cine-MRI measurements. The left panel in each subset shows the cine MRI and the right one shows the simulated cross-sections, with the boundary colour indicating.

3.3.3.IF Displacement, TMP and Pressure

Contour

Figure 3. 4 illustrates the displacement of the IF at the PET, DA, VAO, and TMP along the IF for each case at four different points in the cardiac cycle (T0, T1, T2, and T3). In the patient-specific simulation (D1), the maximum IF displacement reaches 0.5, 0.6, and 1 mm at the PET, DA, and VAO, respectively. While displacements are small and potentially within the error margins of the displacement measurement methods used in 4DMRI, the maximum displacement at the VAO matches the target. Further details on these limitations are discussed in Section 3.5.

In the patient-specific case (D1), TMP values increase with the distance from the PET at each time point. Specifically, the TMP is negative at T0, T2, and T3 and increases linearly with the distance from the PET, with a maximum of about -4 mmHg.

At T2, the TMP is positive and correlates with the decreasing part of the displacement curve when the IF moves back towards its diastolic position and the FL is compressed.

The TMP magnitude is lower in the case of a rigid IF simulation (D0) and increases with higher IF displacements. Additionally, it is worth noting that the TMP remains near 0 mmHg in D0 at T3, which inaccurately represents the TMP behaviour compared to the patient-specific simulation (D1). The rigid IF simulation (D0) fails to capture the expected TMP increase and distribution, showing a value close to zero, except for a slight rise near the DA location. Moreover, in the most mobile IF simulation (D3) the TMP curve deviates from the trend seen in the patient-specific simulation (D1) at T2 and T3, relatively close to the entry tear. These differences suggest the importance of modelling the intimal flap to improve predictions of luminal pressure dynamics, which could have implications for the progression of the tear.

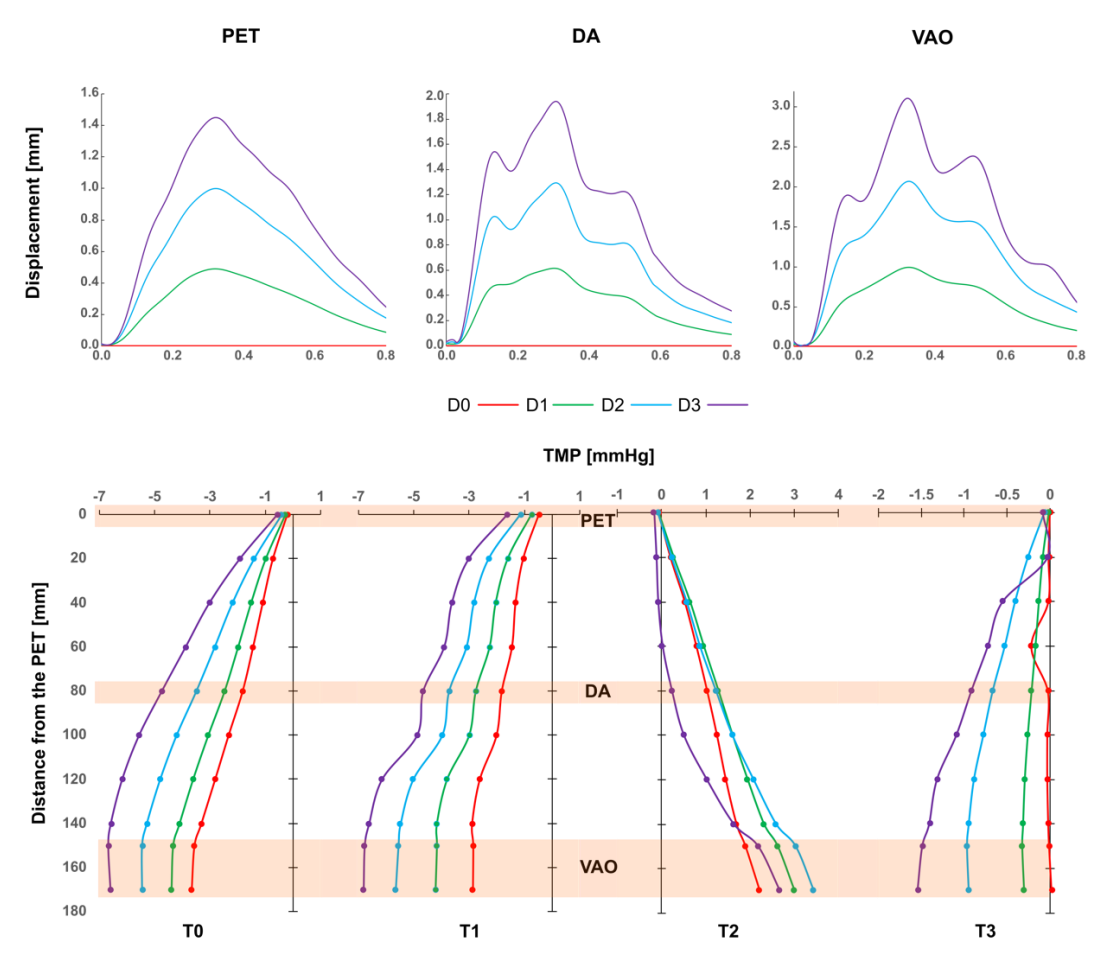


Figure 3. 4. IF displacement at the PET, DA and VAO over the cardiac cycle and TMP starting from the PET at T0, T1, T2 and T3 for all cases.

The pressure distribution for the patient-specific case (D1) is shown in Figure 3. 5 for two instants in the cardiac cycle (T1 and T2). The FL is highly pressurised at T1, with a pressure of 116 mmHg. Conversely, at T2, the TL becomes more pressurised and compressed. Comparisons against the pressure values obtained in the other cases indicate lower pressures in the case of a rigid IF (D0), especially at T1 in the FL, where a maximum difference of 2.4 mmHg is observed. On the contrary, when the IF is more mobile (D2, D3), simulations exhibit higher pressures, reaching up to 122.34 mmHg at the visceral branches in D3, close to the location of the highest IF displacement.

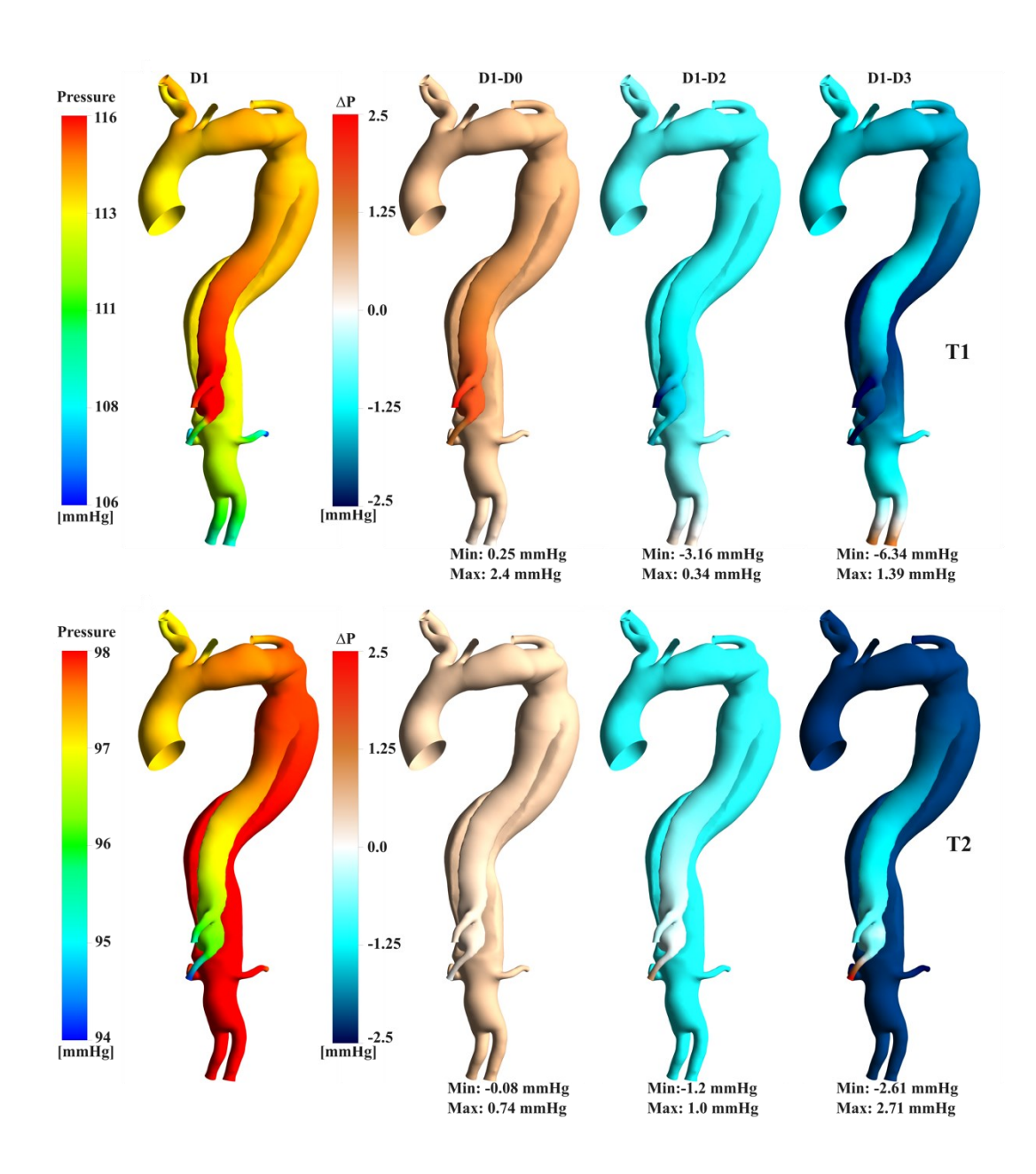


Figure 3. 5. Pressure contours for D1 and point-wise difference against additional cases at T1 and T2.

3.3.4. Rotational Flow Features

Vorticity patterns are analysed at selected locations (PET, DA, and VAO) (Figure 3. 6). In the patient-specific simulation (D1), vorticity patterns at PET reveal ongoing dynamic interactions between the TL and FL. In the PET region, counterrotating vortices are clearly present in the TL, with vorticity peaking at peak systole (T2). This indicates significant rotational flow dynamics that may influence the motion of the flap separating the TL and FL. The persistent vorticity in the FL near the PET, even after TEVAR, indicates the presence of non-uniform flow that could contribute to flap displacement, potentially impacting FL growth and remodelling. Additionally, there are persistent vortices in the FL near the PET, even after TEVAR, that may influence flap displacement, potentially impacting FL growth and remodelling. In the DA region, vorticity is less pronounced, indicating lower recirculation and more uniform flow patterns compared to the PET region. This suggests that the flow dynamics in the DA are less likely to significantly influence flap motion. However, in the VAO region, despite overall lower vorticity values, some vortical structures are still observed in T1 for all cases and some clear differences in circulation at T2 (with two clearly distinct regions) for the patient-specific case (D1). These affect the flow dynamics, influencing the haemodynamics environment near the VAO and might potentially be of interest when assessing thrombotic risk.

Vorticity differences between the patient-specific case (D1) and the additional cases (D0, D2, and D3) are relatively mild at the PET. At the DA, particularly at T1, where peak IF displacement is observed, significant differences in both vorticity values and vortical structures are evident in both lumina for the patient-specific case (D1) compared to the rigid IF case (D0). Increased IF displacement (D2, D3) also leads to differences compared to the patient-specific case, especially at T1, where negative vorticity in the TL is lower and vortical structures in the FL differ. At the VAO, where the highest IF displacements occur, vortical structures differ substantially

between the patient-specific case (D1) and the rigid IF case (D0) at T0, T1, and T2. Vortical structures are also different when the IF is more mobile (D2, D3) as depicted at T1 and T2, additionally, minimum and maximum vorticity values are higher.

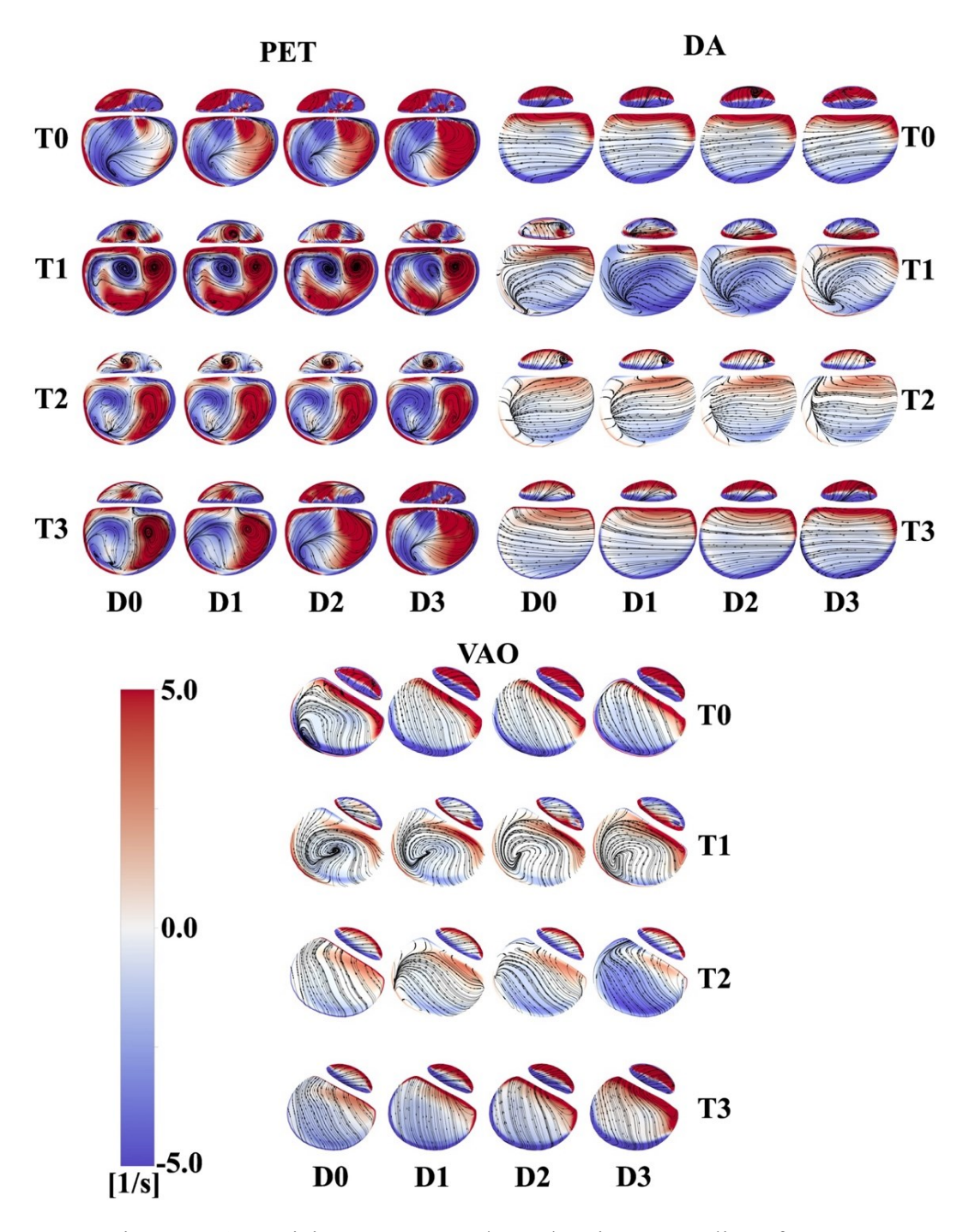


Figure 3. 6. Vorticity contours and overlapping streamlines for every case at the PET, DA and VAO at T0, T1, T2 and T3.

The rotational flow characteristics observed across different regions, particularly at the FL, are reflected in the IRF values summarised in Table 3. 2. In D1, IRF values tend to increase from T0 to T1 and then decrease during the deceleration phases (regardless of the sign), at the AA, DA, VAO, and ABAO (Table 3. 2). High IRF magnitudes (>20 cm²/s) are particularly noted in the AA, PET, and VAO at T1, suggesting significant rotational flow in these regions. Conversely, IRF values at the DA remain close to zero, indicating a balance between positive and negative vorticity. At the PET, notable differences are observed between the patient-specific simulation (D1) and the rigid IF model (D0). These disparities are most evident at T1, where the IRF is underpredicted in the TL and overpredicted in the FL, which may affect predictions related to growth and vascular remodelling. Furthermore, at the PET, the increased magnitude of the IRF suggests a higher risk of growth, particularly with greater displacement of the more mobile IF (D2 and D3).

Table 3. 2. IRF measured at the AA and ABAO, and in both lumina at the PET, DA, and VAO for every case at T0, T1, T2 and T3.

		IRF[cm²/s]							
		D0		D	1	D2		D3	
=		T0	T1	Т0	T1	Т0	T1	T0	T1
AA		5.51	34.30	5.54	34.22	5.60	34.08	5.98	33.92
PET	TL	5.13	25.72	5.30	33.92	5.47	44.56	5.63	56.37
	FL	-10.65	-13.33	-11.34	-6.01	-12.71	2.21	-13.87	11.20
DA	TL	-0.09	-1.11	-0.11	-0.99	-0.14	-0.83	-0.18	-0.61
	FL	0.29	-1.84	0.21	-1.48	0.15	-1.05	0.02	-0.57
VAO	TL	-2.84	-19.47	-3.53	-18.15	-4.97	-15.86	-6.83	-12.47
	FL	-0.23	-0.7	-0.18	-0.52	-0.13	-0.27	-0.03	0.059
ABAO		0.66	5.38	0.51	5.62	0.44	5.95	0.33	6.36
		T2	T3	T2	T3	T2	T3	T2	Т3
AA		22.94	1.22	22.9	1.12	22.86	0.95	22.79	0.78
PET	TL	50.69	-4.5	53.24	-3.53	57.25	-3.48	61.23	-2.82
	FL	21.50	-7.18	25.43	-8.62	30.16	-8.77	36.57	-4.25
DA	TL	-0.72	-0.11	-0.51	-0.23	-0.34	-0.45	-0.09	-0.89
	FL	-0.26	-0.07	-0.18	-0.13	-0.13	-0.19	-0.01	-0.24
VAO	TL	-0.73	0.12	-0.81	0.65	-0.89	1.28	-1.11	2.12
	FL	-0.26	-0.34	-0.63	-0.33	-0.99	-0.37	-1.34	-0.43
ABAO		3.89	0.85	4.01	0.84	4.3	0.84	4.78	0.74

3.3.5. Wall Shear Stress-Related Indices

Figure 3. 7, Figure 3. 8 and Figure 3. 9 display the contours of time-average wall shear stress (TAWSS), oscillatory shear index (OSI) and relative residence time (RRT) obtained for the patient-specific case (D1), alongside point-wise differences of these metrics from the additional cases.

Figure 3. 7 displays qualitatively similar TAWSS distributions. High values (>5 Pa) are found at the outlets and PET, where high velocities occur. Significant point-wise differences are observed between the cases at the TL, celiac trunk (CTA), and superior mesenteric artery (SMA) locations. TAWSS values tend to be higher for D0 at the FL and lower for more mobile IF simulations, with the highest difference being -3.35 Pa at the SMA compared to D3.

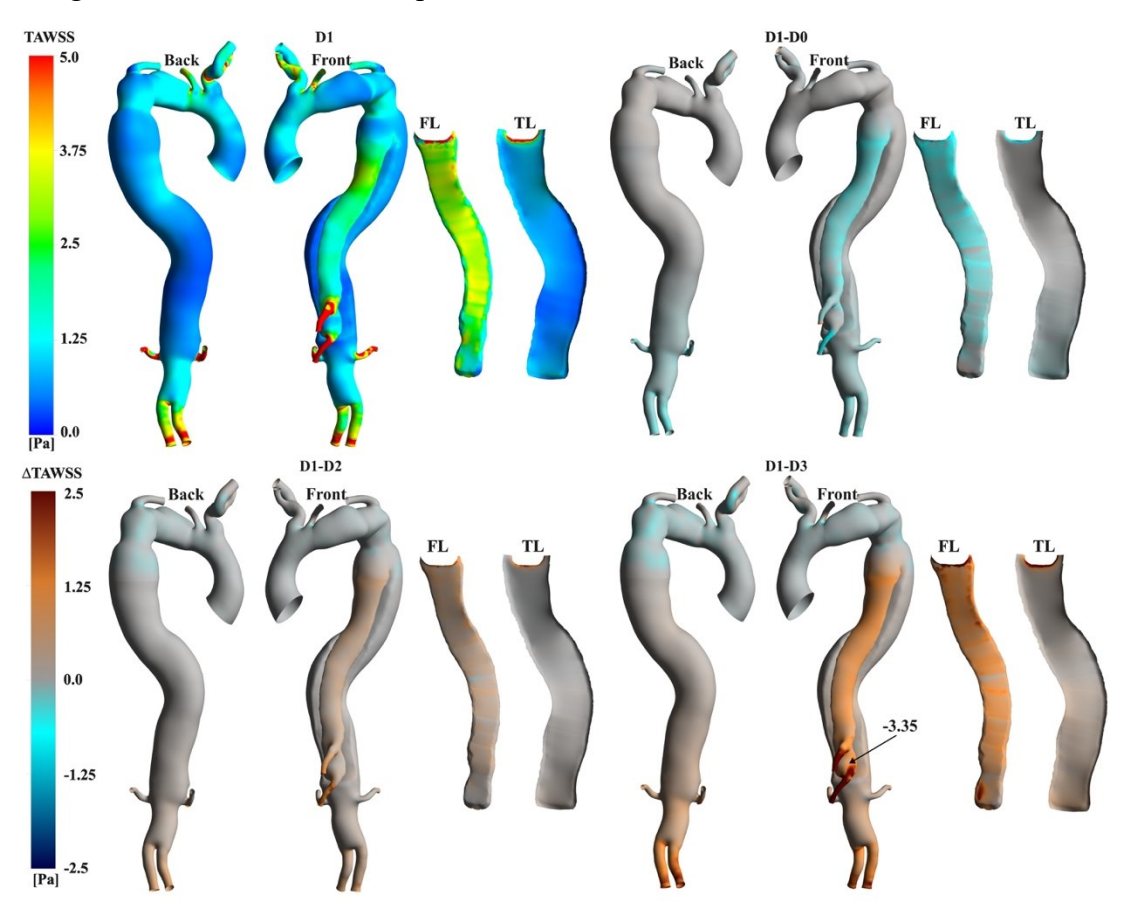


Figure 3. 7. Contours of TAWSS for the patient-specific simulation (D1) and point-wise differences against additional cases.

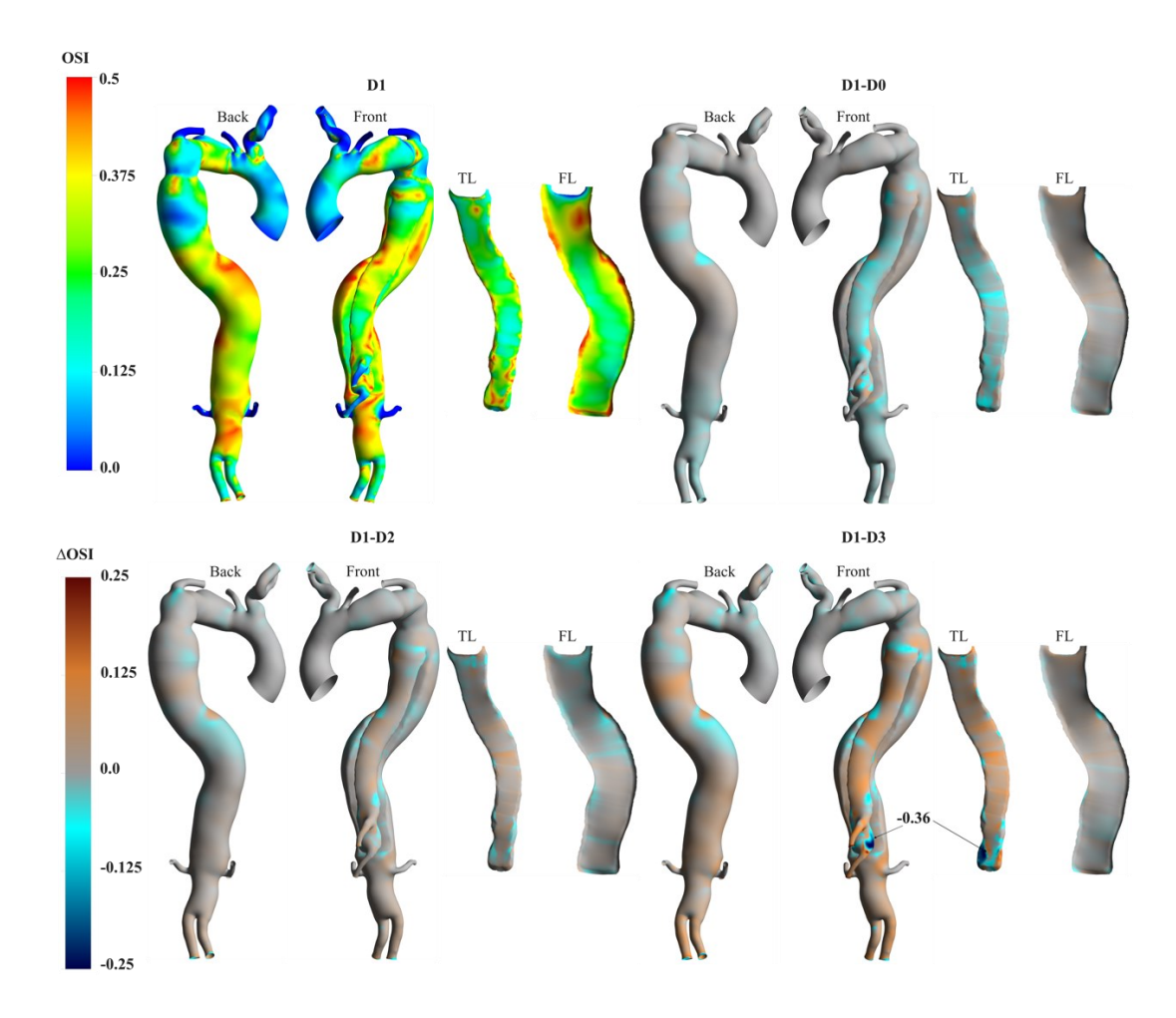


Figure 3. 8. Contours of OSI for D1 and point-wise differences against additional cases.

The distributions of OSI values indicate highly fluctuating flow in lumina in all cases (Figure 3. 8). Notably, regions of high OSI are present at the arch, along both lumina and proximal to the VAO. The D1-D0 point-wise differences highlight that the rigid IF simulation slightly underpredicts OSI values at the FL. Conversely, higher OSI values are predicted at the TL in D2 and D3. Additionally, proximal to the VAO at the bottom of the FL, where higher displacements occur, a -0.36 point-wise difference is measured in the D1-D3 comparison (Figure 3. 8).

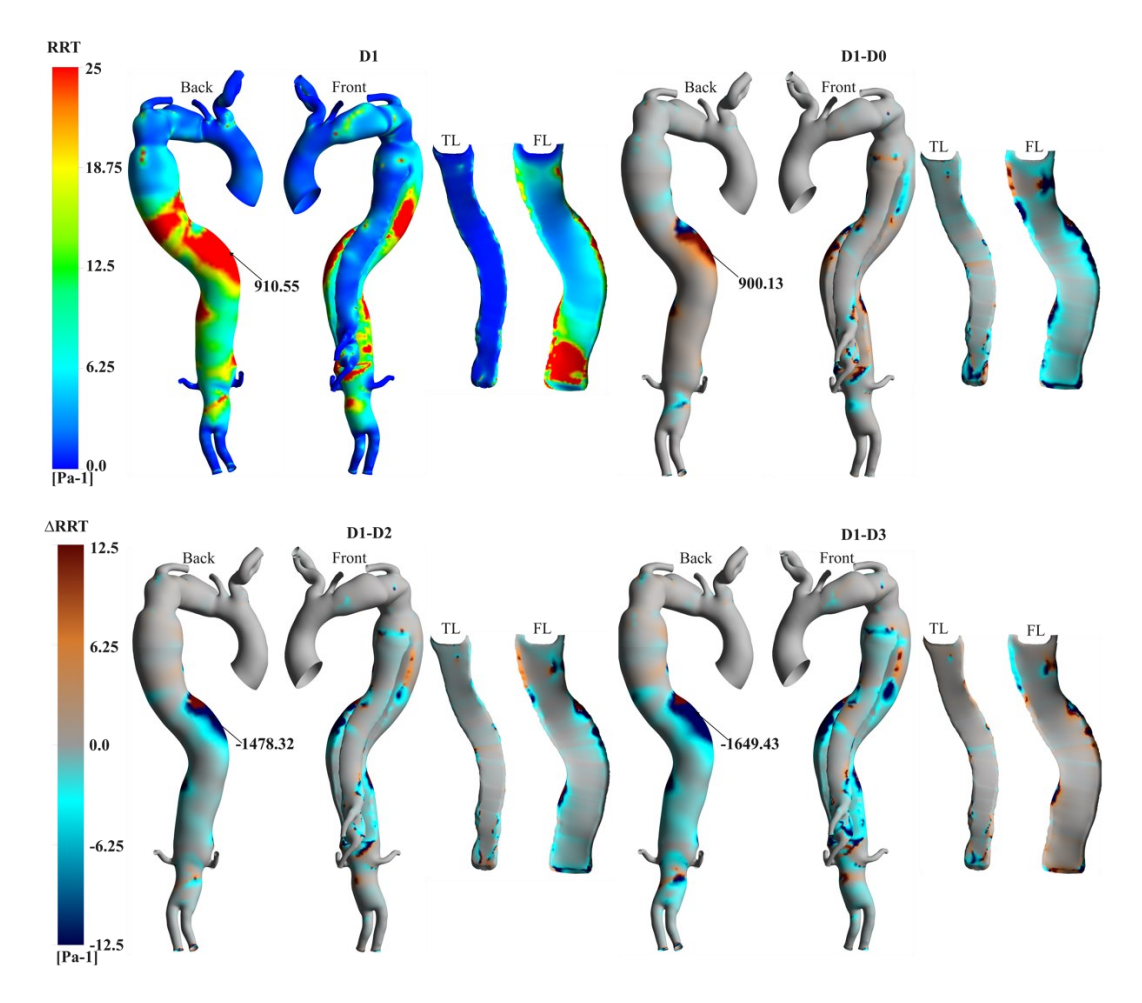


Figure 3. 9. Contours of RRT for D1 and point-wise differences against additional cases.

Relatively low TAWSS and fluctuating OSI lead to high RRT (>25 Pa⁻¹) at both lumina and the VAO in D1 (Figure 3. 9). The highest RRT value observed is 910.55 Pa⁻¹ at the DA. The rigid flap simulation does not capture this localised region of elevated RRT. Conversely, this high RRT region is accentuated in D2 and D3, with the maximum point-wise difference reaching -1649.43 Pa⁻¹ in D3.

3.4. Discussion

This chapter aimed to understand the impact of IF displacement in TBAD haemodynamics by further developing the MBM used in Chapter 2 to account for intimal flap motion. The new approach relies solely on MRI sequences acquired during

a single session, including 4D Flow MRI, cine-MRI, and high-resolution TRUFI, along with brachial pressure measurements as input clinical data.

Quantifying IF mobility, a highly patient-specific variable, has been explored in various studies, revealing its crucial role in influencing malperfusion, haemodynamics, and treatment efficacy throughout different stages of TBAD (Ganten et al., 2009, Karmonik et al., 2012b). IF displacement is typically found to range from 0 to 3mm in chronic cases (Lortz et al., 2019). The patient-specific simulations (D1) revealed detailed insights into the interplay between intimal flap (IF) displacement, transmural pressure (TMP), and associated area changes throughout the cardiac cycle. These findings align with literature observations, demonstrating that these factors are associated with TL compression, FL expansion, and increased risk of rupture (Aghilinejad et al., 2022, Lee et al., 2023). The IF displacement reaches its maximum at peak systole (T1), resulting in TL compression and FL expansion due to high pressure within the FL (Figure 3. 4 and Figure 3. 5). During the deceleration phase, these FL/TL-compression/expansion patterns were inverted as the IF moved back towards its diastolic position, promoting a positive TMP and aligning with the reduction of cross-sectional area at the VAO observable in Appendix B.3 (see Figure IV). Neglecting the motion of IF in numerical simulations of TBAD (D0) results in a lower TMP at every time point in the cardiac cycle. This has clinical implications since it suggests that rigid IF simulations may lead to inaccurate luminal remodelling predictions, as a TMP close to zero is associated with better FL remodelling outcomes (Fatma et al., 2022, Xu et al., 2021a). While the pressure differences are small, they can be attributed to the IF displacement, as both rigid IF (D0) and the patient-specific IF stiffness (D1) share identical boundary conditions, inlet profiles, and geometry, isolating the effect on the compliant IF motion. This highlights the sensitivity of local flow dynamics to small pressure variations driven by the flap mobility. Conversely, simulations assuming a more compliant IF exhibited higher pressures within the FL during peak systole. This facilitated higher cross-sectional area variations, with the most significant expansions noted at the VAO for the D3 case. This suggests that a more mobile IF could contribute to higher TMP, possibly influencing luminal expansion and impacting flow conditions. The TMP trends observed align with previous studies (Figure 3. 4), which proposed a correlation between IF motion and

risk of FL growth (Zhu et al., 2022b, Zimmermann et al., 2023). This highlights the potential of the model to further explore the mechanism of disease progression, particularly for highly mobile IF.

Compliant models, whether experimental or simulation-based, have been shown to more accurately mimic aortic flow compared to 4DMRI, according to recent research (Bäumler et al., 2020, Stokes et al., 2021, Zimmermann et al., 2021). Studies on TBAD showed that 4DMRI provides a good qualitative overview of flow patterns in regions of interest within the aorta. However, 4DMRI fails to accurately quantify flows in low-velocity and highly aneurysmal regions, where a poor signal-to-noise ratio degrades flow measurement quality (Figure 3. 2) (Stemkens et al., 2018, Takehara, 2022). CFD simulations informed by 4DMRI, as in the present study, offer an opportunity for detailed haemodynamics analyses (Armour et al., 2022, Stokes et al., 2023a) even in regions that 4DMRI fails to capture, e.g. low flow velocity regions during diastole and near wall haemodynamics (Figure 3. 2, Figure 3. 7 and Figure 3. 9). Notably, using the 3DIVP at the inlet successfully replicated the velocity magnitude distribution in the AA as seen in the 4DMRI (Figure 3. 2).

In the proximal region to the IF, the patient-specific simulation (D1) exhibited good agreement with 4DMRI during the systolic time points (T0, T1, and T2). Notably, at the PET, DA, and VAO, the simulation accurately captured the high-velocity magnitudes within the TL, which were linked to elevated pressure and IF displacement, as well as the overall luminal velocity magnitude distribution. The accuracy of this simulation is critical as it not only validated the model but also facilitated the evaluation of additional haemodynamics metrics essential for assessing the risk of aortic degeneration.

In contrast, the rigid IF simulation (D0) displayed underpredicted TL and overpredicted FL velocity magnitudes at the PET, DA, and VAO, along with inaccurate flow distributions, particularly during T1 and T2 (Figure 3. 2). These discrepancies were most pronounced in the proximal region of the IF, where limited displacement did not capture well the local haemodynamics. These findings underscore that it is important to incorporate IF movement in these simulations, as this plays an important role when calculating haemodynamic indices that attempt to predict patient-specific outcomes derived from these models.

At the visceral branches, higher flow rate differences were observed with a more mobile IF than *in vivo* measurements, with differences reaching up to 4.5%. This has implications for the potential prediction of malperfusion since a highly mobile IF can alter flow through the visceral branches.

The complex geometry of the aortic arch has been found to induce rotational flow and vortices, potentially contributing to the development of aortic dissection (Marrocco-Trischitta and Sturla, 2022, Sturla et al., 2019). Furthermore, the presence of rotational flow/vortical structures has been recently linked to the remodelling and growth of localised regions in both TBAD and reconstructed TBAD (Guala et al., 2020, Naim et al., 2016, Stokes et al., 2023a), found that vortical structures dominated the FL in a TBAD study. These structures expanded and clustered around the entry tear during systole, causing frequent platelet collisions and likely promoting thrombus formation. Additionally, recent studies demonstrated that the intensity and the topology of helical flow structures can be affected when comparing compliant to rigid wall simulations (Calò et al., 2023, Capellini et al., 2021). In the present study, the vorticity contours at the PET in the patient-specific case (D1) highlighted the presence of counter-rotating vortices, leading to high IRF values (Figure 3. 6) The most complex patterns were observed at peak systole (T1). Such vortical patterns were less evident at the DA and VAO, where a separation between clockwise and anticlockwise vorticity was clear in both lumina. Swirling flows are not well captured when a rigid IF was assumed (D0) in regions where high IF displacements were predicted, for example, at the VAO during systole (T0, T1 and T2). Similar vorticity locations with higher magnitudes were simulated when the IF reached greater displacements in D2 and D3 (Figure 3. 6). At the PET and VAO, swirling patterns differed at peak systole. This local haemodynamics impact the WSS distributions as observed in Figure 3. 7, Figure 3. 8 and Figure 3. 9 (Von Spiczak et al., 2015).

The IRF, which gives a measure of the intensity of the rotation of the flow on a plane, has been proposed as a marker of ascending aorta dilation (Dux-Santoy et al., 2019, Rodríguez-Palomares et al., 2018). Additionally, in TBAD pre- and post-surgery studies, it was also indicated that reduced IRF can be linked to low WSS at the descending aorta, and, hence, the promotion of thrombosis and local growth (Guala et al., 2020, Guala et al., 2019, Gil-Sala et al., 2021, Ruiz-Muñoz et al., 2022, Ruiz-

Muñoz et al., 2024). In line with these findings, the study demonstrated that the patient-specific three-dimensional inlet velocity used as an inlet boundary condition contributed to high circulation intensity at the AA. Moreover, our model provided a finer distinction between the TL and FL compared to the 4DMRI-based studies cited earlier, and the patient-specific simulation (D1) predicted elevated IRF values specifically within the TL at the PET and VAO, coinciding with vortical structures (Table 3. 2). This suggests that under certain flow conditions, high IRF may not be confined to the AA but may also arise along the compressed lumen, in this case the FL, where patient-specific aortic morphology and flow dynamics contribute to increased rotational flow intensity. Conversely, as observed in the literature, IRF was reduced within the FL, potentially indicating an increased risk of local growth (Table 3. 2).

Given the interplay between IF motion, flow dynamics, and pressure variations observed in the literature and this study, it is essential to consider its broader implications on thrombus formation and vessel remodelling. Chong et al., (2022) demonstrated that IF motion significantly influences thrombus formation in TBAD by altering local flow patterns and WSS, which affect platelet aggregation and clot stability. Abnormal aortic haemodynamics have been shown to affect WSS distributions and associated metrics (Osswald et al., 2017). For example, collocation of low TAWSS and high OSI has been linked to aortic growth, thrombosis and high RRT (Figure 3. 7) (Wang et al., 2024, Trenti et al., 2022). Thus, in this study, high OSI values, triggered by the flow circulation close to the visceral branches, and low TAWSS in the distal and narrowed portion of the FL in the patient-specific case (D1) (Figure 3. 8), suggest the likelihood of cell deposition therein. Such conditions were also observed at the DA. More specifically, RRT >900 Pa⁻¹ values were predicted at the DA, coinciding with locations of disturbed and unstable flow and indicating an increased risk of aortic remodelling (Figure 3. 9). Similar observations can be made at the PET, where the high values of TAWSS>5Pa observed, due to a high velocity and chaotic vortical structures, could promote a risk of aneurysmal formation or local wall rupture (Figure 3. 7). In the case of a rigid IF simulation (D0), such observations were not possible close to the SMA, suggesting that accounting for compliant IF simulations may be important for assessing markers related to the risk of aortic wall remodelling in TBAD.

3.5. Limitations

The new MBM formulation employed in this study makes certain simplifications, such as assuming a linear relationship between displacement and force. Due to limitations in the temporal resolution of 4DMRI and cine-MRI, it was not possible to obtain a transient description of the discrete radial and non-elastic behaviour of the aorta. Additionally, since only one plane of cine-MRI captures the displacement of the IF, a constant stiffness had to be applied across the entire IF. Although the wall and IF displacement measurements taken from the cine-MRI fall within the resolution error margin of the imaging technique, the simulation results remained consistent with these measurements, demonstrating the accuracy of the model.

The method assumes that each pair of IF patches share the same normal, whereas a more granular approach would consider pairs of nearest neighbouring nodes individually. This would result in a very high number of node pairs, on the order of the mesh elements along the IF, significantly increasing the complexity of the model, and ultimately making it computationally expensive. However, the current accuracy of the method in simulating the in vivo target IF displacement at the VAO in the patient-specific simulation (D1) demonstrates that it offers a balance between accuracy and computational feasibility. While future research will aim to incorporate higher-resolution in vivo data for a broader patient cohort, the findings from this study remain valuable for understanding the haemodynamics effects of IF mobility in similar cases.

3.6. Conclusions

This chapter presented significant advancements in simulating the impact of IF displacement on TBAD haemodynamics. Through the development of an enhanced MBM, the study was able to capture the dynamics of aortic wall displacement,

including the motion of the intimal flap, using patient-specific 4DMRI data. The new formulation of the MBM ensured that the displacement of both the exterior wall of the aorta and the thick intimal flap was accounted for in the simulations, providing more accurate and representative results than previous models that assumed a rigid IF. The IF was divided into segments along its curvature, each pair of patches from the TL and FL sections was synchronised to ensure realistic displacement during the cardiac cycle. This technique proved essential in capturing the nuanced flow dynamics and pressure variations that arise due to IF motion.

By accurately simulating patient-specific IF displacement, the simulations revealed that increased IF mobility exacerbates TMP and promotes chaotic and disorganised flow conditions, potentially leading to luminal expansion, thrombus formation, and aortic rupture.

The findings also highlighted notable differences in simulation results and derived markers when comparing a patient-specific compliant IF model to a rigid IF model. Specifically, differences in vorticity distribution, IRF, TAWSS, and RRT were co-located, factors that have been associated with adverse aortic remodelling risks such as aneurysmal growth, tear expansion, or rupture. This underscores the importance of compliant IF models, while it remains uncertain to what extent rigid models may misguide predictive assessments.

Clinically, these insights may guide more effective intervention strategies, including tailored surgical planning to mitigate the adverse effects of a mobile IF and evaluate whether a conservative approach might lead to optimal outcomes in the natural resolution of TBAD. Future work should focus on acquiring higher-resolution *in vivo* data to further refine these models and enhance their clinical relevance.

In conclusion, the incorporation of patient-specific, compliant models that account for the motion of the intimal flap has significantly enhanced the accuracy of haemodynamics simulations in TBAD. However, to refine post-surgical assessments, further improvement is needed to more precisely capture aortic mechanics beyond intimal flap motion alone. The next chapter builds upon these advancements by incorporating regional pulse wave velocity, offering a more comprehensive framework for simulating aortic distensibility post-TEVAR. By integrating RPWV into patient-

specific models, Chapter 4 aims to refine the understanding of aortic stiffness and its influence on the haemodynamics of the repaired aorta.

Chapter 4

A patient-specific compliant simulation framework informed by 4DMRI-extracted Pulse Wave Velocity: Application post-TEVAR

4.1. Introduction

Aortic stiffening is commonly found in elderly patients as part of aortic ageing, as well as in diseased aortas and following surgery. Aortic ageing can be attributed to the breakdown of elastin, a protein that provides elasticity, and an increase in collagen, which makes the arteries more rigid (Cavalcante et al., 2011). Calcification, i.e. the buildup of calcium deposits, and plaque from atherosclerosis also contributes to ageing. Ageing affects the endothelial cells lining the arteries, reducing their ability to relax, while chronic inflammation and oxidative stress damage the arterial walls. In diseased aortas, such as those affected by type B aortic dissection (TBAD), rigidification occurs due to the septum and false lumen remodeling in the chronic phase (Papakonstantinou et al., 2022, Schepens, 2018). The increased mechanical stress on the aortic wall and altered haemodynamics promote further damage and stiffening. Additionally, the underlying conditions that predispose individuals to aortic dissection, such as hypertension and atherosclerosis, contribute to the rigidity of the aorta. In TBAD surgery, either a thoracic endovascular aortic repair (TEVAR) or opensurgery (OS), the device implanted introduces a compliance mismatch with the native proximal vessel and leads to a ortic stiffening (Hori et al., 2020, Spadaccio et al., 2016).

Elevated pulse wave velocity (PWV) is a clinically used marker which is associated with aortic stiffening and TEVAR (De Beaufort et al., 2017, Hori et al., 2020). Increased PWV has been linked with cardiovascular outcomes such as stroke and left ventricular hypertrophy (Valencia-Hernández et al., 2022). PWV can be determined through 2D flow MRI or cine-MRI by assessing the pulse wave travel time along the aortic centreline or the distensibility by measuring the cross-sectional variations of the vessel throughout the cardiac cycle (Wentland et al., 2014). The regional PWV (RPWV) can also be measured using 4D Flow MRI (4DMRI), providing local stiffness information along the vessel (Wentland et al., 2014, Nguyen et al., 2023). Estimation of RPWV is important in the context of TEVAR due to the proximal aortic stiffening after endograft placement (Bissacco et al., 2022).

4DMRI allows the assessment of various functional parameters, such as blood flow dynamics, which are not routinely measured in the clinical assessment of TEVAR (Cosset et al., 2022, Takahashi et al., 2022). However, its low spatial resolution limits the quantification of pressure and wall shear stress (WSS) in abnormal regions (Lamata et al., 2014, Markl et al., 2011b). Computational fluid dynamics (CFD) simulations can be fused with 4DMRI to calculate these haemodynamics variables accurately (Armour et al., 2022, Black et al., 2023), enhancing the quality of clinical information for decision-making.

In this chapter³, a 4DMRI-informed computational method based on the moving boundary methods (MBM), as described in previous chapters, is developed. This method uses 4DMRI and non-invasive pressure measurements to inform patient-specific, compliant CFD simulations of TBAD post-TEVAR. Specifically, RPWVs, a routinely used clinical marker, are extracted from 4DMRI using a cross-correlation method to iteratively tune the aortic stiffness in the simulations, ensuring that it captures the propagation of the pressure wave inside the vessel.

Compared to a simulation informed by area-based distensibility, the RPWV-based simulation results in significant improvements in both computational efficiency

³ This work has been published in the Journal of Biomechanics in 2024 (Girardin et al., 2024b). Please refer to Research Declaration Form C for details.

and predictive accuracy. The RPWV-based simulation not only outperforms the area-based method in terms of accuracy but also minimises discrepancies in key haemodynamics indices, such as systolic and diastolic pressures, velocity magnitudes, rotational flow metrics, and WSS-driven metrics. By adjusting stiffness to match RPWV measurements, the simulation framework enhances the prediction of these indices, providing a more reliable tool for assessing the post-surgical condition of patients with TBAD.

4.2. Methods

4.2.1. Data Acquisition

A patient with chronic TBAD previously treated with TEVAR was presented for follow-up at Inselspital Bern. Their aorta was imaged following an ethically approved protocol (Local Institutional Review Board ID 2019-00556). MRI sequences of the thoracic aorta down to the abdominal aorta were acquired using a MAGNETOM Sola fit scanner (Siemens Healthineers). 4DMRI was acquired with a resolution of 2.5 mm*2.5 mm*2.5 mm. A T2/T1 weighted TRUFI MRI sequence was acquired with a 1 mm*1 mm* 1 mm resolution. Brachial pressures were also acquired before the scanning.

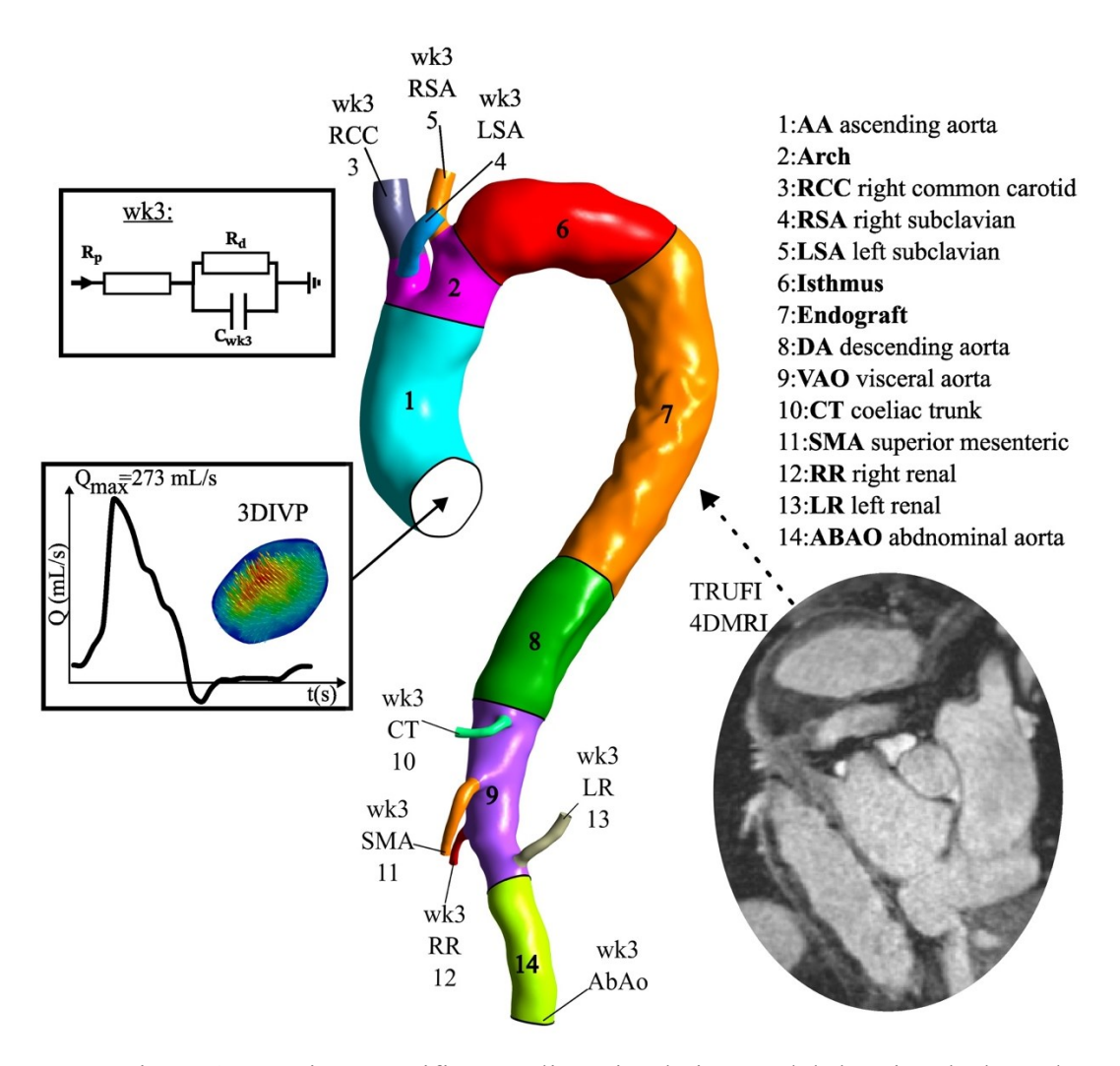


Figure 4. 1. Patient-specific compliant simulation model showing the boundary conditions used at the inlet and outlets.

4.2.2.Geometry and Mesh

The aorta was segmented from the T2/T1 TRUFI using ScanIP (Synopsis Simpleware, USA) as in previous chapters. The combined geometry was smoothed using MeshMixer (Autodesk, USA). Inlet and outlets were trimmed perpendicularly to their cross-sectional area using Fluent Mesh (Ansys Fluent, USA) (Figure 4. 1). To facilitate the implementation of the MBM, the geometry was divided into discrete regions along the aortic centerline based on anatomical landmarks and stiffness characteristics (Figure 4. 1). The segmentation followed major regions of the aorta, including ascending aorta (AA), arch, right common carotid (RCC), right subclavian

(RSA), left subclavian (LSA), isthmus, proximal and distal ends of the endograft, descending aorta (DA), visceral aorta (VAO), coeliac trunk (CTA), superior mesenteric (SMA), right renal (RR), left renal (LR) and abdominal aorta (ABAO), ensuring physiological relevance. Additionally, variations in the mechanical properties of the aortic wall were identified using wall displacement features observed in 4DMRI. These variations helped define regions with distinct elastic behaviours such as the ends of the endograft.

A mesh with tetrahedral elements was generated using the methods outlined in Chapter 2. Similarly to Chapter 3, ten prism layers were incorporated to accurately capture the turbulent boundary layer, with the initial layer thickness adjusted to achieve a y+ value of approximately 1. The mesh consisted of elements ranging in size from 0.5 mm to 1.5 mm, resulting in a total of 1.7 million elements. This medium-density mesh, used for the simulations in this study, was evaluated through a mesh sensitivity analysis. A similar process to that described in Chapter 2 and Chapter 3 was followed, with further details provided in Appendix C.1.

4.2.3. Wall Compliance

The MBM described in section 2.2.5 was used to simulate the compliant behaviour of the aorta. The stiffness K_i was calculated using equation 2. 13. The distensibility, D_k , was evaluated using two different methods, an area-based and an RPWV-based one.

The area-based distensibility $D_{k,ab}$ was calculated as described in equation 2. 9 for each segment k depicted in Figure 4. 1. The stiffness obtained from the area-based distensibility was used in the simulation case denoted S1 (Figure 4. 3).

The distensibility was also estimated from the RPWV using the empirical relationship (Reymond et al., 2009):

$$D_{k,RPWV} = \rho^{-1}RPWV_k^{-2}$$
 4. 1

where ρ is the density of blood (kg/m³). RPWVs were estimated from the 4DMRI velocity data within each segment k depicted by the red lines in Figure 4. 2A using a cross-correlation method (Markl et al., 2010, Fielden et al., 2008), as illustrated in Figure 4. 2B. The segments were chosen to be representative of the major aortic

landmarks and were the following: AA-Arch-Isthmus-Endograft-DA-VAO and ABAO. However, 4DMRI resolution limited measurements in the aortic branches and hence the $D_{k,RPWV}$ values of the proximal segment to each branch were assigned therein.

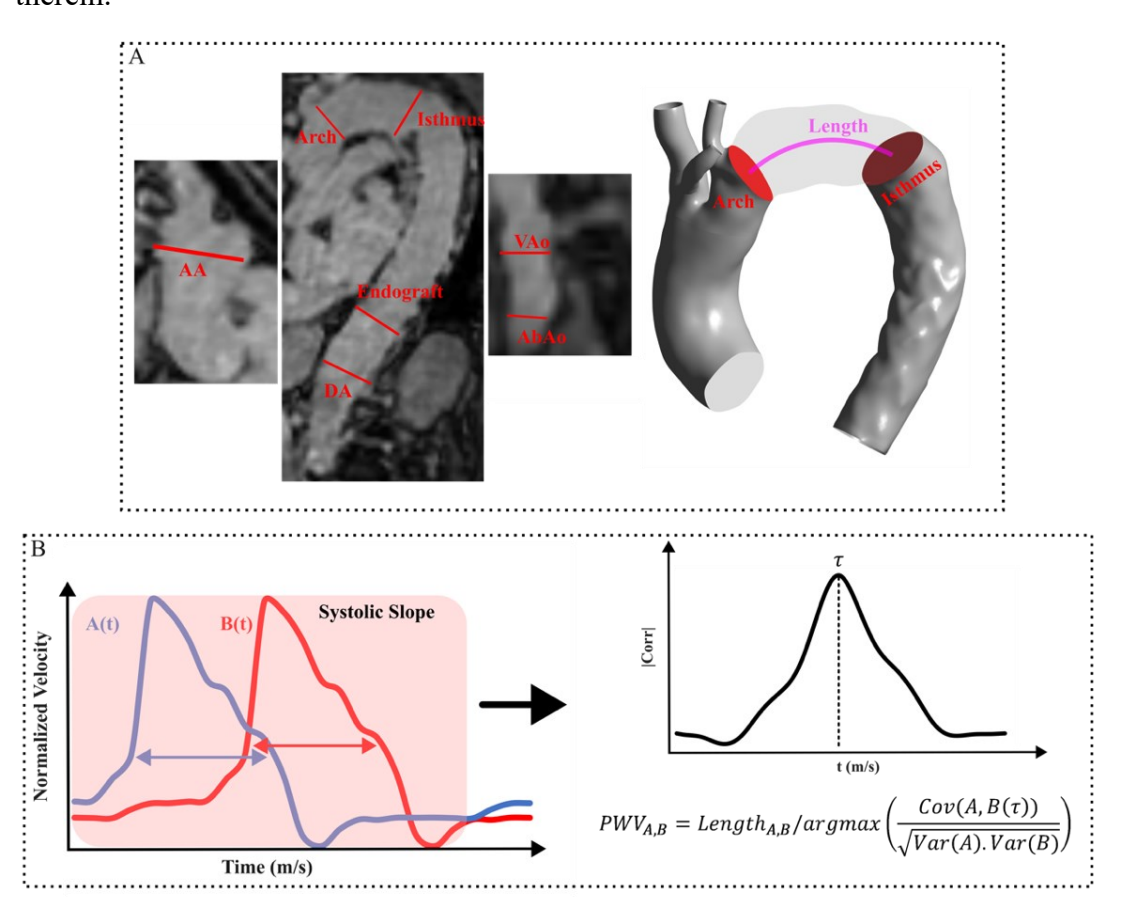


Figure 4. 2. (A).- Red lines depict the 4DMRI planes on which the flow rates were measured. (B) schematic of the cross-correlation method used to calculate the PWV between planes A and B (Markl et al., 2010, Fielden et al., 2008).

In the endograft region, this method yielded a distensibility of $1.6*10^{-3}$ mmHg⁻¹, which is an order of magnitude higher than reported values in the literature (Johnston et al., 2010, Rovas et al., 2023, Tremblay et al., 2009). The area near the endograft is typically subject to measurement noise, and hence a literature-based distensibility value of $1.6*10^{-4}$ mmHg⁻¹ was employed in the calculation of stiffness in this region.

An automatic iterative method was developed to tune the stiffness field to match the 4DMRI-derived RPWVs. The calibration process involved the following

two steps: **1.** An initial stiffness calculation using equations 2. 13 and 4. 1 on the distensibility derived from 4DMRI data. **2.** An iterative tuning method for the stiffness, K_n , was implemented using MATLAB to call CFX (Ansys Inc., USA). In each iteration, the simulation script is updated with new stiffness values $K_{n,new}(N/m^3)$. This includes running a systolic phase simulation to avoid wave reflections during diastole and to reduce computational time. At the end of each run, the flow rates from planes enclosing regions of interest are extracted, and the RPWVs are calculated (Figure 4. 2B). The distensibility of each region k is updated such as:

$$D_{k,RPWV}^{i} = D_{k,RPWV}^{i-1} * \frac{TD_{4DMRI}}{TD^{i-1}}$$
 4. 2

where TD_{4DMRI} is the time delay (s) measured from the 4DMRI data and TD^{i-1} (s) is the time delay measured at the *i-1* CFD simulation. Finally, the new stiffness values are updated in each iteration, such as:

$$K_{n,new} = \frac{2}{D_{k,RPWV}^i} \sqrt{\frac{\pi}{A_k^0}}$$
 4. 3

The process was run until the time delay error was lower than 10%. Seven iterations were required, each taking 3 hours in an 8 Intel Core i9-11900K. The final stiffness map was inputted to the final simulation denoted S2 (Fig. 3). An algorithm was used to smooth the stiffness between the different regions, as can be observed in Figure 4. 3. S1 and S2 are the final simulations, which are run and post-processed.

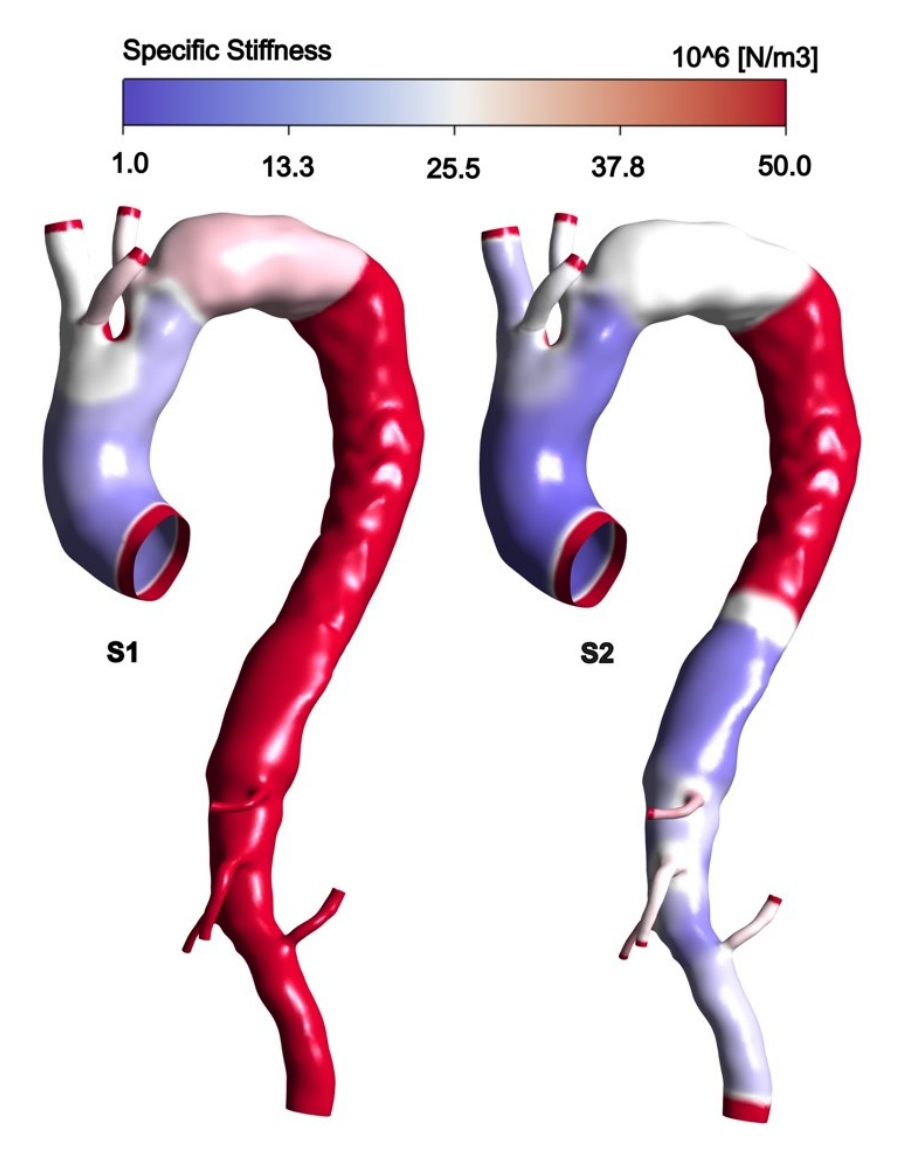


Figure 4. 3. Stiffness maps derived from area- and RPWV-based distensibility to compare S1 and S2, using a logarithmic scale in both the colour bar and the contours to highlight differences in stiffness across regions introduced by the RPWV-based stiffness tuning.

4.2.4.Boundary Conditions

A 3D inlet velocity profile (3DIVP) (Figure 4. 1) and outlet mean flow rates, extracted from the 4DMR data using GTFlow (GyroTools LLC, Switzerland) (Table 4. 1), were employed as in Chapter 3. The cardiac cycle period was 0.93 s; the stroke volume was 53.2 mL. The 3DIVP was spline-interpolated to apply a 1ms CFD timestep using MATLAB (MathWorks Inc., USA).

Table 4. 1. Target mean flow rates at outflow boundaries and inlet systolic and diastolic pressures against CFD values.

	Flow rate [mL/s]						Pressure [mmHg]			
	RCC	RSA	LCC	CT	SMA	LR	RR	AbAo	Systole	Diastole
Target	18.88	7.41	8.12	3.13	8.25	1.87	1.50	14.70	101.8	70
S1	18.98	7.38	8.09	3.17	8.21	1.89	1.50	14.63	100.36	68.4
S2	18.75	7.35	8.15	3.12	8.33	1.84	1.53	14.75	102.5	70.5

A 0D lumped parameter model of the vasculature (20-sim, Controllab Products, Netherlands) was used to calibrate three-element Windkessel (WK3) parameters, used as pressure boundary conditions at the outlets of the domain, as described in Chapters 2 and 3 and previous works (Stokes et al., 2023b, Westerhof et al., 2009). Parameter values are listed in Appendix C.2. The boundary conditions were used both to tune the RPWVs described in the prior section and to run the final simulation cases S1 and S2.

4.2.5.CFD Simulation

The simulation settings used in this chapter were identical to those in Chapter 3. The k- ω shear stress transport model was employed as the peak and critical Reynolds numbers were 6855 and 6000, indicating the transition to turbulence (see Section 1.6.7 for details on turbulence model).

4.2.6. Haemodynamics Analysis

The time average wall shear stress (TAWSS), the oscillatory shear index (OSI) and the endothelial activation potential (ECAP) previously described in Chapter 1 and Chapter 2 were computed (see equations 1. 1, 1. 2 and 1. 4).

To assess the extent of rotation present in the flow, the in-plane rotational flow (IRF) metric, was utilised similarly to Chapter 3 and computed using equation 3. 5.

IRF was computed both area- (S1) and RPWV-based (S2) distensibility simulations, on each plane delimiting regions of interest (Figure 4. 1) at peak systole.

Additionally, the systolic flow reversal ratio (SFRR) was also quantified to measure the amount of retrograde flow at the interface between the regions of interest (Figure 4. 1). Increased SFRR may contribute to asymmetric increases and directional variations in wall shear stress, potentially playing a role in aortic dilation (Rodríguez-Palomares et al., 2018). SFRR was calculated as the ratio of total systolic backward flow volume to total systolic forward flow volume, expressed as a percentage:

$$SFRR = \frac{\int_0^{Tsystole} v_{SBF}(t)dt}{\int_0^{Tsystole} v_{SFF}(t)dt}.100$$
4. 4

4.3. Results

4.3.1. Validation

Mean flow rates and diastolic and systolic pressures are compared against target values in Table 4. 1. In both area- (S1) and RPWV-based (S2) distensibility simulations, inlet pressures and outlet mean flow rates are predicted within 2.3% of differences.

The simulated RPWVs are compared against the 4DMRI ones in the regions of interest (Figure 4. 4). The results indicate that in the RPWVs-based distensibility simulation (S2), a maximum difference of 8% is observed in the arch and DA regions, excluding the endograft; this corresponds to a 1 ms difference in travel time. These findings suggest that the tuning process effectively minimises differences in pulse wave travel time predictions throughout the aorta. In contrast, the area-based distensibility simulation (S1) shows substantial discrepancies, with predicted PWV values exceeding 20 m/s higher than the 4DMRI measurements. These significant differences arise from the high stiffness assigned by the area-based distensibility calculations, particularly between the isthmus and the ABAO, where the discrepancies are most pronounced (Figure 4. 3).

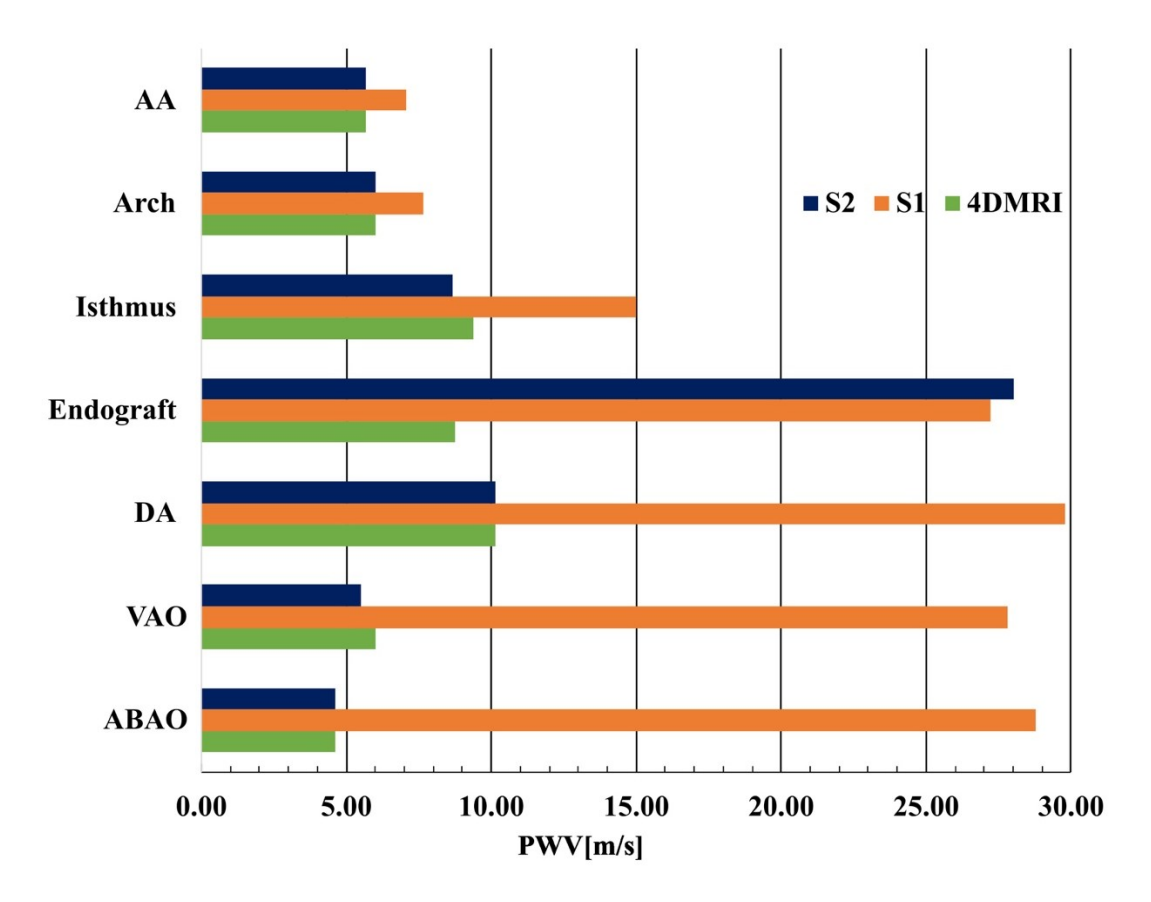


Figure 4. 4. Comparison of predicted RPWVs, S1 (orange) and RPWV-based S2 (green), against 4DMRI extracted (blue).

4.3.2.Flow Characteristics

Figure 4. 5 compares velocity magnitude contours obtained from two simulation approaches, the area- (S1) and RPWVs-based (S2) distensibility, against *in vivo* 4DMRI data at three selected cross-sectional planes (i, ii, iii) along the aortic geometry. The velocity distributions are presented at four key time steps in the cardiac cycle: T0 (mid-acceleration), T1 (peak systole), T2 (mid-deceleration), and T3 (end diastole).

In the RPWVs-based simulation (S2), at the AA (Figure 4. 5i), the tuned stiffness and 3DIVP allow a good qualitative agreement with the 4DMRI. Especially at T0 and T1, where the peak velocity magnitude values and distributions are well predicted. At T2, the high-velocity magnitudes observed in the bottom-left quadrant of the plane are not well-captured compared to the *in vivo* 4DMRI data. At the end of

diastole (T3), the comparison becomes less evident due to the overall reduction in blood velocity at this phase of the cardiac cycle. Similarly to what was observed in Chapter 3, low blood velocity leads to a weaker flow signal, which, combined with the inherent limitations of 4DMRI, results in a low signal-to-noise ratio (SNR). Such an observation is made on the two additional planes (Figure 4. 5ii, iii). In this study, the downstream part of the VAO has a maximum of 8 pixels in the diameter length of the cross-sectional area, making it highly prone to low SNR.

At the plane located proximally to the isthmus and endograft connection (Figure 4. 5ii), similar observations are made to those at the AA. The velocity magnitude distribution and values are well predicted in the RPWVs-based case (S2) at T0 and T2. However, at peak systole (T1), the simulation does not accurately replicate the velocity magnitude distribution. In the in vivo 4DMRI, high-velocity values are located in the bottom quadrants of the plane, whereas this pattern is not well reproduced in S2 (Figure 4. 5ii).

Similarly, at the downstream plane (Figure 4.5iii), the RPWVs-based simulation (S2) accurately predicts the velocity magnitude during the three systolic time points (T0, T1, and T2).

In contrast, in the area-based simulation (S1), discrepancies in velocity magnitude values and distributions are observed compared to the in vivo 4DMRI. At the AA (Figure 4. 5i), velocity magnitudes are overpredicted at T0, and distributions differ significantly from 4DMRI at T2. Proximal to the isthmus (Figure 4. 5ii), similar distribution patterns to the RPWVs-based simulation are observed; however, velocity values are underpredicted compared to the 4DMRI. Finally, at the downstream VAO (Figure 4. 5iii), the results from the area-based simulation (S1) are qualitatively similar to those of the RPWVs-based simulation (S2).

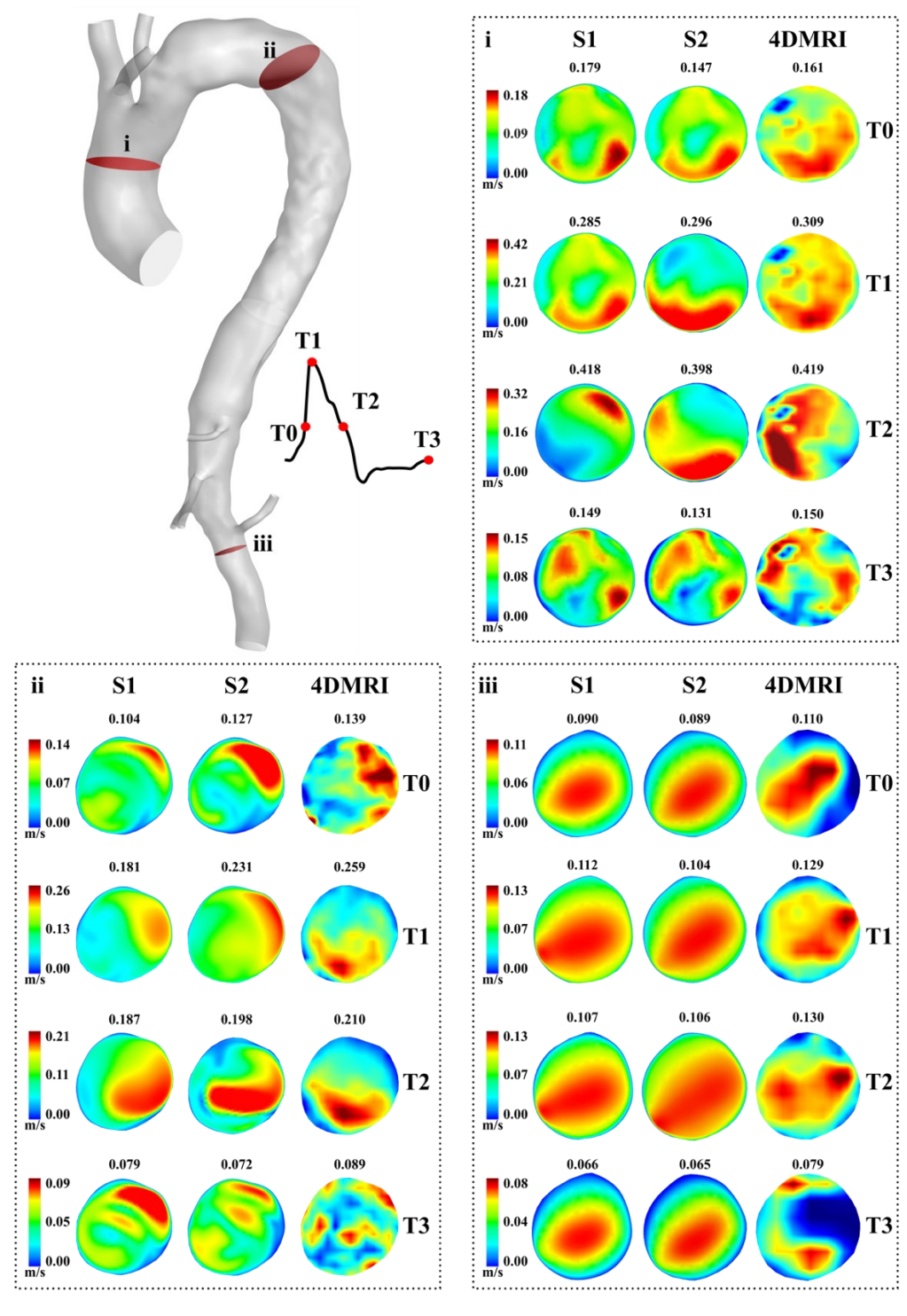


Figure 4. 5. Contours of velocity magnitude at different flow phases for the 4DMRI, the area- (S1) and RPWVs-based (S2) simulations at the AA (i), endograft (ii) and VAO (iii) at T0 (mid-acceleration), T1 (peak systole), T2 (mid-deceleration), and T3 (end diastole). The value on top of each contour is the maximum velocity magnitude.

Figure 4. 6 presents a comparison of SFRR values obtained from in vivo 4DMRI measurements and area-based distensibility (S1) and RPWVs-based distensibility (S2) approaches. The SFRR is evaluated at the planes separating the aortic regions, as illustrated in Figure 4. 1. Each plane represents the interface between two adjacent regions, with the ascending aorta (AA) corresponding to the boundary between region 1 and region 2.

4DMRI-estimated SFRR values exceed 30% in the AA region (Figure 4. 6), which can be attributed to the circulating flow pattern at the inlet. The elevated SFRR suggests significant flow reversal due to recirculation near the aortic root. The stenosis at the aortic arch causes upstream flow acceleration, recirculation, and pressure build-up before the constriction, leading to nearly half of the flow moving backwards during systole. This effect is reflected in the high SFRR values at the arch. The compliance mismatch between the proximal aorta and the endograft is known to produce pronounced flow disturbances and higher SFRR values (Sultan et al., 2021). In this study, an SFRR >30% is found at the interface between the isthmus and the DA) with the endograft, consistent with previously reported values. Downstream of the endograft, where the compliance mismatch is reduced and the aortic geometry becomes more tubular and straighter, the SFRR decreases progressively, reaching 18% at the VAO and 14% at the ABAO.

While the RPWVs-based (S2) simulation differs from 4DMRI measurements, predictions at all plane locations remain consistently closer to the 4DMRI values compared to the area-based distensibility (S1) approach (Figure 4. 6). This is particularly evident from the isthmus and further downstream, where high discrepancies in flow reversal predictions are observed. Overall, the stiffness tuning applied in the RPWVs-based (S2) simulation improved the ability to capture SFRR patterns, particularly downstream of the isthmus, where the area-based (S1) approach assigned high stiffness values, leading to an inaccurate representation of flow reversal.

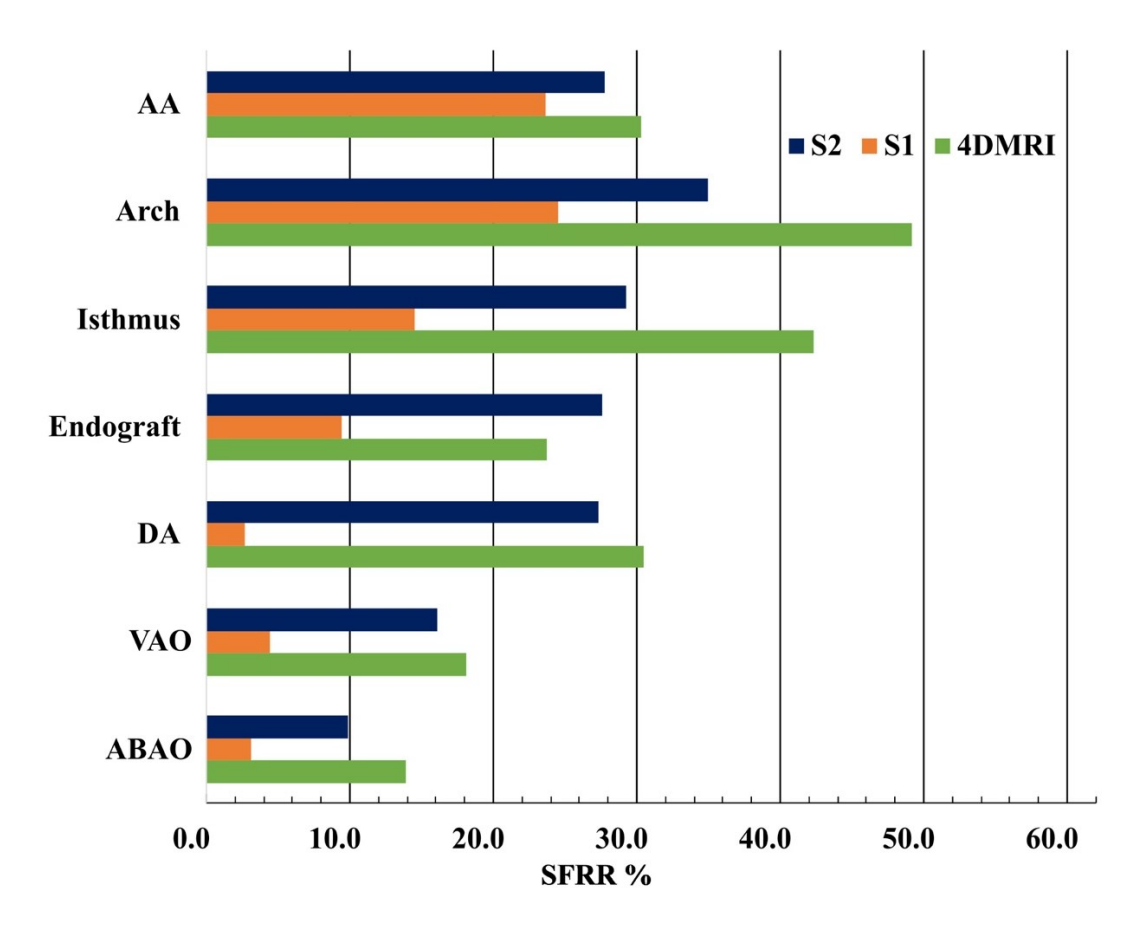


Figure 4. 6. Comparison between 4DMRI (blue) measured and predicted, area-(S1, orange) and RPWVs-based (S2, green) simulations SFRR values along the aortic domain.

Figure 4. 7 presents a bar chart comparing IRF measured at planes delimiting regions of interest between two simulation approaches: area-based (S1, orange) and RPWVs-based (S2, blue). Due to spatial resolution limitations in this study, IRF could not be accurately estimated from the 4DMRI, which might have led to errors in the velocity gradient determination and vorticity.

Similarly to the SFRR trends discussed above, the area-based simulation (S1) consistently overestimates IRF compared to the RPWVs-based simulation (S2) (blue). Particularly, in regions where significant stiffness differences exist between the two simulation methods, i.e., for the isthmus and downwards to the ABAO, differences exceeding 10% are simulated (Figure 4. 7).

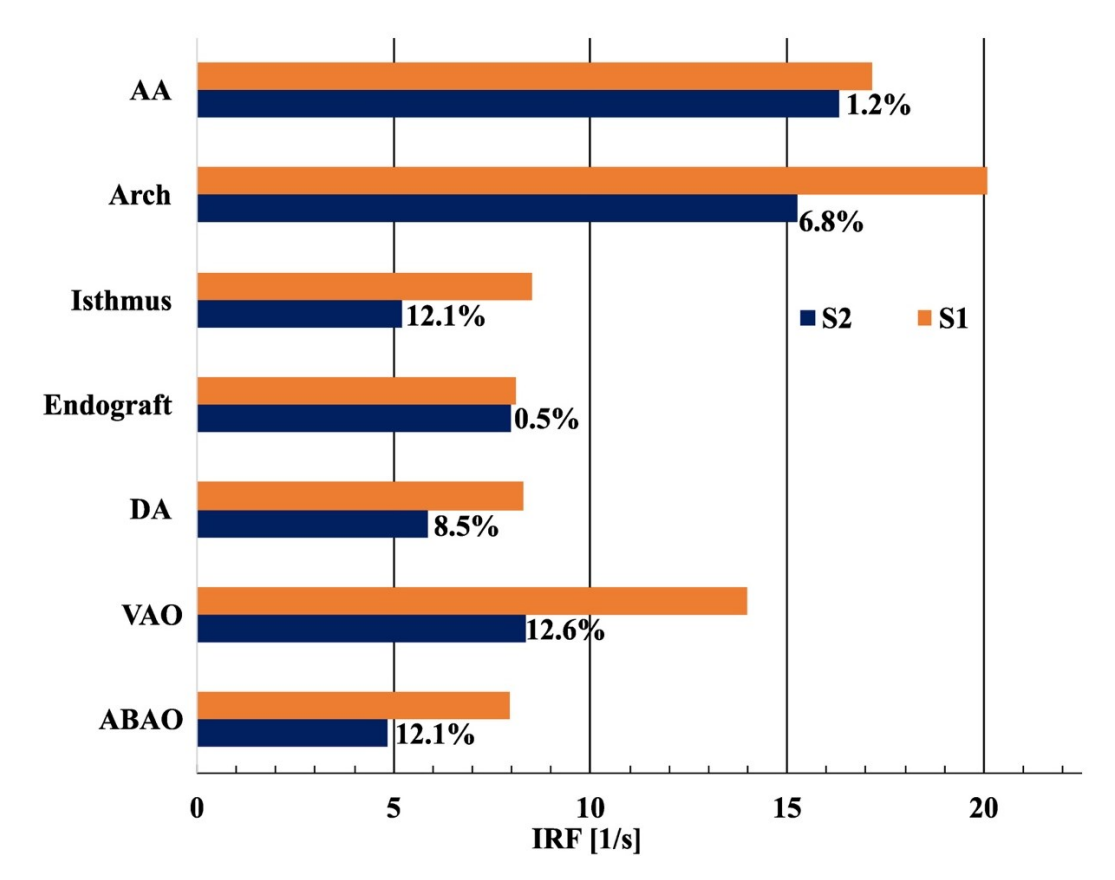


Figure 4. 7. IRF for the area- (S1, blue) and RPWVs-based (S2, orange) simulations with the difference between the two cases reported next to the bar, such as $\Delta\% = \frac{|\mathit{IRF}_{S2} - \mathit{IRF}_{S1}|}{\frac{|\mathit{IRF}_{S2} + \mathit{IRF}_{S1}|}{2}} * 100 \ .$

4.3.3. Wall Shear Stress Indices

Figure 4. 8 presents contours of the aorta, coloured according to TAWSS, OSI, and ECAP, for both the area-based (S1) and RPWVs-based (S2) simulations. Additionally, on the right side of the figure, an extra contour is shown, highlighting the point-wise difference between S1 and S2.

Table 4. 2 presents the minimum, maximum, and mean values of each WSS-driven metric shown in Figure 4. 8 or the regions of interest. Furthermore, the mean percentage difference between the two simulations is computed, such as $\Delta\% = \frac{|\text{metric}_{S2}\text{-metric}_{S1}|}{\frac{\text{metric}_{S2}\text{+metric}_{S1}|}{\text{metric}_{S2}\text{+metric}_{S1}}} *100.$

High TAWSS is found in regions where high velocities occur (Figure 4. 8), as seen in previous chapters (Figure 2. 8, Figure 2. 9 and Figure 3. 7). In the RPWVs-based (S2) simulation, the highest TAWSS values are observed in the AA, arch, and particularly in the VAO, where it reaches 13.35 Pa. While the overall TAWSS distributions are comparable between the two simulations (S1, S2), notable differences emerge in regions where both high velocities and stiffness variations are present, such as the AA, arch, and isthmus. Specifically, the area-based (S1) simulation predicts higher TAWSS values in the AA, whereas, at the arch, S1 underpredicts TAWSS compared to the RPWVs-based (S2) simulation, as highlighted by the dotted circle in Figure 4. 8.

The OSI distribution in the RPWVs-based (S2) simulation reveals highly disorganised flow throughout most of the aortic geometry, particularly proximal to the endograft and in the DA, where compliance mismatches occur due to differences in regional stiffness Figure 4. 8. The point-wise difference between the two simulations highlights these broad discrepancies, with specific locations of variation marked by dotted circles at the arch, isthmus, and areas proximal to the visceral branches. The minimum and maximum OSI differences are observed at the VAO (-0.22 to 0.24), while the isthmus shows a minimum difference of 0.24. Downstream of the arch, the OSI mean differences between S2 and S1 range between 4.7% and 8.9%, reflecting substantially different flow conditions predicted by the two models (Table 4. 2).

The ECAP contour identifies multiple regions exceeding the critical threshold of 1.4 Pa⁻¹ (Di Achille et al., 2014) indicating a potential risk for endothelial cell deposition. Specifically, at-risk locations are found at the isthmus, the endograft struts, the DA, and areas proximal to the visceral branches. While qualitative similarities exist between the ECAP distributions in S1 and S2, significant differences are observed in the sinotubular junction, isthmus, and ABAO regions characterised by stiffness variations Figure 4. 8. Additionally, the location of overestimated TAWSS and OSI in the area-based (S1) simulation also corresponds to an overprediction of ECAP, suggesting a greater risk of endothelial cell deposition. Conversely, S1 underpredicts ECAP values at the isthmus and DA, where a maximum difference of 1.71 Pa⁻¹ is reported (Figure 4. 8). These findings are further supported by mean

regional percentage differences computed in Table 4. 2, which indicate discrepancies exceeding 5% at the isthmus, endograft, and DA.

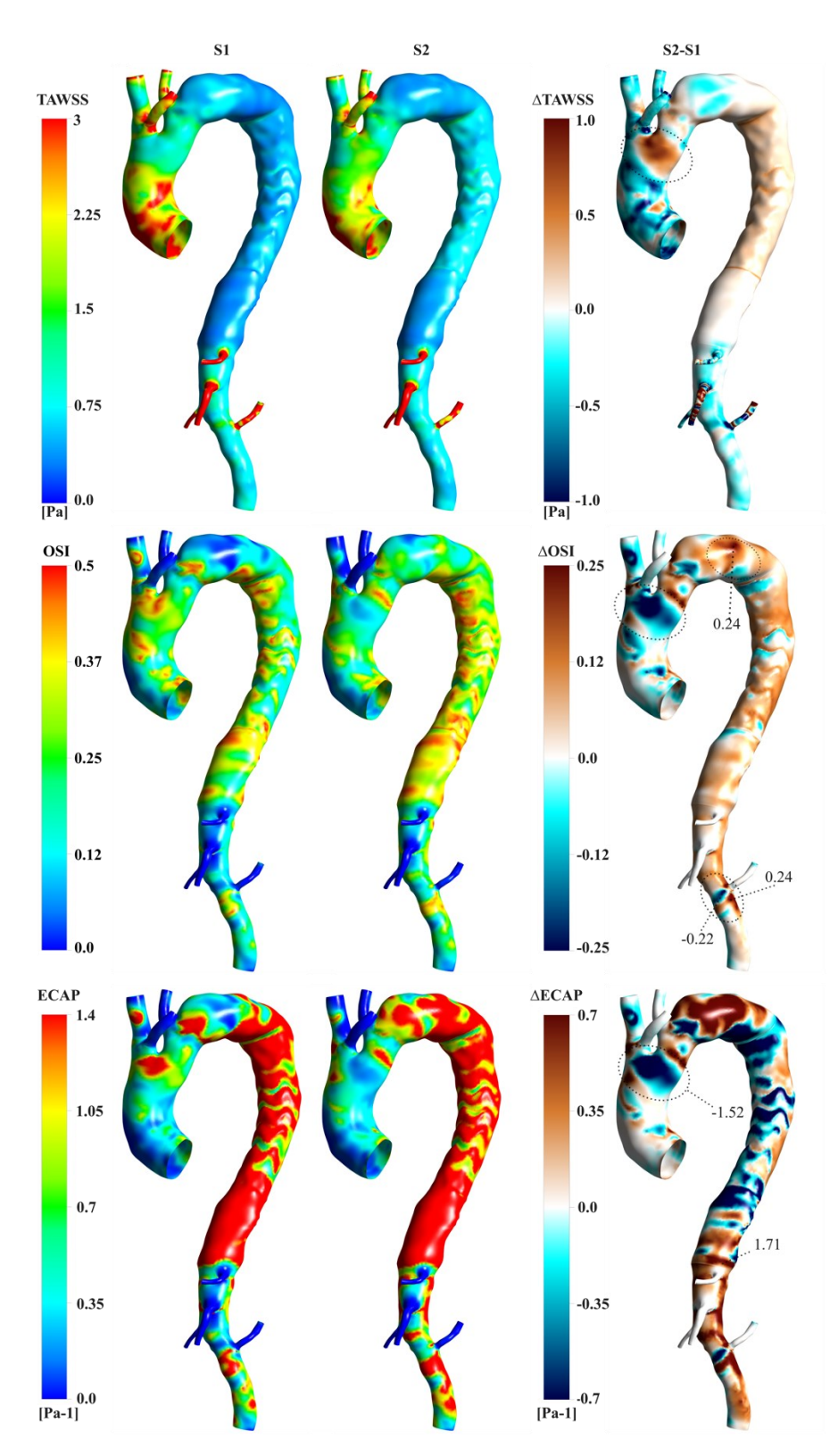


Figure 4. 8. Contours of TAWSS, OSI, RRT and ECAP for S1 (left) and S2 (centre) and point-wise differences such as S1-S2 (right). Values on regions discussed in the core text are reported with dotted circles and lines.

Table 4. 2. Minimum, maximum and mean values per region for S2. Also shown are percentage differences ($\Delta\%$) values such as $\Delta\% = \frac{|\text{metric}_{S2}\text{-metric}_{S1}|}{\frac{|\text{metric}_{S2}\text{+metric}_{S1}|}{2}}*100$.

	ı	TAWSS	OSI	ECAP
) f'	[Pa]	- 0.01	[Pa-1]
	Min	0.26	0.01	0.00
1:AA	Max	1.83	0.49	1.68
	Mean	1.74	0.17	0.31
	$\Delta\%$	0.3%	0.4%	1.3%
	Min	0.18	0.00	0.00
2:Arch	Max	2.14	0.49	2.01
2.AICII	Mean	0.62	0.19	0.44
	$\Delta\%$	3.5%	3.7%	-3.0%
	Min	0.07	0.04	0.18
6.Iathmus	Max	1.29	0.49	5.18
6:Isthmus	Mean	0.25	0.28	1.88
	$\Delta\%$	11.0%	8.9%	5.4%
7:Endograft	Min	0.07	0.15	0.31
	Max	0.70	0.50	4.24
	Mean	0.26	0.34	1.40
	$\Delta\%$	16.0%	8.1%	5.0%
	Min	0.08	0.04	0.07
8:DA	Max	0.50	0.50	5.13
ð:DA	Mean	0.17	0.37	2.35
	$\Delta\%$	2.3%	7.2%	6.2%
	Min	0.09	0.00	0.00
0.374.0	Max	13.35	0.49	3.77
9:VAO	Mean	0.56	0.14	0.65
	$\Delta\%$	0.3%	6.4%	1.3%
	Min	0.12	0.01	0.04
14:ABAO	Max	0.43	0.47	3.05
14:ABAU	Mean	0.23	0.21	0.96
	$\Delta\%$	6.6%	4.7%	3.4%

4.4. Discussion

A novel simulation framework was developed, driven entirely by a single image modality, 4DMRI, and informed by routinely used PWV measurements. The computational framework was applied to a patient-specific, compliant CFD simulation of TBAD after TEVAR. Two simulation approaches were compared, differing in how the local wall stiffness informing the MBM is calculated: RPWV-based (S2) and areabased (S1). Comparing S1 and S2 simulation results highlighted that it is possible to obtain very good agreement with clinical measurements when using the RPWV-based distensibility approach whilst showing that relying solely on the area-based distensibility may not accurately capture patient-specific haemodynamics.

Accurate simulation of RPWVs is crucial for evaluating the haemodynamics impact of increased aortic wall stiffness after TEVAR. In this study, aortic wall stiffness, coupled with the spatiotemporal resolution limits of 4DMRI, hinders the measurement of smaller changes in aortic luminal area. Consequently, the aortic wall downstream of the arch was considered stiff in area-based (S1) simulation, leading to inaccuracies in simulated RPWVs (Figure 4. 4).

In contrast, the RPWVs-based (S2) approach, with iterative stiffness tuning, closely matched *in vivo* RPWVs, except for the endograft. A similar method in an FSI-based Marfan syndrome study demonstrated improved agreement with 4DMRI compared to rigid CFD simulations, particularly in peak velocity predictions (Pons et al., 2020). Similarly, in this chapter, the RPWVs-based simulation (S2) achieves superior agreement with 4DMRI when comparing velocity magnitude values and distributions, especially at systolic phases (T0, T1, T2) (Figure 4. 5). While limitations persist at diastole (T3) due to low SNR, the proposed computational framework in S2 refines CFD simulations, helping bypass the spatiotemporal constraints of 4DMRI and enhancing diastolic flow characterisation. The 4DMRI was obtained in a clinical setting for qualitative observation of the aorta. Hence, the quality of the measurements should be interpreted with a degree of caution due to potential limitations in accuracy and precision.

After TEVAR, a compliance mismatch is introduced between the device and the native aorta (Sultan et al., 2022). At the interface between the native aorta and the endograft, different radial displacements occur (Cao et al., 2022), resulting in increased pressure gradient and disturbed flow dynamics. A study on flow abnormalities post-TEVAR showed an increased SFRR after the treatment (Gil-Sala et al., 2021). This is well demonstrated in this study at the endograft-vessel interfaces, where limited device dilation capacity leads to flow reversal ranges of 27-42% (Figure 4. 6). Despite differences due to SNR and the limitations of 4DMRI and CFD, the RPWVs-based (S2) simulation captures SFRR more accurately and highlights the impact of compliance mismatch, particularly near the endograft ends (Figure 4. 6). While its predictions differ from 4DMRI, they remain consistently closer than those of the area-based (S1) simulation, especially downstream of the isthmus, where the S1 simulation fails to indicate flow abnormalities.

A reduction in vorticity in aortic flow has been associated with promoting aortic growth and dilation (Guallo et al., 2012, Guala et al., 2019, Stokes et al., 2023a). The IRF metric was found to reduce drastically after TEVAR in 19 patients (Guala et al., 2020). Previous research showed the reduction of the IRF in rigidified and dilated aortae and can serve as valuable markers for TBAD and TEVAR outcomes (Gil-Sala et al., 2021, Dux-Santoy et al., 2019). In this study, the IRF is overpredicted in the area-based (S1) simulation compared to the RPWVs-based (S2) simulation (Figure 4. 7). Differences of up to 12% at the isthmus, VAO, and ABAO suggest a lower risk of local growth, which could be misleading if only S1 results were considered.

High TAWSS occurs in regions characterised by elevated velocities and risks of local disruption (Chen et al., 2013). In this study, regions of TAWSS >3Pa were found at the AA, supra-aortic and visceral branches (Figure 4. 8). While both simulations showed similar TAWSS distributions, local differences are evident at the AA. The area-based (S1) simulation predicts more high-TAWSS regions (>3Pa) than the RPWVs-based (S2) simulation, suggesting a higher rupture risk in S1. However, these results could be misleading, as the RPWVs-based (S2) simulation consistently matched *in vivo* 4DMRI data more accurately across all comparisons.

Additionally, the OSI contour in the RPWVs-based (S2) simulation shows distinct variations along the aorta (Figure 4. 8). As noted, differences in flow

conditions between S1 and S2 translate into OSI differences, particularly at the arch, isthmus, and proximal VAO. These OSI disparities further influenced ECAP distribution, with notable differences at the isthmus, where the mean ECAP in the RPWVs-based (S2) simulation reached 1.88 Pa⁻¹, exceeding the critical threshold—an effect not captured in the area-based (S1) simulation. Such disparities have significant implications for predicting thrombosis and vascular remodelling as high ECAP has been correlated with aneurysmal growth, as noted in previous chapters and the literature (Liu et al., 2019, Zhu et al., 2021).

4.5. Limitations

As mentioned in previous chapters, the MBM simulates only radial displacements and assumes a linear elastic model with a uniform radial stiffness distribution. Research has found that in the aorta, mainly the AA undergoes nonuniform radial and longitudinal displacements while behaving non-elastically. However, these longitudinal displacements are limited distally from the AA (Morrison et al., 2009, Wedding et al., 2002). In this study, longitudinal displacements can be neglected as the isthmus and descending aorta are sealed with the endograft. The total volume compliance, defined as the sum of the radial and longitudinal compliance, is responsible for the RPWV in an aortic segment. In this study, the stiffness at the ascending aorta was reduced to match the RPWV, which resulted in increasing the radial compliance and the volume compliance. To some extent, longitudinal compliance was indirectly accounted for within the volume compliance by adding some radial compliance. Moreover, the ability to accurately describe the *in vivo* radial displacement of the aortic wall in this study is constrained by the spatiotemporal resolution of the 4D MRI images. Additionally, 4DMRI did not allow for the measurement of RPWV in any of the branches. The stiffness attributed to each branch was shared with its most proximal region. This assumption did not affect the simulation, as S2 matched the in vivo RPWVs well. While there are limitations with the method, this study is patient-specific and has been shown to provide accurate results using routinely available clinical in vivo data.

Similarly to Chapter 2 and Chapter 3, this study was performed with data from a single patient. The aim was to develop a methodology to better simulate the *in vivo* pulse wave propagation in the aorta. Future work will include validating the method in a patient cohort.

4.6. Conclusions

In this chapter, a new CFD framework, making use of PWV, a clinical metric to assess cardiovascular health, is proposed. The framework is informed by 4DMRI images and derived measurements and is applied in patient-specific simulations of a reconstructed aorta following TEVAR. Through detailed comparison with in vivo data, the RPWVs-based simulation demonstrates well-replicated haemodynamics of reconstructed aortas. Notably, the analyses can capture the compliance disparities induced by TEVAR, unveiling significant alterations in SFRR and reduced IRF at the interfaces of the endograft. This approach offers unique insight into predicting potential regions prone to cell deposition, which is crucial for assessing risks associated with aortic wall degeneration. By contrast, methods reliant on area-based distensibility exhibit notable differences from in vivo 4DMRI, underlining the advantages of RPWV-based simulations for more accurate clinical assessments. It would be interesting to assess the function of the graft using PIV on a compliant and transparent phantom, as the device's material limits 4DMRI in the stented region. This would provide an essential understanding of the aortic function post-TEVAR and could help to validate the simulation model. This methodology presents a compelling case which could empower clinicians to explore different virtual interventional scenarios, thus improving clinical decision-making.

The next chapter summarises the key findings and novel contributions presented in this thesis. It also provides suggestions for future research directions and discusses the potential advancements of these simulation techniques.

Chapter 5

Conclusions and Future Work

The work presented in this thesis aimed to enhance the understanding of the impact of patient-specific compliance modelling on post-surgical TBAD in CFD simulations of aortic haemodynamics by enhancing and developing novel computational techniques and by leveraging clinically available *in vivo* data. Specifically, the research focused on better capturing and understanding the impact of aortic graft morphology, IF compliance and displacement, and the use of PWV as a proxy for aortic stiffness. This final chapter summarises the key contributions, main findings, and prospective directions for future work.

5.1. Contributions

The main contributions of this work to the aortic community can be summarised as follows:

- 1. In Chapter 2, a modelling framework for evaluating aortic graft impact using personalised CFD simulations of complex TBAD post-surgery implemented with commonly available clinical data was developed. Leveraging the MBM, this work represented the first aortic graft sizing study focusing on the compliance mismatch between the synthetic graft and the native vessel using compliant CFD simulations in a TBAD case. The work was published in the Journal of Cardiovascular Engineering and Technology in 2024 (Girardin et al., 2024a).
- 2. A fully MRI-based, patient-specific computational framework incorporating an improved MBM to account for aortic wall and IF motion in TBAD CFD simulations was developed in Chapter 3. The

MBM was tuned using 4DMRI and allowed for a personalised and spatially varying stiffness of the aorta. This study marked the first application of the MBM to a finite IF, addressing limitations of widely used FSI simulations, such as high computational costs. The work is currently in revision in the *Annals of Biomedical Engineering* (2025).

3. In Chapter 4, a fully MRI-based, patient-specific CFD framework was developed, where compliance was iteratively tuned using a clinically relevant parameter, the RPWV, was developed. The methodology was applied to a reconstructed TBAD post-TEVAR case and compared to an alternative compliance tuning approach based on cross-sectional area variation. The proposed framework effectively captures the impact of aortic wall motion on haemodynamics, overcoming the limitations of area-based distensibility, which is constrained by the spatiotemporal resolution of MRI. This work was published in the *Journal of Biomechanics* in 2024 (Girardin et al., 2024b).

5.2. Main Findings

The research presented in this thesis leveraged CFD applications to advance the understanding of TBAD haemodynamics, particularly in assessing the impact of surgical and endovascular interventions on aortic haemodynamics.

In Chapter 2, the MBM was leveraged to study the impact of graft length and compliance on post-surgical TBAD outcomes and haemodynamics. A comparison between virtual surgeries and the patient-specific simulation indicated that longer DA grafts can increase pressure by up to 4%, which in turn elevated parameters associated with LV hypertrophy, namely wall displacement, PWV, and EL, by up to 7%, 15%, and 4%, respectively. Such increases were linked to elevated cardiovascular risks such as LV hypertrophy due to increased cardiac workload. Full thoracoabdominal graft replacement showed haemodynamics benefits, such as an EL decrease of 24%, but

raised concerns such as malperfusion of visceral branches. However, such an invasive surgery must be carefully balanced with the significant risks of spinal cord injury. A compliance-matching graft effectively mitigated these risks by reducing pressure reflections and impedance mismatch, while an overly compliant graft led to increased pulse pressure, potentially contributing to localised aortic growth and a higher risk of rupture near the graft sutures. The study underscored the importance of tailoring graft length and compliance to patient-specific aortic conditions to optimise surgical outcomes and minimise risks.

In Chapter 3, the MBM was enhanced to be able to model and better understand the impact of IF displacement in TBAD. By integrating 4DMRI and brachial pressures as input data, this approach builds upon the framework from Chapter 2 to simulate the dynamic behaviour of the IF more accurately. The simulations revealed that IF motion significantly influences local haemodynamics, especially in regions with disturbed flow, such as the visceral branches and aortic arch. Using metrics such as pressure, rotational flow features and WSS-indices, the model highlighted how a mobile IF can amplify haemodynamics variations, thus altering the risk of aortic degeneration, including thrombus formation, vessel wall damage, and an increased risk of aneurysmal rupture. In contrast, a rigid IF simulation failed to capture these effects, especially in areas where flap motion significantly influences flow dynamics, potentially misrepresenting the risks associated with a ortic degeneration. Additionally, simulations with higher degrees of flap mobility, beyond the patient-specific case, provided further insights into how such mobility affects haemodynamics. By improving the MBM to enable the modelling of a compliant IF, this study introduced a novel capability, and underscored the critical importance of incorporating patientspecific IF compliance in TBAD simulations to enhance the accuracy of CFD-driven haemodynamics predictions.

In Chapter 4, a CFD framework using RPWV to tune aortic compliance successfully, replicated haemodynamics metrics measured *in vivo* with 4DMRI. This alignment between simulation and imaging is crucial for accurately identifying regions at risk of aortic degeneration. Specifically, the simulation demonstrated overall good agreement in predicting velocity magnitude values and distribution. At the aortic arch, isthmus and endograft-vessel interface, SFRR, which has been shown to correlate with

risk of local aortic dilatation and compliance mismatch, was well predicted compared to 4DMRI data. In contrast, an area-based simulation failed to capture these effects adequately, especially downstream of the isthmus. There, the spatiotemporal resolution limitations of the 4DMRI led to inaccurate measurements and the application of high local stiffness to the aortic wall. As a result, haemodynamics were mispredicted compared to the RPWV-based simulation, such as the PWV being about three times higher than the *in vivo* measurements. Such discrepancies may lead to misleading conclusions about the risk of local growth and aneurysmal rupture. This chapter emphasised the importance of accurately simulating pulse wave propagation in the reconstructed aorta to capture compliance disparities and predict regions prone to aortic degeneration, offering valuable insights for clinical decision-making.

5.3. Limitations

The methodologies proposed in each chapter of this thesis, along with the conclusions drawn from the simulation results, are subject to certain limitations. These limitations stem from assumptions made in the modelling approach, the quality of the *in vivo* data used, and the scope of each chapter. Specifically, the extent to which the findings can be generalised to a broader patient population and varying aortic conditions. These limitations have been discussed in detail in the preceding chapters and are summarised in this section.

First, there are inherent limitations regarding the medical images used in this thesis. The simulation methodologies make use of patient-specific cine-MRI, 2D-MRI, and 4D-MRI to inform and validate patient-specific TBAD modelling. While these imaging techniques have demonstrated significant value in the observation and diagnosis of TBAD, they are not yet routinely or widely available in clinical practice (Isselbacher et al., 2022). Furthermore, even when accessible, acquiring high-resolution MRI data at multiple critical locations, such as the AA, aortic arch, DA, visceral segment, and abdominal aorta, is not standard clinical protocol. This limitation affects the broader applicability of the methodologies developed in this

thesis, as they depend on detailed imaging data that are not consistently available in routine clinical workflows. As discussed in the limitations sections of each chapter, the imaging data used in this study are subject to acquisition-related errors that introduce inaccuracies in the calibration of simulation parameters. While the segmentations were semi-automated using specialised software, human input was still required, introducing an additional source of variability. This manual involvement, coupled with artefacts arising from implanted devices and limitations of the imaging modalities, affected the accuracy of anatomical reconstructions and the reliability of parameter calibration in CFD simulations. Aditionnally, CTA and TRUFI MRI images, particularly the latter, are prone to errors due to motion artefacts and variable contrast enhancement levels, which can obscure the aortic wall and complicate accurate boundary delineation. These challenges, inherent to the imaging techniques and human involvement in segmentation, can result in inaccuracies that impact both the analyses and clinical decisions derived from the simulations.

Secondly, while each chapter focused on modelling improvements, such as the enhancement of the MBM, the conclusions drawn from these works are limited by the small cohort size, with only one patient analysed in each of the three chapters. This limitation restricts the generalisability of the findings, despite the in-depth exploration of the clinical presentation, management, and haemodynamics outcomes in TBAD.

Thirdly, there are inherent limitations in measuring certain parameters used in the simulations. For example, in Chapter 2, 3 and 4, the brachial pressure calibration formula is derived from data on healthy aortas, which may not apply to conditions such as TBAD, where the aortic structure deviates from the idealised shape. Similarly, the RPWV formula used in Chapter 4 is based on a one-dimensional model that assumes a tube. Although the aorta is reconstructed in this context, factors such as endograft struts, aortic curvatures, and morphological variations can introduce inaccuracies in the calculations. Additionally, the distensibility calculation in Chapter 2 relies on radius-based simplifications to estimate the area, assuming a perfectly round aorta. This method fails to account for the irregular geometries often observed in TBAD, potentially leading to significant errors in parameter estimation.

Fourthly, the MBM employed throughout each chapter has several key limitations. It only simulates radial displacements and assumes a uniform radial

stiffness distribution. This fails to capture the complex non-uniform radial and longitudinal displacements observed in the aorta, especially in the AA. The AA undergoes intricate non-elastic behaviours not represented by this simplified model. Additionally, the MBM assumes a linear relationship between displacement and force, which does not accurately reflect the nonlinear and anisotropic response of aortic tissue. Aortic behaviour varies with direction and load, exhibiting complex characteristics oversimplified by linear elasticity. This affects the precision of simulated haemodynamics responses, particularly under physiological conditions.

Finaly, a notable limitation of this study is the extensive computational time required for simulations. Each methodology employed across the chapters was novel and relied on distinct *in vivo* data sources, contributing to a prolonged completion timeline spanning several months. However, once established, applying these frameworks to similar patient cases with comparable *in vivo* data structures would reduce the processing time to approximately one to two weeks. While this timeframe aligns more closely with decision-making in chronic TBAD, it remains suboptimal for acute TBAD and entirely impractical for TAAD, where rapid intervention is critical. These constraints highlight the need for improvements in computational efficiency, whether through algorithmic optimisation, enhanced processing power, streamlined data acquisition methods or machine learning approaches to better integrate these advanced modelling techniques into clinical practice.

5.4. Future Work

The limitations outlined in Section 5.3 highlight the key challenges that must be addressed before patient-specific simulations can be widely adopted in clinical practice. These include the reliance on high-quality, non-standard imaging data, the small patient cohort, and the computational complexity of the current workflows. While the simulation tools developed in this thesis, based on clinically available data, show great promise for clinical decision-making, their deployment remains constrained by both complexity and substantial computational demands.

Two critical limitations are likely to be overcome in the near future. First, as previously discussed, incorporating a longitudinal displacement component into the model is essential. This remains particularly challenging in the context of TBAD due to the spatiotemporal limitations of current imaging techniques, often further complicated by the presence of implanted devices. However, in the case of the AA, particularly in healthy individuals where imaging quality is less affected by artefacts or large deformations, this approach appears feasible. Furthermore, with the availability of high-quality in vivo data, it would be possible to incorporate more sophisticated and physiologically accurate models of aortic tissue. This would allow for better representation of non-uniform radial and longitudinal displacements, and facilitate the modelling of the nonlinear and anisotropic material properties of the aorta. Once validated, these advancements could be extended to more complex conditions such as ascending aortic aneurysms and TAAD, and eventually to TBAD cases, provided imaging quality supports such detailed analyses.

The second achievable point is the deployment of the methodologies demonstrated in this thesis on a larger cohort of patients. The current models, while promising, have primarily been tested on a small sample size. Expanding the cohort to include a wider range of patients will help to validate and refine these methods, ensuring they can be generalized to diverse clinical scenarios. This step is crucial for assessing the scalability of the simulation tools and ensuring their effectiveness in real-world clinical practice.

Addressing these challenges will require close collaboration between clinicians and researchers. Furthermore, establishing standardised data acquisition and storage protocols will ensure seamless integration into clinical workflows. Advanced techniques such as machine learning and reduced-order modeling can play a pivotal role in overcoming some of these challenges. Machine learning can automate tasks such as image denoising, segmentation, and enhancement of limited datasets, while reduced-order modelling can reduce the computational load by simplifying the model without sacrificing accuracy.

The combination of these advanced techniques could therefore accelerate the integration of patient-specific simulations into clinical decision-making. With ongoing advances in computational power, data storage, and artificial intelligence, the future

of personalised medicine in the management of aortic diseases holds considerable promise. Ultimately, the clinical adoption of these simulation methods has the potential to improve patient outcomes, enhance quality of life for patients and their families, and ease the burden on increasingly strained healthcare systems and clinicians around the world.

Appendix A

This appendix concerns the contents of Chapter 2.

A.1. Mesh Sensitivity Analysis

A description of the mesh sensitivity study can be found in this section. The quality of the mesh and the analysis were assessed on six planes (Figure I) of interest using the following metrics f_i : mean and maximum velocity and time average wall shear stress (TAWSS). In addition, the relative error between the metrics was computed between the coarse (M1) and medium (M2), and M2 and the fine (M3) meshes. Also, the grid convergence index (GCI) was computed following the study of Craven et al., 2009, and the GCI was calculated as follows:

$$r \sim \left(\frac{N_3}{N_2}\right)^{1/3} \sim \left(\frac{N_3}{N_2}\right)^{1/3}$$
 A. 1

$$p = \frac{\ln(\frac{|f_1 - f_2|}{|f_2 - f_3|})}{\ln(r)}$$
 A. 2

$$E_{2,1} = \frac{|f_1 - f_2|}{f_2 \cdot (r^p - 1)}$$
 A. 3

$$E_{3,2} = \frac{|f_2 - f_3|}{f_3 \cdot (r^p - 1)}$$
 A. 4

$$GCI_{2,1}=F_s|E_2|$$
 A. 5

$$GCI_{3,2}=F_{s}|E_{3}|$$
 A. 6

With $N_{1,2,3}$ the number of elements of M1, M2 and M3, $f_{1,2,3}$ is the evaluated metric for each mesh, F_S is a safety factor equal to 1.25 (Celik et al., 2008).

Region 1 2 3 4 5 6	
Region 1 M 3 T 3 U	7
M1 [Pa] 0.1357 0.1788 0.1292 0.1155 0.1542 0.145 (.1241
M2 [Pa] 0.1369 0.1852 0.1305 0.1162 0.1569 0.144 (.1272
M3 [Pa] 0.1391 0.1830 0.1300 0.1167 0.1562 0.1440 0	.1280
%m,c 0.9% 3.6% 1.0% 0.6% 1.8% -0.7%	2.5%
%f,m 1.6% -1.2% -0.4% 0.4% -0.4% 0.0%	0.6%
GCI 2,1 0.41 7.29 6.94 2.60 3.03 1.50	2.53
GCI 3,2 0.02 1.64 3.54 0.64 0.77 0.37	0.37
Mean velocity	
Plane 1 2 3 4 5 6	
M1 [m/s] 0.614 0.685 0.612 0.427 0.370 0.313	
M2 [m/s] 0.651 0.845 0.583 0.455 0.346 0.302	
M3 [m/s] 0.653 0.863 0.598 0.462 0.352 0.299	
%m,c 6.0% 23.4% -4.8% 6.6% -6.5% -3.6% %f,m 0.3% 2.1% 2.6% 1.6% 1.8% -0.9%	
GCI 2,1 2.41 2.26 0.78 1.88 0.75 1.56	
GCI 3,2 4.35 0.79 0.30 1.34 0.20 1.04	
6	
Max Velocity	
Plane 1 2 3 4 5 6	
M1 [m/s] 1.209 0.5409 0.4775 0.4221 0.9172 0.616.	2
M2 [m/s] 1.228 0.5903 0.479 0.4255 0.9283 0.623	2
M3 [m/s] 1.238 0.5811 0.486 0.431 0.933 0.623)
%m,c 1.6% 9.1% 0.3% 0.8% 1.2% 1.1%	
%f,m 0.8% -1.6% 1.5% 1.3% 0.5% 0.1%	
GCI 2,1 2.15 2.39 0.50 2.62 1.10 0.16	
GCI 3,2 1.12 0.45 2.29 4.18 0.46 0.02	

Figure I. Left is the geometry on which regions, numbered from 1 to 7, and planes of interest, highlighted by a black line, are depicted. Tables gather mean TAWSS, mean and max velocity relative error and GCI comparisons.

Mean and maximum velocities were measured on planes delimiting regions numbered from 1 to 7, on which the mean time-averaged wall shear stress (TAWSS) was calculated. The relative error between the metrics was calculated for both M1 versus M2 and M2 versus M3. The relative error in the metrics of interest between M2 and M3 was less than 3.0%. Additionally, $GCI_{3,2}$ did not exceed 4.32%, consistent with the previous study (Craven et al., 2009).

A.2. Comparison Between Laminar and Turbulent Flow Simulations

In this study, the flow throughout the aorta is unlikely to be strictly laminar, as transitional flow has been observed even in vessels at very low Reynolds numbers (Saqr et al., 2022). The assumption of using a laminar flow model was evaluated. A turbulent flow simulation was run using the RANS model $k\omega$ -SST model in CFX with 1% turbulent intensity was used previously in the literature (Kousera et al., 2013; Stokes, Haupt, et al., 2023). RANS models characteristic turbulence parameters like turbulent kinetic energy and dissipation rate through transport equations without directly resolving turbulent scales. In many simulations of aortic blood flow, the RANS $k-\omega$ SST model is commonly employed (Lantz et al., 2011). However, a comparative investigation by Andersson and Karlsson, 2021, scrutinising RANS and LES in the context of aortic coarctation revealed notable disparities. RANS simulations exhibited limited agreement with LES, significantly underestimating turbulence anisotropy and turbulent kinetic energy, particularly in near-wall regions. Despite its limitations, the RANS model is still widely adopted for its cost-effectiveness.

This analysis compared the contours of point-wise differences of TAWSS, OSI and ECAP, and mean and max values were evaluated (Figure II). Additionally, systolic and diastolic pressures, mean flow rates at the outlets, pulse wave velocity and energy loss were compared between the two models.

Comparing the point-wise differences of TAWSS, OSI, and ECAP, similar distributions are observed between the laminar and turbulent flow simulations. Although there is a slight shift in the distribution of high TAWSS values in the turbulent flow simulation, the overall pattern remains consistent with the laminar flow simulation. Peak TAWSS are found at the entry tear, the narrowed dissection and the right renal, indicating areas of high near-wall velocity. While there is a local maximum increase of 3.29 Pa at the right renal region in the turbulent simulation, it is important to note that the laminar values are already above 5 Pa. This suggests that, despite the shift in the peak values, the conclusions regarding the potential risks associated with

elevated TAWSS (>5Pa) remain valid in the turbulent flow simulation. OSI and ECAP point-wise distributions did not exhibit any differences, which could alter the message of the paper. Additionally, systolic and diastolic pressures were 0.8 mmHg higher in the turbulent case Table I. The turbulent flow simulation also led to a maximum relative error of 3% in mean flow rates. Energy loss and pulse wave velocity increased by less than 1%.

The differences in comparing the laminar and SST flow simulations did not affect conclusions on these clinical metrics. Thus, the original laminar flow simulations were retained in this study.

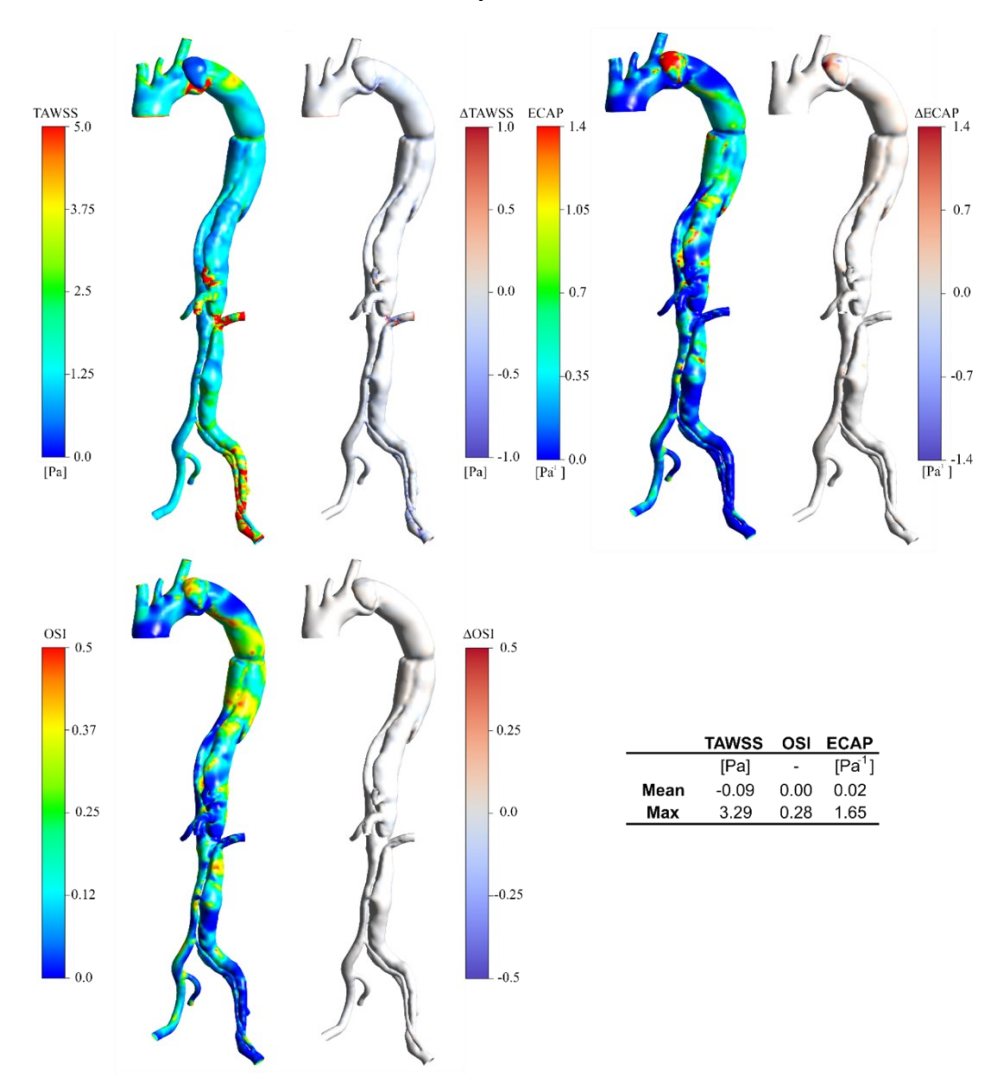


Figure II. TAWSS, OSI and ECAP contour map of the laminar simulation and point-wise differences between the laminar and turbulent simulations. The table shows the mean and max point differences for TAWSS, OSI and ECAP.

	Laminar	Turbulent	Diff
Mean Flow		[mL/s]	
Brachiocephalic trunk	18.9	18.74	0.16
Left common carotid	5.26	5.09	0.17
Left subclavian	12.4	12.41	-0.01
Celiac trunk	5.78	5.69	0.09
Superior mesenteric	10.32	10.6	-0.28
Left renal	3.11	3.21	-0.1
Right renal	14.71	14.51	0.2
Left exterior iliac	9.46	9.63	-0.17
Left interiror iliac	4.01	4.14	-0.13
Right exterior iliac	26.2	26.23	-0.03
Right interior iliac	11.22	11.1	0.12
Pressure		[mmHg]	
Systole	97.5	98.27	-0.77
Diastole	68	68.8	-0.8
Energy Loss		[W]	
	81.1	81.74	-0.64
Pulse wave velocity		[m/s]	
	6.9	6.91	-0.01

Table I. Mean flow rates at the outlets, inlet systolic and diastolic pressures, energy loss and pulse wave velocity for the laminar and turbulent simulation; the last column is the difference between the laminar and turbulent simulations

Appendix B

This appendix concerns the contents of Chapter 3.

B.1. Mesh Sensitivity Analysis

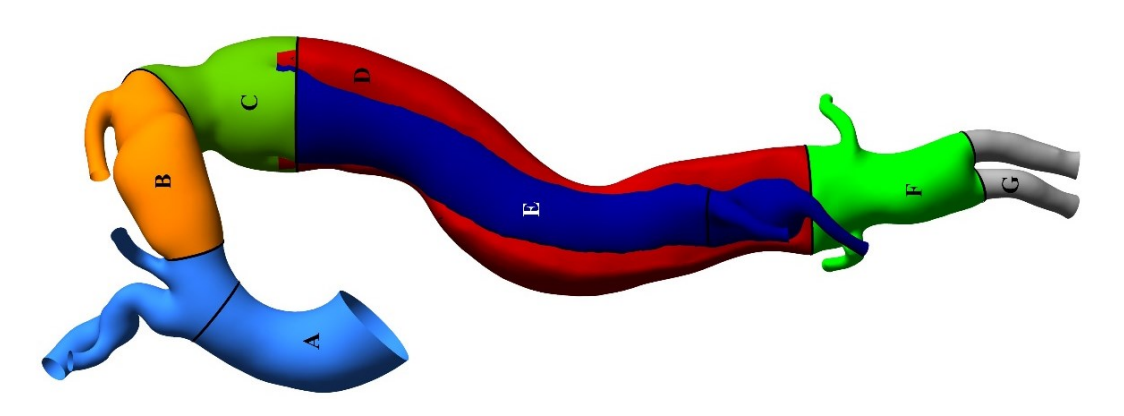
A process similar to that in Chapter 2 was used in this chapter to conduct the mesh independence study. A medium mesh, referred to as M2, with cell sizes ranging from 2 mm to 0.5 mm, was part of a mesh independence study. Detailed elements count data for each mesh is provided in Table II:

	Mesh			Change	
	M1	M2	M3	M1/M2	M2/M3
Element Count	924994	1931786	4251967	47.9%	45.4%
Minimum Element Size [mm]	1	0.5	0.25		
Maximum Element Size [mm]	4	2	1		

Table II. Element count of M1, M2 and M3 and percentage change between M1/M2 and M2/M3.

The mesh quality and analysis were evaluated across seven planes and regions of interest (refer to Figure III). Mean and maximum velocities were measured on the planes, while the mean TAWSS was recorded in each region. The relative error in the metrics of interest between M2 and M3 was less than 4.6%. Additionally, $GCI_{3,2}$ did not exceed 4.3%, a consistent previous study (Craven et al., 2009). Consequently, the medium mesh, M2, was selected for the study and subsequent analysis.

Mean TAWSS									
Region	A	В	C	D	E	F	G		
M1 [Pa]	1.229	1.026	0.566	0.238	1.268	0.771	1.049		
M2 [Pa]	1.200	1.009	0.565	0.236	1.370	0.911	1.040		
M3 [Pa]	1.2087	0.996	0.569	0.240	1.333	0.921	1.034		
%M2,M1	-2.4%	-1.7%	-0.1%	-1.0%	8.1%	18.2%	-0.8%		
%M3,M2	0.7%	-1.3%	0.6%	1.6%	-2.7%	1.1%	-0.5%		
GCI 2,1	0.3%	0.0%	0.4%	0.5%	1.5%	1.7%	0.0%		
GCI 3,2	0.1%	4.3%	0.5%	0.2%	0.3%	0.0%	0.0%		
				n velocity					
Plane	1	2	3	4	5	6	7		
M1 [m/s]	0.1559	0.1632	0.0938	0.057	0.0881	0.0356	0.0356		
M2 [m/s]	0.155	0.167	0.093	0.057	0.091	0.036	0.036		
M3 [m/s]	0.1573	0.1746	0.0943	0.0588	0.0920	0.0353	0.0353		
%M2,M1	-0.3%	2.3%	-0.5%	0.5%	2.7%	-0.3%	-0.3%		
%M3,M2	1.2%	4.6%	1.1%	2.6%	1.7%	-0.6%	-0.6%		
GCI 2,1	1.8%	9.0%	5.1%	4.8%	6.0%	3.7%	0.6%		
GCI 3,2	3.0%	1.4%	0.1%	0.3%	0.3%	1.6%	2.3%		
				20.00					
				x Velocity					
Plane	1	2	3	4	5	6	7		
M1 [m/s]	0.5078	0.5737	0.2909	0.1367	0.3372	0.1318	0.1318		
M2 [m/s]	0.503	0.571	0.289	0.136	0.336	0.132	0.132		
M3 [m/s]	0.504	0.573	0.289	0.135	0.337	0.133	0.133		
%M2,M1	-0.9%	-0.4%	-0.6%	-0.9%	-0.3%	-0.2%	-0.2%		
%M3,M2	0.1%	0.3%	0.0%	-0.3%	0.1%	1.1%	1.1%		
GCI 2,1	1.8%	9.0%	5.1%	4.8%	6.0%	3.7%	0.6%		



0.3%

0.3%

1.6%

2.3%

Figure III. Mean TAWSS, mean and max velocity relative error and GCI comparisons. Below the tables is the geometry on which regions and planes of interest, denoted by capital letters and numbers, respectively, are depicted.

GCI 3,2

3.0%

1.4%

0.1%

B.2. Three Element Windkessel Parameters

Below is Table III, which regroups the three-element Windkessel parameters used at the outlets of the aorta to apply a pressure condition mimicking the effects of the peripheral vasculature system (Westerhof, 2009). The abbreviations stand for right common carotid (RCC), right subclavian (RSA), left common carotid (LCC), left subclavian (LSA), coeliac trunk (CTA), superior mesenteric (SMA), right renal (RR), left renal (LR), left iliac (LI) and right iliac (RI). Considering the compliance of the aorta downstream of the arch in S2 after the specific stiffness leads to an increase in aortic compliance.

R2[mmhg/mL.s]	R1[mmhg/mL.s]	C[mL/mmHg
9.03	0.54	0.16
13.05	0.77	0.11
13.82	0.82	0.11
8.69	0.52	0.17
26.58	0.77	0.06
15.91	0.46	0.09
10.08	3.92	0.11
8.16	3.17	0.13
14.91	0.43	0.10
16.82	0.48	0.09
	9.03 13.05 13.82 8.69 26.58 15.91 10.08 8.16 14.91	13.050.7713.820.828.690.5226.580.7715.910.4610.083.928.163.1714.910.43

Table III. Three-element Windkessel parameters were used for all simulations in the paper.

B.3. Area Changes over the Cardiac Cycle

The cross-sectional area variation over the cardiac cycle is plotted at multiple locations to demonstrate the compliant behaviour of each case (Figure IV). As expected, the displacement at AA and ABAO is the highest. Additionally, the interplay between FL expansion and TL contraction is depicted at the IF locations, with the maximum FL expansion occurring at the VAO for D3, reaching about 25%.

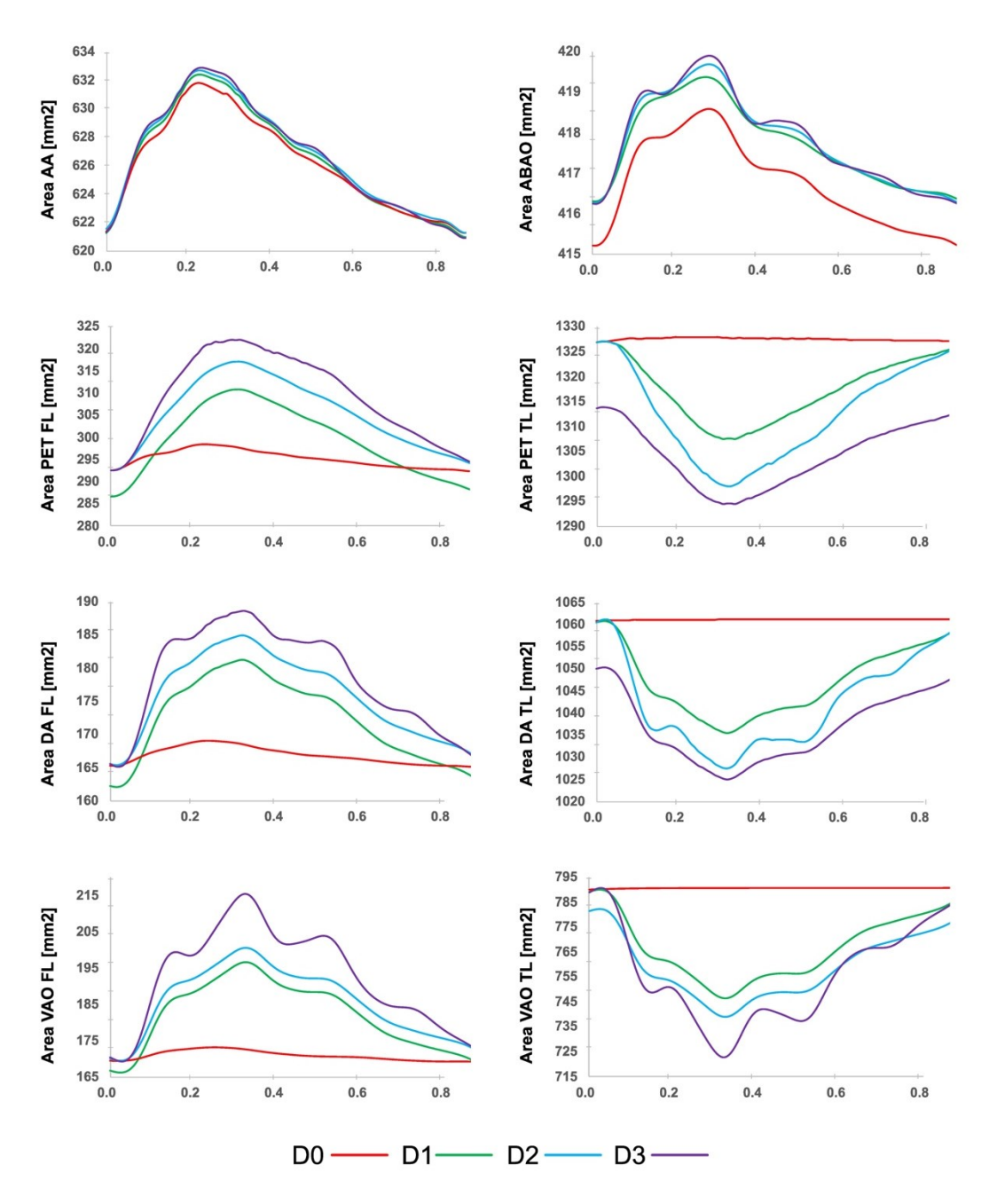


Figure IV. Cross-sectional area variation over the cardiac cycle in selected locations for all simulated cases

Appendix C

This appendix concerns the contents of Chapter 4.

C.1. Mesh Sensitivity Analysis

A similar process as in Chapter 2 and Chapter 3 was used in this chapter to conduct the mesh independence study. The medium mesh, M2, had maximum and minimum cell sizes of 1.5 mm and 0.5 mm, respectively. Detailed information on the element counts for each mesh is provided in Table IV:

	Mesh			Change	
_	M1	M2	M3	M1/M2	M2/M3
Element Count	838452	1761218	3393476	47.6%	51.9%
Maximum Element Size [mm]	0.8	0.5	0.25		
Minimum Element Size [mm]	2	1.5	0.8		

Table IV. Element count of M1, M2 and M3 and % change between coarse/medium and medium/fine

The quality of the mesh and the analysis were assessed on seven planes and regions of interest (see Figure V). The relative error in the metrics of interest between M2 and M3 was less than 4.3%. Additionally, GCI_{3,2} did not exceed 4.3%, which aligns with past research (Craven et al., 2009). Hence, the medium mesh, M2, was chosen for the study and the analysis.

			Mea	n TAWSS			
Region	A	В	C	D	E	F	G
M1 [Pa]	0.661	0.578	0.292	0.233	0.220	2.240	0.590
M2 [Pa]	0.721	0.538	0.162	0.134	0.108	0.558	0.228
M3 [Pa]	0.731	0.558	0.168	0.139	0.103	0.542	0.227
%M2,M1	9.1%	-6.9%	-44.4%	-42.4%	-50.9%	-75.1%	-61.4%
%M3,M2	1.4%	3.7%	3.6%	3.6%	-4.6%	-2.9%	-0.5%
GCI 2,1	1.8%	9.0%	5.1%	4.8%	6.0%	3.7%	0.6%
GCI 3,2	0.1%	4.3%	0.5%	0.2%	0.3%	0.0%	0.0%
			Mea	n velocity			
Plane	1	2	3	4	5	6	7
M1 [m/s]	0.078	0.067	0.021	0.023	0.017	0.059	0.058
M2 [m/s]	0.082	0.059	0.032	0.036	0.026	0.048	0.053
M3 [m/s]	0.0840	0.0610	0.0310	0.0350	0.0270	0.0500	0.0510
⁴ %M2,M1	5.1%	-11.9%	50.5%	56.5%	54.7%	-19.3%	-9.0%
%M3,M2	2.4%	3.4%	-1.9%	-2.8%	2.7%	5.0%	-3.4%
GCI 2,1	6.1%	5.6%	2.5%	3.8%	3.6%	8.0%	6.5%
GCI 3,2	3.0%	1.4%	0.1%	0.3%	0.3%	1.6%	2.3%
			Max	x Velocity			
Plane	1	2	3	4	5	6	7
M1 [m/s]	0.256	0.25	0.171	0.168	0.175	0.271	0.257
M2 [m/s]	0.281	0.343	0.267	0.218	0.157	0.244	0.207
M3 [m/s]	0.285	0.346	0.259	0.224	0.162	0.252	0.209
%M2,M1	9.8%	37.2%	56.1%	29.8%	-10.3%	-10.0%	-19.5%
%M3,M2	1.4%	0.9%	-3.0%	2.8%	3.2%	3.3%	1.0%
GCI 2,1	2.1%	1.1%	4.1%	3.9%	5.5%	5.8%	1.3%
GCI 3,2	0.3%	0.0%	0.4%	0.5%	1.5%	1.7%	0.0%

Figure V. On the left side are planes and regions of interest, denoted by numbers and capital letters. On the right side, tables display the relative error and GCI comparison for M1, M2, and M3 regarding the mean TAWSS and mean and maximum velocity.

C.2. Three Element Windkessel Parameters and Outlet Boundary Conditions

Similarly to Appendix B.1, in Table V, are gathered three-element Windkessel parameters used in S1 and S2; ABAO stands for abdominal aorta. Considering the compliance of the aorta downstream of the arch in S2 after the specific stiffness leads to an increase in aortic compliance. As the total compliance does not vary, the peripheral compliance and Windkessel compliance were proportionally decreased in S2 (Westerhof, 2009).

		RCC	RSA	LCC	CT	SMA	LR	RR	AbAo
S1	R1	0.33	0.62	0.57	1.47	0.55	12.31	15.33	0.31
	R2	4.03	10.47	9.57	24.82	9.19	31.65	39.42	5.29
	C	0.143	0.056	0.061	0.024	0.062	0.014	0.011	0.111
S2	R1	0.35	0.65	0.59	1.54	0.57	12.89	16.06	0.33
	R2	4.22	10.97	10.02	26.00	9.63	33.15	41.29	5.54
	C	0.037	0.014	0.016	0.006	0.016	0.004	0.003	0.029

Table V. Three-element Windkessel parameters for S1 and S2. R1 and R2 are in [mmHg.mL.s] and C is in [mL/mmHg].

References

- Abdulwahab, M. R., Ali, Y. H., Habeeb, F. J., Borhana, A. A., Abdelrhman, A. M. & Al-Obaidi, S. M. A. 2020. A Review in Particle Image Velocimetry Techniques (Developments and Applications). Journal of Advanced Research in Fluid Mechanics and Thermal Sciences Journal homepage, 65, 213-229.
- Aghilinejad, A., Wei, H., Magee, G. A. & Pahlevan, N. M. 2022. Model-Based Fluid-Structure Interaction Approach for Evaluation of Thoracic Endovascular Aortic Repair Endograft Length in Type B Aortic Dissection. 10, 1-14. 10.3389/fbioe.2022.825015.
- Ahmed, S. H., Hasan, S. U., Samad, S., Mushtaq, R., Rehman Usmani, S. U., Kumar, D., Atif, A. R., Timbalia, S. & Zubair, M. M. 2024. A network meta-analysis comparing the efficacy and safety of thoracic endovascular aortic repair with open surgical repair and optimal medical therapy for type B aortic dissection. JVS-Vascular Insights, 2, 100068-100068. 10.1016/j.jvsvi.2024.100068.
- Akin, I. & Nienaber, C. A. 2020. Prediction of aortic dissection. *Heart*. BMJ Publishing Group. 10.1136/heartjnl-2020-316617.
- Alexy, T., Detterich, J., Connes, P., Toth, K., Nader, E., Kenyeres, P., Arriola-Montenegro, J., Ulker, P. & Simmonds, M. J. 2022. Physical Properties of Blood and their Relationship to Clinical Conditions. *Frontiers in Physiology*. Frontiers Media S.A. 10.3389/fphys.2022.906768.
- Alimohammadi, M., Bhattacharya-Ghosh, B., Seshadhri, S., Penrose, J., Agu, O., Balabani, S. & Díaz-Zuccarini, V. 2014. Evaluation of the hemodynamic effectiveness of aortic dissection treatments via virtual stenting. International Journal of Artificial Organs, 37, 753-762. 10.5301/ijao.5000310.
- Alimohammadi, M., Sherwood, J. M., Karimpour, M., Agu, O., Balabani, S. & Díaz-Zuccarini, V. 2015. Aortic dissection simulation models for clinical support: Fluid-structure interaction vs. rigid wall models. BioMedical Engineering Online, 14, 1-16. 10.1186/s12938-015-0032-6.
- Allen, B. D., Kilinc, O., Pradella, M., Chu, S., Mehta, C. K., Malaisrie, S. C., Hoel, A. W., Carr, J. C. & Markl, M. 2023. Entry Tear Hemodynamics Detect Patients With Adverse Aorta-Related Outcomes in Type B Aortic Dissection. *JACC: Cardiovascular Imaging*. Elsevier Inc. 10.1016/j.jcmg.2022.10.027.
- Amanuma, M., Mohiaddin, R. H., Hasegawa, M., Heshiki, A. & Longmore, D. B. 1992. Abdominal aorta: characterisation of blood flow and measurement of its regional distribution by cine magnetic resonance phase-shift velocity mapping. European Radiology, 2, 559-564. 10.1007/BF00187552.
- Andersson, M. & Karlsson, M. 2021. Characterization of anisotropic turbulence behaviour in pulsatile blood flow. Biomechanics and Modelling in Mechanobiology, 20, 491-506. 10.1007/s10237-020-01396-3.
- Armour, C. H., Guo, B., Pirola, S., Saitta, S., Liu, Y., Dong, Z. & Xu, X. Y. 2020a. The influence of inlet velocity profile on predicted flow in type B aortic dissection. Biomechanics and Modelling in Mechanobiology. 10.1007/s10237-020-01395-4.

- Armour, C. H., Guo, B., Saitta, S., Pirola, S., Liu, Y., Dong, Z. & Xu, X. Y. 2022. Evaluation and verification of patient-specific modelling of type B aortic dissection. Computers in Biology and Medicine, 140. 10.1016/j.compbiomed.2021.105053.
- Armour, C. H., Menichini, C., Milinis, K., Gibbs, R. G. J. & Xu, X. Y. 2020b. Location of Reentry Tears Affects False Lumen Thrombosis in Aortic Dissection Following TEVAR. Journal of Endovascular Therapy, 27, 396-404. 10.1177/1526602820917962.
- Ashok, M. & Gupta, A. 2021. A Systematic Review of the Techniques for the Automatic Segmentation of Organs-at-Risk in Thoracic Computed Tomography Images. Archives of Computational Methods in Engineering, 28, 3245-3267. 10.1007/s11831-020-09497-z.
- Atkins, A. D., Reardon, M. J. & Atkins, M. D. 2023. Endovascular Management of the Ascending Aorta: State of the Art. *Methodist DeBakey cardiovascular journal*. NLM (Medline). 10.14797/mdcvj.1173.
- Auricchio, F., Conti, M., Lefieux, A., Morganti, S., Reali, A., Sardanelli, F., Secchi, F., Trimarchi, S. & Veneziani, A. 2014. Patient-specific analysis of post-operative aortic hemodynamics: A focus on thoracic endovascular repair (TEVAR). Computational Mechanics, 54, 943-953. 10.1007/s00466-014-0976-6.
- Azoulay, A., Serrand, C., Belarbi, A., Branchereau, P., Prouse, G., Hireche, K., Canaud, L. & Alric, P. 2024. Acute Type B Aortic Dissection: Insights From a Single-Center Retrospective Experience Over 12 Years. Journal of Endovascular Therapy. 10.1177/15266028241258401.
- Babin, D., Devos, D., Pižurica, A., Westenberg, J., Vansteenkiste, E. & Philips, W. 2014. Robust segmentation methods with an application to aortic pulse wave velocity calculation. Computerised Medical Imaging and Graphics, 38, 179-189. 10.1016/j.compmedimag.2013.12.001.
- Babu, A. R., Byju, A. G. & Gundiah, N. 2015. Biomechanical Properties of Human Ascending Thoracic Aortic Dissections. Journal of Biomechanical Engineering, 137. 10.1115/1.4030752.
- Bäumler, K., Vedula, V., Sailer, A. M., Seo, J., Chiu, P., Mistelbauer, G., Chan, F. P., Fischbein, M. P., Marsden, A. L. & Fleischmann, D. 2020. Fluid–structure interaction simulations of patient-specific aortic dissection. Biomechanics and Modelling in Mechanobiology, 19, 1607-1628. 10.1007/s10237-020-01294-8.
- Bellala, A. P., Valakkada, J., Ayappan, A., Kannath, S. & Shivanesan, P. 2024. False lumen regurgitation fraction and energy loss in the aorta measured using four-dimensional flow MRI to predict expansion of acute uncomplicated type B aortic dissection: a prospective study. Clinical Radiology, 79, e616-e623. 10.1016/j.crad.2023.12.007.
- Benedetto, U., Dimagli, A., Kaura, A., Sinha, S., Mariscalco, G., Krasopoulos, G., Moorjani, N., Field, M., Uday, T., Kendal, S., Cooper, G., Uppal, R., Bilal, H., Mascaro, J., Goodwin, A., Angelini, G., Tsang, G. & Akowuah, E. 2022. Acute type A aortic dissection reconsidered: It's all about the location of the primary entry tear and the presence or absence of malperfusion. *European Heart Journal*. Oxford University Press. 10.1093/eurheartj/ehab664.

- Beris AN, Horner JS, Jariwala S, Armstrong MJ, Wagner NJ. Recent advances in blood rheology: a review. Soft Matter. 2021 Dec 8;17(47):10591-10613. 10.1039/d1sm01212f. PMID: 34787149.
- Berhane, H., Scott, M., Elbaz, M., Jarvis, K., McCarthy, P., Carr, J., Malaisrie, C., Avery, R., Barker, A. J., Robinson, J. D., Rigsby, C. K. & Markl, M. 2020. Fully automated 3D aortic segmentation of 4D flow MRI for hemodynamic analysis using deep learning. Magnetic Resonance in Medicine, 84, 2204-2218. 10.1002/mrm.28257.
- Bertoglio, C., Barber, D., Gaddum, N., Valverde, I., Rutten, M., Beerbaum, P., Moireau, P., Hose, R. & Gerbeau, J. F. 2014. Identification of artery wall stiffness: In vitro validation and in vivo results of a data assimilation procedure applied to a 3D fluid-structure interaction model. Journal of Biomechanics, 47, 1027-1034. 10.1016/j.jbiomech.2013.12.029.
- Bian, Z., Zhong, J., Dominic, J., Christensen, G. E., Hatt, C. R. & Burris, N. S. 2022. Validation of a robust method for quantification of three-dimensional growth of the thoracic aorta using deformable image registration. Medical Physics, 49, 2514-2530. 10.1002/mp.15496.
- Biasetti, J., Spazzini, P. G., Swedenborg, J. & Christian Gasser, T. 2012. An integrated fluid-chemical model toward modelling the formation of intraluminal thrombus in abdominal aortic aneurysms. Frontiers in Physiology, 3 JUL. 10.3389/fphys.2012.00266.
- Biesdorf, A., Rohr, K., Feng, D., von Tengg-Kobligk, H., Rengier, F., Böckler, D., Kauczor, H. U. & Wörz, S. 2012. Segmentation and quantification of the aortic arch using joint 3D model-based segmentation and elastic image registration. Medical Image Analysis, 16, 1187-1201. 10.1016/j.media.2012.05.010.
- Birjiniuk, J., Timmins, L. H., Young, M., Leshnower, B. G., Oshinski, J. N., Ku, D. N. & Veeraswamy, R. K. 2017. Pulsatile Flow Leads to Intimal Flap Motion and Flow Reversal in an In Vitro Model of Type B Aortic Dissection. Cardiovascular Engineering and Technology, 8, 378-389. 10.1007/s13239-017-0312-3.
- Bissacco, D., Conti, M., Domanin, M., Bianchi, D., Scudeller, L., Mandigers, T. J., Allievi, S., Auricchio, F. & Trimarchi, S. 2022. Modifications in Aortic Stiffness After Endovascular or Open Aortic Repair: A Systematic Review and Meta-Analysis. European Journal of Vascular and Endovascular Surgery, 63, 567-577. 10.1016/j.ejvs.2022.01.008.
- Black, S. M. D., Maclean, C., Hall Barrientos, P., Ritos, K., McQueen, A. & Kazakidi, A. 2023. Calibration of patient-specific boundary conditions for coupled CFD models of the aorta derived from 4D Flow-MRI. Frontiers in Bioengineering and Biotechnology, 11. 10.3389/fbioe.2023.1178483.
- Blount, K. J. & Hagspiel, K. D. 2009. Aortic diameter, true lumen, and false lumen growth rates in chronic type B aortic dissection. American Journal of Roentgenology, 192. 10.2214/AJR.07.3986.
- Boccadifuoco, A., Mariotti, A., Celi, S., Martini, N. & Salvetti, M. V. 2018. Impact of uncertainties in outflow boundary conditions on the predictions of hemodynamic simulations of ascending thoracic aortic aneurysms.

 Computers and Fluids, 165, 96-115. 10.1016/j.compfluid.2018.01.012.

- Bock, J., Frydrychowicz, A., Lorenz, R., Hirtler, D., Barker, A. J., Johnson, K. M., Arnold, R., Burkhardt, H., Hennig, J. & Markl, M. 2011. In vivo noninvasive 4D pressure difference mapping in the human aorta: Phantom comparison and application in healthy volunteers and patients. Magnetic Resonance in Medicine, 66, 1079-1088. 10.1002/mrm.22907.
- Bologna, E., Dinoto, E., Di Simone, F., Pecoraro, F., Ragusa, S., Siciliano, K. & Zingales, M. 2023. Computational Fluid Dynamics (CFD) and Finite Element Analysis (FEM) of a Customised Stent-Graft for Endovascular (EVAR) Treatment of Abdominal Aortic Aneurism (AAA). Applied Sciences (Switzerland), 13. 10.3390/app13095712.
- Bonfanti, M., Balabani, S., Alimohammadi, M., Agu, O., Homer-Vanniasinkam, S. & Díaz-Zuccarini, V. 2018. A simplified method to account for wall motion in patient-specific blood flow simulations of aortic dissection: Comparison with fluid-structure interaction. Medical Engineering and Physics, 58, 72-79. 10.1016/j.medengphy.2018.04.014.
- Bonfanti, M., Balabani, S., Greenwood, J. P., Puppala, S., Homer-Vanniasinkam, S. & Diáz-Zuccarini, V. 2017. Computational tools for clinical support: A multiscale compliant model for haemodynamic simulations in an aortic dissection based on multi-modal imaging data. Journal of the Royal Society Interface, 14. 10.1098/rsif.2017.0632.
- Bonfanti, M., Franzetti, G., Homer-Vanniasinkam, S., Díaz-Zuccarini, V. & Balabani, S. 2020. A Combined In Vivo, In Vitro, In Silico Approach for Patient-Specific Haemodynamic Studies of Aortic Dissection. Annals of Biomedical Engineering, 48, 2950-2964. 10.1007/s10439-020-02603-z.
- Bonfanti, M., Franzetti, G., Maritati, G., Homer-Vanniasinkam, S., Balabani, S. & Díaz-Zuccarini, V. 2019. Patient-specific haemodynamic simulations of complex aortic dissections informed by commonly available clinical datasets. Medical Engineering and Physics, 71, 45-55. 10.1016/j.medengphy.2019.06.012.
- Booher, A. M., Isselbacher, E. M., Nienaber, C. A., Trimarchi, S., Evangelista, A., Montgomery, D. G., Froehlich, J. B., Ehrlich, M. P., Oh, J. K., Januzzi, J. L., O'Gara, P., Sundt, T. M., Harris, K. M., Bossone, E., Pyeritz, R. E. & Eagle, K. A. 2013. The IRAD classification system for characterizing survival after aortic dissection. American Journal of Medicine, 126, 730.e19-730.e24. 10.1016/j.amjmed.2013.01.020.
- Bossone, E., Carbone, A. & Eagle, K. A. 2022. Gender Differences in Acute Aortic Dissection. *Journal of Personalised Medicine*. MDPI. 10.3390/jpm12071148.
- Boufi, M., Patterson, B. O., Loundou, A. D., Boyer, L., Grima, M. J., Loftus, I. M. & Holt, P. J. 2019. Endovascular Versus Open Repair for Chronic Type B Dissection Treatment: A Meta-Analysis. The Society of Thoracic Surgeons. 10.1016/j.athoracsur.2018.10.
- Bourantas, G. C., Lampropoulos, D. S., Zwick, B. F., Loukopoulos, V. C., Wittek, A. & Miller, K. 2021. Immersed boundary finite element method for blood flow simulation. Computers and Fluids, 230. 10.1016/j.compfluid.2021.105162.
- Bozzi, S., Morbiducci, U., Gallo, D., Ponzini, R., Rizzo, G., Bignardi, C. & Passoni, G. 2017. Uncertainty propagation of phase contrast-MRI derived inlet boundary conditions in computational hemodynamics models of thoracic

- aorta. Computer Methods in Biomechanics and Biomedical Engineering, 20, 1104-1112. 10.1080/10255842.2017.1334770.
- Brandon, H., Prabhvir, M., Carlos Alberto Campello, J., David, M., Nicholas, B. & David, N. 2024. Mapping Stiffness of the False Lumen Wall in Type B Aortic Dissection a Multimodal Study of Regional Aortic Wall Biomechanics for False Lumen Growth Rate Prediction. Journal of Cardiovascular Magnetic Resonance, 26, 100614-100614. 10.1016/j.jocmr.2024.100614.
- Brown, A. G., Shi, Y., Marzo, A., Staicu, C., Valverde, I., Beerbaum, P., Lawford, P. V. & Hose, D. R. 2012. Accuracy vs. computational time: Translating aortic simulations to the clinic. Journal of Biomechanics, 45, 516-523. 10.1016/j.jbiomech.2011.11.041.
- Brubakk, A. 1982. Measurement of instantaneous blood-flow velocity in the human aorta using pulsed Doppler ultrasouid. *Cardiovascular Research*. 10.1093/cvr/16.1.26.
- Bruening, J., Hellmeier, F., Yevtushenko, P., Kelm, M., Nordmeyer, S., Sündermann, S. H., Kuehne, T. & Goubergrits, L. 2018. Impact of patient-specific LVOT inflow profiles on aortic valve prosthesis and ascending aorta hemodynamics. Journal of Computational Science, 24, 91-100. 10.1016/j.jocs.2017.11.005.
- Brüning, J., Hellmeier, F., Yevtushenko, P., Kühne, T. & Goubergrits, L. 2018. Uncertainty Quantification for Non-invasive Assessment of Pressure Drop Across a Coarctation of the Aorta Using CFD. Cardiovascular Engineering and Technology, 9, 582-596. 10.1007/s13239-018-00381-3.
- Buetow, B. S. & Laflamme, M. A. 2017. Cardiovascular. *Comparative Anatomy and Histology: A Mouse, Rat, and Human Atlas, Second Edition*. Elsevier. 10.1016/B978-0-12-802900-8.00010-5.
- Bustos, C. A., García-Herrera, C. M. & Celentano, D. J. 2016. Modelling and simulation of the mechanical response of a Dacron graft in the pressurization test and an end-to-end anastomosis. Journal of the Mechanical Behaviour of Biomedical Materials, 61, 36-44. 10.1016/j.jmbbm.2016.01.005.
- Cagney, N. & Balabani, S. 2019. Influence of Shear-Thinning Rheology on the Mixing Dynamics in Taylor-Couette Flow. Chemical Engineering and Technology, 42, 1680-1690. 10.1002/ceat.201900015.
- Callaghan, F. M., Bannon, P., Barin, E., Celemajer, D., Jeremy, R., Figtree, G. & Grieve, S. M. 2019. Age-related changes of shape and flow dynamics in healthy adult aortas: A 4D flow MRI study. Journal of Magnetic Resonance Imaging, 49, 90-100. 10.1002/jmri.26210.
- Callaghan, F. M. & Grieve, S. M. 2018. Normal patterns of thoracic aortic wall shear stress measured using four-dimensional flow MRI in a large population. Am J Physiol Heart Circ Physiol, 315, 1174-1181. 10.1152/ajpheart.00017.
- Callaghan, F. M., Kozor, R., Sherrah, A. G., Vallely, M., Celermajer, D., Figtree, G. A. & Grieve, S. M. 2016. Use of multi-velocity encoding 4D flow MRI to improve quantification of flow patterns in the aorta. Journal of Magnetic Resonance Imaging, 43, 352-363. 10.1002/jmri.24991.
- Calò, K., Capellini, K., De Nisco, G., Mazzi, V., Gasparotti, E., Gallo, D., Celi, S. & Morbiducci, U. 2023. Impact of wall displacements on the large-scale flow coherence in ascending aorta. Journal of Biomechanics, 154, 111620-111620. 10.1016/j.jbiomech.2023.111620.

- Camasão, D. B. & Mantovani, D. 2021. The mechanical characterization of blood vessels and their substitutes in the continuous quest for physiological-relevant performances. A critical review. *Materials Today Bio*. Elsevier B.V. 10.1016/j.mtbio.2021.100106.
- Cao, L., Shi, R., Ge, Y., Xing, L., Zuo, P., Jia, Y., Liu, J., He, Y., Wang, X., Luan, S., Chai, X. & Guo, W. 2019. Fully automatic segmentation of type B aortic dissection from CTA images enabled by deep learning. European Journal of Radiology, 121. 10.1016/j.ejrad.2019.108713.
- Cao, T., Jiang, Z., Zhao, H., Zhang, K. Q. & Meng, K. 2022. Numerical simulation to study the impact of compliance mismatch between artificial and host blood vessel on hemodynamics. Medicine in Novel Technology and Devices, 15. 10.1016/j.medntd.2022.100152.
- Capellini, K., Gasparotti, E., Cella, U., Costa, E., Fanni, B. M., Groth, C., Porziani, S., Biancolini, M. E. & Celi, S. 2021. A novel formulation for the study of the ascending aortic fluid dynamics with in vivo data. Medical Engineering and Physics, 91, 68-78. 10.1016/j.medengphy.2020.09.005.
- Capellini, K., Vignali, E., Costa, E., Gasparotti, E., Biancolini, M. E., Landini, L., Positano, V. & Celi, S. 2018. Computational Fluid Dynamic Study for aTAA Hemodynamics: An Integrated Image-Based and Radial Basis Functions Mesh Morphing Approach. Journal of Biomechanical Engineering, 140. 10.1115/1.4040940.
- Carrel, T., Sundt, T. M., von Kodolitsch, Y. & Czerny, M. 2023. Acute aortic dissection. *The Lancet*. Elsevier B.V. 10.1016/S0140-6736(22)01970-5.
- Catapano, F., Pambianchi, G., Cundari, G., Rebelo, J., Cilia, F., Carbone, I., Catalano, C., Francone, M. & Galea, N. 2020. 4D flow imaging of the thoracic aorta: is there an added clinical value? Cardiovascular Diagnosis and Therapy, 10, 1068-1089. 10.21037/cdt-20-452.
- Cavalcante, J. L., Lima, J. A. C., Redheuil, A. & Al-Mallah, M. H. 2011. Aortic stiffness: Current understanding and future directions. *Journal of the American College of Cardiology*. 10.1016/j.jacc.2010.12.017.
- Chatpattanasiri, C., Franzetti, G., Bonfanti, M., Diaz-Zuccarini, V. & Balabani, S. 2023. Towards Reduced Order Models via Robust Proper Orthogonal Decomposition to capture personalised aortic haemodynamics. Journal of Biomechanics, 158. 10.1016/j.jbiomech.2023.111759.
- Chemla, D., HÉBert, J.-L., Aptecar, E., Mazoit, J.-X., Zamani, K., Frank, R., Fontaine, G., Nitenberg, A. & Lecarpentier, Y. 2002. Empirical estimates of mean aortic pressure: advantages, drawbacks and implications for pressure redundancy. Clinical Science, 103, 7-7. 10.1042/cs20010300.
- Chen, D., Müller-Eschner, M., von Tengg-Kobligk, H., Barber, D., Böckler, D., Hose, R. & Ventikos, Y. 2013. A patient-specific study of type-B aortic dissection: Evaluation of true-false lumen blood exchange. BioMedical Engineering Online, 12, 1-16. 10.1186/1475-925X-12-65.
- Chen, H., Chi, Q., He, Y., Mu, L. & Luan, Y. 2022a. Effects of size and location of distal tear on hemodynamics and wave propagation in type B aortic dissection. Applied Mathematics and Mechanics (English Edition), 43, 1449-1468. 10.1007/s10483-022-2898-6.

- Chen, H. Y., Peelukhana, S. V., Berwick, Z. C., Kratzberg, J., Krieger, J. F., Roeder, B., Chambers, S. & Kassab, G. S. 2016. Editor's Choice Fluid–Structure Interaction Simulations of Aortic Dissection with Bench Validation. European Journal of Vascular and Endovascular Surgery, 52, 589-595. 10.1016/j.ejvs.2016.07.006.
- Chen, S., Sedghi Gamechi, Z., Dubost, F., van Tulder, G. & de Bruijne, M. 2022b. An end-to-end approach to segmentation in medical images with CNN and posterior-CRF. Medical Image Analysis, 76. 10.1016/j.media.2021.102311.
- Cheng, L., Xiang, D., Zhang, S., Zheng, C. & Wu, X. 2023. Reintervention after Thoracic Endovascular Aortic Repair of Uncomplicated Type B Aortic Dissection. Journal of Clinical Medicine, 12. 10.3390/jcm12041418.
- Cheng, Z., Juli, C., Wood, N. B., Gibbs, R. G. J. & Xu, X. Y. 2014. Predicting flow in aortic dissection: Comparison of computational model with PC-MRI velocity measurements. Medical Engineering and Physics, 36, 1176-1184. 10.1016/j.medengphy.2014.07.006.
- Cheng, Z., Wood, N. B., Gibbs, R. G. J. & Xu, X. Y. 2015. Geometric and Flow Features of Type B Aortic Dissection: Initial Findings and Comparison of Medically Treated and Stented Cases. Annals of Biomedical Engineering, 43, 177-189. 10.1007/s10439-014-1075-8.
- Cherry, M., Khatir, Z., Khan, A. & Bissell, M. 2022. The impact of 4D-Flow MRI spatial resolution on patient-specific CFD simulations of the thoracic aorta. Scientific Reports, 12. 10.1038/s41598-022-19347-6.
- Chi, Q., Chen, H., Yang, S., Mu, L., Ji, C., He, Y. & Luan, Y. 2022. Study of Effect of Boundary Conditions on Patient-Specific Aortic Hemodynamics. CMES Computer Modelling in Engineering and Sciences, 131, 31-47. 10.32604/cmes.2022.018286.
- Chlupác, J., Filová, E. & Bačáková, L. 2009. Blood vessel replacement: 50 years of development and tissue engineering paradigms in vascular surgery. Physiological Research, 58, 119-140. 10.33549/physiolres.931918.
- Cho, Y. I., & Kensey, K. R. (1991). Effects of the non-Newtonian viscosity of blood on flows in a diseased arterial vessel. Part 1: Steady flows. *Biorheology*, 28(3–4), 241–262. https://doi.org/10.3233/BIR-1991-283-415
- Chong, M. Y., Gu, B., Armour, C. H., Dokos, S., Ong, Z. C., Xu, X. Y. & Lim, E. 2022. An integrated fluid–structure interaction and thrombosis model for type B aortic dissection. Biomechanics and Modelling in Mechanobiology, 21, 261-275. 10.1007/s10237-021-01534-5.
- Chong, M. Y., Gu, B., Chan, B. T., Ong, Z. C., Xu, X. Y. & Lim, E. 2020. Effect of intimal flap motion on flow in acute type B aortic dissection by using fluid-structure interaction. International Journal for Numerical Methods in Biomedical Engineering, 36. 10.1002/cnm.3399.
- Chou, H. P., Chang, H. T., Chen, C. K., Shih, C. C., Sung, S. H., Chen, T. J., Chen, I. M., Lee, M. H., Sheu, M. H., Wu, M. H. & Chang, C. Y. 2015. Outcome comparison between thoracic endovascular and open repair for type B aortic dissection: A population-based longitudinal study. Journal of the Chinese Medical Association, 78, 241-248. 10.1016/j.jcma.2014.10.003.
- Christodoulou, K. C., Karangelis, D., Efenti, G. M., Sdrevanos, P., Browning, J. R., Konstantinou, F., Georgakarakos, E., Mitropoulos, F. A. & Mikroulis, D.

- 2023. Current knowledge and contemporary management of non-A non-B aortic dissections. *World Journal of Cardiology*. Baishideng Publishing Group Inc. 10.4330/wjc.v15.i5.244.
- Chung, E., Chen, G., Alexander, B. & Cannesson, M. 2013. Non-invasive continuous blood pressure monitoring: A review of current applications. *Frontiers of Medicine in China*. Higher Education Press Limited Company. 10.1007/s11684-013-0239-5.
- Chung, J., Lachapelle, K., Wener, E., Cartier, R., De Varennes, B., Fraser, R. & Leask, R. L. 2014. Energy loss, a novel biomechanical parameter, correlates with aortic aneurysm size and histopathologic findings. Journal of Thoracic and Cardiovascular Surgery, 148, 1082-1089. 10.1016/j.jtcvs.2014.06.021.
- Clough, R. E., Waltham, M., Giese, D., Taylor, P. R. & Schaeffter, T. 2012. A new imaging method for assessment of aortic dissection using four-dimensional phase contrast magnetic resonance imaging. Journal of Vascular Surgery, 55, 914-923. 10.1016/j.jvs.2011.11.005.
- Comunale, G., di Micco, L., Boso, D. P., Susin, F. M. & Peruzzo, P. 2021. Numerical models can assist choice of an aortic phantom for in vitro testing. Bioengineering, 8. 10.3390/bioengineering8080101.
- Corso, P., Giannakopoulos, G., Gulan, U., Frouzakis, C. E. & Holzner, M. 2021. A Novel Estimation Approach of Pressure Gradient and Haemodynamic Stresses as Indicators of Pathological Aortic Flow Using Subvoxel Modelling. IEEE Transactions on Biomedical Engineering, 68, 980-991. 10.1109/TBME.2020.3018173.
- Coselli, J. S., Spiliotopoulos, K., Preventza, O., de la Cruz, K. I., Amarasekara, H. & Green, S. Y. 2016. Open aortic surgery after thoracic endovascular aortic repair. *General Thoracic and Cardiovascular Surgery*. Springer Tokyo. 10.1007/s11748-016-0658-8.
- Cosset, B., Boussel, L., Davila Serrano, E., Millon, A., Douek, P., Farhat, F. & Sigovan, M. 2022. Hemodynamic Changes Before and After Endovascular Treatment of Type B Aortic Dissection by 4D Flow MRI. Frontiers in Cardiovascular Medicine, 9. 10.3389/fcvm.2022.873144.
- Craven, B. A., Paterson, E. G., Settles, G. S. & Lawson, M. J. 2009. Development and verification of a high-fidelity computational fluid dynamics model of canine nasal airflow. Journal of Biomechanical Engineering, 131, 1-11. 10.1115/1.3148202.
- Cuellar-Calabria, H., Burcet, G., Roque, A., Rodríguez-Palomares, J., Teixidó, G., Rodríguez, R., Bellmunt, S., Zebdi, N., Reyes-Juárez, J., Sao-Avilés, A., Escobar, M. & Evangelista, A. 2021. Differences in the area of proximal and distal entry tears at ct angiography predict long-term clinical outcomes in aortic dissection. Radiology: Cardiothoracic Imaging, 3. 10.1148/ryct.2021210029.
- Curtiss, C. F. & Hirschfelder, J. 1952. Integration of Stiff Equations. *Comm. on Pure and Applied Math.* 10.1073/pnas.38.3.235.
- Cury, M., Zeidan, F. & Lobato, A. C. 2013. Aortic disease in the young: Genetic aneurysm syndromes, connective tissue disorders, and familial aortic aneurysms and dissections. *International Journal of Vascular Medicine*. 10.1155/2013/267215.

- Davies, P. F. 2009. Hemodynamic shear stress and the endothelium in cardiovascular pathophysiology. *Nature Clinical Practice Cardiovascular Medicine*. 10.1038/ncpcardio1397.
- De Beaufort, H. W. L., Coda, M., Conti, M., Van Bakel, T. M. J., Nauta, F. J. H., Lanzarone, E., Moll, F. L., Van Herwaarden, J. A., Auricchio, F. & Trimarchi, S. 2017. Changes in aortic pulse wave velocity of four thoracic aortic stent grafts in an ex vivo porcine model. PLoS ONE, 12. 10.1371/journal.pone.0186080.
- DeMartino, R. R., Sen, I., Huang, Y., Bower, T. C., Oderich, G. S., Pochettino, A., Greason, K., Kalra, M., Johnstone, J., Shuja, F., Harmsen, W. S., Macedo, T., Mandrekar, J., Chamberlain, A. M., Weiss, S., Goodney, P. P. & Roger, V. 2018. Population-Based Assessment of the Incidence of Aortic Dissection, Intramural Hematoma, and Penetrating Ulcer, and Its Associated Mortality From 1995 to 2015. Circulation. Cardiovascular quality and outcomes, 11, e004689-e004689. 10.1161/CIRCOUTCOMES.118.004689.
- Deplano, V. & Guivier-Curien, C. 2024. Fluid-structure interaction in aortic dissections. *Biomechanics of the Aorta*. Elsevier. 10.1016/B978-0-323-95484-6.00002-6.
- Derycke, L., Avril, S. & Millon, A. 2023. Patient-Specific Numerical Simulations of Endovascular Procedures in Complex Aortic Pathologies: Review and Clinical Perspectives. Journal of Clinical Medicine, 12, 766-766. 10.3390/jcm12030766.
- Dey, D., Slomka, P. J., Leeson, P., Comaniciu, D., Shrestha, S., Sengupta, P. P. & Marwick, T. H. 2019. Artificial Intelligence in Cardiovascular Imaging: JACC State-of-the-Art Review. *Journal of the American College of Cardiology*. Elsevier USA. 10.1016/j.jacc.2018.12.054.
- Deyranlou, A., Miller, C. A., Revell, A. & Keshmiri, A. 2021. Effects of Ageing on Aortic Circulation During Atrial Fibrillation; a Numerical Study on Different Aortic Morphologies. Annals of Biomedical Engineering. 10.1007/s10439-021-02744-9.
- Di Achille, P., Tellides, G., Figueroa, C. A. & Humphrey, J. D. 2014. A haemodynamic predictor of intraluminal thrombus formation in abdominal aortic aneurysms. Proceedings of the Royal Society A: Mathematical, Physical and Engineering Sciences, 470. 10.1098/rspa.2014.0163.
- di Gioia, C. R. T., Ascione, A., Carletti, R. & Giordano, C. 2023. Thoracic Aorta: Anatomy and Pathology. *Diagnostics*. Multidisciplinary Digital Publishing Institute (MDPI). 10.3390/diagnostics13132166.
- Dillon-Murphy, D., Noorani, A., Nordsletten, D. & Figueroa, C. A. 2016. Multi-modality image-based computational analysis of haemodynamics in aortic dissection. Biomechanics and Modelling in Mechanobiology, 15, 857-876. 10.1007/s10237-015-0729-2.
- Donati, T., Wilson, J., Kölbel, T. & Clough, R. E. 2015. Moderne Diagnostik für Aortendissektion Typ B. Gefasschirurgie, 20, 420-427. 10.1007/s00772-015-0078-6.
- Dong, F., Song, J., Chen, B., Xie, X., Cheng, J., Song, J. & Huang, Q. 2024. Improved detection of aortic dissection in non-contrast-enhanced chest CT

- using an attention-based deep learning model. Heliyon, 10. 10.1016/j.heliyon.2024.e24547.
- Du, M., Zhang, C., Xie, S., Pu, F., Zhang, D. & Li, D. 2023. Investigation on aortic hemodynamics based on physics-informed neural network. Mathematical Biosciences and Engineering, 20, 11545-11567. 10.3934/mbe.2023512.
- Dux-Santoy, L., Guala, A., Teixidó-Turà, G., Ruiz-Muñoz, A., Maldonado, G., Villalva, N., Galian, L., Valente, F., Gutiérrez, L., González-Alujas, T., Sao-Avilés, A., Johnson, K. M., Wieben, O., Huguet, M., García-Dorado, D., Evangelista, A. & Rodríguez-Palomares, J. F. 2019. Increased rotational flow in the proximal aortic arch is associated with its dilation in bicuspid aortic valve disease. European Heart Journal Cardiovascular Imaging, 20, 1407-1417. 10.1093/ehjci/jez046.
- Eken, A. & Sahin, M. 2017. A parallel monolithic approach for fluid-structure interaction in a cerebral aneurysm. Computers and Fluids, 153, 61-75. 10.1016/j.compfluid.2017.05.005.
- Emendi, M., Sturla, F., Ghosh, R. P., Bianchi, M., Piatti, F., Pluchinotta, F. R., Giese, D., Lombardi, M., Redaelli, A. & Bluestein, D. 2021. Patient-Specific Bicuspid Aortic Valve Biomechanics: A Magnetic Resonance Imaging Integrated Fluid–Structure Interaction Approach. Annals of Biomedical Engineering, 49, 627-641. 10.1007/s10439-020-02571-4.
- Erbel, R. & Eggebrecht, H. 2006. Aortic dimensions and the risk of dissection. *Heart.* 10.1136/hrt.2004.055111.
- Evangelista, A., Sitges, M., Jondeau, G., Nijveldt, R., Pepi, M., Cuellar, H., Pontone, G., Bossone, E., Groenink, M., Dweck, M. R., Roos-Hesselink, J. W., Mazzolai, L., van Kimmenade, R., Aboyans, V. & Rodríguez-Palomares, J. 2023. Multimodality imaging in thoracic aortic diseases: a clinical consensus statement from the European Association of Cardiovascular Imaging and the European Society of Cardiology working group on aorta and peripheral vascular diseases. European Heart Journal Cardiovascular Imaging. 10.1093/ehjci/jead024.
- Fatma, K., Carine, G.-C., Marine, G., Philippe, P. & Valérie, D. 2022. Numerical modelling of residual type B aortic dissection: longitudinal analysis of favorable and unfavorable evolution. Medical & Biological Engineering & Computing. 10.1007/s11517-021-02480-1.
- Feiger, B., Lorenzana, E., Ranney, D., Bishawi, M., Doberne, J., Vekstein, A., Voigt, S., Hughes, C. & Randles, A. Predicting aneurysmal degeneration of type B aortic dissection with computational fluid dynamics. Proceedings of the 12th ACM Conference on Bioinformatics, Computational Biology, and Health Informatics, BCB 2021, 2021/1// 2021. Association for Computing Machinery, Inc. 10.1145/3459930.3469563.
- Ferrari, G., Balasubramanian, P., Tubaldi, E., Giovanniello, F. & Amabili, M. 2019. Experiments on dynamic behaviour of a Dacron aortic graft in a mock circulatory loop. Journal of Biomechanics, 86, 132-140. 10.1016/j.jbiomech.2019.01.053.
- Ferziger, J. H., Perić, M., & Street, R. L. (2020). Computational Methods for Fluid Dynamics (4th ed.). Springer.

- Fielden, S. W., Fornwalt, B. K., Jerosch-Herold, M., Eisner, R. L., Stillman, A. E. & Oshinski, J. N. 2008. A new method for the determination of aortic pulse wave velocity using cross-correlation on 2D PCMR velocity data. Journal of Magnetic Resonance Imaging, 27, 1382-1387. 10.1002/jmri.21387.
- Fleischmann, D., Afifi, R. O., Casanegra, A. I., Elefteriades, J. A., Gleason, T. G., Hanneman, K., Roselli, E. E., Willemink, M. J. & Fischbein, M. P. 2022. Imaging and Surveillance of Chronic Aortic Dissection: A Scientific Statement from the American Heart Association. Circulation: Cardiovascular Imaging, 15, E000075-E000075. 10.1161/HCI.00000000000000075.
- Flower, L., Arrowsmith, J. E., Bewley, J., Cook, S., Cooper, G., Flower, J., Greco, R., Sadeque, S. & Madhivathanan, P. R. 2023. Management of acute aortic dissection in critical care. *Journal of the Intensive Care Society*. SAGE Publications Inc. 10.1177/17511437231162219.
- Franzetti, G., Bonfanti, M., Tanade, C., Lim, C. S., Tsui, J., Hamilton, G., Díaz-Zuccarini, V. & Balabani, S. 2022. A Computational Framework for Pre-Interventional Planning of Peripheral Arteriovenous Malformations. Cardiovascular Engineering and Technology, 13, 234-246. 10.1007/s13239-021-00572-5.
- Franzetti, G., Díaz-Zuccarini, V. & Balabani, S. 2019. Design of an In Vitro Mock Circulatory Loop to Reproduce Patient-Specific Vascular Conditions: Toward Precision Medicine. Journal of Engineering and Science in Medical Diagnostics and Therapy, 2. 10.1115/1.4044488.
- Frydrychowicz, A., Berger, A., Del Rio, A. M., Russe, M. F., Bock, J., Harloff, A. & Markl, M. 2012. Interdependencies of aortic arch secondary flow patterns, geometry, and age analysed by 4-dimensional phase contrast magnetic resonance imaging at 3 Tesla. European Radiology, 22, 1122-1130. 10.1007/s00330-011-2353-6.
- Fujiwara, T., Berhane, H., Scott, M. B., Englund, E. K., Schäfer, M., Fonseca, B., Berthusen, A., Robinson, J. D., Rigsby, C. K., Browne, L. P., Markl, M. & Barker, A. J. 2022. Segmentation of the Aorta and Pulmonary Arteries Based on 4D Flow MRI in the Pediatric Setting Using Fully Automated Multi-Site, Multi-Vendor, and Multi-Label Dense U-Net. Journal of Magnetic Resonance Imaging, 55, 1666-1680. 10.1002/jmri.27995.
- Fumagalli, I. & Vergara, C. 2024. Novel approaches for the numerical solution of fluid-structure interaction in the aorta. *Biomechanics of the Aorta*. Elsevier. 10.1016/B978-0-323-95484-6.00017-8.
- Gallo, D., Santis, G. D., Tresoldi, D., National, I. & Ponzini, R. 2014. On the Use of In Vivo Measured Flow Rates as Boundary Conditions for Image-Based Hemodynamic Models of the Human Aorta: Implications for Indicators of Abnormal Flow On the Use of In Vivo Measured Flow Rates as Boundary Conditions for Image-Based Hemodyn. 10.1007/s10439-011-0431-1.
- Gallo, D., Steinman, D. A., Bijari, P. B. & Morbiducci, U. 2012. Helical flow in carotid bifurcation as surrogate marker of exposure to disturbed shear. Journal of Biomechanics, 45, 2398-2404. 10.1016/j.jbiomech.2012.07.007.
- Ganten, M. K., Weber, T. F., von Tengg-Kobligk, H., Böckler, D., Stiller, W., Geisbüsch, P., Kauffmann, G. W., Delorme, S., Bock, M. & Kauczor, H. U. 2009. Motion characterization of aortic wall and intimal flap by ECG-gated

- CT in patients with chronic B-dissection. European Journal of Radiology, 72, 146-153. 10.1016/j.ejrad.2008.06.024.
- Garcia, J., Barker, A. J. & Markl, M. 2019. The Role of Imaging of Flow Patterns by 4D Flow MRI in Aortic Stenosis. *JACC: Cardiovascular Imaging*. Elsevier Inc. 10.1016/j.jcmg.2018.10.034.
- Gargiulo, M., Bianchini Massoni, C., Gallitto, E., Freyrie, A., Trimarchi, S., Faggioli, G., Stella, A. & Surgery, V. 2014. Lower limb malperfusion in type B aortic dissection: a systematic review. Ann Cardiothorac Surg, 3, 351-367. 10.3978/j.issn.2225-319X.2014.07.05.
- Gijsen, F. J. H., Allanic, E., Van De Vosse, F. N. & Janssen, J. D. 1999. The influence of the non-Newtonian properties of blood on the flow in large arteries: Unsteady flow in a 90° curved tube. Journal of Biomechanics, 32, 705-713. 10.1016/S0021-9290(99)00014-7.
- Gil-Sala, D., Guala, A., Garcia Reyes, M. E., Azancot, M. A., Dux-Santoy, L., Allegue Allegue, N., Teixido Turà, G., Goncalves Martins, G., Ruiz Muñoz, A., Constenla García, I., Evangelista, A., Tello Díaz, C., Ferreira González, I., Rodríguez-Palomares, J. F. & Bellmunt, S. 2021. Geometric, Biomechanic and Haemodynamic Aortic Abnormalities Assessed by 4D Flow Cardiovascular Magnetic Resonance in Patients Treated by TEVAR Following Blunt Traumatic Thoracic Aortic Injury. European Journal of Vascular and Endovascular Surgery, 62, 797-807. 10.1016/j.ejvs.2021.07.016.
- Girardin, L., Lind, N., von Tengg-Kobligk, H., Balabani, S. & Díaz-Zuccarini, V. 2024a. Patient-specific compliant simulation framework informed by 4DMRI-extracted pulse wave Velocity: Application post-TEVAR. Journal of Biomechanics, 175. 10.1016/j.jbiomech.2024.112266.
- Girardin, L., Stokes, C., Thet, M. S., Oo, A. Y., Balabani, S. & Díaz-Zuccarini, V. 2024b. Patient-Specific Haemodynamic Analysis of Virtual Grafting Strategies in Type-B Aortic Dissection: Impact of Compliance Mismatch. Cardiovascular Engineering and Technology. 10.1007/s13239-024-00713-6.
- Gouveia e Melo, R., Mourão, M., Caldeira, D., Alves, M., Lopes, A., Duarte, A., Fernandes e Fernandes, R. & Mendes Pedro, L. 2022. A systematic review and meta-analysis of the incidence of acute aortic dissections in population-based studies. *Journal of Vascular Surgery*. Elsevier Inc. 10.1016/j.jvs.2021.08.080.
- Gu, L. & Cai, X. C. 2021. Fusing 2D and 3D convolutional neural networks for the segmentation of aorta and coronary arteries from CT images. Artificial Intelligence in Medicine, 121. 10.1016/j.artmed.2021.102189.
- Guala, A., Gil Sala, D., Ruiz-Munoz, A., Garcia Reyes, M. E., Dux-Santoy, L., Teixido-Tura, G., Tello, C., Cinque, A., Valente, F., Lopez Sainz, A., Galian Gay, L., Ferreira, I., Evangelista, A., Bellmunt Montoya, S. & Rodriguez Palomares, J. F. 2020. Patients with blunt traumatic thoracic aortic injury treated with TEVAR present increased flow dynamics alterations and pulse wave velocity: a 4D flow CMR study. European Heart Journal, 41. 10.1093/ehjci/ehaa946.2351.
- Guala, A., Teixido-Tura, G., Dux-Santoy, L., Granato, C., Ruiz-Muñoz, A., Valente, F., Galian-Gay, L., Gutiérrez, L., González-Alujas, T., Johnson, K. M.,

- Wieben, O., Sao Avilés, A., Evangelista, A. & Rodriguez-Palomares, J. 2019. Decreased rotational flow and circumferential wall shear stress as early markers of descending aorta dilation in Marfan syndrome: A 4D flow CMR study. Journal of Cardiovascular Magnetic Resonance, 21. 10.1186/s12968-019-0572-1.
- Han, S., Schirmer, C. M. & Modarres-Sadeghi, Y. 2020. A reduced-order model of a patient-specific cerebral aneurysm for rapid evaluation and treatment planning. Journal of Biomechanics, 103. 10.1016/j.jbiomech.2020.109653.
- Harky, A., Chan, J. S. K., Wong, C. H. M., Francis, N., Grafton-Clarke, C. & Bashir, M. 2019. Systematic review and meta-analysis of acute type B thoracic aortic dissection, open, or endovascular repair. *Journal of Vascular Surgery*. Mosby Inc. 10.1016/j.jvs.2018.08.187.
- Helps, E. P. W. & McDonald, D. A. 1954. Observations on laminar flow in veins. *J. Physiol.* (1954).
- Hernandez, G., Messina, A. & Kattan, E. 2022. Invasive arterial pressure monitoring: much more than mean arterial pressure! *Intensive Care Medicine*. Springer Science and Business Media Deutschland GmbH. 10.1007/s00134-022-06798-8.
- Higashigaito, K., Sailer, A. M., van Kuijk, S. M. J., Willemink, M. J., Hahn, L. D., Hastie, T. J., Miller, D. C., Fischbein, M. P. & Fleischmann, D. 2021. Aortic growth and development of partial false lumen thrombosis are associated with late adverse events in type B aortic dissection. Journal of Thoracic and Cardiovascular Surgery, 161, 1184-1190.e2. 10.1016/j.jtcvs.2019.10.074.
- Himburg, H. A., Grzybowski, D. M., Hazel, A. L., Lamack, J. A., Li, X.-M., Friedman, M. H. & Friedman, M. H. 2004. Spatial comparison between wall shear stress measures and porcine arterial endothelial permeability. Am J Physiol Heart Circ Physiol, 286, 1916-1922. 10.1152/ajpheart.00897.2003.-A.
- Hiratzka, L. F., Bakris, G. L., Beckman, J. A., Bersin, R. M., Carr, V. F., Casey, D. E., Eagle, K. A., Hermann, L. K., Isselbacher, E. M., Kazerooni, E. A., Kouchoukos, N. T., Lytle, B. W., Milewicz, D. M., Reich, D. L., Sen, S., Shinn, J. A., Svensson, L. G., Williams, D. M., Jacobs, A. K., ... Yancy, C. W. (2010). 2010 ACCF/AHA/AATS/ACR/ASA/SCA/SCAI/SIR/STS/SVM guidelines for the diagnosis and management of patients with thoracic aortic disease: Executive summary: A report of the american college of cardiology foundation/american heart association task force on practice guidelines, american association for thoracic surgery, american college of radiology, american stroke association. In *Circulation* (Vol. 121, Issue 13). Lippincott Williams and Wilkins. https://doi.org/10.1161/CIR.0b013e3181d4739e
- Hirschhorn, M., Tchantchaleishvili, V., Stevens, R., Rossano, J. & Throckmorton, A. 2020. Fluid–structure interaction modelling in cardiovascular medicine A systematic review 2017–2019. *Medical Engineering and Physics*. Elsevier Ltd. 10.1016/j.medengphy.2020.01.008.

- Hori, D., Yuri, K., Kusadokoro, S., Shimizu, T., Kimura, N. & Yamaguchi, A. 2020. Effect of endoprostheses on pulse wave velocity and its long-term outcomes after thoracic endovascular aortic repair. General Thoracic and Cardiovascular Surgery, 68, 1134-1141. 10.1007/s11748-020-01343-0.
- Hou, B. C., Huang, Y. T., Hsiao, F. C., Wu, C. C., Cheng, Y. T., Liu, K. S., Chang, S. H., Chu, P. H., Chou, A. H. & Chen, S. W. 2023. Learning curve for open surgical repair of acute type A aortic dissection. Scientific Reports, 13. 10.1038/s41598-023-30397-2.
- Howard, C., Sheridan, J., Picca, L., Reza, S., Smith, T., Ponnapalli, A., Calow, R., Cross, O., Iddawela, S., George, M., Livra Dias, D., Srinivasan, A., Munir, W., Bashir, M. & Idhrees, M. 2021. TEVAR for complicated and uncomplicated type B aortic dissection—Systematic review and meta-analysis. *Journal of Cardiac Surgery*. John Wiley and Sons Inc. 10.1111/jocs.15827.
- Hsieh, R. W., Hsu, T. C., Lee, M., Hsu, W. T., Chen, S. T., Huang, A. H., Hsieh, A. L. & Lee, C. C. 2019. Comparison of type B dissection by open, endovascular, and medical treatments. Journal of Vascular Surgery, 70, 1792-1800.e3. 10.1016/j.jvs.2019.02.062.
- Humphrey, J. D., Schwartz, M. A., Tellides, G. & Milewicz, D. M. 2015. Role of mechanotransduction in vascular biology: Focus on thoracic aortic aneurysms and dissections. *Circulation Research*. Lippincott Williams and Wilkins. 10.1161/CIRCRESAHA.114.304936.
- Hysa, L., Khor, S., Starnes, B. W., Chow, W. B., Sweet, M. P., Nguyen, J. & Shalhub, S. Cause-specific mortality of type B aortic dissection and assessment of competing risks of mortality. Journal of Vascular Surgery, 2021/1// 2021. Mosby Inc., 48-60.e1. 10.1016/j.jvs.2020.04.499.
- Ikeno, Y., Truong, V. T. T., Tanaka, A. & Prakash, S. K. 2022. The Effect of Ascending Aortic Repair on Left Ventricular Remodelling. American Journal of Cardiology, 182, 89-94. 10.1016/j.amjcard.2022.07.027.
- Isselbacher, E. M., Preventza, O., Black, J. H., Augoustides, J. G., Beck, A. W., Bolen, M. A., Braverman, A. C., Bray, B. E., Brown-Zimmerman, M. M., Chen, E. P., Collins, T. J., DeAnda, A., Fanola, C. L., Girardi, L. N., Hicks, C. W., Hui, D. S., Jones, W. S., Kalahasti, V., Kim, K. M., Milewicz, D. M., Oderich, G. S., Ogbechie, L., Promes, S. B., Ross, E. G., Schermerhorn, M. L., Times, S. S., Tseng, E. E., Wang, G. J. & Joseph Woo, Y. 2022. 2022 ACC/AHA Guideline for the Diagnosis and Management of Aortic Disease: A Report of the American Heart Association/American College of Cardiology Joint Committee on Clinical Practice Guidelines. *Circulation*. Lippincott Williams and Wilkins. 10.1161/CIR.000000000001106.
- J. R. Levick, N. H. D. J. P. 2018. Introduction to Cardiovascular Physiology. 10.1016/C2013-0-06523-1.
- Jafarinia, A., Melito, G. M., Müller, T. S., Rolf-Pissarczyk, M., Holzapfel, G. A., Brenn, G., Ellermann, K. & Hochrainer, T. 2023. Morphological parameters affecting false lumen thrombosis following type B aortic dissection: a systematic study based on simulations of idealised models. Biomechanics and Modelling in Mechanobiology, 22, 885-904. 10.1007/s10237-023-01687-5.

- Jafarinia, A., Müller, T. S., Windberger, U., Brenn, G. & Hochrainer, T. 2020. Blood Rheology Influence on False Lumen Thrombosis in Type B Aortic Dissection. Journal of Biomedical Engineering and Biosciences. 10.11159/jbeb.2020.002.
- Jayendiran, R., Nour, B. & Ruimi, A. 2018. Fluid-structure interaction (FSI) analysis of stent-graft for aortic endovascular aneurysm repair (EVAR): Material and structural considerations. Journal of the Mechanical Behaviour of Biomedical Materials, 87, 95-110. 10.1016/j.jmbbm.2018.07.020.
- Jayendiran, R., Nour, B. & Ruimi, A. 2020. A fluid–structure interaction analysis of anisotropic Dacron fabric used for aortic replacement. Journal of Fluids and Structures, 97, 103108-103108. 10.1016/j.jfluidstructs.2020.103108.
- Jin, Y., Pepe, A., Li, J., Gsaxner, C., Zhao, F.-h., Pomykala, K. L., Kleesiek, J., Frangi, A. F. & Egger, J. 2021. AI-based Aortic Vessel Tree Segmentation for Cardiovascular Diseases Treatment: Status Quo. 10.48550/arXiv.2108.02998.
- Johnston, C. R., Lee, K., Flewitt, J., Moore, R., Dobson, G. M. & Thornton, G. M. 2010. The mechanical properties of endovascular stents: An in vitro assessment. Cardiovascular Engineering, 10, 128-135. 10.1007/s10558-010-9097-9.
- Jonathan Golledge, P. N. 2003. Vascular grafts. Expert review of cardiovascular therapy, 1, 581-594. 10.1586/14779072.1.4.581.
- Jubouri, M., Al-Tawil, M., Cheung, H., Yip, A., Bashir, A., Cian, S. Z., Tan, P., Bashir, M., Anderson, R., Bailey, D., Nienaber, C., Coselli, J., Williams, I., Brompton, R. & Hospitals, H. 2022. Mid-and long-term outcomes of thoracic endovascular aortic repair in acute and subacute uncomplicated type B aortic dissection. 10.22541/au.164303660.08786441/v1.
- Juffermans, J. F., Westenberg, J. J. M., van den Boogaard, P. J., Roest, A. A. W., van Assen, H. C., van der Palen, R. L. F. & Lamb, H. J. 2021. Reproducibility of Aorta Segmentation on 4D Flow MRI in Healthy Volunteers. Journal of Magnetic Resonance Imaging, 53, 1268-1279. 10.1002/jmri.27431.
- Kaji, S. 2018. Update on the therapeutic strategy of type B aortic dissection. *Journal of Atherosclerosis and Thrombosis*. Japan Atherosclerosis Society. 10.5551/jat.RV17017.
- Kamada, H., Nakamura, M., Ota, H., Higuchi, S. & Takase, K. 2022. Blood flow analysis with computational fluid dynamics and 4D-flow MRI for vascular diseases. *Journal of Cardiology*. Japanese College of Cardiology (Nippon-Sinzobyo-Gakkai). 10.1016/j.jjcc.2022.05.007.
- Kamman, A. V., Brunkwall, J., Verhoeven, E. L., Heijmen, R. H., Trimarchi, S.,
 Kasprzak, P., Heijmen, R., Alric, P., Verhoeven, E., Schumacher, H., Fabiani,
 J. N., Eckstein, H. H., Taylor, P., Mailina, M., Mangialardi, N., Larzon, T.,
 Böckler, D., Lönn, L., Dialetto, G. & Lammer, J. 2017a. Predictors of aortic growth in uncomplicated type B aortic dissection from the Acute Dissection
 Stent Grafting or Best Medical Treatment (ADSORB) database. Journal of Vascular Surgery, 65, 964-971.e3. 10.1016/j.jvs.2016.09.033.
- Kamman, A. V., Yang, B., Kim, K. M., Williams, D. M., Michael Deeb, G. & Patel, H. J. 2017b. Visceral Malperfusion in Aortic Dissection: The Michigan Experience. Seminars in Thoracic and Cardiovascular Surgery, 29, 173-178. 10.1053/j.semtcvs.2016.10.002.

- Kan, X., Ma, T., Jiang, X., Holzapfel, G. A., Dong, Z. & Xu, X. Y. 2024. Towards biomechanics-based pre-procedural planning for thoracic endovascular aortic repair of aortic dissection. Computer Methods and Programs in Biomedicine, 244. 10.1016/j.cmpb.2023.107994.
- Karlsson, J., Stålhand, J., Carlhäll, C. J., Länne, T. & Engvall, J. 2023. An in vivo study of isotropic and anisotropic wall stress in a hyperelastic holzapfel-gasser-ogden model in the human abdominal aorta: Effects of age and sex. Frontiers in Physiology, 14. 10.3389/fphys.2023.1128131.
- Karmonik, C., Bismuth, J., Redel, T., Anaya-Ayala, J. E., Davies, M. G., Shah, D. J. & Lumsden, A. B. 2012a. Impact of Tear Location on Hemodynamics in a Type B Aortic Dissection investigated with Computational Fluid Dynamics. IEEE EMBS. 10.1109/IEMBS.2010.5627193.
- Karmonik, C., Duran, C., Shah, D. J., Anaya-Ayala, J. E., Davies, M. G., Lumsden, A. B. & Bismuth, J. 2012b. Preliminary findings in quantification of changes in septal motion during follow-up of type B aortic dissections. Journal of Vascular Surgery, 55. 10.1016/j.jvs.2011.10.127.
- Karmonik, C., Partovi, S., Müller-Eschner, M., Bismuth, J., Davies, M. G., Shah, D. J., Loebe, M., Böckler, D., Lumsden, A. B. & Von Tengg-Kobligk, H. 2012c. Longitudinal computational fluid dynamics study of aneurysmal dilatation in a chronic DeBakey type III aortic dissection. Journal of Vascular Surgery, 56, 260-263.e1. 10.1016/j.jvs.2012.02.064.
- Kaufman, J. A. 2004. Thoracic Aorta, Elsevier Inc. 10.1016/b978-0-8151-4369-7.50017-2.
- Kauhanen, P., Korpela, T. & Hedman, M. 2022. Dilatation of the ascending aorta Growth rate, risk factors and clinical outcomes in the long-term follow-up. European Journal of Radiology, 150. 10.1016/j.ejrad.2022.110234.
- Kelsey, L. J., Powell, J. T., Norman, P. E., Miller, K. & Doyle, B. J. 2017. A comparison of hemodynamic metrics and intraluminal thrombus burden in a common iliac artery aneurysm. International Journal for Numerical Methods in Biomedical Engineering, 33. 10.1002/cnm.2821.
- Keramati, H., Birgersson, E., Ho, J. P., Kim, S., Chua, K. J. & Leo, H. L. 2020. The effect of the entry and re-entry size in the aortic dissection: a two-way fluid–structure interaction simulation. Biomechanics and Modelling in Mechanobiology, 19, 2643-2656. 10.1007/s10237-020-01361-0.
- Khanna, A., Oropeza, B. P. & Huang, N. F. 2022. Engineering Spatiotemporal Control in Vascularised Tissues. *Bioengineering*. MDPI. 10.3390/bioengineering9100555.
- Kilinc, O., Baraboo, J., Engel, J., Giese, D., Jin, N., Weiss, E. K., Maroun, A., Chow, K., Bi, X., Davids, R., Mehta, C., Malaisrie, S. C., Hoel, A., Carr, J., Markl, M. & Allen, B. D. 2023. Aortic Hemodynamics with Accelerated Dual-Venc 4D Flow MRI in Type B Aortic Dissection. Applied Sciences (Switzerland), 13. 10.3390/app13106202.
- Kim, T., van Bakel, P. A. J., Nama, N., Burris, N., Patel, H. J., Williams, D. M. & Figueroa, C. A. 2023. A Computational Study of Dynamic Obstruction in Type B Aortic Dissection. Journal of biomechanical engineering, 145. 10.1115/1.4056355.

- Kolipaka, A., Illapani, V. S. P., Kalra, P., Garcia, J., Mo, X., Markl, M. & White, R. D. 2017. Quantification and comparison of 4D-flow MRI-derived wall shear stress and MRE-derived wall stiffness of the abdominal aorta. Journal of Magnetic Resonance Imaging, 45, 771-778. 10.1002/jmri.25445.
- Komutrattananont, P., Mahakkanukrauh, P. & Das, S. 2019. Morphology of the human aorta and age-related changes: Anatomical facts. *Anatomy and Cell Biology*. Korean Association of Anatomists. 10.5115/acb.2019.52.2.109.
- Kotelis, D., Grebe, G., Kraus, P., Müller-Eschner, M., Bischoff, M., von Tengg-Kobligk, H. & Böckler, D. 2016. Morphologic predictors of aortic expansion in chronic type B aortic dissection. Vascular, 24, 187-193. 10.1177/1708538115591941.
- Kousera, C. A., Wood, N. B., Seed, W. A., Torii, R., O'Regan, D. & Xu, X. Y. 2013. A numerical study of aortic flow stability and comparison with in vivo flow measurements. Journal of Biomechanical Engineering, 135. 10.1115/1.4023132.
- Krissian, K., Carreira, J. M., Esclarin, J. & Maynar, M. 2014. Semi-automatic segmentation and detection of aorta dissection wall in MDCT angiography. Medical Image Analysis, 18, 83-102. 10.1016/j.media.2013.09.004.
- Kroeger, J. R., Pavesio, F. C., Mörsdorf, R., Weiss, K., Bunck, A. C., Baeßler, B., Maintz, D. & Giese, D. 2021. Velocity quantification in 44 healthy volunteers using accelerated multi-VENC 4D flow CMR. European Journal of Radiology, 137. 10.1016/j.ejrad.2021.109570.
- Krupa, K. & Bekiesińska-Figatowska, M. 2015. Artifacts in magnetic resonance imaging. Polish Journal of Radiology, 80, 93-106. 10.12659/PJR.892628.
- Ku, D. N., Giddens, D. P., Zarins, C. K. & Glagov, S. 1985. Pulsatile flow and atherosclerosis in the human carotid bifurcation. Positive correlation between plaque location and low and oscillating shear stress. Arteriosclerosis, 5, 293-302. 10.1161/01.atv.5.3.293.
- Lamata, P., Pitcher, A., Krittian, S., Nordsletten, D., Bissell, M. M., Cassar, T., Barker, A. J., Markl, M., Neubauer, S. & Smith, N. P. 2014. Aortic relative pressure components derived from four-dimensional flow cardiovascular magnetic resonance. Magnetic Resonance in Medicine, 72, 1162-1169. 10.1002/mrm.25015.
- Lantz, J., Gårdhagen, R. & Karlsson, M. 2012. Quantifying turbulent wall shear stress in a subject specific human aorta using large eddy simulation. Medical Engineering and Physics, 34, 1139-1148. 10.1016/j.medengphy.2011.12.002.
- Lawrence, A. R. & Gooch, K. J. 2009. Transmural pressure and axial loading interactively regulate arterial remodelling ex vivo. Am J Physiol Heart Circ Physiol, 297, 475-484. 10.1152/ajpheart.00972.2008.-Physiological.
- Ledda, P. G., Badas, M. G., Matta, G. & Querzoli, G. 2023. Flow dynamics in a model of a dilated thoracic aorta prior to and following prosthetic replacement. Theoretical and Computational Fluid Dynamics, 37, 375-396. 10.1007/s00162-023-00651-4.
- Lee, G. H., Heo, W., Lee, Y., Kim, T. H., Huh, H., Song, S. W. & Ha, H. 2023. Fluid–structure interaction simulation of visceral perfusion and impact of different cannulation methods on aortic dissection. Scientific Reports, 13. 10.1038/s41598-023-27855-2.

- Lee, W., Cho, S. W., Allahwala, U. K. & Bhindi, R. 2020. Numerical study to identify the effect of fluid presence on the mechanical behaviour of the stents during coronary stent expansion. Computer Methods in Biomechanics and Biomedical Engineering, 23, 744-754. 10.1080/10255842.2020.1763967.
- Les, A. S., Shadden, S. C., Figueroa, C. A., Park, J. M., Tedesco, M. M., Herfkens, R. J., Dalman, R. L. & Taylor, C. A. 2010. Quantification of hemodynamics in abdominal aortic aneurysms during rest and exercise using magnetic resonance imaging and computational fluid dynamics. Annals of Biomedical Engineering, 38, 1288-1313. 10.1007/s10439-010-9949-x.
- Lescan, M. 2022. Type B dissection risk assessment-can aortic flow visualization solve the morphological puzzle? European Journal of Cardio-thoracic Surgery, 61, 140-141. 10.1093/ejcts/ezab346.
- Levilly, S., Castagna, M., Idier, J., Bonnefoy, F., Le Touzé, D., Moussaoui, S., Paul-Gilloteaux, P. & Serfaty, J. M. 2020. Towards quantitative evaluation of wall shear stress from 4D flow imaging. Magnetic Resonance Imaging, 74, 232-243. 10.1016/j.mri.2020.08.017.
- Li, D., Yuan, D., Peng, L., Zheng, T. & Fan, Y. 2021. The characteristics of distal tears affect false lumen thrombosis rate after thoracic endovascular aortic repair for acute type B dissection. Interactive Cardiovascular and Thoracic Surgery, 33, 755-762. 10.1093/icvts/ivab166.
- Li, F. R., Wu, X., Yuan, J., Wang, J., Mao, C. & Wu, X. 2018. Comparison of thoracic endovascular aortic repair, open surgery and best medical treatment for type B aortic dissection: A meta-analysis. International Journal of Cardiology, 250, 240-246. 10.1016/j.ijcard.2017.10.050.
- Li, S., Chopard, B. & Latt, J. 2019. Continuum model for flow diverting stents in 3D patient-specific simulation of intracranial aneurysms. Journal of Computational Science, 38. 10.1016/j.jocs.2019.101045.
- Liepsch, D. W. & Wallis, H. B. 1986. Flow in tubes and arteries: a comparison. *Biorheology*.
- Lim, L. J., Tison, G. H. & Delling, F. N. 2020. Artificial Intelligence in Cardiovascular Imaging. Methodist DeBakey Cardiovascular Journal. 10.14797/mdcj-16-2-138.
- Litmanovich, D., Bankier, A. A., Cantin, L., Raptopoulos, V. & Boiselle, P. M. 2009. CT and MRI in diseases of the aorta. American Journal of Roentgenology, 193, 928-940. 10.2214/AJR.08.2166.
- Liu, D., Luo, H., Lin, S., Zhao, L. & Qiao, C. 2020. Comparison of the efficacy and safety of thoracic endovascular aortic repair with open surgical repair and optimal medical therapy for acute type B aortic dissection: A systematic review and meta-analysis. *International Journal of Surgery*. Elsevier Ltd. 10.1016/j.ijsu.2020.08.051.
- Liu, F., Ge, Y., Rong, D., Xue, Y., Fan, W., Miao, J., Ge, X., Zhao, Z., Zhang, L. & Guo, W. 2022. The Distance From the Primary Intimal Tear to the Left Subclavian Artery Predicts Thoracic Aortic Enlargement After Thoracic Endovascular Aortic Repair of Type B Aortic Dissection: A Retrospective Cohort Study. Journal of Endovascular Therapy, 29, 32-41. 10.1177/15266028211054764.

- Liu, Q., Jiang, P., Wu, J., Gao, B. & Wang, S. 2019. The Morphological and Hemodynamic Characteristics of the Intraoperative Ruptured Aneurysm. Frontiers in Neuroscience, 13. 10.3389/fnins.2019.00233.
- Liu, S. Z., Engel, J. S., Bisen, J. B., Kilinc, O., Quinn, S., Hoel, A. W., Mehta, C. K., Markl, M. & Allen, B. D. 2023. Entry tear hemodynamics using 4D flow MRI in a patient with acute type B aortic dissection. Radiology Case Reports, 18, 1037-1040. 10.1016/j.radcr.2022.12.033.
- Lombardi, J. V., Hughes, G. C., Appoo, J. J., Bavaria, J. E., Beck, A. W., Cambria, R. P., Charlton-Ouw, K., Eslami, M. H., Kim, K. M., Leshnower, B. G., Maldonado, T., Reece, T. B. & Wang, G. J. 2020. Society for Vascular Surgery (SVS) and Society of Thoracic Surgeons (STS) reporting standards for type B aortic dissections. Journal of Vascular Surgery, 71, 723-747. 10.1016/j.jvs.2019.11.013.
- Looyenga, E. M. & Gent, S. P. 2018. Examination of fluid-structure interaction in stent grafts and its hemodynamic implications.
- Lopes, A., Mendes Pedro, L., Gouveia e Melo, R., Moutinho, M., Sobrinho, G., Amorim, P., Silvestre, L., Fernandes e Fernandes, R., Ministro, A., Martins, C., Gomes Almeida, A., Nobre, Â., Pinto, F. & Fernandes e Fernandes, J. 2023. The evolution of management of type B aortic dissection in a series of 100 consecutive cases in a tertiary center. Revista Portuguesa de Cardiologia, 42, 603-612. 10.1016/j.repc.2022.11.006.
- Lopes, D., Puga, H., Teixeira, J., Lima, R., Grilo, J., Dueñas-Pamplona, J. & Ferrera, C. 2024. Comparison of RANS and LES turbulent flow models in a real stenosis. International Journal of Heat and Fluid Flow, 107. 10.1016/j.ijheatfluidflow.2024.109340.
- Lopez-Marco, A., Adams, B. & Oo, A. Y. 2022. Retrograde type A aortic dissection: A different evil. Interactive Cardiovascular and Thoracic Surgery, 35. 10.1093/icvts/ivac264.
- Lortz, J., Papathanasiou, M., Rammos, C., Steinmetz, M., Lind, A., Tsagakis, K., Schlosser, T., Jakob, H., Rassaf, T. & Jánosi, R. A. 2019. High intimal flap mobility assessed by intravascular ultrasound is associated with better shortterm results after TEVAR in chronic aortic dissection. Scientific Reports, 9. 10.1038/s41598-019-43856-6.
- Loudon, C. & Tordesillas, A. 1998. The use of the Dimensionless Womersley Number to Characterize the Unsteady Nature of Internal Flow. Journal of Theoretical Biology. 10.1006/jtbi.1997.0564.
- Lovatt, S., Wong, C. W., Schwarz, K., Borovac, J. A., Lo, T., Gunning, M., Phan, T., Patwala, A., Barker, D., Mallen, C. D. & Kwok, C. S. 2022. Misdiagnosis of aortic dissection: A systematic review of the literature. American Journal of Emergency Medicine, 53, 16-22. 10.1016/j.ajem.2021.11.047.
- Lu, Y., Xue, Y., Zhang, H., Xie, W., Zhao, W., Wang, D. & Zhou, Q. 2020.

 Management strategy of Type A aortic dissection in a developing center from China: 16 Years experiences. Journal of Thoracic Disease, 12, 6780-6788. 10.21037/jtd-20-1866.
- Luebke, T. & Brunkwall, J. 2014. Type B Aortic Dissection. *AORTA*. Thieme Medical Publishers, Inc. 10.12945/j.aorta.2014.14-040.

- Ma, Z., Jin, L., Zhang, L., Yang, Y., Tang, Y., Gao, P., Sun, Y. & Li, M. 2023. Diagnosis of Acute Aortic Syndromes on Non-Contrast CT Images with Radiomics-Based Machine Learning. Biology, 12. 10.3390/biology12030337.
- MacGillivray, T. E., Gleason, T. G., Patel, H. J., Aldea, G. S., Bavaria, J. E., Beaver, T. M., Chen, E. P., Czerny, M., Estrera, A. L., Firestone, S., Fischbein, M. P., Hughes, G. C., Hui, D. S., Kissoon, K., Lawton, J. S., Pacini, D., Reece, T. B., Roselli, E. E. & Stulak, J. 2022. The Society of Thoracic Surgeons/American Association for Thoracic Surgery Clinical Practice Guidelines on the Management of Type B Aortic Dissection. Annals of Thoracic Surgery, 113, 1073-1092. 10.1016/j.athoracsur.2021.11.002.
- Malek, A. M., Alper, S. L. & Izumo, S. 1999. Hemodynamic Shear Stress and Its Role in Atherosclerosis. 10.1001/jama.282.21.2035.
- Manchester, E. L., Pirola, S., Salmasi, M. Y., O'Regan, D. P., Athanasiou, T. & Xu, X. Y. 2021. Analysis of Turbulence Effects in a Patient-Specific Aorta with Aortic Valve Stenosis. Cardiovascular Engineering and Technology, 12, 438-453. 10.1007/s13239-021-00536-9.
- Mandigers, T. J., Ramella, A., Bissacco, D., Domanin, M., van Herwaarden, J. A., Heijmen, R., Luraghi, G., Migliavacca, F. & Trimarchi, S. 2023. Thoracic Stent Graft Numerical Models To Virtually Simulate Thoracic Endovascular Aortic Repair: A Scoping Review. *European Journal of Vascular and Endovascular Surgery*. W.B. Saunders Ltd. 10.1016/j.ejvs.2023.06.006.
- Marin-Castrillon, D. M., Lalande, A., Leclerc, S., Ambarki, K., Morgant, M.-C., Cochet, A., Lin, S., Bouchot, O., Boucher, A. & Presles, B. 2023. 4D segmentation of the thoracic aorta from 4D flow MRI using deep learning.
- Mariotti, A., Celi, S., Antonuccio, M. N. & Salvetti, M. V. 2023. Impact of the Spatial Velocity Inlet Distribution on the Hemodynamics of the Thoracic Aorta. Cardiovascular Engineering and Technology, 14, 713-725. 10.1007/s13239-023-00682-2.
- Markl, M., Frydrychowicz, A., Kozerke, S., Hope, M. & Wieben, O. 2012. 4D flow MRI. *Journal of Magnetic Resonance Imaging*. 10.1002/jmri.23632.
- Markl, M., Kilner, P. J. & Ebbers, T. 2011a. Comprehensive 4D velocity mapping of the heart and great vessels by cardiovascular magnetic resonance. Journal of Cardiovascular Magnetic Resonance, 13, 7-7. 10.1186/1532-429X-13-7.
- Markl, M., Wallis, W., Brendecke, S., Simon, J., Frydrychowicz, A. & Harloff, A. 2010. Estimation of global aortic pulse wave velocity by flow-sensitive 4D MRI. Magnetic Resonance in Medicine, 63, 1575-1582. 10.1002/mrm.22353.
- Markl, M., Wallis, W. & Harloff, A. 2011b. Reproducibility of flow and wall shear stress analysis using flow-sensitive four-dimensional MRI. Journal of Magnetic Resonance Imaging, 33, 988-994. 10.1002/jmri.22519.
- Marlevi, D., Sotelo, J. A., Grogan-Kaylor, R., Ahmed, Y., Uribe, S., Patel, H. J., Edelman, E. R., Nordsletten, D. A. & Burris, N. S. 2021. False lumen pressure estimation in type B aortic dissection using 4D flow cardiovascular magnetic resonance: comparisons with aortic growth. Journal of Cardiovascular Magnetic Resonance, 23. 10.1186/s12968-021-00741-4.
- Marrocco-Trischitta, M. M. & Sturla, F. 2022. Blood flow helical pattern in type III arch configuration as a potential risk factor for type B aortic dissection.

- European Journal of Cardio-thoracic Surgery, 61, 132-139. 10.1093/ejcts/ezab307.
- McDavid, R. M. 2001. Macroscopic Modelling. Encyclopedia of Materials: Science and Technology (Second Edition) 2001, Pages 4720-4732, 4720-4732.
- McElroy, M. & Keshmiri, A. 2018. Impact of Using Conventional Inlet/Outlet Boundary Conditions on Haemodynamic Metrics in a Subject-Specific Rabbit Aorta. Proceedings of the Institution of Mechanical Engineers, Part H: Journal of Engineering in Medicine, 232, 103-113. 10.1177/0954411917699237.
- MdMolla, M. & Paul, M. C. 2017. Large eddy simulation of pulsatile flow through a channel with double constriction. Fluids, 2. 10.3390/fluids2010001.
- Mega, J. L., Opotowsky, A. R., Curillova, Z. & O'Gara, P. T. 2006. Dynamic aortic obstruction in a patient with acute type B dissection. Cardiology in Review, 14, 151-154. 10.1097/01.crd.0000181623.56678.e2.
- Meidert, A. S. & Saugel, B. 2017. Techniques for non-invasive monitoring of arterial blood pressure. *Frontiers in Medicine*. Frontiers Media S.A. 10.3389/fmed.2017.00231.
- Meier, S., Hennemuth, A., Friman, O., Bock, J., Markl, M. & Preusser, T. 2010. Non-invasive 4D Blood Flow and Pressure Quantification in Central Blood Vessels via PC-MRI.
- Meiselman, H. J. & Baskurt, O. K. 2003. Blood rheology and hemodynamics. 10.1055/s-2003-44551.
- Memiç Sancar, K., Kahraman, S., Tükenmez Karakurt, S., Tekin, M., Çörekcioğlu, B., Ateşli, A., Satılmışoğlu, H., Demirci, G. & Yıldız, M. 2022. Subclinical Inflammation As an Independent Risk Factor for All-Cause Mortality in Patients with Left Main Coronary Artery Disease. Koşuyolu Heart Journal, 25, 14-22. 10.51645/khj.2022.m264.
- Meng, J., Mellnick, V. M., Monteiro, S. & Patlas, M. N. 2019. Acute Aortic Syndrome: Yield of Computed Tomography Angiography in Patients With Acute Chest Pain. Canadian Association of Radiologists Journal, 70, 23-28. 10.1016/j.carj.2018.10.011.
- Menichini, C., Cheng, Z., Gibbs, R. G. J. & Xu, X. Y. 2016. Predicting false lumen thrombosis in patient-specific models of aortic dissection. Journal of the Royal Society Interface, 13. 10.1098/rsif.2016.0759.
- Menichini, C., Cheng, Z., Gibbs, R. G. J. & Xu, X. Y. 2018. A computational model for false lumen thrombosis in type B aortic dissection following thoracic endovascular repair. Journal of Biomechanics, 66, 36-43. 10.1016/j.jbiomech.2017.10.029.
- Menichini, C. & Xu, X. Y. 2016. Mathematical modelling of thrombus formation in idealised models of aortic dissection: initial findings and potential applications. Journal of Mathematical Biology, 73, 1205-1226. 10.1007/s00285-016-0986-4.
- Menter, F. R. (1994). Two-equation eddy-viscosity turbulence models for engineering applications. *AIAA Journal*, *32*(8), 1598–1605. https://doi.org/10.2514/3.12149
- Mesri, Y., Niazmand, H. & Deyranlou, A. 2017. Numerical study on fluid-structure interaction in a patient-specific abdominal aortic aneurysm for evaluating

- wall heterogeneity and material model effects on its rupture. Journal of Applied Fluid Mechanics, 10, 1699-1709. 10.29252/jafm.73.245.27678.
- Michel, J. B., Jondeau, G. & Milewicz, D. M. 2018. From genetics to response to injury: Vascular smooth muscle cells in aneurysms and dissections of the ascending aorta. *Cardiovascular Research*. Oxford University Press. 10.1093/cvr/cvy006.
- Moersdorf, R., Treutlein, M., Kroeger, J. R., Ruijsink, B., Wong, J., Maintz, D., Weiss, K., Bunck, A. C., Baeßler, B. & Giese, D. 2019. Precision, reproducibility and applicability of an undersampled multi-venc 4D flow MRI sequence for the assessment of cardiac hemodynamics. Magnetic Resonance Imaging, 61, 73-82. 10.1016/j.mri.2019.05.015.
- Mohajeri, D., Rammos, C., Tsagakis, K., Schlosser, T., Ruhparwar, A., Rassaf, T., Jánosi, R. A. & Lortz, J. 2023. Complications in Patients with Chronic Type B Aortic Dissection (cTBAD)—A Long-Term Analysis. Life, 13. 10.3390/life13030851.
- Mohan, I. V., Laheij, R. J. F. & Harris, P. L. 2001. Risk factors for endoleak and the evidence for stent-graft oversizing in patients undergoing endovascular aneurysm repair. European Journal of Vascular and Endovascular Surgery, 21, 344-349. 10.1053/ejvs.2000.1341.
- Mongeon, F. P., Marcotte, F. & Terrone, D. G. 2016. Multimodality Noninvasive Imaging of Thoracic Aortic Aneurysms: Time to Standardize? *Canadian Journal of Cardiology*. Pulsus Group Inc. 10.1016/j.cjca.2015.09.025.
- Morbiducci, U., Gallo, D., Massai, D., Consolo, F., Ponzini, R., Antiga, L., Bignardi, C., Deriu, M. A. & Redaelli, A. 2010. Outflow conditions for image-based hemodynamic models of the carotid bifurcation: Implications for indicators of abnormal flow. Journal of Biomechanical Engineering, 132. 10.1115/1.4001886.
- Morbiducci, U., Ponzini, R., Gallo, D., Bignardi, C. & Rizzo, G. 2013. Inflow boundary conditions for image-based computational hemodynamics: Impact of idealised versus measured velocity profiles in the human aorta. Journal of Biomechanics, 46, 102-109. 10.1016/j.jbiomech.2012.10.012.
- Moreno, M. J., Ajji, A., Mohebbi-Kalhori, D., Rukhlova, M., Hadjizadeh, A. & Bureau, M. N. 2011. Development of a compliant and cytocompatible microfibrous polyethylene terephthalate vascular scaffold. Journal of Biomedical Materials Research Part B Applied Biomaterials, 97 B, 201-214. 10.1002/jbm.b.31774.
- Moretti, S., Tauro, F., Orrico, M., Mangialardi, N. & Facci, A. L. 2023. Comparative Analysis of Patient-Specific Aortic Dissections through Computational Fluid Dynamics Suggests Increased Likelihood of Degeneration in Partially Thrombosed False Lumen. Bioengineering, 10. 10.3390/bioengineering10030316.
- Morris, L., Stefanov, F., Hynes, N., Diethrich, E. B. & Sultan, S. 2016. An Experimental Evaluation of Device/Arterial Wall Compliance Mismatch for Four Stent-Graft Devices and a Multi-layer Flow Modulator Device for the Treatment of Abdominal Aortic Aneurysms. European Journal of Vascular and Endovascular Surgery, 51, 44-55. 10.1016/j.ejvs.2015.07.041.

- Morrison, T. M., Choi, G., Zarins, C. K. & Taylor, C. A. 2009. Circumferential and longitudinal cyclic strain of the human thoracic aorta: Age-related changes. Journal of Vascular Surgery, 49, 1029-1036. 10.1016/j.jvs.2008.11.056.
- Mourato, A., Valente, R., Xavier, J., Brito, M., Avril, S., de Sá, J. C., Tomás, A. & Fragata, J. 2022. Computational Modelling and Simulation of Fluid Structure Interaction in Aortic Aneurysms: A Systematic Review and Discussion of the Clinical Potential. *Applied Sciences (Switzerland)*. MDPI. 10.3390/app12168049.
- Munshi, B., Parker, L. P., Norman, P. E. & Doyle, B. J. 2020. The application of computational modelling for risk prediction in type B aortic dissection. Journal of Vascular Surgery, 71, 1789-1801.e3. 10.1016/j.jvs.2019.09.032.
- Murillo, H., Molvin, L., Chin, A. S. & Fleischmann, D. 2021. Aortic dissection and other acute aortic syndromes: Diagnostic imaging findings from acute to chronic longitudinal progression. Radiographics, 41, 425-446. 10.1148/rg.2021200138.
- Musajee, M., Katsogridakis, E., Kiberu, Y., Banerjee, C., George, R., Modarai, B., Saratzis, A. & Sandford, B. 2023. Acute Kidney Injury in Patients with Acute Type B Aortic Dissection. European Journal of Vascular and Endovascular Surgery, 65, 256-262. 10.1016/j.ejvs.2022.10.032.
- Mylonas, K. S., Zoupas, I., Tasoudis, P. T., Vitkos, E., Stavridis, G. T. & Avgerinos,
 D. V. 2023. Endovascular Treatment of Type A Aortic Dissection: A
 Systematic Review and Meta-Analysis Using Reconstructed Time-to-Event
 Data. Journal of Clinical Medicine, 12. 10.3390/jcm12227051.
- Naim, W. N. W. A., Ganesan, P. B., Sun, Z., Liew, Y. M., Qian, Y., Lee, C. J., Jansen, S., Hashim, S. A. & Lim, E. 2016. Prediction of thrombus formation using vortical structures presentation in Stanford type B aortic dissection: A preliminary study using CFD approach. Applied Mathematical Modelling, 40, 3115-3127. 10.1016/j.apm.2015.09.096.
- Nappi, F., Gambardella, I., Singh, S. S. A., Salsano, A., Santini, F., Spadaccio, C., Biancari, F., Dominguez, J. & Fiore, A. 2023. Survival following acute type A aortic dissection: a multicenter study. Journal of Thoracic Disease, 15, 6604-6622. 10.21037/jtd-23-1137.
- Nauta, F. J. H., de Beaufort, H. W. L., Conti, M., Marconi, S., Kamman, A. V., Ferrara, A., van Herwaarden, J. A., Moll, F. L., Auricchio, F. & Trimarchi, S. 2017. Impact of thoracic endovascular aortic repair on radial strain in an ex vivo porcine model. European Journal of Cardio-thoracic Surgery, 51, 783-789. 10.1093/ejcts/ezw393.
- Nauta, F. J. H., Trimarchi, S., Kamman, A. V., Moll, F. L., Van Herwaarden, J. A., Patel, H. J., Figueroa, C. A., Eagle, K. A. & Froehlich, J. B. 2016. Update in the management of type B aortic dissection. *Vascular Medicine (United Kingdom)*. SAGE Publications Ltd. 10.1177/1358863X16642318.
- Nguyen, L. A., Houriez-Gombaud-Saintonge, S., Puymirat, E., Gencer, U., Dietenbeck, T., Bouaou, K., De Cesare, A., Bollache, E., Mousseaux, E., Kachenoura, N. & Soulat, G. 2023. Aortic Stiffness Measured from Either 2D/4D Flow and Cine MRI or Applanation Tonometry in Coronary Artery Disease: A Case–Control Study. Journal of Clinical Medicine, 12. 10.3390/jcm12113643.

- Nguyen, Y. & Bora, V. 2023. Arterial Pressure Monitoring. StatPearls.
- Nienaber, C. A. & Clough, R. E. Management of acute aortic dissection. The Lancet, 2015/2// 2015. Lancet Publishing Group, 800-811. 10.1016/S0140-6736(14)61005-9.
- Nienaber, C. A., Kische, S., Skriabina, V. & Ince, H. 2009. Noninvasive imaging approaches to evaluate the patient with known or suspected aortic disease. *Circulation: Cardiovascular Imaging.* 10.1161/CIRCIMAGING.109.850206.
- Nienaber, C. A. & Yuan, X. 2022. Taming Hypertension to Prevent Aortic Dissection: Universal Recognition of a "new Normal" Blood Pressure? *Circulation*. Lippincott Williams and Wilkins. 10.1161/CIRCULATIONAHA.121.058133.
- O'Rourke, M. F., Blazek, J. V., Morreels, C. L. & Krovetz, L. J. 1968. Pressure Wave Transmission along the Human Aorta. Circulation Research, 23, 567-579. 10.1161/01.res.23.4.567.
- Olson, S. L., Wijesinha, M. A., Panthofer, A. M., Blackwelder, W. C., Upchurch, G. R., Terrin, M. L., Curci, J. A., Baxter, B. T. & Matsumura, J. S. 2021. Evaluating Growth Patterns of Abdominal Aortic Aneurysm Diameter with Serial Computed Tomography Surveillance. JAMA Surgery, 156, 363-370. 10.1001/jamasurg.2020.7190.
- Ong, C. W., Wee, I., Syn, N., Ng, S., Leo, H. L., Richards, A. M. & Choong, A. M. T. L. 2020. Computational Fluid Dynamics Modelling of Hemodynamic Parameters in the Human Diseased Aorta: A Systematic Review. Annals of Vascular Surgery, 63, 336-381. 10.1016/j.avsg.2019.04.032.
- Ong, C. W., Xiong, F., Kabinejadian, F., Praveen Kumar, G., Cui, F. S., Chen, G., Ho, P. & Leo, H. L. 2019. Hemodynamic analysis of a novel stent graft design with slit perforations in thoracic aortic aneurysm. Journal of Biomechanics, 85, 210-217. 10.1016/j.jbiomech.2019.01.019.
- Orelaru, F., Monaghan, K., Ahmad, R. A., Amin, K., Titsworth, M., Yang, J., Kim, K. M., Fukuhara, S., Patel, H. & Yang, B. Midterm outcomes of open repair versus endovascular descending thoracic aortic aneurysm repair. JTCVS Open, 2023/12// 2023. Elsevier B.V., 25-35. 10.1016/j.xjon.2023.09.034.
- Osswald, A., Karmonik, C., Anderson, J. R., Rengier, F., Karck, M., Engelke, J., Kallenbach, K., Kotelis, D., Partovi, S., Böckler, D. & Ruhparwar, A. 2017. Elevated Wall Shear Stress in Aortic Type B Dissection May Relate to Retrograde Aortic Type A Dissection: A Computational Fluid Dynamics Pilot Study. European Journal of Vascular and Endovascular Surgery, 54, 324-330. 10.1016/j.ejvs.2017.06.012.
- Padro, T., Manfrini, O., Bugiardini, R., Canty, J., Cenko, E., de Luca, G., Duncker, D. J., Eringa, E. C., Koller, A., Tousoulis, D., Trifunovic, D., Vavlukis, M., de Wit, C., & Badimon, L. (2020). ESC Working Group on Coronary Pathophysiology and Microcirculation position paper on "coronary microvascular dysfunction in cardiovascular disease." In *Cardiovascular Research* (Vol. 116, Issue 4, pp. 741–755). Oxford University Press. https://doi.org/10.1093/cvr/cvaa003
- Papakonstantinou, P. E., Benia, D., Polyzos, D., Papakonstantinou, K., Rorris, F. P., Toulgaridis, F., Manousiadis, K., Xydonas, S. & Sideris, A. 2022. Chronic

- Thoracic Aortic Dissection: How to Treat, When to Intervene. *Life*. MDPI. 10.3390/life12101511.
- Pape, L. A., Awais, M., Woznicki, E. M., Suzuki, T., Trimarchi, S., Evangelista, A., Myrmel, T., Larsen, M., Harris, K. M., Greason, K., Di Eusanio, M., Bossone, E., Montgomery, D. G., Eagle, K. A., Nienaber, C. A., Isselbacher, E. M. & O'Gara, P. 2015. Presentation, diagnosis, and outcomes of acute aortic dissection: 17-year trends from the international registry of acute aortic dissection. Journal of the American College of Cardiology, 66, 350-358. 10.1016/j.jacc.2015.05.029.
- Parker, L. P., Reutersberg, B., Syed, M. B. J., Munshi, B., Richards, S., Kelsey, L. J., Sakalihasan, N., Eckstein, H. H., Norman, P. E. & Doyle, B. J. 2022. Proximal false lumen thrombosis is associated with low false lumen pressure and fewer complications in type B aortic dissection. Journal of Vascular Surgery, 75, 1181-1190.e5. 10.1016/j.jvs.2021.10.035.
- Pathrose, A., Ma, L., Berhane, H., Scott, M. B., Chow, K., Forman, C., Jin, N., Serhal, A., Avery, R., Carr, J. & Markl, M. 2021. Highly accelerated aortic 4D flow MRI using compressed sensing: Performance at different acceleration factors in patients with aortic disease. Magnetic Resonance in Medicine, 85, 2174-2187. 10.1002/mrm.28561.
- Peacock, J., Jones, T., Tock, C. & Lutz, R. 1998. The onset of turbulence in physiological pulsatile flow in a straight tube. Experiments in Fluids, 24, 1-9. 10.1007/s003480050144.
- Pegolotti, L., Pfaller, M. R., Rubio, N. L., Ding, K., Brugarolas Brufau, R., Darve, E. & Marsden, A. L. 2024. Learning reduced-order models for cardiovascular simulations with graph neural networks. Computers in Biology and Medicine, 168. 10.1016/j.compbiomed.2023.107676.
- Pepe, A., Li, J., Rolf-Pissarczyk, M., Gsaxner, C., Chen, X., Holzapfel, G. A. & Egger, J. 2020. Detection, segmentation, simulation and visualization of aortic dissections: A review. Medical Image Analysis, 65. 10.1016/j.media.2020.101773.
- Pepe, A., Melito, G. M. & Egger, J. 2023. Segmentation of the Aorta Towards the Automatic Segmentation, Modelling, and Meshing of the Aortic Vessel Tree from Multicenter Acquisition. 10.1007/978-3-031-53241-2.
- Petroff, D., Czerny, M., Kölbel, T., Melissano, G., Lonn, L., Haunschild, J., Von Aspern, K., Neuhaus, P., Pelz, J., Epstein, D. M., Romo-Avilés, N., Piotrowski, K. & Etz, C. D. 2019. Paraplegia prevention in aortic aneurysm repair by thoracoabdominal staging with 'minimally invasive staged segmental artery coil embolisation' (MIS2ACE): Trial protocol for a randomised controlled multicentre trial. BMJ Open, 9. 10.1136/bmjopen-2018-025488.
- Pirola, S., Cheng, Z., Jarral, O. A., O'Regan, D. P., Pepper, J. R., Athanasiou, T. & Xu, X. Y. 2017. On the choice of outlet boundary conditions for patient-specific analysis of aortic flow using computational fluid dynamics. Journal of Biomechanics, 60, 15-21. 10.1016/j.jbiomech.2017.06.005.
- Pirola, S., Guo, B., Menichini, C., Saitta, S., Fu, W., Dong, Z. & Xu, X. Y. 2019. 4-D Flow mri-based computational analysis of blood flow in patient-specific

- aortic dissection. IEEE Transactions on Biomedical Engineering, 66, 3411-3419. 10.1109/TBME.2019.2904885.
- Pirola, S., Jarral, O. A., O'Regan, D. P., Asimakopoulos, G., Anderson, J. R., Pepper, J. R., Athanasiou, T. & Xu, X. Y. 2018. Computational study of aortic hemodynamics for patients with an abnormal aortic valve: The importance of secondary flow at the ascending aorta inlet. APL Bioengineering, 2. 10.1063/1.5011960.
- Polanczyk, A., Piechota-Polanczyk, A., Domenig, C., Nanobachvili, J., Huk, I. & Neumayer, C. 2018. Computational fluid dynamic accuracy in mimicking changes in blood hemodynamics in patients with acute type IIIb aortic dissection treated with TEVAR. Applied Sciences (Switzerland), 8, 1-14. 10.3390/app8081309.
- Popieluszko, P., Henry, B. M., Sanna, B., Hsieh, W. C., Saganiak, K., Pękala, P. A., Walocha, J. A. & Tomaszewski, K. A. 2018. A systematic review and meta-analysis of variations in branching patterns of the adult aortic arch. Journal of Vascular Surgery, 68, 298-306.e10. 10.1016/j.jvs.2017.06.097.
- Preim, B. & Botha, C. 2014. Image Analysis for Medical Visualization. *Visual Computing for Medicine*. Elsevier. 10.1016/b978-0-12-415873-3.00004-3.
- Qanadli, S. D., Malekzadeh, S., Villard, N., Jouannic, A. M., Bodenmann, D., Tozzi,
 P. & Rotzinger, D. C. 2020. A New Clinically Driven Classification for Acute
 Aortic Dissection. Frontiers in Surgery, 7. 10.3389/fsurg.2020.00037.
- Qiao, A., Yin, W. & Chu, B. 2015. Numerical simulation of fluid–structure interaction in bypassed DeBakey III aortic dissection. Computer Methods in Biomechanics and Biomedical Engineering, 18, 1173-1180. 10.1080/10255842.2014.881806.
- Qiao, Y., Fan, J., Ding, Y., Zhu, T. & Luo, K. 2019a. A primary computational fluid dynamics study of pre-and post-tevar with intentional left subclavian artery coverage in a type b aortic dissection. Journal of Biomechanical Engineering, 141, 1-7. 10.1115/1.4043881.
- Qiao, Y., Luo, K. & Fan, J. 2022. Component quantification of aortic blood flow energy loss using computational fluid-structure interaction hemodynamics. Computer Methods and Programs in Biomedicine, 221, 106826-106826. 10.1016/j.cmpb.2022.106826.
- Qiao, Y., Mao, L., Ding, Y., Fan, J., Zhu, T. & Luo, K. 2020a. Hemodynamic consequences of TEVAR with in situ double fenestrations of left carotid artery and left subclavian artery. Medical Engineering and Physics, 76, 32-39. 10.1016/j.medengphy.2019.10.016.
- Qiao, Y., Mao, L., Ding, Y., Zhu, T., Luo, K. & Fan, J. 2021. Fluid-structure interaction: Insights into biomechanical implications of endograft after thoracic endovascular aortic repair. Computers in Biology and Medicine, 138, 104882-104882. 10.1016/j.compbiomed.2021.104882.
- Qiao, Y., Mao, L., Zhu, T., Fan, J. & Luo, K. 2020b. Biomechanical implications of the fenestration structure after thoracic endovascular aortic repair. Journal of Biomechanics, 99, 109478-109478. 10.1016/j.jbiomech.2019.109478.
- Qiao, Y., Zeng, Y., Ding, Y., Fan, J., Luo, K. & Zhu, T. 2019b. Numerical simulation of two-phase non-Newtonian blood flow with fluid-structure interaction in

- aortic dissection. Computer Methods in Biomechanics and Biomedical Engineering, 22, 620-630. 10.1080/10255842.2019.1577398.
- Ramaekers, M. J. F. G., van der Vlugt, I. B., Westenberg, J. J. M., Perinajová, R., Lamb, H. J., Wildberger, J. E., Kenjereš, S. & Schalla, S. 2024. Flow patterns in ascending aortic aneurysms: Determining the role of hypertension using phase contrast magnetic resonance and computational fluid dynamics. Computers in Biology and Medicine, 172. 10.1016/j.compbiomed.2024.108310.
- Ramaekers, M. J. F. G., Westenberg, J. J. M., Adriaans, B. P., Nijssen, E. C., Wildberger, J. E., Lamb, H. J. & Schalla, S. 2023. A clinician's guide to understanding aortic 4D flow MRI. *Insights into Imaging*. Springer Science and Business Media Deutschland GmbH. 10.1186/s13244-023-01458-x.
- Rausch, M. K. & Humphrey, J. D. 2017. A Computational Model of the Biochemomechanics of an Evolving Occlusive Thrombus. Journal of Elasticity, 129, 125-144. 10.1007/s10659-017-9626-5.
- Rawson, J. V. & Pelletier, A. L. 2013. When to Order Contrast-Enhanced CT. Am Fam Physician. 013;88(5):312-316.
- Reymond, P., Merenda, F., Perren, F., Rü, D. & Stergiopulos, N. 2009. Validation of a one-dimensional model of the systemic arterial tree. Am J Physiol Heart Circ Physiol, 297, 208-222. 10.1152/ajpheart.00037.2009.-A.
- Rissland, P., Alemu, Y., Einav, S., Ricotta, J. & Bluestein, D. 2009. Abdominal aortic aneurysm risk of rupture: Patient-specific FSI simulations using anisotropic model. Journal of Biomechanical Engineering, 131. 10.1115/1.3005200.
- Rodríguez-Palomares, J. F., Dux-Santoy, L., Guala, A., Kale, R., Maldonado, G., Teixidó-Turà, G., Galian, L., Huguet, M., Valente, F., GutiΩrrez, L., González-Alujas, T., Johnson, K. M., Wieben, O., García-Dorado, D. & Evangelista, A. 2018. Aortic flow patterns and wall shear stress maps by 4D-flow cardiovascular magnetic resonance in the assessment of aortic dilatation in bicuspid aortic valve disease. Journal of Cardiovascular Magnetic Resonance, 20. 10.1186/s12968-018-0451-1.
- Rong, L. Q., Palumbo, M. C., Rahouma, M., Meineri, M., Arguelles, G. R., Kim, J., Lau, C., Devereux, R. B., Pryor, K. O., Girardi, L. N., Redaelli, A., Gaudino, M. F. L. & Weinsaft, J. W. 2019. Immediate Impact of Prosthetic Graft Replacement of the Ascending Aorta on Circumferential Strain in the Descending Aorta. European Journal of Vascular and Endovascular Surgery, 58, 521-528. 10.1016/j.ejvs.2019.05.003.
- Rovas, G., Bikia, V. & Stergiopulos, N. 2023. Design and computational optimization of compliance-matching aortic grafts. Frontiers in Bioengineering and Biotechnology, 11. 10.3389/fbioe.2023.1179174.
- Rudenick, P. A., Bijnens, B. H., García-Dorado, D. & Evangelista, A. 2013. An in vitro phantom study on the influence of tear size and configuration on the hemodynamics of the lumina in chronic type B aortic dissections. Journal of Vascular Surgery, 57, 464-474.e5. 10.1016/j.jvs.2012.07.008.
- Rueda-Ochoa, O. L., Bons, L. R., Zhu, F., Rohde, S., El Ghoul, K., Budde, R. P. J., Ikram, M. K., Deckers, J. W., Vernooij, M. W., Franco, O. H., van der Lugt, A., Bos, D., Roos-Hesselink, J. W. & Kavousi, M. 2022. Thoracic Aortic

- Diameter and Cardiovascular Events and Mortality among Women and Men. Radiology, 304, 208-215. 10.1148/radiol.210861.
- Ruiz-Muñoz, A., Guala, A., Dux-Santoy, L., Teixidó-Turà, G., Servato, M. L., Valente, F., Garrido-Oliver, J., Galian-Gay, L., Gutiérrez, L., Fernandez-Galera, R., Casas, G., González-Alujas, T., Cuéllar-Calabria, H., Johnson, K. M., Wieben, O., Ferreira-Gonzalez, I., Evangelista, A. & Rodriguez-Palomares, J. 2022. False lumen rotational flow and aortic stiffness are associated with aortic growth rate in patients with chronic aortic dissection of the descending aorta: a 4D flow cardiovascular magnetic resonance study. Journal of Cardiovascular Magnetic Resonance, 24. 10.1186/s12968-022-00852-6.
- Ruiz-Muñoz, A., Guala, A., Dux-Santoy, L., Teixidó-Turà, G., Valente, F., Garrido-Oliver, J., Galian-Gay, L., Gutiérrez, L., Fernandez-Galera, R., Casas-Masnou, G., González-Alujas, T., Cuéllar-Calabria, H., Carrasco-Poves, A., Morales-Galán, A., Johnson, K. M., Wieben, O., Ferreira-González, I., Evangelista, A. & Rodriguez-Palomares, J. 2024. False lumen hemodynamics and partial thrombosis in chronic aortic dissection of the descending aorta. European Radiology. 10.1007/s00330-023-10513-6.
- Ruszala, M. W., Reimer, A. P., Hickman, R. L., Clochesy, J. M. & Hustey, F. M. 2014. Use of arterial catheters in the management of acute aortic dissection. Air Medical Journal, 33, 326-330. 10.1016/j.amj.2014.06.001.
- Sadi, L., Tønnessen, T. & Pillgram-Larsen, J. 2012. Short and long-term survival in type A aortic dissection justifies the operative risk and effort. Scandinavian Cardiovascular Journal, 46, 45-50. 10.3109/14017431.2011.626439.
- Saitta, S., Guo, B., Pirola, S., Menichini, C., Guo, D., Shan, Y., Dong, Z., Xu, X. Y. & Fu, W. 2021. Qualitative and Quantitative Assessments of Blood Flow on Tears in Type B Aortic Dissection With Different Morphologies. Frontiers in Bioengineering and Biotechnology, 9. 10.3389/fbioe.2021.742985.
- Saitta, S., Maga, L., Armour, C., Votta, E., O'Regan, D. P., Salmasi, M. Y., Athanasiou, T., Weinsaft, J. W., Xu, X. Y., Pirola, S. & Redaelli, A. 2023. Data-driven generation of 4D velocity profiles in the aneurysmal ascending aorta. Computer Methods and Programs in Biomedicine, 233. 10.1016/j.cmpb.2023.107468.
- Sakata, K., Yamashita, A., Takeuchi, K., Matsuo, T., Aoki, M. & Yoshimura, N. 2015. Cardiac Arrest Due to Dynamic Obstruction of Aorta during Course of the Acute Type B Aortic Dissection. Annals of Vascular Diseases, 8, 321-323. 10.3400/avd.cr.15-00028.
- Salmasi, M. Y., Pirola, S., Sasidharan, S., Fisichella, S. M., Redaelli, A., Jarral, O. A., O'Regan, D. P., Oo, A. Y., Moore, J. E., Xu, X. Y. & Athanasiou, T. 2021. High Wall Shear Stress can Predict Wall Degradation in Ascending Aortic Aneurysms: An Integrated Biomechanics Study. Frontiers in Bioengineering and Biotechnology, 9, 1-13. 10.3389/fbioe.2021.750656.
- Santini, F., Montalbano, G., Messina, A., D'Onofrio, A., Casali, G., Viscardi, F., Luciani, G. B. & Mazzucco, A. 2006. Survival and quality of life after repair of acute type A aortic dissection in patients aged 75 years and older justify intervention. European Journal of Cardio-thoracic Surgery, 29, 386-391. 10.1016/j.ejcts.2005.12.016.

- Schenkenfelder, B., Fenz, W., Thumfart, S., Ebenhofer, G., Stübl, G., Lumenta, D. B., Reishofer, G. & Scharinger, J. 2021. Elastic registration of abdominal mri scans and rgb-d images to improve surgical planning of breast reconstruction.
- Schepens, M. A. A. M. 2018. Type B aortic dissection: new perspectives. Journal of Visualised Surgery, 4, 75-75. 10.21037/jovs.2018.03.16.
- Schiffrin, E. L. 2004. Vascular stiffening and arterial compliance: Implications for systolic blood pressure. American Journal of Hypertension, 17, S39-S48. 10.1016/j.amjhyper.2004.08.019.
- Schoenborn, S., Pirola, S., Woodruff, M. A. & Allenby, M. C. 2022. Fluid-Structure Interaction Within Models of Patient-Specific Arteries: Computational Simulations and Experimental Validations. IEEE Reviews in Biomedical Engineering. 10.1109/RBME.2022.3215678.
- Schönfeld, J. C. 1954. Analogy of Hydraulic, Mechanical, Acoustic and Electric Systems. Appl. sci. Res, 3, 417-450. 10.1007/BF02123920.
- Schwarze, R. & Obermeier, F. 2006. Performance and limitations of the unsteady RANS approach. PAMM, 6, 543-544. 10.1002/pamm.200610252.
- Sel, K., Osman, D., Zare, F., Masoumi Shahrbabak, S., Brattain, L., Hahn, J., Inan, O. T., Mukkamala, R., Palmer, J., Paydarfar, D., Pettigrew, R. I., Quyyumi, A. A., Telfer, B., & Jafari, R. (2024). Building Digital Twins for Cardiovascular Health:
- From Principles to Clinical Impact. *Journal of the American Heart Association*. https://doi.org/10.1161/jaha.123.031981
- Sengupta, S., Hamady, M. & Xu, X. Y. 2022. Haemodynamic Analysis of Branched Endografts for Complex Aortic Arch Repair. Bioengineering, 9. 10.3390/bioengineering9020045.
- Shang, E. K., Nathan, D. P., Fairman, R. M., Bavaria, J. E., Gorman, R. C., Gorman, J. H. & Jackson, B. M. Use of computational fluid dynamics studies in predicting aneurysmal degeneration of acute type B aortic dissections. Journal of Vascular Surgery, 2015/8// 2015. Mosby Inc., 279-284. 10.1016/j.jvs.2015.02.048.
- Sherman, T. F. 1981. On Connecting Large Vessels to Small The Meaning of Murray's Law. Journal Gen Physiol, 431-453. https://doi.org/10.1085/jgp.78.4.431.
- Sherrah, A. G., Callaghan, F. M., Puranik, R., Jeremy, R. W., Bannon, P. G., Vallely, M. P. & Grieve, S. M. 2017. Multi-Velocity Encoding Four-Dimensional Flow Magnetic Resonance Imaging in the Assessment of Chronic Aortic Dissection. AORTA, 5, 80-90. 10.12945/j.aorta.2017.16.046.
- Sherrah, A. G., Grieve, S. M., Jeremy, R. W., Bannon, P. G., Vallely, M. P. & Puranik, R. 2015. MRI in Chronic Aortic Dissection: A Systematic Review and Future Directions. *Frontiers in Cardiovascular Medicine*. Frontiers Media S.A. 10.3389/fcvm.2015.00005.
- Shi, Y., Lawford, P. & Hose, R. 2011. Review of Zero-D and 1-D Models of Blood Flow in the Cardiovascular System. 10.1186/1475-925X-10-33.
- Sieren, M. M., Widmann, C., Weiss, N., Moltz, J. H., Link, F., Wegner, F., Stahlberg, E., Horn, M., Oecherting, T. H., Goltz, J. P., Barkhausen, J. & Frydrychowicz, A. 2021. Automated segmentation and quantification of the healthy and diseased aorta in CT angiographies using a dedicated deep

- learning approach. European Society of Radiology. 10.1007/s00330-021-08130-2/Published.
- Skiadopoulos, A., Neofytou, P. & Housiadas, C. 2017. Comparison of blood rheological models in patient specific cardiovascular system simulations. Journal of Hydrodynamics, 29, 293-304. 10.1016/S1001-6058(16)60739-4.
- Song, J., Gao, S., Xie, E., Wang, W., Dai, L., Zhao, R., Zhou, C., Qiu, J. & Yu, C. 2023. Systematic Review of the Application of Computational Fluid Dynamics for Adult Aortic Diseases. *Reviews in Cardiovascular Medicine*. IMR Press Limited. 10.31083/j.rcm2412355.
- Soudah, E., Casacuberta, J., Gamez-Montero, P. J., Pérez, J. S., Rodríguez-Cancio, M., Raush, G., Li, C. H., Carreras, F. & Castilla, R. 2017. Estimation of wall shear stress using 4D flow cardiovascular MRI and computational fluid dynamics. Journal of Mechanics in Medicine and Biology, 17. 10.1142/S0219519417500464.
- Spadaccio, C., Nappi, F., Al-Attar, N., Sutherland, F. W., Acar, C., Nenna, A., Trombetta, M., Chello, M. & Rainer, A. 2016. Old Myths, New Concerns: the Long-Term Effects of Ascending Aorta Replacement with Dacron Grafts. Not All That Glitters Is Gold. Journal of Cardiovascular Translational Research, 9, 334-342. 10.1007/s12265-016-9699-8.
- Spanos, K., Kölbel, T., Rohlffs, F., Heidemann, F., Giannoukas, A. D., Debus, S. E. & Tsilimparis, N. 2019. Intentional Targeted False Lumen Occlusion after Aortic Dissection: A Systematic Review of the Literature. Annals of vascular surgery., 56, 317-329. 10.1016/j.avsg.2018.08.086.
- Stankovic, Z., Allen, B. D., Garcia, J., Jarvis, K. B. & Markl, M. 2013. 4D flow imaging with MRI. Cardiovascular Diagnosis and Therapy. 10.3978/j.issn.2223-3652.2014.01.02.
- Stemkens, B., Paulson, E. S. & Tijssen, R. H. N. 2018. Nuts and bolts of 4D-MRI for radiotherapy. Physics in Medicine and Biology, 63. 10.1088/1361-6560/aae56d.
- Stokes, C., Ahmed, D., Lind, N., Haupt, F., Becker, D., Hamilton, J., Muthurangu, V., von Tengg-Kobligk, H., Papadakis, G., Balabani, S. & Díaz-Zuccarini, V. 2023a. Aneurysmal growth in type-B aortic dissection: assessing the impact of patient-specific inlet conditions on key haemodynamic indices. Journal of The Royal Society Interface, 20. 10.1098/rsif.2023.0281.
- Stokes, C., Bonfanti, M., Li, Z., Xiong, J., Chen, D., Balabani, S. & Díaz-Zuccarini, V. 2021. A novel MRI-based data fusion methodology for efficient, personalised, compliant simulations of aortic haemodynamics. Journal of Biomechanics, 129, 110793-110793. 10.1016/j.jbiomech.2021.110793.
- Stokes, C., Haupt, F., Becker, D., Muthurangu, V., von Tengg-Kobligk, H., Balabani, S. & Díaz-Zuccarini, V. 2023b. The Influence of Minor Aortic Branches in Patient-Specific Flow Simulations of Type-B Aortic Dissection. Annals of Biomedical Engineering. 10.1007/s10439-023-03175-4.
- Sturla, F., Romarowski, R., Alaidroos, M., Secchi, F., Nano, G. & Marrocco-Trischitta, M. M. 2019. Blood Flow Helicity Pattern in Type III Arch Configuration as a Potential Risk Factor for Type B Aortic Dissection. European Journal of Vascular and Endovascular Surgery, 58, e584-e586. 10.1016/j.ejvs.2019.09.058.

- Sturla, F., Votta, E., Stevanella, M., Conti, C. A. & Redaelli, A. 2013. Impact of modelling fluid-structure interaction in the computational analysis of aortic root biomechanics. Medical Engineering and Physics, 35, 1721-1730. 10.1016/j.medengphy.2013.07.015.
- Sueyoshi, E., Sakamoto, I., Hayashi, K., Yamaguchi, T. & Imada, T. 2004. Growth rate of aortic diameter in patients with type B aortic dissection during the chronic phase. Circulation, 110. 10.1161/01.CIR.0000138386.48852.b6.
- Sultan, S., Acharya, Y., Chua Vi Long, K., Hatem, M., Hezima, M., Veerasingham, D., Soliman, O. & Hynes, N. 2023. Management of acute aortic syndrome with evolving individualised precision medicine solutions: Lessons learned over two decades and literature review. Frontiers in Surgery, 10. 10.3389/fsurg.2023.1157457.
- Sultan, S., Acharya, Y., Hazima, M., Salahat, H., Parodi, J. C. & Hynes, N. 2021. Combined thoracic endovascular aortic repair and endovascular aneurysm repair and the long-term consequences of altered cardiovascular haemodynamics on morbidity and mortality: Case series and literature review. European Heart Journal Case Reports, 5, 1-10. 10.1093/ehjcr/ytab339.
- Sultan, S., Acharya, Y., Soliman, O., Parodi, J. C. & Hynes, N. 2022. TEVAR and EVAR, the unknown knowns of the cardiovascular hemodynamics; and the immediate and long-term consequences of fabric material on major adverse clinical outcome. *Frontiers in Surgery*. Frontiers Media S.A. 10.3389/fsurg.2022.940304.
- Sun, Z. & Chaichana, T. 2016. A systematic review of computational fluid dynamics in type B aortic dissection. International Journal of Cardiology, 210, 28-31. 10.1016/j.ijcard.2016.02.099.
- Sundström, E. & Laudato, M. 2023. Machine Learning-Based Segmentation of the Thoracic Aorta with Congenital Valve Disease Using MRI. Bioengineering, 10. 10.3390/bioengineering10101216.
- Sutera, S. P. & Skalak, R. 1993. The history of Poiseuille's law. Annual Review of Fluid Mechanics. 10.1146/annurev.fl.25.010193.000245.
- Suzuki, T., Mehta, R. H., Ince, H., Nagai, R., Sakomura, Y., Weber, F., Sumiyoshi, T., Bossone, E., Trimarchi, S., Cooper, J. V., Smith, D. E., Isselbacher, E. M., Eagle, K. A. & Nienaber, C. A. 2003. Clinical profiles and outcomes of acute type B aortic dissection in the current era: Lessons from the International Registry of Aortic Dissection (IRAD). Circulation, 108. 10.1161/01.cir.0000087386.07204.09.
- Szabo, L., Raisi-Estabragh, Z., Salih, A., McCracken, C., Ruiz Pujadas, E., Gkontra, P., Kiss, M., Maurovich-Horvath, P., Vago, H., Merkely, B., Lee, A. M., Lekadir, K. & Petersen, S. E. 2022. Clinician's guide to trustworthy and responsible artificial intelligence in cardiovascular imaging. 10.3389/fcvm.2022.1016032.
- Tadic, M., Gherbesi, E., Sala, C., Carugo, S. & Cuspidi, C. 2022. Is Thoracic Aortic Diameter an Independent Predictor of Cardiovascular Disease and Mortality? A Narrative Review. Frontiers in Cardiovascular Medicine. Frontiers Media S.A. 10.3389/fcvm.2022.867026.

- Tadros, R. O., Tang, G. H. L., Barnes, H. J., Mousavi, I., Kovacic, J. C., Faries, P., Olin, J. W., Marin, M. L. & Adams, D. H. 2019. Optimal Treatment of Uncomplicated Type B Aortic Dissection: JACC Review Topic of the Week. *Journal of the American College of Cardiology.* Elsevier USA. 10.1016/j.jacc.2019.07.063.
- Tahir, A. M., Mutlu, O., Bensaali, F., Ward, R., Ghareeb, A. N., Helmy, S. M. H. A., Othman, K. T., Al-Hashemi, M. A., Abujalala, S., Chowdhury, M. E. H., Alnabti, A. R. D. M. H. & Yalcin, H. C. 2023. Latest Developments in Adapting Deep Learning for Assessing TAVR Procedures and Outcomes. *Journal of Clinical Medicine*. Multidisciplinary Digital Publishing Institute (MDPI). 10.3390/jcm12144774.
- Tajeddini, F., Romero, D. A., McClarty, D., Chung, J. & Amon, C. H. 2023.
 Workflow Comparison for Combined 4D MRI/CFD Patient-Specific
 Cardiovascular Flow Simulations of the Thoracic Aorta. Journal of Fluids
 Engineering, Transactions of the ASME, 145. 10.1115/1.4057047.
- Takahashi, K., Sekine, T., Ando, T., Ishii, Y. & Kumita, S. 2022. Utility of 4D Flow MRI in Thoracic Aortic Diseases: A Literature Review of Clinical Applications and Current Evidence. Magnetic Resonance in Medical Sciences, 21, 327-339. 10.2463/mrms.rev.2021-0046.
- Takahashi, K., Sekine, T., Miyagi, Y., Shirai, S., Otsuka, T., Kumita, S. & Ishii, Y. 2021. Four-dimensional flow analysis reveals mechanism and impact of turbulent flow in the dissected aorta. European Journal of Cardio-thoracic Surgery, 60, 1064-1072. 10.1093/ejcts/ezab201.
- Takazawa, A., Asakura, T., Nakazawa, K., Kinoshita, O., Nakajima, H. & Yoshitake, A. 2024. Long-term results of etiology-based thoracic endovascular aortic repair: a single-center experience. Heart and Vessels. 10.1007/s00380-024-02392-8.
- Takeda, Y., Sakata, Y., Ohtani, T., Tamaki, S., Omori, Y., Tsukamoto, Y., Aizawa, Y., Shimamura, K., Shirakawa, Y., Kuratani, T., Sawa, Y., Yamamoto, K., Mano, T. & Komuro, I. 2014. Endovascular aortic repair increases vascular stiffness and alters cardiac structure and function. Circulation Journal, 78, 322-328. 10.1253/circj.CJ-13-0877.
- Takehara, Y. 2022. Clinical Application of 4D Flow MR Imaging for the Abdominal Aorta. *Magnetic Resonance in Medical Sciences*. Japanese Society for Magnetic Resonance in Medicine. 10.2463/mrms.rev.2021-0156.
- Tian, D. H., De Silva, R. P., Wang, T., Yan, T. D. & of Cardiovascular, P. 2014. Open surgical repair for chronic type B aortic dissection: a systematic review Systematic Review Background. Ann Cardiothorac Surg, 3, 340-350. 10.3978/j.issn.2225-319X.2014.07.10.
- Tolenaar, J. L., Froehlich, W., Jonker, F. H. W., Upchurch, G. R., Rampoldi, V., Tsai, T. T., Bossone, E., Evangelista, A., O'Gara, P., Pape, L., Montgomery, D., Isselbacher, E. M., Nienaber, C. A., Eagle, K. A. & Trimarchi, S. 2014. Predicting in-hospital mortality in acute type B aortic dissection evidence from international registry of acute aortic dissection. Circulation, 130, S45-S50. 10.1161/CIRCULATIONAHA.113.007117.

- Tomaiuolo, G. et al., 2014. Biomechanical properties of red blood cells in health and disease towards microfluidics, Biomicrofluidics, 8(5), 051501. 10.1063/1.4895755.
- Tomasi, J., Shao, C., Lederlin, M., Verhoye, J. P., Rochette, M. & Haigron, P. 2023. Fast closed-loop CFD model for patient-specific aortic-dissection management. *Reduced Order Models for the Biomechanics of Living Organs*. Elsevier. 10.1016/b978-0-32-389967-3.00015-9.
- Trahanas, J. M., Jarral, O. A., Long, C. & Hughes, G. C. 2022. Management of chronic type B aortic dissection. Vessel Plus, 6. 10.20517/2574-1209.2021.125.
- Tremblay, D., Zigras, T., Cartier, R., Leduc, L., Butany, J., Mongrain, R. & Leask, R. L. 2009. A Comparison of Mechanical Properties of Materials Used in Aortic Arch Reconstruction. Annals of Thoracic Surgery, 88, 1484-1491. 10.1016/j.athoracsur.2009.07.023.
- Trenti, C., Ziegler, M., Bjarnegård, N., Ebbers, T., Lindenberger, M. & Dyverfeldt, P. 2022. Wall shear stress and relative residence time as potential risk factors for abdominal aortic aneurysms in males: a 4D flow cardiovascular magnetic resonance case—control study. Journal of Cardiovascular Magnetic Resonance, 24. 10.1186/s12968-022-00848-2.
- Trimarchi, S., Tolenaar, J. L., Jonker, F. H. W., Murray, B., Tsai, T. T., Eagle, K. A., Rampoldi, V., Verhagen, H. J. M., Van Herwaarden, J. A., Moll, F. L., Muhs, B. E. & Elefteriades, J. A. Importance of false lumen thrombosis in type B aortic dissection prognosis. Journal of Thoracic and Cardiovascular Surgery, 2013/3// 2013. 10.1016/j.jtcvs.2012.11.048.
- Tsai, T. T., Evangelista, A., Nienaber, C. A., Meinhardt, G., Cooper, J. V., Smith, D. E., Suzuki, T., Fattori, R., Llovet, A., Froehlich, J., Hutchison, S., Distante, A., Sundt, T., Beckman, J., Januzzi, J. L., Isselbacher, E. M. & Eagle, K. A. 2007. Partial Thrombosis of the False Lumen in Patients with Acute Type B Aortic Dissection A BS T R AC T. N Engl J Med, 357;4-357;4. 10.1056/NEJMoa063232.
- Tsai, T. T., Schlicht, M. S., Khanafer, K., Bull, J. L., Valassis, D. T., Williams, D. M., Berguer, R., Eagle, K. A. & Arbor, A. 2008. Tear size and location impacts false lumen pressure in an ex vivo model of chronic type B aortic dissection. 5869, 844-851. 10.1016/j.jvs.2007.11.059.
- Tse, K. M., Chiu, P., Lee, H. P. & Ho, P. 2011. Investigation of hemodynamics in the development of dissecting aneurysm within patient-specific dissecting aneurismal aortas using computational fluid dynamics (CFD) simulations. Journal of Biomechanics, 44, 827-836. 10.1016/j.jbiomech.2010.12.014.
- Uchida, T. & Sadahiro, M. 2018. Thoracic Endovascular Aortic Repair for Acute Aortic Dissection. Annals of Vascular Diseases, 11, 464-472. 10.3400/avd.ra.18-00127.
- Urbanek, T., Biolik, G., Zelawski, W., Hapeta, B., Jusko, M. & Kuczmik, W. 2020. The risk of renal function deterioration in abdominal aortic stent graft patients with and without previous kidney function failure an analysis of risk factors. Polish Journal of Radiology, 85, e643-e649. 10.5114/PJR.2020.102194.

- Valencia-Hernández, C. A., Lindbohm, J. V., Shipley, M. J., Wilkinson, I. B.,
 McEniery, C. M., Ahmadi-Abhari, S., Singh-Manoux, A., Kivimäki, M. &
 Brunner, E. J. 2022. Aortic Pulse Wave Velocity as Adjunct Risk Marker for
 Assessing Cardiovascular Disease Risk: Prospective Study. Hypertension, 79,
 836-843. 10.1161/HYPERTENSIONAHA.121.17589.
- Van Bakel, T. M. J., Arthurs, C. J., Nauta, F. J. H., Eagle, K. A., Van Herwaarden, J. A., Moll, F. L., Trimarchi, S., Patel, H. J. & Figueroa, C. A. 2019. Cardiac remodelling following thoracic endovascular aortic repair for descending aortic aneurysms. European Journal of Cardio-thoracic Surgery, 55, 1061-1070. 10.1093/ejcts/ezy399.
- van Hout, M. J., Scholte, A. J., Juffermans, J. F., Westenberg, J. J., Zhong, L., Zhou, X., Schalla, S. M., Hope, M. D., Bremerich, J., Kramer, C. M., Dewey, M., Ordovas, K. G., Bluemke, D. A. & Lamb, H. J. 2020. How to Measure the Aorta Using MRI: A Practical Guide. *Journal of Magnetic Resonance Imaging*. John Wiley and Sons Inc. 10.1002/jmri.27183.
- van Ooij, P. 2024. Imaging aortic flows in 4D using MRI. *Biomechanics of the Aorta*. Elsevier. 10.1016/B978-0-323-95484-6.00015-4.
- Veger, H. T. C., Pasveer, E. H., Westenberg, J. J. M., Wever, J. J. & van Eps, R. G. S. 2021. Wall Shear Stress Assessment of the False Lumen in Acute Type B Aortic Dissection Visualised by 4-Dimensional Flow Magnetic Resonance Imaging: An Ex-Vivo Study. Vascular and Endovascular Surgery, 55, 696-701. 10.1177/15385744211017117.
- Versteeg, H.K. and Malalasekera, W. (2007) An Introduction to Computational Fluid Dynamics. 2nd Edition, Pearson, London, Chapter 04 & 05.
- Vignali, E., Gasparotti, E., Celi, S. & Avril, S. 2021. Fully-Coupled FSI Computational Analyses in the Ascending Thoracic Aorta Using Patient-Specific Conditions and Anisotropic Material Properties. Frontiers in Physiology, 12. 10.3389/fphys.2021.732561.
- Vignon-Clementel, I. E., Alberto Figueroa, C., Jansen, K. E. & Taylor, C. A. 2006. Outflow boundary conditions for three-dimensional finite element modelling of blood flow and pressure in arteries. Computer Methods in Applied Mechanics and Engineering, 195, 3776-3796. 10.1016/j.cma.2005.04.014.
- Vilacosta, I., San Román, J. A., di Bartolomeo, R., Eagle, K., Estrera, A. L., Ferrera, C., Kaji, S., Nienaber, C. A., Riambau, V., Schäfers, H. J., Serrano, F. J., Song, J. K. & Maroto, L. 2021. Acute Aortic Syndrome Revisited: JACC State-of-the-Art Review. *Journal of the American College of Cardiology*. Elsevier Inc. 10.1016/j.jacc.2021.09.022.
- Von Spiczak, J., Crelier, G., Giese, D., Kozerke, S., Maintz, D. & Bunck, A. C. 2015. Quantitative analysis of vortical blood flow in the thoracic aorta using 4D phase contrast MRI. PLoS ONE, 10. 10.1371/journal.pone.0139025.
- Wada, T., Yamamoto, H., Takagi, D., Kadohama, T., Yamaura, G., Kiryu, K. & Igarashi, I. 2022. Aortic remodelling, reintervention, and survival after zone 0 arch repair with frozen elephant trunks for acute type A aortic dissection: Midterm results. JTCVS Techniques, 14, 29-38. 10.1016/j.xjtc.2022.05.013.
- Wagenseil, J. E. & Mecham, R. P. 2009. Vascular extracellular matrix and arterial mechanics. *Physiological Reviews*. 10.1152/physrev.00041.2008.

- Wan Ab Naim, W. N., Ganesan, P. B., Sun, Z., Osman, K. & Lim, E. 2014. The impact of the number of tears in patient-specific Stanford type b aortic dissecting aneurysm: CFD simulation. Journal of Mechanics in Medicine and Biology, 14. 10.1142/S0219519414500171.
- Wang, Q., Guo, X., Brooks, M., Chuen, J., Poon, E. K. W., Ooi, A. & Lim, R. P. 2022. MRI in CFD for chronic type B aortic dissection: Ready for prime time? *Computers in Biology and Medicine*. Elsevier Ltd. 10.1016/j.compbiomed.2022.106138.
- Wang, X., Carpenter, H. J., Ghayesh, M. H., Kotousov, A., Zander, A. C., Amabili, M. & Psaltis, P. J. 2023a. A review on the biomechanical behaviour of the aorta. Journal of the Mechanical Behaviour of Biomedical Materials, 144, 105922-105922. 10.1016/j.jmbbm.2023.105922.
- Wang, Y., Luan, J., Luo, K., Zhu, T. & Fan, J. 2023b. Multi-constituent simulation of thrombosis in aortic dissection. International Journal of Engineering Science, 184. 10.1016/j.ijengsci.2023.103817.
- Wang, Y., Luo, K., Qiao, Y. & Fan, J. 2021. An integrated fluid-chemical model toward modelling the thrombus formation in an idealised model of aortic dissection. Computers in Biology and Medicine, 136. 10.1016/j.compbiomed.2021.104709.
- Wang, Y., Zhou, C., Wu, X., Liu, L. & Deng, L. 2024. Haemodynamic effects of non-Newtonian fluid blood on the abdominal aorta before and after double tear rup-ture. Medical Engineering & Physics, 104205-104205. 10.1016/j.medengphy.2024.104205.
- Wedding, K. L., Draney, M. T., Herfkens, R. J., Zarins, C. K., Taylor, C. A. & Pelc,
 N. J. 2002. Measurement of vessel wall strain using cine phase contrast MRI.
 Journal of Magnetic Resonance Imaging, 15, 418-428. 10.1002/jmri.10077.
- Wee, I., Ong, C. W., Syn, N. & Choong, A. 2018. Computational Fluid Dynamics and Aortic Dissections: Panacea or Panic? Vascular and Endovascular Review, 1, 27-29. 10.15420/ver.2018.8.2.
- Wee, I., Varughese, R. S., Syn, N. & Choong, A. M. T. L. 2019. Non-operative Management of Type A Acute Aortic Syndromes: A Systematic Review and Meta-Analysis. *European Journal of Vascular and Endovascular Surgery*. W.B. Saunders Ltd. 10.1016/j.ejvs.2018.10.015.
- Weiss, G., Wolner, I., Folkmann, S., Sodeck, G., Schmidli, J., Grabenwöger, M., Carrel, T. & Czerny, M. 2012. The location of the primary entry tear in acute type B aortic dissection affects early outcome. European Journal of Cardiothoracic Surgery, 42, 571-576. 10.1093/ejcts/ezs056.
- Wentland, A. L., Grist, T. M. & Wieben, O. 2014. Review of MRI-based measurements of pulse wave velocity: a biomarker of arterial stiffness. Cardiovascular diagnosis and therapy, 4, 193-206. 10.3978/j.issn.2223-3652.2014.03.04.
- Westerhof, N., Cornelis de Vries, Sman. J., & Noordergraaf, A. (1969). Analog studies of the human systemic arterial tree (Vol. 2). Pergamon Press.
- Westerhof, N., Lankhaar, J. W. & Westerhof, B. E. 2009. The arterial windkessel. *Medical and Biological Engineering and Computing*. 10.1007/s11517-008-0359-2.

- Westerhof, N., Stergiopulos, N., Noble, M. I. M. & Westerhof, B. E. 2018. Snapshots of hemodynamics: An aid for clinical research and graduate education. 10.1007/978-3-319-91932-4.
- Weston, M. W., Rhee, K. & Tarbell, J. M. 1996. Compliance and Diameter Mismatch Affect the Wall Shear Rate Distribution Near an End-To-End Anastomosis. Journal of Biomechanics. 0021-9290(95)00028-3.
- Wilson, J. S., Virag, L., Di Achille, P., Karšaj, I. & Humphrey, J. D. 2013. Biochemomechanics of intraluminal thrombus in abdominal aortic aneurysms. *Journal of Biomechanical Engineering*. 10.1115/1.4023437.
- Womersley JR. Method for the calculation of velocity, rate of flow and viscous drag in arteries when the pressure gradient is known. J Physiol. 1955 Mar 28;127(3):553-63. doi: 10.1113/jphysiol.1955.sp005276. PMID: 14368548; PMCID: PMC1365740.
- Wörz, S., Alrajab, A., Arnold, R., Eichhorn, J., von Tengg-Kobligk, H., Schenk, J.-P. & Rohr, K. 3D geometric analysis of the aorta in 3D MRA follow-up pediatric image data. Medical Imaging 2014: Image Processing, 2014/3//2014. SPIE, 90340K-90340K. 10.1117/12.2041755.
- Xiong, Z., Yang, P., Li, D., Qiu, Y., Zheng, T. & Hu, J. 2020. A computational fluid dynamics analysis of a patient with acute non-A-non-B aortic dissection after type I hybrid arch repair. Medical Engineering and Physics, 77, 43-52. 10.1016/j.medengphy.2019.10.019.
- Xu, D. & Avila, M. 2018. The effect of pulsation frequency on transition in pulsatile pipe flow. Journal of Fluid Mechanics, 857, 937-951. 10.1017/jfm.2018.789.
- Xu, H., Baroli, D. & Veneziani, A. 2021a. Global sensitivity analysis for patient-specific aortic simulations: The role of geometry, boundary condition and large eddy simulation modelling parameters. Journal of Biomechanical Engineering, 143, 1-12. 10.1115/1.4048336.
- Xu, H., Li, Z., Dong, H., Zhang, Y., Wei, J., Watton, P. N., Guo, W., Chen, D. & Xiong, J. 2017. Hemodynamic parameters that may predict false-lumen growth in type-B aortic dissection after endovascular repair: A preliminary study on long-term multiple follow-ups. Medical Engineering and Physics, 50, 12-21. 10.1016/j.medengphy.2017.08.011.
- Xu, H., Piccinelli, M., Leshnower, B. G., Lefieux, A., Taylor, W. R. & Veneziani, A. 2018. Coupled Morphological–Hemodynamic Computational Analysis of Type B Aortic Dissection: A Longitudinal Study. Annals of Biomedical Engineering, 46, 927-939. 10.1007/s10439-018-2012-z.
- Xu, H., Xiong, J., Han, X., Mei, Y., Shi, Y., Wang, D., Zhang, M. & Chen, D. 2021b. Computed tomography-based hemodynamic index for aortic dissection. Journal of Thoracic and Cardiovascular Surgery, 162, e165-e176. 10.1016/j.jtcvs.2020.02.034.
- Xu, L., Yang, T., Yin, L., Kong, Y., Vassilevski, Y. & Liang, F. 2020. Numerical simulation of blood flow in aorta with dilation: A comparison between laminar and les modelling methods. CMES Computer Modelling in Engineering and Sciences, 124, 509-526. 10.32604/cmes.2020.010719.
- Yadollahi-Farsani, H., Scougal, E., Herrmann, M., Wei, W., Frakes, D. & Chong, B. 2019. Numerical study of hemodynamics in brain aneurysms treated with flow diverter stents using porous medium theory. Computer Methods in

- Biomechanics and Biomedical Engineering, 22, 961-971. 10.1080/10255842.2019.1609457.
- Yang, B., Norton, E. L., Rosati, C. M., Wu, X., Kim, K. M., Khaja, M. S., Deeb, G. M., Williams, D. M., & Patel, H. J. (2019). Managing patients with acute type A aortic dissection and mesenteric malperfusion syndrome: A 20-year experience. *Journal of Thoracic and Cardiovascular Surgery*, 158(3), 675-687.e4. https://doi.org/10.1016/j.jtcvs.2018.11.127
- Yang, S., Li, X., Chao, B., Wu, L., Cheng, Z., Duan, Y., Wu, D., Zhan, Y., Chen, J., Liu, B., Ji, X., Nie, P. & Wang, X. 2014. Abdominal aortic intimal flap motion characterization in acute aortic dissection: Assessed with retrospective ECG-gated thoracoabdominal aorta dual-source CT angiography. PLoS ONE, 9. 10.1371/journal.pone.0087664.
- Yaşar, E., Duman, Z. M., Timur, B., Bayram, M., Kaplan, M. C. & Kadiroğulları, E. 2023. Fate of the Patent False Lumen of the Descending Aorta After Surgical Treatment for Acute Type 1 Aortic Dissection. Brazilian Journal of Cardiovascular Surgery, 38. 10.21470/1678-9741-2022-0257.
- Yazdi, S. G., Geoghegan, P. H., Docherty, P. D., Jermy, M. & Khanafer, A. 2018. A Review of Arterial Phantom Fabrication Methods for Flow Measurement Using PIV Techniques. *Annals of Biomedical Engineering*. Springer New York LLC. 10.1007/s10439-018-2085-8.
- Yokosawa, S., Nakamura, M., Wada, S., Isoda, H., Takeda, H. & Yamaguchi, T. 2005. Quantitative Measurements on the Human Ascending Aortic Flow Using 2D Cine Phase-Contrast Magnetic Resonance Imaging. JSME International Journal Series C Mechanical Systems, Machine Elements and Manufacturing. 10.1299/jsmec.48.459.
- Youssefi, P., Gomez, A., Arthurs, C., Sharma, R., Jahangiri, M. & Figueroa, C. A. 2018. Impact of patient-specific inflow velocity profile on hemodynamics of the thoracic aorta. Journal of Biomechanical Engineering, 140, 1-14. 10.1115/1.4037857.
- Yuan, Y., Xia, Z., Wang, L., Sun, Q., Wang, W., Chai, C., Wang, T., Zhang, X., Wu, L. & Tang, Z. 2023. Risk factors for in-hospital death in 2,179 patients with acute aortic dissection. Frontiers in Cardiovascular Medicine, 10. 10.3389/fcvm.2023.1159475.
- Zadrazil, I., Corzo, C., Voulgaropoulos, V., Markides, C. N. & Xu, X. Y. 2020. A combined experimental and computational study of the flow characteristics in a Type B aortic dissection: Effect of primary and secondary tear size. Chemical Engineering Research and Design, 160, 240-253. 10.1016/j.cherd.2020.05.025.
- Zhan, S., Hong, S., Shan-Shan, L., Chen-Ling, Y., Lai, W., Dong-Wei, S., Chao-Yang, T., Xian-Hong, S. & Chun-Sheng, W. 2012. Misdiagnosis of Aortic Dissection: Experience of 361 Patients. Journal of Clinical Hypertension, 14, 256-260. 10.1111/j.1751-7176.2012.00590.x.
- Zhang, L., Zhao, Z., Chen, Y., Sun, Y., Bao, J., Jing, Z. & Zhou, J. 2016. Reintervention after endovascular repair for aortic dissection: A systematic review and meta-analysis. Journal of Thoracic and Cardiovascular Surgery, 152, 1279-1288.e3. 10.1016/j.jtcvs.2016.06.027.

- Zhang, X., Mao, B., Che, Y., Kang, J., Luo, M., Qiao, A., Liu, Y., Anzai, H., Ohta, M., Guo, Y. & Li, G. 2023. Physics-informed neural networks (PINNs) for 4D hemodynamics prediction: An investigation of optimal framework based on vascular morphology. Computers in Biology and Medicine, 164. 10.1016/j.compbiomed.2023.107287.
- Zhou, J. C., Zhang, N., Zhang, Z. H., Wang, T. T., Zhu, Y. F., Kang, H., Zhang, W. M., Li, D. L., Li, W. D., Liu, Z. J., Qian, X. M., Zhang, M. Y., Wang, J., Zhou, M., Yang, Z. T., Yu, Y. X., Li, H. Y., Zhang, J., Wang, Y. G., Gao, J. P., Ling, L. & Pan, K. H. 2017. Intensive blood pressure control in patients with acute type B aortic dissection (RAID): Study protocol for randomised controlled trial. Journal of Thoracic Disease, 9, 1369-1374. 10.21037/jtd.2017.03.180.
- Zhou, M., Yu, Y., Chen, R., Liu, X., Hu, Y., Ma, Z., Gao, L., Jian, W. & Wang, L. 2023. Wall shear stress and its role in atherosclerosis. *Frontiers in Cardiovascular Medicine*. Frontiers Media S.A. 10.3389/fcvm.2023.1083547.
- Zhou, S., Xu, L., Hao, L., Xiao, H., Yao, Y., Qi, L. & Yao, Y. 2019. A review on low-dimensional physics-based models of systemic arteries: Application to estimation of central aortic pressure. *BioMedical Engineering Online*. BioMed Central Ltd. 10.1186/s12938-019-0660-3.
- Zhou, Z., Cecchi, A. C., Prakash, S. K. & Milewicz, D. M. 2022. Risk Factors for Thoracic Aortic Dissection. *Genes*. MDPI. 10.3390/genes13101814.
- Zhu, W., Wang, Y., Chen, Y., Liu, J., Zhou, C., Shi, Q., Huang, S., Yang, C., Li, T. & Xiong, B. 2022a. Dynamic Changes in the Aorta During the Cardiac Cycle Analysed by ECG-Gated Computed Tomography. Frontiers in Cardiovascular Medicine, 9, 1-8. 10.3389/fcvm.2022.793722.
- Zhu, Y., Mirsadraee, S., Asimakopoulos, G., Gambaro, A., Rosendahl, U., Pepper, J. & Xu, X. Y. 2021. Association of hemodynamic factors and progressive aortic dilatation following type A aortic dissection surgical repair. Scientific Reports, 11. 10.1038/s41598-021-91079-5.
- Zhu, Y., Mirsadraee, S., Rosendahl, U., Pepper, J. & Xu, X. Y. 2022b. Fluid-Structure Interaction Simulations of Repaired Type A Aortic Dissection: a Comprehensive Comparison With Rigid Wall Models. Frontiers in Physiology, 13. 10.3389/fphys.2022.913457.
- Zhu, Y., Xu, X. Y., Rosendahl, U., Pepper, J. & Mirsadraee, S. 2023. Advanced risk prediction for aortic dissection patients using imaging-based computational flow analysis. *Clinical Radiology*. W.B. Saunders Ltd. 10.1016/j.crad.2022.12.001.
- Zhuang, B., Sirajuddin, A., Zhao, S. & Lu, M. 2021. The role of 4D flow MRI for clinical applications in cardiovascular disease: Current status and future perspectives. *Quantitative Imaging in Medicine and Surgery*. AME Publishing Company. 10.21037/qims-20-1234.
- Zilber, Z. A., Boddu, A., Malaisrie, S. C., Hoel, A. W., Mehta, C. K., Vassallo, P., Burris, N. S., Roldán-Alzate, A., Collins, J. D., François, C. J. & Allen, B. D. 2021. Noninvasive morphologic and hemodynamic evaluation of type b aortic dissection: State of the art and future perspectives. *Radiology:*

- *Cardiothoracic Imaging*. Radiological Society of North America Inc. 10.1148/ryct.2021200456.
- Zimmermann, J., Bäumler, K., Loecher, M., Cork, T. E., Kolawole, F. O., Gifford, K., Marsden, A. L., Fleischmann, D. & Ennis, D. B. Quantitative Hemodynamics in Aortic Dissection: Comparing in Vitro MRI with FSI Simulation in a Compliant Model. Lecture Notes in Computer Science (including subseries Lecture Notes in Artificial Intelligence and Lecture Notes in Bioinformatics), 2021. Springer Science and Business Media Deutschland GmbH, 575-586. 10.1007/978-3-030-78710-3 55.
- Zimmermann, J., Bäumler, K., Loecher, M., Cork, T. E., Marsden, A. L., Ennis, D. B. & Fleischmann, D. 2023. Hemodynamic Effects of Entry and Exit Tear Size in Aortic Dissection Evaluated with In Vitro Magnetic Resonance Imaging and Fluid-Structure Interaction Simulation. 10.1038/s41598-023-49942-0.
- Zimmermann, J., Demedts, D., Mirzaee, H., Ewert, P., Stern, H., Meierhofer, C., Menze, B. & Hennemuth, A. 2018. Wall shear stress estimation in the aorta: Impact of wall motion, spatiotemporal resolution, and phase noise. Journal of Magnetic Resonance Imaging, 48, 718-728. 10.1002/jmri.26007.
- Zorrilla, R., Soudah, E. & Rossi, R. 2020. Computational modelling of the fluid flow in type B aortic dissection using a modified finite element embedded formulation. Biomechanics and Modelling in Mechanobiology, 19, 1565-1583. 10.1007/s10237-020-01291-x.